Explaining auditory event-related fields by a dynamical network of oscillators emerging from the anatomical structure of auditory cortex

Dissertation

for the degree of

doctor rerum naturalium (Dr. rer. nat.)

approved by the Faculty of Natural Sciences of Otto von Guericke University Magdeburg

by M.Sc. Aida Hajizadeh

born on 11.06.1989 in Tehran, Iran

Examiner: PD Dr. Reinhard König
Prof. Dr. Nikolaus Weiskopf

Submitted on 21.06.2022
Defended on 26.01.2023

حق با بهار بود، با همان ساقه‌های لخت. بر این پهنه‌ی خاک چیزی هست که به رغم ما ادامه می‌دهد. خوب است که جلوه‌های بودن را به غم و شادی ما نبسته‌اند.

هوشنگ گلشیری (۱۳۱۶-۱۳۷۹)

Spring was right, with those bare twigs. There is something on this soil that goes on in spite of us. Good that the manifestations of being are not tied to our sadness and happiness.[1]

Houshang Golshiri (1938–2000)

---

[1] Unofficial translation

Abstract

Explaining auditory event-related fields by a dynamical network of oscillators emerging from the anatomical structure of auditory cortex

Author: M.Sc. Aida Hajizadeh

Auditory cortex (AC) is part of the auditory system where acoustic stimuli are represented and processed. It plays a central role in different situations such as recognising threats, communication and learning through vocalisation, and expressing emotions through music. One way of studying how human AC functions and how acoustic stimuli are represented in AC is using noninvasive brain imaging techniques such as magnetoencephalography (MEG). Responses to stimuli measured by MEG are called event-related fields (ERFs). Auditory ERFs are distinguishable in their characteristic morphology where a series of deflections can be recognised by their temporal occurrence although there is a certain variability in ERFs across subjects where different deflections occur with different amplitudes and latencies. Source localisation of MEG signals, however, is an ill-posed problem for which there is no unique solution. In this regard, there is an ongoing debate about how ERFs are generated, what they signify, and why they have this specific morphology. By computational modelling of AC, this thesis revisits the generation mechanisms of auditory ERFs. Here, the dynamics of AC are characterised by independent spatiotemporal oscillations, i.e., normal modes, spreading over the entire AC. In so doing, a new view on the generation mechanisms of ERFs is offered and the question about the origin of the variability of ERFs across subjects is addressed.

The computational units of the model are simplified cortical columns consisting of a mean-field excitatory and a mean-field inhibitory cell population which are represented by their own state variables in coupled first-order differential equations. Both cell populations are characterised by nonlinear firing rates and their dynamics are coupled to the dynamics of short-term synaptic depression (STSD), which is governed by its own first-order differential equation. The cortical columns are organised based on the serial core-belt-parabelt network structure of AC, a feature which is central to the mammalian AC. In this thesis, instead of solving the state equations by numerical solvers, where in each simulation only a snippet of the whole possible solution space is revealed, the model dynamics are analysed. This was achieved by linearising the state equations and solving the STSD equation by time-scale separation. In so doing, it could be shown that ERFs emerge from normal modes whose properties depend on the entire AC network structure as well as the input. Unlike the prevailing view that ERFs arise out of the linear combination of activity in discrete sources, in the normal mode view each deflection of an ERF waveform is the result of the constructive or destructive interference pattern of superimposed normal modes. Also, it could be shown that the adaptation of ERFs, i.e., the reduction of ERF magnitude with stimulus repetition, is due to modulations of normal modes where, as a result of STSD, the modulation itself is a function of the temporal pattern of the stimulus sequence.

Moreover, in a combined study with simulated and experimental ERFs it was investigated whether the dynamics of AC, in addition to its gross anatomy, also play a role in the subject-specificity of ERFs. Contrary to the prevailing view on the origin of variability in ERFs across subjects where this variability is attributed to subject-specific cortical gross anatomy, it could be shown that the dynamics of AC also account for the variability of ERFs across subjects. This means that network dynamics, which is a function of the network structure of AC and the excitation-inhibition balance, is reflected in ERF waveforms.

Zusammenfassung

Beschreibung auditorischer ereigniskorrelierter Felder durch ein dynamisches Netzwerk von Oszillatoren, das aus der anatomischen Struktur des auditorischen Kortex hervorgehen

Authorin: M.Sc. Aida Hajizadeh

Der Hörkortex oder auditorische Kortex (AC) ist Teil des auditorischen Systems, in dem akustische Reize repräsentiert und verarbeitet werden. Er spielt eine zentrale Rolle in verschiedenen Situationen, wie das Erkennen von Gefahren, die Kommunikation und das Lernen durch Vokalisationen und für das Ausdrücken von Emotionen mit Musik. Nicht-invasive Bildgebungsverfahren, wie die Magnetoenzephalographie (MEG), sind eine Möglichkeit, die Funktionsweise und die Repräsentation von akustischen Reizen im menschlichen Hörkortex zu untersuchen. Die mit MEG gemessenen Reaktionen auf Reize werden als ereigniskorrelierte Felder („event-related fields"; ERFs) bezeichnet. Auditorische ERFs haben eine charakteristische Morphologie, die sich durch eine zeitliche Abfolge von Ausschlägen auszeichnet. Allerdings gibt es eine gewisse Variabilität der auditorischen ERFs zwischen Probanden, die sich in unterschiedlichen Amplituden und Latenzen der verschiedenen Ausschläge niederschlägt. Außerdem ist die Quellenlokalisierung von MEG-Signalen ein unterbestimmtes und schwieriges Problem, für das es keine eindeutige Lösung gibt. Wie auditorische ERFs tatsächlich erzeugt werden, was sie bedeuten und warum sie diese spezifische Morphologie haben, ist Gegenstand des laufenden wissenschaftlichen Diskurses. In dieser Arbeit werden die Entstehungsmechanismen von auditorischen ERFs mithilfe von mathematischer Modellierung des Hörkortex untersucht. Dabei wird die Dynamik des AC durch Eigenmoden, d. h. raumzeitlich unabhängige Oszillationen, charakterisiert, die sich über den gesamten AC ausbreiten. Dies führt zu einer neuen Sicht auf die Entstehungsmechanismen auditorischer ERFs und auf den Ursprung ihrer Variabilität bei verschiedenen Personen.

Die Recheneinheiten des Modells sind vereinfachte kortikale Kolumnen, die aus einer exzitatorischen und einer inhibitorischen Zellpopulation im Mean-Field bestehen. Beide Zellpopulationen werden durch ihre Zustandsvariablen in gekoppelten Differentialgleichungen erster Ordnung beschrieben. Sie sind gekennzeichnet durch nicht-lineare Feuerraten. Zusätzlich ist ihre Dynamik mit der Dynamik der kurzzeitigen synaptischen Depression („short-term synaptic depression“, STSD) gekoppelt, die auch durch eine eigene Differentialgleichung erster Ordnung beschrieben wird. Die kortikalen Kolumnen sind auf der Grundlage der seriellen Core-Belt-Parabelt-Netzwerkstruktur des Hörkortex organisiert - ein Merkmal, das für den AC der Säugetiere charakteristisch ist.

Bei der numerischen Lösung der Zustandsgleichungen stellt jede Simulation nur einen kleinen Ausschnitt des gesamten möglichen Lösungsraums dar. Daher wird in dieser Arbeit die Modelldynamik analysiert. Dies wurde durch Linearisierungen der Zustandsgleichungen erreicht, sowie durch Zeitskalentrennung beim Lösen der STSD-Gleichung. Auf diese Weise konnte gezeigt werden, dass auditorische ERFs aus Eigenmoden entspringen, deren Eigenschaften von der gesamten AC-Netzwerkstruktur und den Eingängen abhängen. Im Gegensatz zu der vorherrschenden Ansicht, dass auditorische ERFs als Linearkombination von Aktivität in diskreten Quellen entstehen, ist nach diesem Modell jede Auslenkung einer ERF-Wellenform das Ergebnis von konstruktiven oder destruktiven Interferenzmustern von überlagerten Eigenmoden. Es konnte auch gezeigt werden, dass die Adaption der auditorischen ERFs, d. h. die Verringerung der ERF-Magnitude bei Reizwiederholung auf Modulationen der Eigenmoden zurückgeführt werden kann. Dabei ist die Modulation selbst, und als Konsequenz von STSD, eine Funktion der zeitlichen Reizabfolge.

Darüber hinaus wurde in einer kombinierten Studie mit simulierten und experimentellen auditorischen ERFs untersucht, ob auch die Dynamik des AC, zusätzlich zu seiner Anatomie, einen Einfluss auf die Probandenspezifizität der ERFs hat. Entgegen der vorherrschenden Ansicht, dass die Variabilität der ERFs zwischen Probanden auf Unterschiede in der AC-Anatomie zurückzuführen ist, konnte gezeigt werden, dass die Dynamik des AC auch für diese Variabilität der ERFs zwischen Probanden verantwortlich ist. Diese Netzwerkdynamik hängt von der Netzwerkstruktur und dem Gleichgewicht zwischen Exzitation und Inhibition ab.

Contents

1 Introduction **1**

1.1 Measuring activity in auditory cortex 2
  1.1.1 Basics of auditory cortex anatomy and neural communication 2
  1.1.2 Basics of electromagnetic activity of brain 3
  1.1.3 Subject-specificity of event-related responses 4
  1.1.4 N1(m) reflects memory in auditory cortex 6
1.2 The generation mechanism of event-related responses 8
1.3 Motivation 10

2 Computational model of auditory cortex **12**

2.1 Unfurling the model of auditory cortex 14
  2.1.1 Linearisation of the firing rate 14
  2.1.2 Non-general solution with symmetric connectivity 15
  2.1.3 Dynamics of the short-term synaptic depression and the slow-fast approximation . 16
2.2 Simulating MEG signals 18

3 Modelling results: novel views on ERF generation **19**

3.1 ERF generation and its adaptation based on normal modes 19
3.2 The topology of auditory cortex contributes to the shape of ERF 22
3.3 Variability of ERFs across subjects 23

4 Discussion **26**

4.1 Main findings 26
4.2 Comparison to other models of ERF generation 27
4.3 Normal modes in the brain 30
4.4 The network structure of the model and the input 31
4.5 Subject-specificity of ERFs 33

Bibliography **35**

5 Explaining event-related fields by a mechanistic model encapsulating the anatomical structure of auditory cortex 42

6 Why do humans have unique auditory event-related fields? Evidence from computational modeling and MEG experiments 68

7 Auditory cortex modelled as a dynamical network of oscillators: understanding event-related fields and their adaptation 87

Declaration of honour 113

Chapter 1

Introduction

Our ability to hear sounds is one of the first senses which develops during the gestational age (Clark-Gambelunghe and Clark, 2015). This allows communication between the fetus and the world outside womb. It also seems that the sense of hearing is "the last to go" (Blundon et al., 2020), which gives the loved ones an opportunity to comfort an unresponsive patient, specifically, those who are at the end of their lives. Also, between the fetal age and the end of one's life hearing plays a key role in survival as well as enjoyment. From survivals perspective, it helps not only humans but also animals to recognise dangerous situations in advance. Our body stays alert in the absence of light or when we are asleep by relying on our sense of hearing together with senses of smell and touch. Hearing also helps us orienting ourselves in space by recognising which objects at which distance and location are around us. Moreover, audition allows communication in the form of vocalisation between different species. Specifically, we humans with the sense of hearing are equipped with the ability to efficiently communicate via vocal languages. Further, sense of hearing brings us colorful feelings by music. We tend to move our body to the beats of a cheerful music even if we are exhausted at the end of a day. A piece of music can soothe the pain at a time of despair or an other piece of music becomes a part of the collective memory and cultural identity of a nation or multiple nations. It helps us feel power and unity with others when we hear a crowd chants slogans during a demonstration or a competition.

There are, certainly, different and complicated brain circuitries involved in all the aforementioned tasks. However, all these great abilities require a correctly functioning auditory system in the first place. Nevertheless, these abilities which hearing endows us with is restricted by the structure of the human brain, and, in the context of this thesis, the structure of the auditory system. For example, we do not perceive the complete soundscape but a soundscape which the structure of our brain allows for. In particular, we are only able to hear sound frequencies between 20 Hz to 20 kHz while we are deaf to the other frequencies (Schnupp et al., 2011). Even for this frequency range, the sound should be audible so that it would be processed further in different stations along the auditory pathway up to the auditory cortex. Therefore, in order to find out how our hearing works, we need to understand the structure of the auditory system and the way sounds, vibrations of molecules in terms of compression and decompression in a medium, are registered, processed, and represented in our brain. In this vein, there are different tasks which the auditory system needs to solve in order to deal with an acoustic environment: (1) sound localisation, (2) spectral analysis and integration, and (3) temporal integration of sounds (Schnupp et al., 2011). Sound localisation takes place in the subcortical areas (Grothe et al., 2010) and the spectral analysis of sounds starts already in the cochlea where on the basilar membrane the frequency content of sounds are first mapped (von Békésy and Wever, 1960). This tonotopic organization is preserved along the auditory pathway up to the auditory cortex (Kaas and Hackett, 2000; Saenz and Langers, 2013). Unlike sound localisation and spectral analysis, the temporal and spectral integration of sounds seem to occur in the auditory cortex where finally all the information from a sound source unites over time and is represented in terms of cortical neural activity (Nelken, 2004).

In order to understand how the auditory cortex functions and how stimuli are represented in auditory cortex, we can probe it in different conditions and measure its neural activity. One can study neural activity in the human auditory cortex by different measuring techniques. For example, electroencephalography (EEG) and magnetoencephalography (MEG) are noninvasive techniques which, due to their high temporal resolution, are suitable for measuring neural activity in the cortex. However, these techniques only *reflect* cortical neural activity which appear in terms of electromagnetic waves in the brain. Moreover, source localisation of MEG and EEG signals is an ill-posed inverse problem. Therefore, we need to first understand what we measure and how the neural activity is translated by our measuring techniques into *reflections* which we call brain signals.

1.1 Measuring activity in auditory cortex

Electroencephalography and magnetoencephalography have a high temporal resolution and, therefore, are ideal for studying cortical activity propagation which has a time scale of milliseconds. In addition to a high temporal resolution, EEG and MEG are acoustically silent measurement devices which make them superior for auditory experiments compared to functional magnetic resonance imaging. The cellular and electrophysiological basis behind the EEG and MEG signals are well-established. In Sects. 1.1.1 and 1.1.2, I briefly review textbook knowledge on the basics of the neural communication and the general biophysics behind the generation of the EEG and MEG signals with a focus on auditory cortex. For a full treatment, see, for example, Williamson and Kaufman (1981); Hämäläinen et al. (1993); Mitzdorf (1994); Buzsáki et al. (2012); Kandel et al. (2013); Ilmoniemi and Sarvas (2019). Specific knowledge on certain topics, however, are cited accordingly.

1.1.1 Basics of auditory cortex anatomy and neural communication

Cerebral cortex is the outer layer of the brain which is characterised by its gyrification and has a laminar structure. The grooves and folds are called sulcus and gyri, respectively. The cerebral cortex is mainly divided into four lobes: frontal, parietal, occipital, and temporal lobe. The auditory cortex of humans is part of the temporal lobe and is located inside the lateral sulcus, a deep cut in the cortex which is visible on the lateral view of the human brain. The auditory cortex includes Heschl's gyrus, the planum temporale, and, partly, the superior temporal gyrus (Hackett, 2011) and is subdivided into three main areas which are the core, the belt, and the parabelt. The auditory areas are composed of tonotopically organized fields (Kaas and Hackett, 2000). The core area, also known as the primary auditory cortex, is surrounded by the belt area. The parabelt area is then neighboring the lateral fields of the belt area (Kaas and Hackett, 2000; Nourski et al., 2014; Hackett, 2015). The core area directly receives information from the medial geniculate complex of thalamus and it feeds the information forward serially to the belt and the parabelt areas. In turn, the parabelt area feeds the information via the belt area back to the core (Kaas and Hackett, 2000; Hackett, 2011, 2015).

The computational units of brains are neurons. Neurons are composed of three main parts: cell body (soma), dendrite, and axon. The nucleus is located in the soma which connects the dendrites and the axon. Dendrites and axons are like thin fibers which branch out from the soma. Neurons receive inputs via their dendrites, whereas they send out an output via their axon to their neighbouring neurons. Neurons make contact points with each other via synapses and communicate with each other via chemicals, namely neurotransmitters, which are secreted from the synapses into the synaptic cleft, the space between the synapses. Based on how neurons affect their neighboring cells, they divide into two main groups: excitatory and inhibitory neurons. Excitatory neurons secret specific neurotransmitters which lead to an excitation of the neighboring cells, whereas inhibitory neurons secret neurotransmitters which inhibit the activity of the neighboring cells. Inhibitory and excitatory neurons are also different in their shape. The main excitatory neurons are pyramidal cells which have a long vertical arborization, with respect to soma, and are called apical dendrites. The main class of inhibitory neurons are stellate cells whose shape, unlike the pyramidal cells, is symmetric and like a sphere.

Neurons are separated by their semipermeable membrane from the extracellular space which contains different ions and proteins. The neuronal membrane keeps a potential difference between the inside and the outside of a neuron which is known as the membrane potential. At rest, when a neuron does not receive any input, the membrane potential is roughly at $-70\,\mathrm{mV}$. However, the membrane potential changes when a pre-synaptic neuron receives inputs from post-synaptic neurons. The diffused neurotransmitters from the sending neuron (i.e., pre-synaptic neuron) binds to channels which are located on the synapses of the post-synaptic neuron (i.e., post-synaptic neuron). This action initiates certain dynamics in the post-synaptic neuron which lead to sodium and potassium ions, Na^+ and K^+, flowing into and out of the channels on its membrane. This causes a net current flow along the dendrite and, therefore, a transient change in the membrane potential of the post-synaptic neuron which is known as post-synaptic potential.

1.1.2 Basics of electromagnetic activity of brain

It is believed that the main generator of the MEG and EEG signals are the dendritic currents known as the primary current $\mathbf{J}^{\mathrm{p}}$. The ion flow in the dendrites also exerts a disturbance in the potential of the extracellular space in the proximity of the neuronal membrane. This leads to a current flow in the extracellular space which is known as the volume current $\mathbf{J}^{\mathrm{v}}$. Due to a change in the charge distribution ρ in the extracellular space together with the continuity equation of electromagnetism, i.e., $\partial\rho/\partial t = -\nabla\cdot(\mathbf{J}^{\mathrm{p}} + \mathbf{J}^{\mathrm{v}})$, an electric field $\mathbf{E}$ according to the Gauss' law $\nabla\cdot\mathbf{E} = \rho/\epsilon_0$ is formed, where ϵ_0 is the constant of vacuum permittivity. Simultaneously, the electric field $\mathbf{E}$, according to $\mathbf{J}^{\mathrm{v}} = \sigma\mathbf{E}$, leads to a return current (i.e., the volume current) which closes the circuit. The magnetic field generated by the primary and the volume currents is then picked up by the MEG sensors. The electric field $\mathbf{E}$ from which a potential difference can be computed is the source of EEG signals. The MEG and EEG signals mainly reflect the simultaneous synaptic activity of the pyramidal cells which are organized locally in parallel to each other in the cortex. Note that the inhibitory neurons, due to their topology and three-dimensional symmetric shape, form a closed field which the MEG and EEG sensors cannot detect (Williamson and Kaufman, 1981; Freeman et al., 2009).

In the absence of external stimuli, EEG and MEG record the brain activity at the resting state which appear as low-amplitude oscillations ranging from 0.5 Hz up to 500 Hz (Buzsáki and Watson, 2012). On the other hand, in EEG and MEG brain responses to stimuli appear as a series of waves known as event-related potential (ERP) and event-related field (ERF), respectively (Davis, 1939). ERPs and ERFs are normally buried in ongoing brain oscillations (e.g., alpha oscillations), and other intrinsic noise (e.g., eye blinks and heart beat), and external noise (any noise from the device itself and outside the magnetically shielded chamber in the case of MEG). Therefore, the stimulus needs to be repeated several times in trials with the assumption that the event-related activity is a time-locked deterministic response to the stimulus in a background of stochastic noise with a zero mean (Dawson, 1954). With this assumption, by averaging the continuous EEG and MEG signal with respect to stimulus onset the noise cancels out and the "noise-free" event-related response remains. The final trial-averaged waveform, which is believed to represent the stimulus characteristics and cognitive processes (Näätänen and Picton, 1987), consists of a few landmarks whose occurrences are in common in most subjects. In EEG, these landmarks are a series of peaks and troughs whose extrema appear roughly at 50 ms, 100 ms, and 200 ms after the stimulus onset and are labeled P1, N1, and P2, respectively. The equivalent deflections in the MEG are P1m, N1m, and P2m. Among these deflections, N1(m) is the most prominent one whose magnitude normally is much larger than the P1(m) and the P2(m) (Näätänen and Picton, 1987). The occurrence of N1(m) is common in the event-related response of most subjects and its latency and amplitude show the highest sensitivity to stimulus properties compared to the P1(m) and the P2(m) (Näätänen and Picton, 1987; Roberts et al., 1998).

1.1.3 Subject-specificity of event-related responses

Before making any inference from studying event-related responses, one important question here would be whether event-related responses are reproducible rather than random. There have been several studies showing that the subject-specific event-related responses in terms of ERPs and ERFs are reproducible in time intervals from days to years (for example see; Kileny and Kripal, 1987; Segalowitz and Barnes, 1993; Dalebout and Robey, 1997; Atcherson et al., 2006; Ahonen et al., 2016). Nevertheless, the overall morphology of event-related responses are quite variable from subject to subject so that human subjects can be distinguished by their event-related responses.

The grey waveforms in Fig. 1.1 represent the trial-averaged auditory ERF waveforms acquired from 25 subjects who passively listened to an identical tone presented with a constant stimulus onset interval (SOI). Here, the SOIs are either 7 s or 10 s to avoid effects of amplitude reduction of ERFs due to stimulus repetition (Lü et al., 1992; Sams et al., 1993). Each subject's ERF was chosen from the MEG sensors with the maximum N1m peak magnitude above the posterior part of the right hemisphere (for further details of the experiment, see Hajizadeh et al. (2021)).

The pronounced deflections (i.e., P1m, N1m, and P2m) are identifiable in the ERFs of most subjects. However, these deflections appear with different latencies and magnitudes. This is featured in the inset of Fig. 1.1, where the latency of the N1m from each waveform is plotted against the corresponding amplitude. Also, the rising and the falling flanks of the N1m response occur with different slopes. The variability of the N1m peak across different subjects is also highlighted in the arithmetic mean (black) and standard deviation (red) of the individual waveforms. The maximum value of the arithmetic mean (black) has an amplitude of roughly 300 fT and occurs at around 100 ms post-stimulus. However, the individual waveforms have their N1m peak amplitude ranging from less than 200 fT up to almost 800 fT. The latency of the individual N1m peaks is also scattered between 80 ms and 125 ms. The standard deviation shows variations only from 50 ms post-stimulus and reaches its maximum at around 80 ms where most of the individual waveforms are at their rising flanks of the N1m response. The standard deviation gradually decreases and stays almost constant after 200 ms.

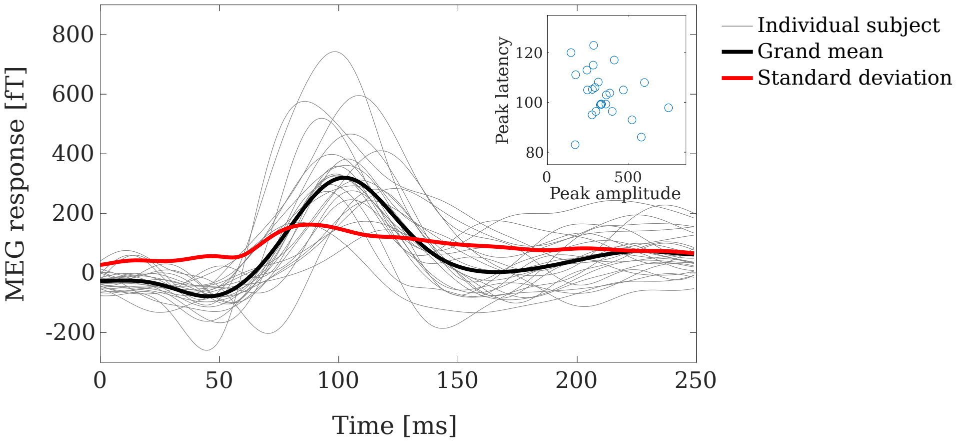

Figure 1.1: Subject-specificity and variability of auditory trial-averaged ERFs: Waveforms from 25 subjects (grey) are shown together with their corresponding arithmetic mean (black) and standard deviation (red). In the inset, the peak latency of the N1m is plotted against the corresponding peak amplitudes. Data and figure are published in Hajizadeh et al. (2021).

In order to trace back where the variability of ERFs across subjects comes from, we can start with Maxwell's equations. The relationship between the current density and the electric and magnetic fields are given in Maxwell's equations whose quasi-static form provides a good approximation for describing the electromagnetic brain activity (Hämäläinen et al., 1993). In this case, the forward solution for computing magnetic fields $\mathbf{B}(\mathbf{r})$ resulting from a current density $\mathbf{J}(\mathbf{r}')$ at a location $\mathbf{r}$ is given by the Ampère-Laplace

(Biot-Savart) law:

$$\mathbf{B}(\mathbf{r}) = \frac{\mu_0}{4\pi} \int \mathbf{J}(\mathbf{r}') \times \frac{\mathbf{r} - \mathbf{r}'}{|\mathbf{r} - \mathbf{r}'|^3} dV'. \tag{1.1}$$

Here, μ_0 is the magnetic permeability of the medium. The integral is computed over the volume V' containing the current density. The magnetic field measured outside the head by the MEG depends on the total current density $\mathbf{J}(\mathbf{r}')$, which is the sum of the primary current $\mathbf{J}^{\mathrm{p}}(\mathbf{r}')$ and the volume current $\mathbf{J}^{\mathrm{v}}(\mathbf{r}')$, and the distance between the current source density and the sensors. Based on Eq. (1.1) the source of variability between ERFs of different subjects can be traced back to (1) dynamics of the electromagnetic activity which is reflected in $\mathbf{J}(\mathbf{r}')$; and (2) the distance from the electromagnetic activity, distributed over an anatomical structure, to the MEG sensors. The study of the anatomy of human brains confirms that there is an inter-subject variability of anatomical structures (see, for example, Heschl, 1878; Rademacher et al., 2001; Morosan et al., 2001; Fischl et al., 2008). Therefore, ERFs should reflect differences in the anatomical structures across subjects. Theoretically, based on Eq. (1.1) dynamics of the brain region under investigation should also contribute to shaping ERF waveforms. This is a topic which has remained under-researched.

1.1.4 N1(m) reflects memory in auditory cortex

An inevitable part of designing experiments with EEG or MEG where event-related responses are measured is to repeat the stimulus. Stimulus repetition leads to a reduction of response magnitude which is known as adaptation or habituation (Megela and Teyler, 1979; Lu et al., 1992; Lü et al., 1992). In EEG and MEG measurements from the auditory cortex, adaptation manifests itself most clearly in the reduction of the event-related potential N1 and its magnetic counterpart N1m peak amplitude which is directly related to the stimulus onset interval between two consecutive stimuli (Hari et al., 1982; Lu et al., 1992). This effect suggests that auditory cortex contains a memory mechanism (Näätänen and Picton, 1987; Lü et al., 1992; Lu et al., 1992; Zacharias et al., 2012); otherwise, the response to subsequent stimuli should have remained invariant with stimulus repetition. When the block-wise stimulus presentation is repeated for several SOIs, it could be shown that the N1(m) peak amplitude is a monotonically increasing function of the time interval between two consecutive stimuli. Lü et al. (1992) and Lu et al. (1992) showed that a single saturating exponential function with three parameters describes the dependency between N1(m) and the SOI. Lü et al. (1992) also showed that the time constant governing the rate at which this exponential function grows estimates the adaptation lifetime and is subject-specific. Also, this time constant was correlated with the behavioural lifetime which indexed the auditory sensory memory in human subjects (Lu et al., 1992; Sams et al., 1993).

A slight modification in the paradigm leading to adaptation of neural activity is when the periodic stimulation of the *standard* stimulus is interrupted by a *deviant* stimulus, which is perceived significantly different from the preceding stimuli. In this paradigm, known as oddball paradigm, neurons elicit an enhanced response to the deviant stimulus rather than a diminished one. This concept was first introduced by Butler (1968) who explained the enhancement in response to the deviant stimulus by the *new units* which are ready to respond, whereas the units responding to the standard stimuli are habituated and, therefore, exhibit a diminished response. In the *memory-based model*, it was suggested that the mismatch response reflects an endogenous cognitive process in the brain which solely encodes change detection (for this view, see, for example, Squires et al., 1975; Näätänen et al., 1978). The oddball paradigm became increasingly important and its link to various cognitive processes and disorders or neurodegenerative diseases were tested (see, for exmaple, Näätänen and Escera, 2000). Also, in the *memory-based model*, mismatch responses are thought to be generated by sources which are different from those generating the N1(m) responses (Näätänen et al., 1978). Later, May et al. (1999) adopted the explanation by Butler (1968) and reformulated it in terms of *fresh afferent neurons*. May and Tiitinen (2010) took an opposite position to the memory-based model and, with computational modelling, showed that the tonotopic organization of auditory cortex and the adaptation of neurons responding to standard stimuli account for the enhanced response of the nonadapted neurons to the deviant stimulus. Unlike the memory-based model, the adaptation model offered a physiological explanation for mismatch generation (May et al., 1999; May and Tiitinen, 2010).

Sensitivity of auditory neural responses to stimulation history is not only reflected in the noninvasive measurements. Invasive measurements from the auditory cortex of several mammals also show sensitivity to stimulation history, that is, the responses of neurons are context sensitive. This was shown in the auditory cortex of macaque monkeys (e.g., Brosch et al., 1999), cats (e.g., Brosch and Schreiner, 2000; Ulanovsky et al., 2003, 2004), rats (e.g., Tasseh et al., 2011), and mice (e.g., Latimer et al., 2019). Therefore, sensitivity of neuronal responses to the historical context seems to be a central feature of the neurons in the mammalian auditory cortex. In this regard, the invasive counterpart of mismatch responses in the single-unit measurements is known as stimulus-specific adaptation (Ulanovsky et al., 2003). Stimulus-specific adaptation does not occur in the single cell recordings from the medial geniculate body of thalamus which is the relay station between the inferior colliculus (IC) in the midbrain and the auditory cortex. Therefore, stimulus-specific adaptation is thought to be a cortical phenomenon (Ulanovsky et al., 2003). It has been shown that stimulus-specific adaptation occurs in different time scales from milliseconds to tens of seconds (Ulanovsky et al., 2004). It was suggested that this property of the neurons in the primary auditory cortex would allow them to dynamically vary their responses and adapt to auditory stimuli with any time scale (Ulanovsky et al., 2004). Ulanovsky et al. (2003) also suggest that stimulus-specific adaptation can be the neural correlates of the mismatch responses measured with EEG and MEG. It is, however, not clear what kind of mechanisms account for stimulus-specific adaptation and other forms of context sensitivity in the auditory cortex (see, for a review, Pérez-González and Malmierca, 2014).

Among possible mechanisms underlying different forms of context sensitivity in the AC, short-term synaptic depression (STSD), which is a form of synaptic plasticity has gained much credibility (Fioravante and Regehr, 2011; Regehr, 2012). Every time a pre-synaptic neuron releases neurotransmitters from the synapses in the synaptic cleft, its synapses undergo depression. There are multiple reasons for this, from which I list the well-established ones here (for a detailed description, see, for example, Forsythe et al., 1998; Zucker and Regehr, 2002; Regehr, 2012). First, there is a limited amount of releasable neurotransmitters and, second, the release site and the calcium channels undergo disensitization, namely they become inactive after repeated stimulation (Regehr, 2012). The voltage-gated calcium channels on the synapses of a pre-synaptic neuron play a central role in the process of neurotransmitter release. They regulate influx of the calcium ions Ca^{2+} into the cell membrane. A complex interplay between the calcium ions and several proteins modulates the neurotransmitter vesicles for docking and priming processes which are essential for the exocytosis of the neurotransmitters into the synaptic cleft (Südhof, 2013). The recovery of the synapses from depression occurs at a similar time scale as the stimulus-specific adaptation occurs (Ulanovsky et al., 2004). Several studies implemented dynamics of STSD in their computational modelling approach and could explain different forms of context sensitivity in the AC. One can name, for example, Loebel et al. (2007); Mill et al. (2011); Yarden and Nelken (2017) who modelled context sensitivity in the AC shown in the invasive measurements and May and Tiitinen (2010); Wang and Knösche (2013); May and Tiitinen (2013); Kudela et al. (2018) who described context sensitivity in the human AC revealed by noninvasive measurements.

1.2 The generation mechanism of event-related responses

Although there is a good understanding and consensus about the biophysics and the physiological basis of the event-related responses, what they represent is still under debate. There are two dominating views on the generation of event-related responses: (1) Event-related responses arise out of the ongoing brain oscillations. These models are either based on the phase-resetting of the ongoing oscillations at the time of stimulus onset (Sayers et al., 1974) or it is based on the alpha oscillations where the stimulus introduces a baseline shift to the ongoing oscillations (Nikulin et al., 2007), also known as amplitude asymmetry (Mazaheri and Jensen, 2010). (2) Stimulus induces an activity in addition to the ongoing oscillations (Dawson, 1954; Shah et al., 2004; Mäkinen et al., 2005). In this view, ongoing oscillations are considered to be noise which cancel out after averaging multiple trials, whereas in the phase-reset and amplitude modulation models ongoing oscillations are required for the generation of event-related responses. In the context of the latter, where a stimulus generates independent activity from the ongoing oscillations, there are computational models which try to explain how the stimulus-induced activity in the auditory cortex forms.

A modelling approach which accounts for event-related responses is dynamic causal modelling (DCM) (Friston, 2005). In explaining evoked responses by dynamic causal modelling, specific assumptions are made which influence the interpretations of brain responses under investigation. These assumptions are briefly summarized here; for a full treatment see Friston et al. (2003) and, for example, Kiebel et al. (2007) and Garrido et al. (2009). The brain activity is modelled by a few sources whose number is an a priori choice. These sources appear in terms of three distinct cortical layers, namely supra-, infra-, and granular layers. The layers are connected with intrinsic connections. The sources are connected via extrinsic excitatory connections of three types: feedforward or bottom-up, feedback or top-down, and lateral. In DCM, the number of sources, the coupling strength between and within the sources which appear in terms of intrinsic and extrinsic connections are free parameters. The best DCM is then the model with a certain number of sources and connections which, based on Bayes' theorem, explains the empirical data best. The event-related responses are then interpreted in terms of the bottom-up, lateral, and top-down modulations between the sources. Wang and Knösche (2013) also implemented DCM in order to describe habituation of activity in the primary auditory cortex in terms of its inter- and intralaminar activity. However, they restricted their analysis to 70–130 ms post-stimulus range where the N1m peak occurs.

Nunez (1981) and Katznelson (1981) have a more holistic approach in explaining spatiotemporal activity of the brain measured by EEG. They suggest that EEG signals appear in terms of traveling electromagnetic waves which originate from the synaptic activity. In their model, the topology of the brain is approximated as spherical shell and the propagation of electromagnetic waves is confined to its surface with periodic boundary conditions. This leads to an interference pattern of the traveling waves resulting in standing waves. In so doing, they could explain the relationship between the cortical source distribution and the scalp potential as a linear combination of spherical harmonics. From physics point of view, spherical harmonics are the fundamental modes of vibration in three-dimensional space of a system given its parameters. The significance of these modes of vibration is that they are independent from each other, that is, excitation of one mode does not drive excitation in other modes. In mathematical terms, these independent modes are a set of orthogonal basis functions. For example, these fundamental modes of vibration also exist on a two-dimensional plane (e.g., a drum) or one-dimensional space (e.g., a string). This general concept is termed normal modes whose properties (e.g., frequency, spatial wave pattern) are functions of the physical features of the oscillating system.

May and Tiitinen (2001) also introduced a computational model which accounts for MEG signals. The dynamics of the model are based on the leaky-integrator neuron and the short-term synaptic depression as the only form of synaptic plasticity. They showed that the model dynamics in its linearised form follow the equation of classical driven harmonic oscillator with damping. These systems are characterised by their natural frequencies which depend on the system's physical properties. In the presence of an external periodic input, the system oscillates at the frequency of the input. The response amplitude, however, depends on the input's frequency. The response amplitude is largest when the frequency of the external input matches with the system's natural frequency. This phenomenon is known as resonance behaviour and the frequency is termed resonance frequency. In this regard, May and Tiitinen (2001) showed that the stimulation rate could be mapped on the neural field where each location (i.e., neural population) is maximally responding to its resonance frequency. Furthermore, they were able to explain omission responses in the MEG and their latency of occurrence which is a function of the stimulation rate. As the name indicates, omission responses occur at the end of tone sequences where there is no stimulus anymore, however, the system keeps oscillating and generating N1m-like responses. Later, May and colleagues developed their computational model further which could account for a wide variety of auditory event-related responses (May and Tiitinen, 2010, 2013; May, 2021).

1.3 Motivation

In sum, there are several models for explaining event-related responses. Each of these models provides different insights to the potential generation mechanisms of event-related responses. With respect to the auditory cortex, however, some models are too global where the entire auditory cortex is represented by just a node (Nunez, 1981; Friston et al., 2003; Ritter et al., 2013). Therefore, in these models the dynamics of auditory cortex remain obscure because the detailed description of auditory cortex is not included. For example, it would not to be feasible to understand and interpret the role of auditory cortex in the ERF adaptation when the model description lacks the dynamics within the auditory cortex. Conversely, some other models are too detailed where only the primary auditory cortex (i.e., core area) is included in the model dynamics (Loebel et al., 2007; Wang and Knösche, 2013; Kudela et al., 2018). Source localisation of auditory event-related responses, however, shows that not only the primary auditory cortex but also the belt and parabelt areas are among the underlying sources of auditory ERP and ERF generation (Näätänen and Picton, 1987; Yvert et al., 2005; Inui et al., 2006). Therefore, computational models which only model the core area would not be able to capture the activity of the entire auditory cortex.

May and colleagues, on the other hand, did include the entire core-belt-parabelt structure of auditory cortex in their modelling approach. They showed that the serial core-belt-parabelt structure together with short-term synaptic depression account for a wide variety of phenomena observed in the auditory cortex, that is, N1m adaptation, mismatch responses in different paradigms, forward suppression and facilitation (May and Tiitinen, 2010, 2013; May et al., 2015). Forward suppression and facilitation are related to responses of neurons to tone pairs, where the response to the second tone is either suppressed or facilitated by the first tone. This observation in the auditory cortex is known also in terms of sequence sensitivity (Brosch et al., 1999; Brosch and Schreiner, 2000). However, the model of May and colleagues is highly nonlinear and, therefore, was so far treated by numerical solvers only. This gives just a snippet of the whole possible solution space in each simulation and only a glimpse of what the model with a given parameter setting is able to achieve. Additionally, due to the nonlinearities it would be very difficult to deduce the impact of different parameters on the solutions. Therefore, the model as such provides little insight on the dynamics of the auditory cortex.

This thesis revisits the generation mechanisms of ERFs. The starting point is the computational model of auditory cortex which is originally developed by May and colleagues (May and Tiitinen, 2010, 2013; May, 2021). However, instead of application of numerical solvers, in this thesis, the system's dynamics are analysed by linearising the state equations and solving the equation representing the dynamics of short-term synaptic depression by time-scale separation. This allows for characterisation of AC dynamics as a superposition of damped harmonic oscillators, so-called normal modes. It is shown that ERFs arise from the interference pattern of superimposed normal modes whose spatiotemporal properties depend on the *entire* network structure of the auditory cortex and the input. With this approach, new views on the potential generation mechanisms of ERFs are offered and mechanistic explanations about their subject-specificity and ERF adaptation are provided.

This thesis is a cumulative dissertation based on the following publications:

1. Hajizadeh et al. (2019): Hajizadeh, A., Matysiak, A., May, P. J. C., König, R., 2019. Explaining event-related fields by a mechanistic model encapsulating the anatomical structure of auditory cortex. Biological Cybernetics 113, 321–345, DOI: 10.1007/s00422-019-00795-9

2. Hajizadeh et al. (2021): Hajizadeh, A., Matysiak, A., Brechmann, A., König, R., May, P. J. C., 2021. Why do humans have unique auditory event-related fields? Evidence from computational modeling and MEG experiments. Psychophysiology 58, e13769, DOI: 10.1111/psyp.13769

3. Hajizadeh et al. (2022): Hajizadeh, A., Matysiak, A., Wolfrum, M., May, P. J. C., König, R., 2022. Auditory cortex modelled as a dynamical network of oscillators: understanding event-related fields and their adaptation. Biological Cybernetics 116, 475–499, DOI:10.1007/s00422-022-00936-7

In Chapter 2, a brief summary of the computational model of auditory cortex and the analysis of its dynamics is introduced. In Chapter 3, a collection of results which are central to the understanding of the normal-mode view on ERFs are presented. In Chapter 4, a general summary and a brief discussion of the results are provided.

Chapter 2

Computational model of auditory cortex

The dynamics of the computational model by May and colleagues were originally inspired by the works of Wilson and Cowan (1972) and Hopfield and Tank (1986). The computational unit is incorporated in terms of cortical columns, each of which consists of a mean-field excitatory and a mean-field inhibitory cell population. These cell populations are characterised by their own state variables $\boldsymbol{u}(t) = (u_1(t), \ldots, u_N(t))^\top$ and $\boldsymbol{v}(t) = (v_1(t), \ldots, v_N(t))^\top$, respectively, where N is the number of columns. The columns do not appear in isolation, but are coupled and arranged based on the well-studied anatomical structure of primates auditory cortex (Hackett, 2015). A schematic diagram of the primates auditory cortex is shown in Fig. 2.1a (Kaas and Hackett, 2000; Hackett, 2015). The core area consists of three fields. It is surrounded by the belt area which consists of eight fields and is laterally neighboring the parabelt area. Dense and sparse connections between the fields are illustrated by the thick and narrow arrows, respectively. The information about the connections between the fields and areas is summarized in a connection matrix shown in Fig. 2.1b.

The activity of the excitatory state variables is modulated by the synaptic efficacy which is characterised by its own variable $\boldsymbol{q}(t) = (q_1(t), \ldots, q_N(t))^\top$. The dynamics of the model are given by the following set of differential equations:

$$\tau_{\mathrm{m}} \dot{\boldsymbol{u}}(t) = -\boldsymbol{u}(t) + W_{\mathrm{ee}} Q(t) \cdot g[\boldsymbol{u}(t)] - W_{\mathrm{ei}} \cdot g[\boldsymbol{v}(t)] + \boldsymbol{i}_{\mathrm{aff,e}}(t), \tag{2.1}$$

$$\tau_{\mathrm{m}} \dot{\boldsymbol{v}}(t) = -\boldsymbol{v}(t) + W_{\mathrm{ie}} \cdot g[\boldsymbol{u}(t)] - W_{\mathrm{ii}} \cdot g[\boldsymbol{v}(t)] + \boldsymbol{i}_{\mathrm{aff,i}}(t), \tag{2.2}$$

$$\dot{\boldsymbol{q}}(t) = -\frac{\boldsymbol{q}(t) g[\boldsymbol{u}(t)]}{\tau_{\mathrm{o}}} + \frac{\boldsymbol{1} - \boldsymbol{q}(t)}{\tau_{\mathrm{rec}}}, \;\; Q(t) = \mathrm{diag}(\boldsymbol{q}(t)). \tag{2.3}$$

Here, τ_{m} is the membrane time constant. The connection between the excitatory (e) and inhibitory (i) cell populations are given by the four weight matrices W_{ee}, W_{ei}, W_{ie}, and W_{ii}. It is assumed that the connections originating from inhibitory cell populations, i.e., W_{ei} and W_{ii}, are short-range and, therefore, exist only within a column. However, the connections originating from excitatory cell populations, i.e., W_{ie} and W_{ee}, are long-range and, therefore, exist also between the columns. Further, W_{ee} encapsulates the connections across fields of the auditory cortex (Fig. 2.1b), which means the inter-field connections have been assumed to be of excitatory type only. The firing rate function is defined as

$$\begin{cases} g[\boldsymbol{u}(t)] = \tanh[\alpha(\boldsymbol{u} - \theta)], & \boldsymbol{u}(t) > \theta \\ g[\boldsymbol{u}(t)] = 0, & \boldsymbol{u}(t) \leq \theta \end{cases} \tag{2.4}$$

where θ is a constant threshold and α is a scalar. The same firing rate function represented in Eq. (2.4) also holds for the inhibitory cell population $\boldsymbol{v}(t)$. The afferent input to the excitatory and inhibitory cell populations are represented by $\boldsymbol{i}_{\mathrm{aff,e}}(t)$ and $\boldsymbol{i}_{\mathrm{aff,i}}(t)$, respectively. As Eq. (2.1) indicates, the dynamics of the excitatory state variables are coupled with the dynamics of synaptic efficacy whereby the strength of the excitatory-to-excitatory connections are modulated. Synaptic efficacy is regulated by short-term synaptic depression which models the effects of neurotransmitter release and replenishment by the first and the second terms in Eq. (2.3), respectively (Tsodyks and Markram, 1997; Loebel et al., 2007). τ_{o} and τ_{rec} are the time constants of the release and the replenishment of neurotransmitters at each synapse; and $\mathbf{1}$ is the 1-vector of size N. In Eq. (2.3), diag is the operator by which the diagonal matrix $Q(t)$ is constructed from $\boldsymbol{q}(t)$ as a vector.

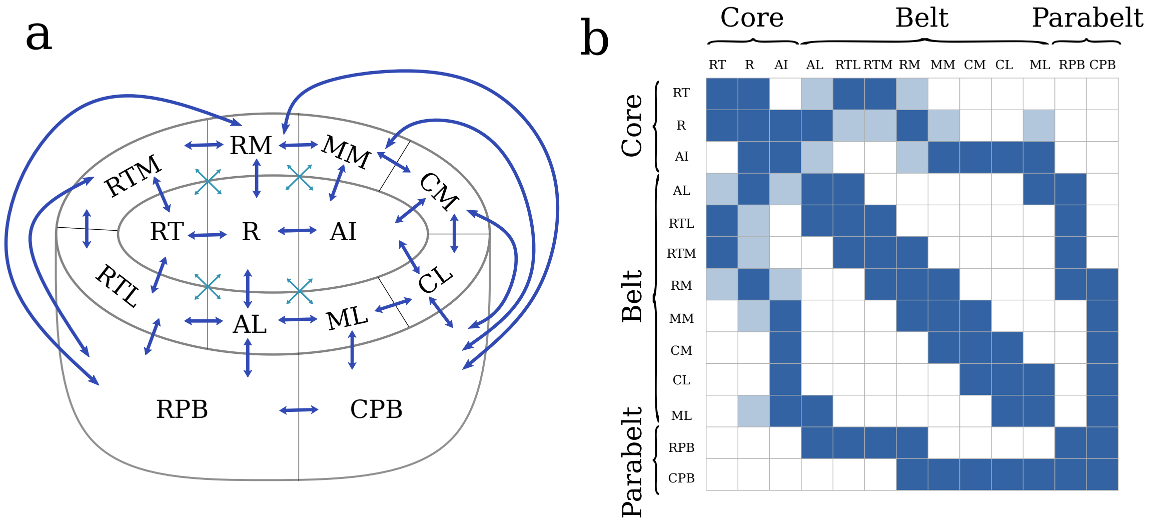

	RT	R	AI	AL	RTL	RTM	RM	MM	CM	CL	ML	RPB	CPB
RT	■	■		▨	■	■	▨						
R	■	■	■	■	▨	▨	■	▨			▨		
AI		■	■	▨			▨	■	■	■	■		
AL	▨	■	▨	■	■						■	■	
RTL	■	▨		■	■	■						■	
RTM	■	▨			■	■	■					■	
RM	▨	■	▨			■	■	■				■	■
MM		▨	■				■	■	■				■
CM			■					■	■	■			■
CL			■						■	■	■		■
ML		▨	■	■						■	■		■
RPB				■	■	■	■					■	■
CPB							■	■	■	■	■	■	■

Figure 2.1: A schematic diagram of the anatomical structure of the model. **a)** There are in total three areas: core, belt, and parabelt. The core area consists of three fields. It has direct strong connections to the eight belt fields which are completely encompassing it. The belt area is the station between the core and parabelt areas as there is no direct physical connection between the core and the parabelt. **b)** The connections in the structure shown in **a** are summarized in an adjacency matrix. The matrix is symmetric representing that there is a feedback connection for any feedforward connection. Strong and weak connections between any two fields are represented by dark and light blue, respectively. White elements indicate no connection between two fields. The diagonal elements represent the lateral (intrafield) connections. The elements above and below the main diagonal represent the feedback and the feedforward connections.

2.1 Unfurling the model of auditory cortex

2.1.1 Linearisation of the firing rate

By assuming that the firing rate function, given in Eq. (2.4), is without a threshold and, therefore, of the form $\tanh(\alpha\boldsymbol{x})$, one can approximate this sigmoid function around zero by a linear function of the form $g[\boldsymbol{x}] = \alpha\boldsymbol{x}$. Here, $\boldsymbol{x}$ stands for $\boldsymbol{u}(t)$ and $\boldsymbol{v}(t)$. In this case, the homogeneous part of Eqs. (2.1) and (2.2) is given by the standard linear system

$$\begin{pmatrix} \dot{\boldsymbol{u}}(t) \\ \dot{\boldsymbol{v}}(t) \end{pmatrix} = M \begin{pmatrix} \boldsymbol{u}(t) \\ \boldsymbol{v}(t) \end{pmatrix} \qquad \text{with} \qquad M = \frac{1}{\tau_{\mathrm{m}}} \begin{pmatrix} \alpha W_{\mathrm{ee}} Q - I & -\alpha W_{\mathrm{ei}} \\ \alpha W_{\mathrm{ie}} & -\alpha W_{\mathrm{ii}} - I \end{pmatrix}, \tag{2.5}$$

where I is the identity matrix. As Eq. (2.5) indicates, the coefficient matrix M includes all the information about the entire connection pattern and their strength in the network of auditory cortex. The general solution to Eq. (2.5) is then given by the linear combinations of normal modes

$$\begin{pmatrix} \boldsymbol{u}(t) \\ \boldsymbol{v}(t) \end{pmatrix} = \sum_{n=1}^{2N} c_n \exp(\lambda_n t) \begin{pmatrix} \boldsymbol{x}_n \\ \boldsymbol{y}_n \end{pmatrix}. \tag{2.6}$$

Here, $\lambda_n \in \mathbb{C}$, $n = 1, \ldots, 2N$ are the eigenvalues of the coefficient matrix M in Eq. (2.5). The eigenvectors $(\boldsymbol{x}_n, \boldsymbol{y}_n)^\top$ are the normal modes, where $\boldsymbol{x}_n$ and $\boldsymbol{y}_n$ represent the collection of the $\boldsymbol{u}$ and $\boldsymbol{v}$ components of the n-th eigenvector. The eigenvalues $\lambda_n = \gamma_n + i\omega_n$ determine whether M is stable or not. That is, for the stable solutions for any angular frequency ω_n, the corresponding decay rate γ_n has to be a nonzero negative value. If the matrix M is not stable, the solutions are not of the form of damped oscillations. That is, the solutions appear as huge increase in the amplitude ($\gamma_n > 0$) or oscillations without damping ($\gamma_n = 0$ and $\omega_n \neq 0$). If the matrix M is stable, the shape of the mode depends on the values of angular frequency. That is, if $\omega_n \neq 0$ or $\omega_n = 0$, the normal mode is of the underdamped or overdamped type, respectively. Underdamped normal modes oscillate around the equilibrium and their amplitude decays gradually to zero. Conversely, overdamped normal modes after excitation decay to the equilibrium without oscillating. For a specific initial condition $(\boldsymbol{u}(0), \boldsymbol{v}(0))^\top = (\boldsymbol{u}_0, \boldsymbol{v}_0)^\top$, the coefficients c_n are given as scalar products

$$c_n = \left\langle \begin{pmatrix} \boldsymbol{u}_0 \\ \boldsymbol{v}_0 \end{pmatrix}, \begin{pmatrix} \boldsymbol{\xi}_n \\ \boldsymbol{\eta}_n \end{pmatrix} \right\rangle, \tag{2.7}$$

with the corresponding left eigenvectors $(\boldsymbol{\xi}_n, \boldsymbol{\eta}_n)^\top$ of the coefficient matrix M. When the modes are of the underdamped type, the eigenvalues and their corresponding eigenvectors appear as complex conjugate pairs. Therefore, in this case for real initial values $(\boldsymbol{u}(0), \boldsymbol{v}(0))^\top$ the corresponding pair of complex coefficients c_n has to be complex conjugate as well. The modulus of the complex coefficient c_n is the initial amplitude of the mode whilst its argument provides the initial phase.

2.1.2 Non-general solution with symmetric connectivity

Equation (2.6) shows that the decay rate and the angular frequency of the normal modes depend on the coefficient matrix M which expresses the connections between the neural population within the network. Also, the initial amplitude by which normal modes contribute to the overall solutions are determined by the initial conditions and the left eigenvectors of M (see Eq. (2.7)). However, the actual dependency between the normal mode parameters and the model parameters is not clear. In a special case, we can tease out this information in order to understand how the normal mode parameters depend on the network parameters. To achieve this, together with the assumption of linearity of firing rates, we also assume $Q = I$ in Eq. (2.1). That is, we ignore the dynamics of the short-term synaptic plasticity. Therefore, we can rewrite Eqs. (2.1) and (2.2) as

$$\tau_{\mathrm{m}}\dot{\boldsymbol{u}}(t) + \boldsymbol{u}(t) - W_{\mathrm{ee}} \cdot [\alpha \boldsymbol{u}(t)] + W_{\mathrm{ei}} \cdot [\alpha \boldsymbol{v}(t)] = \boldsymbol{i}_{\mathrm{aff,e}}(t), \tag{2.8}$$

$$\tau_{\mathrm{m}}\dot{\boldsymbol{v}}(t) + \boldsymbol{v}(t) - W_{\mathrm{ie}} \cdot [\alpha \boldsymbol{u}(t)] + W_{\mathrm{ii}} \cdot [\alpha \boldsymbol{v}(t)] = \boldsymbol{i}_{\mathrm{aff,i}}(t). \tag{2.9}$$

We then analyse the system dynamics given in Eqs. (2.8) and (2.9) by taking the derivative of both equations and transforming them into a system of second-order differential equations given by

$$\ddot{\boldsymbol{u}}(t) + 2\Gamma_u \dot{\boldsymbol{u}}(t) + \Omega_{0,u}^2 \boldsymbol{u}(t) = \boldsymbol{h}(t), \tag{2.10}$$

$$\ddot{\boldsymbol{v}}(t) + 2\Gamma_v \dot{\boldsymbol{v}}(t) + \Omega_{0,v}^2 \boldsymbol{v}(t) = \boldsymbol{j}(t), \tag{2.11}$$

where Γ_u and Γ_v represent the damping coefficients and the $\Omega_{0,u}^2$ and $\Omega_{0,v}^2$ represent the angular frequencies of the excitatory and inhibitory state variables, respectively. $\boldsymbol{h}(t)$ and $\boldsymbol{j}(t)$ represent the driving force to the excitatory and inhibitory state variables and are functions of the connection matrices as well as the afferent inputs. The constant coefficients Γ_u, Γ_v, $\Omega_{0,u}^2$, and $\Omega_{0,v}^2$ are functions of the connection matrices shown in Eqs. (2.8) and (2.9) (for details, see Hajizadeh et al., 2019). In the general setting, these coefficients are not diagonal. Therefore, the dynamics of the state variables are coupled to each other where their trajectories can be revealed only by numerical solvers. However, if we can find a matrix, say Υ, by which we simultaneously diagonalise Γ_u and $\Omega_{0,u}^2$, we can decouple the excitatory state variables from each other. The same is true for the inhibitory state variables. This is a nontrivial problem. However, under certain assumptions one can simultaneously diagonalise the damping coefficient and the angular frequency, separately, in Eqs. (2.10) and (2.11). In brief, when W_{ei}, W_{ie}, and W_{ii} are diagonal matrices and W_{ee} is a symmetric matrix, one can perform this simultaneous diagonalisation for both Eqs. (2.10) and (2.11). For further details, see Appendix A2: Derivation of analytical solution in Hajizadeh et al. (2019). In other words, by changing the coordinates we can transform our system into an equivalent space in which the state variables are decoupled, that is, they are independent from each other. In this case, the explicit solutions to the classic driven damped harmonic oscillators given in Eqs. (2.10) and (2.11) are the normal modes u_{d} and v_{d} (Rayleigh, 1945; Caughey, 1960; Caughey and O'Kelly, 1965).

The equation of one normal mode contributing to the excitatory and inhibitory cell populations is given by

$$u_{\mathrm{d}}(t) = \exp(-\gamma_{\mathrm{d}} t)[a_{\mathrm{u_d}} \sin(\delta_{\mathrm{d}} t) + b_{\mathrm{u_d}} \cos(\delta_{\mathrm{d}} t)] + c_{\mathrm{u_d}}, \tag{2.12}$$

$$v_{\mathrm{d}}(t) = \exp(-\gamma_{\mathrm{d}} t)[a_{\mathrm{v_d}} \sin(\delta_{\mathrm{d}} t) + b_{\mathrm{v_d}} \cos(\delta_{\mathrm{d}} t)] + c_{\mathrm{v_d}}. \tag{2.13}$$

Here, the decay rate γ_{d} and the damping frequency δ_{d} are functions of the connection matrices. The coefficients of the harmonic functions, $a_{\mathrm{u_d}}$, $b_{\mathrm{u_d}}$, $a_{\mathrm{v_d}}$, $b_{\mathrm{v_d}}$, and the constants, $c_{\mathrm{u_d}}$ and $c_{\mathrm{u_d}}$, are functions of the connection matrices and the afferent inputs (for further details, please see section 3: Modeling auditory cortex dynamics with normal modes in Hajizadeh et al., 2019). Note that, the mathematical formulations described in this section is only a special case of the general solution which is described in Section 2.1.1. Both approaches are valid and lead to same solutions for the network dynamics. Also, this approach is based on the symmetry of connections and can be used for one stimulus only because for multiple stimuli the effect of short-term synaptic depression described in Eq. (2.3) should be taken into account. In this case, the matrix as a result of $W_{\mathrm{ee}}Q(t)$ in Eq. (2.1) is a nonsymmetric matrix even if the initial W_{ee} is symmetric. Therefore, the approach described in this subsection cannot be used to solve Eqs. (2.10) and (2.11).

2.1.3 Dynamics of the short-term synaptic depression and the slow-fast approximation

So far, we have analysed the system's dynamics in terms of normal modes only for one stimulus. In order to expand this approach for multiple stimuli, we need to deal with the function describing the afferent input and the dynamics of the short-term synaptic depression in Eq. (2.3).

We assume the afferent input to act as instant pulses which only occur to the excitatory cell population of IC. That is,

$$\boldsymbol{i}_{\mathrm{aff,e}}(t) = \boldsymbol{a} \sum_{s=0}^{S} \delta(t - t_s) \tag{2.14}$$

$$\boldsymbol{i}_{\mathrm{aff,i}}(t) = \mathbf{0}, \tag{2.15}$$

where $\boldsymbol{a}$ is a vector of size N whose nonzero elements represent the input strength (pulse strength) at those given columns; and $\mathbf{0}$ is the zero-vector of size N which means that the inhibitory cell population is not targeted by the afferent input. Approximating the input function by a delta function, the input appears as instant jumps in the initial values $(\boldsymbol{u}(0), \boldsymbol{v}(0))^\top$ in Eq. (2.7) which allows us to use Eq. (2.6) to describe the dynamics of excitatory and inhibitory state variables in terms of the superposition of the normal modes.

We also need to deal with the dynamics of the synaptic efficacy to complete this approach in order to be able to perform a stimulus-wise normal mode analysis of the network dynamics. We can take advantage of the dynamics at the synapses which occur in two different time scales. The first term in Eq. (2.3) corresponds to neurotransmitter release (i.e., synaptic depression) which is a fast process, whereas the second term corresponds to the slow neurotransmitter replenishment (i.e., recovery from depression). The fast and slow processes are regulated by their corresponding time constants τ_{o} and τ_{rec}. In the case of $\tau_{\text{o}} \ll \tau_{\text{rec}}$ (Fioravante and Regehr, 2011), one can characterise the dynamics of short-term synaptic depression by two separate processes which occur independently: A fast drop-off and a slow recovery and, therefore, apply a slow-fast approximation to the dynamics of short-term synaptic depression. For a general treatment of dynamical systems whose processes occur in slow and fast time scales, see, for example, Kuehn (2015). In this case, we keep the synaptic efficacy time-invariant and at a constant value $Q(t) = Q_s$ in each time interval $t \in [t_s, t_{s+1}]$ between two consecutive stimuli and update it together when the instant pulse occurs and causes jumps of $\boldsymbol{u}(t)$ and $\boldsymbol{v}(t)$ at the stimulation times t_s. Subsequently, the fast drop-off $\mathcal{F}_s(\boldsymbol{q}_s)$ which corresponds to the neurotransmitter release is obtained by integrating the first term in Eq. (2.3)

$$\mathcal{F}_s(\boldsymbol{q}_s) = \boldsymbol{q}_s \exp\left(-\frac{1}{\tau_{\text{o}}}\int_{t_s}^{t_{s+1}} g[\boldsymbol{u}(t')]dt'\right). \tag{2.16}$$

Note that, in this way the neurotransmitter release occurs independent from the neurotransmitter replenishment. Inserting $\mathcal{F}_s(\boldsymbol{q}_s)$ as an initial value into the slow recovery process and explicitly integrating the second term, we obtain

$$\boldsymbol{q}_{s+1} = \boldsymbol{1} - (\boldsymbol{1} - \mathcal{F}_s(\boldsymbol{q}_s)) \exp\left(-\frac{t_{s+1} - t_s}{\tau_{\text{rec}}}\right). \tag{2.17}$$

Inserting the general solution from Eq. 2.6 in Eq. 2.16, the fast drop-off $\mathcal{F}_s(\boldsymbol{q}_s)$ can be rewritten in terms of normal modes given by

$$\mathcal{F}_s(\boldsymbol{q}_s) = \boldsymbol{q}_s \prod_{n=1}^{2N} \exp\left(\frac{-c_{n,s}\left(\exp\left(\lambda_{n,s}\left(t_{s+1} - t_s\right)\right) - 1\right)}{\tau_{\text{o}}\lambda_{n,s}} \boldsymbol{x}_{n,s}\right). \tag{2.18}$$

This equation shows that the short-term synaptic depression depends on the normal modes. In sum, the synaptic depression is approximated by the fast-drop off given in Eq. (2.16). The recovery from depression is approximated by the slow recovery given in Eq. (2.17). The recovery occurs to the time point where a new stimulus and, therefore, next drop-off occurs. This cycle repeats for each stimulus. Note that, except τ_{o}, which is a global parameter, and time, the other parameters in Eq. (2.18) are a function of normal modes and the stimulus. In order to perform normal mode analysis for each stimulus, the synaptic efficacy variables are kept piecewise constant. In this way, the coefficient matrix M in Eq. (2.6) is updated only when a stimulus occurs and stays time-invariant during the recovery of the synapses from depression. This approximation is possible because, for suitable parameter settings, the time interval between two stimuli can be assumed to be long enough for the state-variables to completely decay to zero (for a detailed description, see Sects. 2.3 and 2.4 in Hajizadeh et al., 2022).

2.2 Simulating MEG signals

The main contributors to the MEG signals are the primary currents running in the locally aligned apical dendrites of the pyramidal cells in the cortex. The alignment of the apical dendrites depends on the cortical gyrification. In addition to other topographical factors like the position or shape of the source of activity (i.e., auditory cortex), the gyrification makes the primary currents within the apical dendrites to have different orientations and distances with respect to the MEG sensors. Moreover, the orientation of the primary currents are a function of the type of the synapses (i.e., excitatory or inhibitory) and where the synapses make a connection along the apical dendrites (Ahlfors and Wreh, 2015). The excitatory feedforward connections target the dendrites of the pyramidal cells close to the soma which leads to a current away from the soma and towards to the cortical surface (Ahlfors et al., 2015). Opposite to the feedforward connections, the excitatory feedback connections target the distal end of apical dendrites and pump the current towards the soma and away from the cortical surface (Ahlfors et al., 2015). The inhibitory connections have a similar effect as the feedback connections. These connections target the apical dendrites near the soma which lead to a current pointing to the soma within the apical dendrites (Douglas et al., 2004). In this model, there is no description for the primary currents in the dendritic trees. However, one can approximate the primary currents to be directly proportional to the sum of their synaptic input which, here, is the pre-synaptic activity multiplied to the synaptic weight (May, 2002).

Also, the Ampère-Laplace (Biot-Savart) law represented in Eq. (1.1) shows that the a magnetic field from a current source distribution depends on the topology of the source as well as its distance to the sensors where the magnetic field is being measured. Therefore, in addition to the synapse type which leads to different directions of primary currents, the topology of the current source density and the distance between the source and the sensors would also modify the signal which we measure outside the brain. These information are summarized in three matrices K_1, K_2, and K_3 which express specific multipliers of each synaptic connection and contain the information about the topology of the auditory cortex (for a more detailed description, see Hajizadeh et al., 2019, 2021). Therefore, the MEG signal is calculated by

$$R(t) = \sum_{j=1}^{N} \left[K_1 \circ W_{\mathrm{ee}}\boldsymbol{u}(t) + K_2 \circ W_{\mathrm{ei}}\boldsymbol{v}(t) + K_3 \circ W_{\mathrm{ie}}\boldsymbol{u}(t)\right]_j , \tag{2.19}$$

where j runs over the number of cortical columns in the model. The symbol $\circ$ denotes the element-wise multiplication (Hadamard product) between each two given matrices. Figure 5 in Hajizadeh et al. (2019) and Fig. 2a-b in Hajizadeh et al. (2021) represent the structure of the K-matrices for the large AC network ($N = 240$). Figure 3 in Hajizadeh et al. (2022) represents the structure of the K-matrices for the small AC network ($N = 5$).

Chapter 3

Modelling results: novel views on ERF generation

In this section, I show modelling results based on what is described in Sect. 2.1 and qualitatively compare them with experimental results. In Sect. 3.1, it is shown how normal modes account for the generation of ERFs and their adaptation. In Sect. 3.2, it is shown how an ERF can be decomposed to contributions based on synaptic type and how these contributions adapt with stimulus repetition. For further details and model parameters, see Hajizadeh et al. (2022).

In Sect. 3.3, ERFs are simulated in a systematic fashion whereby explanations for the sources of subject-variability of auditory ERFs are provided. Moreover, simulation results suggest that inter-subject variability of ERFs is reflected in their grand mean and standard deviation and in the latency, amplitude and width of the N1m response. For further details and model parameters, see Hajizadeh et al. (2019) and Hajizadeh et al. (2021).

3.1 ERF generation and its adaptation based on normal modes

Figure 3.1a shows trial-averaged ERFs which are acquired experimentally from one subject. The ERFs are measured in an experimental paradigm where the subject is passively listening to a tone sequence where tones were presented at a constant stimulus onset interval within a stimulus block (audio frequency 1.5 kHz, duration 100 ms, sound-pressure level 80 dB; data from Zacharias et al., 2012). The experiment is repeated for five SOIs: 0.5 s, 1 s, 2.5 s, 5 s, and 10 s. The ERFs show that there is a monotonic increase in the N1m peak amplitude and its latency with increasing SOI. The slope of the rising flank of the N1m response is similar across the SOIs, whereas the slope of the falling flanks of the N1m response increases with increasing SOI.

Figure 3.1b shows simulated ERFs of the same paradigm as in Fig. 3.1a. For ERF simulation, the linearised firing rate and the slow-fast approximation of the short-term synaptic depression is used (see Sect. 2.1). Here, a simple version of the anatomical structure of the auditory processing was utilised.

That is, the network is comprised by two subcortical areas, namely IC and the thalamus and the cortical areas core, belt, and parabelt. The dynamics of each area is represented by one column per area only ($N = 5$). This means that the entire dynamics are represented by five columns each comprising an excitatory and an inhibitory cell population. For further details, see Hajizadeh et al. (2022). In general, the main features of the experimentally acquired ERFs with stimulus repetition and, in particular, the variations of the N1m response as a function of SOI are captured in these simulations.

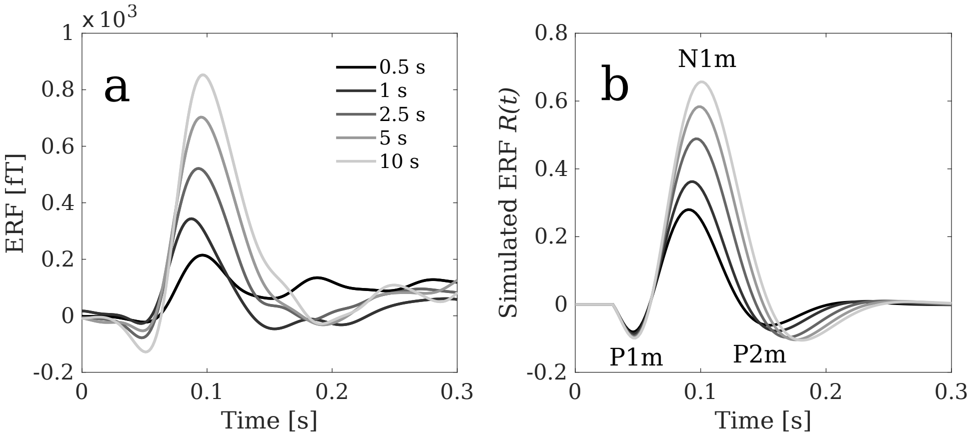

Figure 3.1: Comparison of the experimentally measured ERFs and their adaptation with simulated ERFs. **a)** Each waveform represents a trial-averaged ERF acquired experimentally from one subject who listened to a pure tone presented with a constant SOI. The SOIs are 0.5 s, 1 s, 2.5 s, 5 s, and 10 s. The overall shape of the ERF is SOI-dependent. This dependence is most clear in the N1m peak (data from Zacharias et al. (2012)). **b)** The ERF generation and its dependence on SOI are replicated by the model described in Sect. 2.1.1 where the firing rate is linear and the dynamics of the STSD is solved by a slow-fast approximation. Data and figure are published in Hajizadeh et al. (2022).

Equation (2.19) shows that MEG signals are proportional to the excitatory and inhibitory state variables. If we substitute Eq. (2.6) into Eq. (2.19), MEG signals can be viewed in terms of a superposition of normal modes. Figure 3.2a-b represent the simulated ERFs for SOIs = 0.5 s (black) and 10 s (grey) shown in Fig. 3.1b, decomposed into their underlying normal modes. The same decomposition for all five ERFs shown in Fig. 3.1b is provided in Hajizadeh et al. (2022). The normal modes are characterised by their frequency ($\omega/2\pi = \nu$) given in the legend of Fig. 3.2a-b. The corresponding dispersion relations (ν-$|\gamma|$) of the normal modes are illustrated in Fig. 3.2c-d. Moreover, the initial amplitude $|c_n|$ of each mode is represented by the size of the discs in Fig. 3.2c-d. There are several observations to be made: (1) The normal modes all peak between the stimulus onset and 70 ms post-stimulus time which is much earlier than when the N1m response occurs. (2) The high-frequency modes (blue and red) decay within the first 50 ms time window after the stimulus onset, whereas the low-frequency modes (purple and green) decay later and continue to be active up to almost 200 ms after the stimulus onset. (3) Therefore, all the modes contribute to the generation of P1m although their interference pattern is of a destructive type which leads to the small-magnitude P1m. However, the N1m is built upon the constructive superposition of the low-frequency modes (purple and green) whose interference pattern leads to the large-amplitude N1m response. (4) Normal modes, for both SOIs, are of the underdamped type because their frequency ν are nonzero and their decay rate γ is negative. (5) The stimulus repetition affects not only the magnitude of the normal modes, but it also affects their decay rate and their frequency. The decay rate and the frequency of the normal modes increase as the SOI decreases. (6) The initial amplitude of each mode is also a function of SOI. For SOI $= 0.5\,$s, the initial amplitude of the modes are quite variable, whereas for SOI $= 10\,$s, the initial amplitudes are of a similar size.

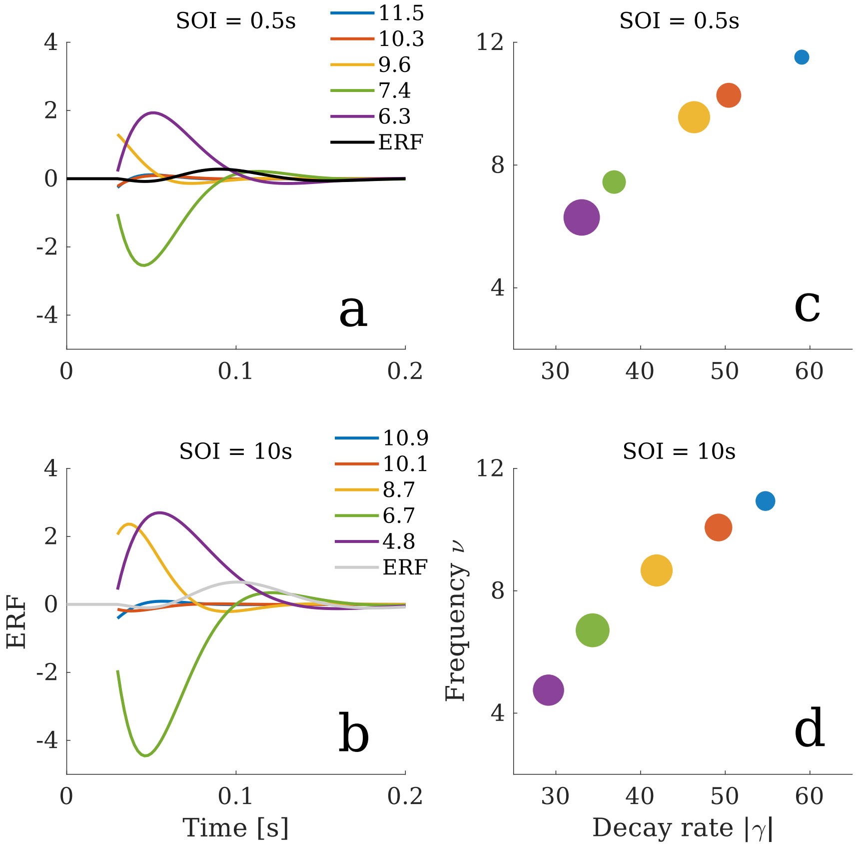

Figure 3.2: Decomposition of ERFs into underlying normal modes. **a-b)** ERFs of SOI $= 0.5\,$s and $10\,$s (black and grey) from Fig. 3.1b are shown together with their underlying normal modes. Normal modes are indicated by their frequency in the legend. Irrespective of SOI, all normal modes peak earlier than the N1m peak. The main contributor of the N1m are the low-frequency modes, whereas all the modes contribute to the P1m response. **c-d)** The dispersion relation of the normal modes shown in **a** and **b**. All normal modes are of the underdamped type. Stimulus repetition affects the properties of normal modes, i.e., frequency, decay rate, and the initial amplitude which is represented by the size of the discs. Data and figure are published in Hajizadeh et al. (2022).

Normal modes are not only characterised by temporal oscillations, but also oscillations in space. This information is given in the right eigenvectors of the coefficient matrix M in Eq. (2.5), i.e., $(\boldsymbol{x}_n, \boldsymbol{y}_n)^\top$. Figure 3.3 shows the spatial wave patterns of the normal modes shown in Fig. 3.2. Here, only the real part of the state variable $\boldsymbol{u}(t)$ is shown. The dark shades represent the modes contributing to the ERF of SOI $= 0.5\,$s and the light shades represent the modes contributing to the ERF of SOI $= 10\,$s. The high-frequency modes (blue and red) appear with large wave number, whereas the low-frequency modes (green and purple) appear with low wave number. The same results can be observed with normal modes contributing to the state variables $\boldsymbol{v}(t)$ which are not shown here.

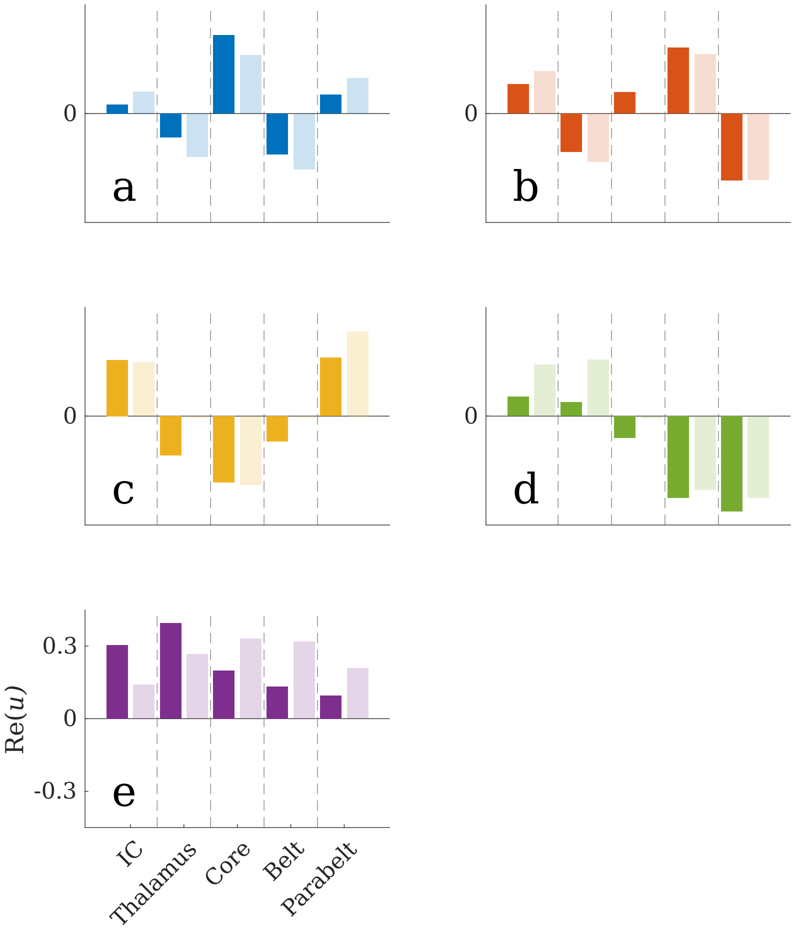

Figure 3.3: Spatial wave patterns of the normal modes shown in Fig. 3.2 identified by their corresponding colour codes. The dark shades and the light shades of each color correspond to SOI = 0.5 s and 10 s, respectively. For both SOIs, the high-frequency modes (blue and red) shown in **a-b** occur also with large wave number and the low-frequency modes (purple and green) shown in **d-e** appear with low wave number. The y-axis in all five panels has the same scale and it is given in panel **e**. Data and figure are published in Hajizadeh et al. (2022).

3.2 The topology of auditory cortex contributes to the shape of ERF

Figure 3.4a-b shows the contribution of different areas to the ERFs (grey) of SOI = 0.5 s and 10 s shown in Fig. 3.1b. Because the subcortical areas are deep sources, their corresponding multipliers in the K_l $l \in \{1, 2, 3\}$ matrix are zero. Therefore, they do not contribute to the ERFs (Hämäläinen et al., 1993). The main generator of the P1m is the core area (purple). The core together with the belt (red) are the main sources of the N1m. The parabelt area (green) contributes minimally to the ERFs. The serial progression of activity from core to belt and parabelt is quite clear. The activity in the core area, as the main target of the subcortical input, possesses the largest amplitude. Moreover, stimulus repetition seems to affect the activity of all areas similarly. Note that, the activity of each area peaks differently, but, in the proximity of 100 ms.

Figure 3.4c-d represent the decomposition of the same ERF waveforms (grey) in terms of the primary currents as a result of feedforward, feedback, and the lateral connections (see Sect. 2.2). In this view, primary currents which are driven by the feedforward connections (purple) are the main contributors to the P1m. On the other hand, primary currents which are the result of feedback (orange) and the lateral (blue) connections contribute to the generation of the N1m and P2m deflections. Primary currents caused by feedforward contributions are less affected by the stimulus repetition than the feedback and the lateral contributions.

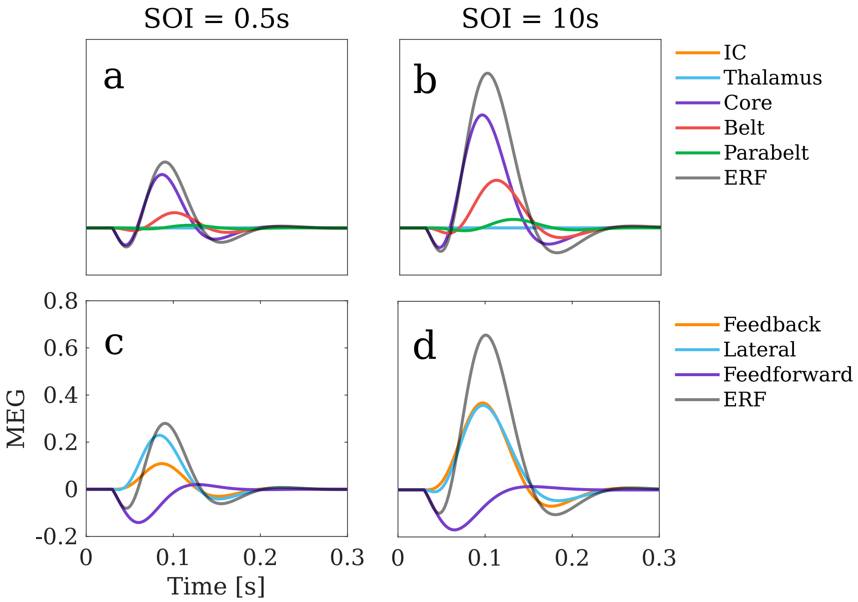

Figure 3.4: Decomposition of ERFs (grey) by different areas and connections. **a-b)** Decomposition of ERFs of SOIs = 0.5 s and 10 s to the contribution of different areas. The subcortical areas as deep sources do not contribute to ERFs. The core and the belt areas are the major generator of the ERFs for both SOIs. Parabelt's contribution is minimal and later in time compared to core and belt. **c-d)** Decomposition of ERFs based on the primary currents driven by feedforward, feedback, and lateral connections. Primary currents resulted from the feedforward connections are the main generator of the P1m, whereas the positive N1m deflection is mainly formed by the primary currents driven by the feedback and the lateral connections. The same also holds for the P2m. Data and figure are published in Hajizadeh et al. (2022).

3.3 Variability of ERFs across subjects

In this section, experimental and simulated ERFs are combined to test the following hypothesis (see Sect. 1.1.3): Is the subject-specificity of ERFs only due to the gross anatomical differences across subjects or is it due to the inter-subject variabilities of the dynamics of the auditory cortex, or both? In the model which is presented in Sect. 2, there are parameters which are part of the dynamics of the auditory cortex, namely the connection matrices and the membrane time constant (W_{ee}, W_{ei}, W_{ie}, W_{ii}, and τ_{m} in Eqs. (2.1)-(2.2)). These parameters, termed here dynamical parameters and denoted by D, regulate the dynamics within the auditory cortex network. On the other hand, there are parameters which represent the topography of the auditory cortex and map its response to the MEG signal measured outside the brain. These parameters, termed here anatomical parameters and denoted by A, are summarized in the K_1, K_2, and K_3 matrices which enter in the simulation of MEG signals (Eq. (2.19)). By having separate parameters for dynamics and topography of the AC, we have the tools at hand to test which aspects of an ERF waveform vary by introducing variations in the dynamical parameters or in the anatomical parameters. For this, ERF waveforms are simulated while the anatomical, dynamical, or both simultaneously were randomly varied in multiple steps. These steps are described in detail in Hajizadeh et al. (2021) and only one example per randomisation is shown in Fig. 3.5.

Figure 3.5a shows 25 trial-averaged ERF waveforms which are also shown in Fig. 1.1. Only the ERFs of long SOIs were chosen to be compared with the simulated ERFs because 7 s and 10 s are enough time for the auditory cortex to recover from adaptation due to stimulus repetition (Lü et al., 1992; Sams et al., 1993). For further details about the experimental setup, see Hajizadeh et al. (2021). The modelling of ERFs for the analysis of subject-specificity of ERFs in this study are performed without the effects of short-term synaptic depression. That is, $Q = I$ in Eq. (2.1). This figure is an example suggesting the variability of ERFs across subjects. The deflections of the ERFs appear with different amplitudes and latencies. This is also reflected in the inset where the N1m peak latencies plotted against their amplitudes. The highest variability occurs at the rising flanks of the N1m response of individual waveforms where the standard deviation peaks.

Figure 3.5b shows individual simulated waveforms (grey) and their corresponding arithmetic mean (black) and standard deviation (red) where the anatomical parameters (i.e., K_l, $l \in \{1, 2, 3\}$) were varied and the dynamical parameters (i.e., W_{ee}, W_{ei}, W_{ie}, and W_{ii}) were kept constant. Changes of the anatomical parameters lead to variations mainly in the peak magnitude of the P1m, N1m, and P2m whilst the overall shape of the waveforms stays almost invariant. This is also highlighted in the inset where the N1m peak latency of individual waveforms is plotted against the N1m peak amplitude. In contrast, by randomising the dynamical parameters and keeping the anatomical parameters constant another picture emerges. In this randomisation shown in Fig. 3.5c, individual waveforms appear in different shapes and are quite different in terms of N1m peak latency and amplitude. This is also reflected in the standard deviation peaking after the N1m as well as in the inset where the N1m peak amplitude versus latency is plotted. Figure 3.5d represents simulated individual waveforms where both anatomical and dynamical parameters were simultaneously varied. In this case, the amplitude and the latency of the N1m are more realistically distributed. These simulations suggest that for the subject variability of ERF waveforms, both anatomical and dynamical parameters play a role.

In order to scrutinize the results shown in Fig. 3.5, in several steps randomisations of the anatomical and dynamical parameters were carried out. These steps allowed to systematically increase or decrease the contributions of the anatomical and dynamical parameters in order to probe their effect on the ERF waveforms. For each randomisation, the distribution of the N1m peak amplitude and its latency as well as the 3-dB width of the N1m deflection of simulated waveforms were compared with the same quantities acquired from the experimental ERFs shown in Fig. 3.5a. These analyses, which are shown and described in detail in Hajizadeh et al. (2021), indicate that the inter-subject variability of ERF waveforms stem from both the dynamics and the anatomy of auditory cortex.

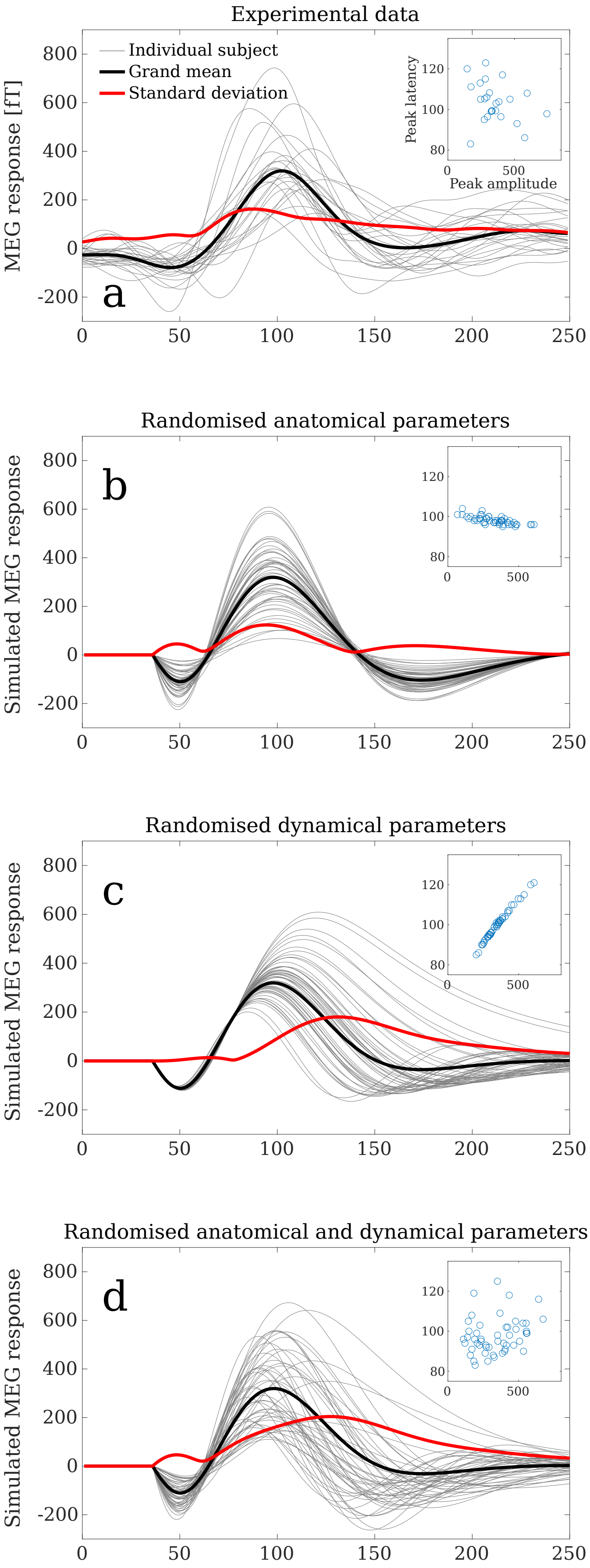

Figure 3.5: An example of the effect of anatomical parameters A and the dynamical parameters D on simulated ERFs. Thin grey waveforms represent individual ERF waveforms. The black and the red lines represent the arithmetic mean and standard deviation, respectively. **a)** Trial-averaged ERF waveforms from 25 different subjects are shown. The ERFs appear with different latencies and amplitudes of P1m, N1m, P2m deflections. Although these deflections are identifiable in most subjects, the overall shape of ERFs are markedly different. The arithmetic mean (black) peaks with the amplitude of almost 300 fT at around 100 ms after the stimulus onset. However, the inset shows the variability of the N1m peak latency and amplitude across subjects which are scattered around 100 ms and 300 fT, respectively. **b)** 50 examples of simulated ERF waveforms and the corresponding grand-averaged waveform and standard deviation were generated by randomising the anatomical parameters while keeping the dynamical parameters fixed. The individual waveforms are similar in shape, however, with a large variation in the peak amplitude of the N1m and a narrow variation of its peak latency. This is also reflected in the inset where the N1m peak latency of the individual waveforms is plotted against the N1m peak amplitude. **c)** 50 examples of simulated ERF waveforms and the corresponding grand-averaged waveform and standard deviation were generated by randomising the dynamical parameters while keeping the anatomical parameters fixed. The individual waveforms are quite different in terms of amplitude, latency, and width of the N1m response. As it is also shown in the inset, there is a large variation in the peak amplitude of the N1m as well as in the peak latency. **d)** 50 examples of simulated ERF waveforms and the corresponding grand-averaged waveform and standard deviation were generated by simultaneous randomisation of the dynamical *and* the anatomical parameters. The ERF waveforms look now more realistic (compare with the waveforms in panel **a**). The distribution of the N1m peak amplitude and its latency shows a closer resemblance to empirical data. Data and figure are published in Hajizadeh et al. (2021).

Chapter 4

Discussion

4.1 Main findings

In this thesis, a new view on ERF generation, adaptation, and inter-subject variability is introduced. This was achieved with a focus on computational modelling of auditory cortex and auditory ERFs. The anatomical structure of the model is based on the serial core-belt-parabelt organization of the auditory cortex. The model dynamics are based on the leaky-integrate neurons with short-term synaptic depression being the only form of synaptic plasticity (Eqs. (2.1)-(2.3)). Due to the functions of firing rates and synaptic efficacy, the state equations representing the dynamics of excitatory and inhibitory cell populations are nonlinear. Here, the network dynamics were analysed by linearising the function of firing rates (Eq. (2.4)) and solving the equation representing dynamics of short-term synaptic depression by time-scale separation (Eqs. (2.16) and (2.17)). The result is a description of the auditory cortex network dynamics in terms of damped harmonic oscillators, i.e., normal modes (see Eqs. (2.6), (2.12), and (2.13); and Fig. 3.2). Auditory ERFs and their adaptation due to stimulus repetition were replicated (Fig. 3.1a) based on the normal-mode description. In this view, ERFs are generated by an interference pattern of independent spatiotemporal oscillations. Each normal mode is characterised by its decay rate γ, angular frequency ω, initial phase $\arg(c_n)$ and amplitude $|c_n|$, and spatial wave pattern $(\boldsymbol{x}_n, \boldsymbol{y}_n)^\top$. Normal modes do not reside in any specific area or field of auditory cortex but, rather, are spread over the entire auditory cortex network (Fig. 3.3). Therefore, the activity of different locations of AC should be seen as unique combinations of this coexisting independent normal modes. In addition to decomposition of ERFs into normal modes, it was shown that ERFs could be decomposed into activity of the cortical columns and the primary currents (Fig. 3.4). These three different, but related, levels of decomposition of ERFs offer a new view on the potential mechanisms of ERF generation which can lead to a paradigm shift in understanding and interpreting ERF waveforms.

In line with previous studies (Loebel et al., 2007; Mill et al., 2011; Wang and Knösche, 2013; Yarden and Nelken, 2017; Kudela et al., 2018), it was shown that short-term synaptic depression, which is composed of a fast and a slow process, accounts for the adaptation of ERFs due to stimulus repetition.

Synaptic depression is directly linked to the normal modes to which an ERF can be decomposed into (see Eq. (2.18) and Figs. 3.2-3.3). Adaptation of ERFs were described in terms of changes of normal mode properties where the reduction of amplitude in the state variables and the ERFs due to stimulus repetition is only a by-product (Fig. 3.2). Therefore, adaptation of ERFs should be viewed in terms of a complete change in the spatiotemporal oscillations throughout the auditory cortex rather than reduction of response magnitude in discrete sources scattered over the auditory cortex.

Auditory ERFs are identifiable by three main characteristic negative and positive peaks P1m, N1m, and P2m. However, these peaks in ERFs of individual subjects appear with different latencies and amplitudes. From structural brain scans, it is already known that there are differences in the gross anatomy across individual subjects which contributes to the subject-specific ERFs (Rademacher et al., 2001; Morosan et al., 2001; Fischl et al., 2008). Nevertheless, the Ampère-Laplace law (Eq. (1.1)) indicates that the current density distribution (i.e., the dynamics of the source of the magnetic field measured by MEG) should also contribute to the inter-subject variability of the ERFs. Here, it was tested whether dynamical variations across auditory cortex of different subjects also play a role in the inter-subject variability of ERFs. This hypothesis was tested by linking simulated ERFs to the experimentally measured ERFs. In the model presented here, there are parameters which directly regulate the dynamics of auditory cortex (e.g., connection matrices in Eqs. (2.1) and (2.2)) and parameters which link the gross anatomy of auditory cortex (K_l, $l \in \{1, 2, 3\}$ in Eq. (2.19)) to the generation of ERFs. In order to find out which ERF properties depend on the dynamics of the auditory cortex or its gross anatomy or both, ERF waveforms were simulated by systematically varying the dynamical and the anatomical parameters. Simulated and experimental ERFs were compared in terms of three quantities extracted from the N1m response: amplitude, latency, and 3-db width. The results show that the latency and the width of the N1m response are predominantly determined by the dynamics of auditory cortex, whereas the amplitude of the N1m peak is a function of both dynamics and the anatomy of auditory cortex (Fig. 3.5 and Figs. 4 and 6 in Hajizadeh et al. (2021)). Therefore, these results suggest that both the anatomy and the dynamics of auditory cortex are reflected in ERFs and both are needed to explain inter-subject variability of the ERF waveforms.

4.2 Comparison to other models of ERF generation

There is an ongoing debate about the generation mechanisms of stimulus-evoked responses in the brain. The phase-reset model advocates that evoked responses emerge from the ongoing brain oscillations (Sayers et al., 1974; Nikulin et al., 2007; Mazaheri and Jensen, 2010), whereas the signal-plus-noise model indicates that stimulus leads to an additional activity which is uncorrelated to ongoing brain oscillations (Dawson, 1954; Shah et al., 2004; Mäkinen et al., 2005). However, it has proven difficult to distinguish which of the two mechanisms accounts for stimulus-evoked responses (Yeung et al., 2004; Sauseng et al., 2007; Telenczuk et al., 2010).

In this thesis, it was shown that ERFs are of an oscillatory nature which emerge from the interference pattern of superimposed damped harmonic oscillations (Hajizadeh et al., 2019, 2022). However, these results as such cannot be compared to ERFs arising out of ongoing brain oscillations (Sayers et al., 1974; Nikulin et al., 2007; Mazaheri and Jensen, 2010) because the approach proposed here does not include background oscillatory activity. Periodic background oscillations can be either separately introduced in the model dynamics or the parameter settings of the weight matrices can be manipulated such that the decay rate γ of, at least, one normal mode is zero. In this way, one normal mode keeps oscillating without decaying to zero. It would be very interesting to see how this oscillating normal mode interacts with other damping modes. How the network reacts to this oscillatory activity would then depend on, for example, the amplitude, frequency and the phase relations between the damping normal modes and the ongoing oscillation. If the ongoing oscillation consists of a frequency close to the frequency of one or more normal modes and appears with a similar phase as of those normal modes, the ongoing oscillation contributes as an enhancement. In contrast, if the ongoing oscillations and decaying normal modes happen to have similar frequencies but appear in opposite phases, the ongoing oscillation leads to a destructive interference pattern. In this regard, it might be possible to explain the persistent field observed in the auditory cortex during a working memory task (Huang et al., 2016), when the dynamics of auditory cortex is characterised by one or more low-frequency normal modes with zero damping rates and the rest of the modes are of the damped type. The damped modes, in this case, can account for the transient information processing of the stimulus properties during the stimulation phase and the oscillating modes without damping can account for the persistent activity during the delay phase (Nachstedt and Tetzlaff, 2017). The addition of ongoing oscillation can lead to complex dynamics which, in any case, demands proper testing and investigation.

Event-related responses as an additive activity to ongoing brain oscillations have been, mainly, considered to emerge from spatially discrete sources which are based on the source reconstruction results. A problem which already arises here is that the source reconstruction of MEG and EEG signals is an ill-posed inverse problem with no unique solution. The traditional way to estimate the sources of cortical electromagnetic activity is by equivalent current dipoles (ECD). ECDs are theoretical constructs and point-like sources which, in the source reconstruction models, approximate the simultaneous activity of pyramidal cells which are aligned together in the cortex (Williamson and Kaufman, 1981; Scherg, 1990). An ECD is characterised by its location, orientation, and amplitude (Williamson and Kaufman, 1981). The number of ECDs for describing the source activity depends on the complexity of the experiment and whether the source of cortical activation is focal or distributed (Mosher et al., 1992). In simple sensory experiments, discrete source modelling is performed where single or multiple ECDs are used. In this case, by an a priori assumption about the location of the electromagnetic source, single or multiple ECDs are seeded whilst one or two parameters of ECDs are kept fixed and the rest of the parameter(s) of the ECDs are determined by an optimisation algorithm. However, in an experiment when several cortical areas are involved distributed source modelling is performed in order to estimate the sources of the electromagnetic activity. Unlike discrete source modelling, in this method hundreds of ECDs on a tessellated cortical surface are placed whose magnitude and orientation are free parameters of an optimisation problem.

In this thesis, modelling ERFs also bases upon discrete sources—cortical columns—which are organized and distributed according to the anatomical structure of the auditory cortex. The model as such confirms the source modelling results with single ECD (Lütkenhöner and Steinsträter, 1998) and multiple ECDs (Inui et al., 2006) where it was shown that the source activity is nonstationary and travels over the supratemporal plane in a medio-lateral direction. These results were regarded as the serial core-belt-parabelt activation which were replicated in this thesis (Fig. 3.4a-b and Figs. 3 and 8 in Hajizadeh et al. (2019)). Nevertheless, the activity of each cortical column is obtained by the superposition of independent normal modes which are spread over the entire AC. There is indeed a mutual relation between the normal modes and the activity of cortical columns. On the one hand, the activity of cortical columns are determined by the normal modes (Eq. (2.6)). On the other hand, the normal mode properties depend on the network structure according to which the cortical columns are organized (matrix M in Eq. (2.5)).

The results from the source modelling of ERP/ERF waveforms may imply that different peaks and troughs of ERFs are the results of a *real* temporal succession of activation with different amplitude in discrete locations of auditory cortex; and this leads to the low-amplitude P1m occurring first followed by the large-amplitude N1m and the low-amplitude P2m. This view might be indeed misleading in a sense that the activity in auditory cortex occurs in terms of spatially discrete and—independently—active sources which are responsive only once at a time. This approach can be a downside of pure source localisation of EEG and MEG signals where the focus shifts away from finding the relation and the connection between the sources. Each field or area of auditory cortex is part of one entity and embedded in a spatially extended object which is the entire auditory cortex. Therefore, while studying auditory cortex activity we need to take the whole network into account. In this vein, the simulations of auditory cortex activity presented here show that all the normal modes reach their global extremum earlier than the N1m peak and they all coexist whilst some decay faster and some decay slower (Fig. 3.2). Subsequently, the whole ERF waveform emerges out of the interference pattern of these normal modes. When the P1m is occurring the interference pattern of the modes is more of a destructive type. In contrast, when the N1m is occurring the interference pattern of the modes is more of a constructive type (see also Fig. 7 in Hajizadeh et al., 2022). Therefore, in the normal mode view, the temporal succession of P1m, N1m, and P2m at their corresponding time points appearing with different magnitudes is incidental.

In DCM, event-related responses also arise from several discrete sources (Friston, 2005), where it is assumed that these sources are connected with extrinsic connections. Each source is composed of excitatory and inhibitory cell populations which are connected via intrinsic connections. The strength of the intrinsic and extrinsic connections are fitting parameters. The main difference between pure source localisation of MEG and EEG signals with ECDs and DCM is that, DCM tries to estimate the coupling strength between and within the sources (for example, see Kiebel et al., 2007; Garrido et al., 2007, 2009), whereas in source localisation of electromagnetic waveforms the objective is only estimating the electromagnetic source location as well as its orientation and magnitude. Finding out the coupling strength between the sources is certainly an improvement to pure source localisation. Nevertheless, this can turn into a big challenge because more sources and more connections lead to a high-dimensional problem for a fitting algorithm.

Although DCM and the view offered in this thesis are similar in terms of modelling event-related responses by discrete sources, they still deviate from each other in a few points. (1) As increasing the number of sources and, subsequently, the coupling strengths can lead to computationally expensive fitting procedures in DCM, increasing the number of cortical columns can be implemented easily in our approach with small computational costs. (2) In contrast to DCM where the description of auditory cortex is limited to the primary and secondary auditory cortices, the focus of our work is to include as much of the network structure of auditory cortex as possible. This includes the serial core-belt-parabelt structure as well as the tonotopic organization of the auditory cortex. (3) In DCM and in our approach, connections between the sources and the changes in the connections account for variations of event-related responses. However, in DCM the coupling strength between the sources are determined in an iterative process with an optimisation algorithm by which adaptation of N1m and mismatch responses are explained. Conversely, in our approach the serial core-belt-parabelt structure together with the short-term synaptic depression which, systematically, acts upon the connection matrices (equivalent to the coupling strength in DCM) account for the ERF waveforms and their adaptation. (4) Despite modelling event-related responses with discrete sources distributed over auditory cortex in DCM and our approach, with the normal-mode explanation of ERFs we explain ERFs on a more fundamental level where ERFs are functions of the whole network structure of auditory cortex and the temporal structure of the input. (5) An advantage of the DCM over our modelling approach is that in DCM the event-related waveforms are quantitatively explained by implementing optimisation algorithms. However, in our modelling approach we only described the ERF waveforms on a qualitative level.

4.3 Normal modes in the brain

Normal modes are well-known concepts which have applications in many areas of sciences and engineering. Although normal mode analysis of dynamical systems often requires simplifications and approximations like linearisation, it is still a powerful technique which provides deep insights about the system's dynamics. Nunez (1981) and Katznelson (1981) used the concept of normal modes and described brain activity recorded by EEG with spherical harmonics. However, they described the whole-brain EEG activity where the dynamics of sensory cortices are embedded in the whole brain dynamics. In this regard, the dynamics of each individual sensory cortex, including auditory cortex, remain in their modelling approach rather obscure. Therefore, their results are not directly comparable to what is presented in this thesis because, here, the dynamics within the auditory cortex has been studied and described in terms of normal modes. However, the views of Nunez (1981) and Katznelson (1981) on how EEG signals are generated is similar to what is offered in this thesis about the MEG signals. That is, the brain activity reflected in the MEG/EEG signals could be described in terms of oscillations which are independent from each other and extend in time and space.

It would be interesting to experimentally test the existence of normal modes and their functional significance in the brain. One possible way of testing whether the electromagnetic activity of the brain appears in terms of normal modes is to investigate the resonance behaviour in the brain due to a certain stimulation paradigm. In this context, Katznelson (1981) predicted that the resonance frequencies of the normal modes underlying the whole-head EEG signals shift to lower values when the synaptic coupling between neurons decreases. This hypothesis was tested by computing the frequency spectrum of the EEG signals of human subjects during the inhalation of halothane (Katznelson, 1981). Halothane is an anaesthetic which reduces the neurons responsiveness by decreasing the synaptic coupling (i.e., synaptic strength) between the neurons (Richards, 1973). Katznelson (1981) confirmed his hypothesis and showed that the increase of halothane concentration gradually shifts the peaks in the EEG spectrum of the human subjects under anaensthesia to lower values.

Short-term synaptic depression also leads to a weakness of synaptic coupling between neurons. However, this weakness is stimulus dependent, local, and transient compared to anaesthetics. In contrast to what Katznelson (1981) based on his theoretical and empirical observations reported, the simulations in this thesis indicate that with stimulus repetition of short SOIs ($< 5\,\mathrm{s}$), which leads to weaker synaptic coupling between the excitatory cell populations, the dispersion relation of the normal modes shift to higher values in frequency and decay rate (Fig. 3.2). This predicts that the underlying oscillations of ERFs are of a higher frequency when the synaptic coupling due to STSD weakens. One can test this hypothesis by applying Fourier transformation to the continuous MEG signal of subjects who passively listen to a regularly-presented pure tone. As the simulations here suggest, the Fourier spectrum should be inversely related to the stimulus onset interval.

Due to resonance behaviour, in the case of a periodic stimulation of neurons in the AC with short SOIs we might observe enhanced responses instead of diminished responses. In this context, resonances might be the reason why a single exponential function is not enough to capture the dependence of the adaptation of N1m response due to stimulus repetition, specifically in the short SOIs ($< 500\,\mathrm{ms}$) (see Fig. 10 in Hajizadeh et al., 2022). Also, resonances might be the reason of the N1m-like responses in MEG signals occurring when the stimulus is omitted in a tone sequence (May and Tiitinen, 2001; May, 2021).

4.4 The network structure of the model and the input

In this thesis, the dynamics of the auditory cortex and its response to periodic stimulation by just one frequency was studied. That is, the input targeted one column in the IC. A natural direction for future is studying the dynamics of auditory cortex and its response to stimulus sequences which contain more than one frequency. Implementing this requires expanding the model's network structure to more than one column per field/area in the AC. Although such a network structure was used in Hajizadeh et al. (2019), where each field of the AC was characterised by 16 tonotopically organized columns, the functional significance of the tonotopic organization of AC was not really examined because the input function was only targeting one column in the IC. In Hajizadeh et al. (2022), the number of columns was reduced to one per AC area. Despite the marked reduction in the dimensions, the model could still fully capture the main features of the auditory ERF adaptation.

The first step towards more complex stimuli is studying the model dynamics in an oddball paradigm where more than one frequency channel in the IC is targeted by the afferent input. Modelling ERFs acquired in an oddball paradigm requires expanding the anatomical structure of the model to, at least, two columns per area. In this case, normal modes can also account for mismatch responses. In the normal mode view, mismatch responses possibly appear because the standard tones excite one set of normal modes which are different from those excited by the deviant tones. The reason is that the excitation of normal modes depends on two factors: (1) The initial amplitude $|c_n|$ which is a function of the input (standard or deviant) (see Eq. (2.7)). (2) The network structure and the connection pattern in the auditory cortex (corresponding to the left eigenvectors $(\boldsymbol{\xi}_n, \boldsymbol{\eta}_n)^\top$ of the coefficient matrix M in Eq. (2.7)). Also, normal modes adapt differently with stimulus repetition (see Eq. (2.18)). Therefore, excitation of different normal modes together with their differential adaptation due to stimulus repetition might provide new insights on the possible generation mechanisms of mismatch responses. The normal mode explanation of mismatch responses would then build upon the *adaptation* model proposed, originally, by Butler (1968) and refined by May et al. (1999).

One of the basic principles of the anatomy of mammalian AC is the core-belt-parabelt structure (Kaas and Hackett, 2000; Hackett, 2015), which is the underlying network structure of the simulations in this thesis. However, the auditory cortex of mammals differ, for example, in the number of fields and the connections between the fields (Hackett, 2015). One can implement the network structure of the AC from different mammals in the model and investigate in which aspects different anatomical structures affect the properties of normal modes. In this regard, it might be possible to better understand the functional significance of the parcellation of the human auditory cortex and its connection pattern. In this context, Fig. 9 in Hajizadeh et al. (2022) indicates that the lifetime of adaptation, τ_{soi}, (Lü et al., 1992) is shaped by the model's underlying network structure and the excitation-inhibition balance. One can solve the state equations in order to find the underlying normal modes of different structures and see if there is a link between the normal mode properties and the τ_{soi}. For example, the dynamics of an AC structure of a mammal which allows for longer τ_{soi} might be composed of more low-frequency and low-decay rate normal modes rather than high-frequency modes which also decay faster.

The invasive measurements from the primary auditory cortex of Mongolian gerbils under anaesthesia, where the local field potential was recorded, shows that the peak latency of the local activity is inversely related to the stimulus onset interval (Ma, 2022). This is in contrast to what is observed in human MEG signals where the latency of the N1m peak is directly proportional to the stimulus onset interval (see Fig. 3.1a). The AC of Mongolian gerbils consists of less fields than the AC of humans and the connection pattern between the fields is also quite different between the two species (Budinger et al., 2000; Kaas and Hackett, 2000; Nourski et al., 2014). Therefore, It might be possible to explain the latency shift in opposite directions as a function of SOI with the differences in the anatomy of AC between Mongolian gerbils and humans (Kaas and Hackett, 2000). The decrease in the peak latency of the activity with decreasing stimulation rates in the Mongolian gerbils might be also due to the effects of anaesthesia which impacts on the excitation-inhibition balance (see, for example, Richards, 1973; Taub et al., 2013; Deane et al., 2020). Moreover, the invasive measurements from the Mongolian gerbils shown in Ma (2022) were performed locally and only from the core area. There is no evidence, yet, for the decrease of the peak latency of the activity due to increase of SOI in the other areas of the AC beyond the core area and in the global activity of the AC of the Mongolian gerbils. However, simulations presented in Fig. 8a1-a5 in

Hajizadeh et al. (2022) show that the increase of the latency with increasing SOI occurs in the N1m peak, as a global activity, as well as in the response peak of all three individual AC areas, as local activities.

4.5 Subject-specificity of ERFs

In Hajizadeh et al. (2021), the results on the inter-subject variability of ERFs were deduced from the comparison of distributions of population data obtained from simulated and experimental ERFs (see Figs. 4, 5, and 6 in Hajizadeh et al. (2021)). Therefore, it could not be concluded whether the inter-subject variability between *any* two ERFs of different subjects is due to anatomical or dynamical differences or both. Moreover, the experimental ERFs which were used for the analysis in Hajizadeh et al. (2021) were generated by periodic stimulation of AC with large SOIs (i.e., SOIs of 7 s and 10 s). The reason was to exclude the effects of N1m amplitude modulation due to the stimulus repetition with short SOIs (see Fig. 3.1a, Sect. 1.1.4, and Lü et al., 1992; Sams et al., 1993). Also, instead of using the information on the subject-specificity of the AC anatomical structure acquired from magnetic resonance imaging for the randomisation of the anatomical parameters, the randomisations of these parameters were done quite arbitrarily. Moreover, the detailed anatomical information on the parcellation of the AC of humans and its connection pattern is not yet available (Baumann et al., 2013; Besle et al., 2019). This was the primary reason why the anatomical structure of the AC of macaque monkey (Kaas and Hackett, 2000), which is the closest to the AC of humans, was used for the simulations in this thesis (see Fig. 2.1) (Nourski et al., 2014).

There is the possibility to expand the study presented in Hajizadeh et al. (2021) in multiple ways. For example, one can start with fitting simulated ERFs to experimental subject-specific ERFs. This would allow not only to better characterise the ERF waveforms, but also to trace back the sources of variability in ERFs across individual subjects. By implementing a given anatomical structure and solving the forward problem it might be possible to fit the simulated ERFs to experimental ERFs in order to estimate the weight values in the weight matrices (i.e., connections between the fields and the columns) and/or the values of the topographical matrices (i.e., K-matrices) underlying an ERF waveform. Fitting the weight matrices and the topographical matrices would require the implementation of an optimisation algorithm which can deal with multi-variate problems. For this, genetic and evolutionary algorithms can be used which are among the suitable optimisation algorithms (Michalewicz, 1996). Genetic algorithms would, then, allow fitting whether any two given fields are connected to each other or not (Rozmarynowski, 2021; Zawadka, 2022) and evolutionary algorithms would allow investigating how strong the connections are (Turczak, 2022).

In the light of the slow-fast approximation of the dynamics of short-term synaptic depression, we can also consider including experimental ERFs of shorter SOIs in our analysis of subject-specificity of the ERFs. By systematically varying the time constants τ_{o} and τ_{rec} which govern the dynamics of short-term synaptic depression, we may be able to explain the variability of ERFs of short SOIs on the level of the dynamics of synapses. Parameters τ_{o} and τ_{rec} might be subject-specific and may be linked to the subject-specificity of the adaptation lifetime which was measured based on the N1m peak amplitudes (see

Sect. 1.1.4 and Lü et al., 1992; Lu et al., 1992). Lu et al. (1992) reported that the adaptation lifetime correlates with the behavioral lifetime of the sensory memory in the auditory cortex of humans. There might be the possibility to link the microscopic physiological time constants of the STSD mechanism (i.e., τ_{o} and τ_{rec}) to the behavioral measurements where the auditory cortex in involved. Inspired by the experiment performed by Lu et al. (1992), for example, a behavioural experiment can be carried out where human subjects perform an auditory working memory task. In order to probe the auditory sensory memory of the subjects, the difficulty of the experiment could be manipulated by varying the time interval between the test stimulus (one which the subject needs to remember) and the probe stimulus (one which the subject needs to compare with the test stimulus). We can, then, conduct the MEG experiment with the same subjects, as it was conducted by Lü et al. (1992) and explained in Sect. 1.1.4, whereby the subject-specific adaptation lifetime can be estimated. In turn, the ERF waveforms from which the adaptation lifetime is estimated can be fitted by the model where τ_{o} and τ_{rec} are the fitting parameters. In this way, we may be able to link the behavioural performance of the subjects to the macroscopic adaptation lifetime *and* to the microscopic time constants which govern the dynamics of synapses. Note that the slow-fast approximation of the dynamics of STSD is only possible when the values of the two time constants τ_{o} and τ_{rec} are sufficiently apart (see Sect. 2.1.3). Therefore, in the implementation of the optimisation algorithms for searching the optimised values of τ_{o} and τ_{rec} in the entire parameter space the implementation of the slow-fast approximation can lead to limitations. In this case, the slow-fast approximation may be abandoned and the numerical methods for solving Eqs. (2.1)-(2.3) should be used.

Bibliography

Ahlfors, S. P., Jones, S. R., Ahveninen, J., Hämäläinen, M. S., Belliveau, J. W., Bar, M., 2015. Direction of magnetoencephalography sources associated with feedback and feedforward contributions in a visual object recognition task. Neuroscience Letters 585, 149–154.

Ahlfors, S. P., Wreh, C., 2015. Modelling the effect of dendritic input location on MEG and EEG source dipoles. Medical & Biological Engineering & Computing 53, 879–887.

Ahonen, L., Huotilainen, M., Brattico, E., 2016. Within- and between-session replicability of cognitive brain processes: An MEG study with an N-back task. Physiology & Behavior 158, 43–53.

Atcherson, S. R., Gould, H. J., Pousson, M. A., Prout, T. M., 2006. Long-term stability of N1 sources using low-resolution electromagnetic tomography. Brain Topography 19 (1/2), 11–20.

Baumann, S., Petkov, C. I., Griffiths, T. D., 2013. A unified framework for the organization of the primate auditory cortex. Frontiers in Systems Neuroscience 7 (11).

Besle, J., Mougin, O., Sánchez-Panchuelo, R. M., Lanting, C., Gowland, P., Bowtell, R., Francis, S., Krumbholz, K., 2019. Is human auditory cortex organization compatible with the monkey model? contrary evidence from ultra-high-field functional and structural MRI. Cerebral Cortex 29, 410–428.

Blundon, E. G., Gallagher, R. E., Ward, L. M., 2020. Electrophysiologcal evidence of preserved hearing at the end of life. Scientific Reports 10, 10336.

Brosch, M., Schreiner, C. E., 2000. Sequence sensitivity of neurons in cat primary auditory cortex. Cerebral Cortex 10, 1155–1167.

Brosch, M., Schulz, A., Scheich, H., 1999. Processing of sound sequences in macaque auditory cortex: response enhancement. Journal of Neurophysiology 82, 1542–1559.

Budinger, E., Heil, P., Scheich, H., 2000. Functional organization of auditory cortex in the mongolian gerbil (meriones unguiculatus). iii. anatomical subdivisions and corticocortical connections. European Journal of Neuroscience 12, 2425–2451.

Butler, R. A., 1968. Effect of changes in stimulus frequency and intensity on habituation of the human vertex potential. The Journal of the Acoustical Society of America 44, 945–950.

Buzsáki, G., Anastassiou, C. A., Koch, C., 2012. The origin of extracellular fields and currents – EEG, ECoG, LFP and spikes. Nature Reviews 13, 407–420.

Buzsáki, G., Watson, B. O., 2012. Brain rhythms and neural syntax: implications for efficient coding of cognitive content and neuropsychiatric disease. Dialogues in Clinical Neuroscience 14, 345–367.

Caughey, T. K., 1960. Classical normal modes in damped linear dynamic systems. Journal of Applied Mechanics 27, 269–271.

Caughey, T. K., O'Kelly, M. E. J., 1965. Classical normal modes in damped linear dynamic systems. Journal of Applied Mechanics 32, 583–588.

Clark-Gambelunghe, M. B., Clark, D. A., 2015. Sensory development. Pediatric Clinics of North America 62, 367–384.

Dalebout, S. D., Robey, R. R., 1997. Comparison of the intersubject and intrasubject variability of exogenous and endogenous auditory evoked potentials. Journal of the American Academy of Audiology 8 (2), 342–354.

Davis, P. A., 1939. Effects of acoustic stimuli on the waking human brain. Journal of Neurophysiology 2, 494–499.

Dawson, G. D., 1954. A summation technique for the detection of small evoked potentials. Electroencephalography and Clinical Neurophysiology 6, 65–84.

Deane, K. E., Brunk, M. G. K., Curran, A. W., Zempeltzi, M. M., Ma, J., Lin, X., Abela, F., Aksit, S., Deliano, M., Ohl, F. W., Happel, M. F. K., 2020. Ketamine anaesthesia induces gain enhancement via recurrent excitation in granular input layers of the auditory cortex. Journal of Physiology 598, 2741–2755.

Douglas, R., Markram, H., Martin, K., 2004. Neocortex. In: Shepherd, G. M. (Ed.), The synaptic organization of the brain. Oxford University Press, New York, pp. 499–558.

Fioravante, D., Regehr, W. G., 2011. Short-term forms of presynaptic plasticity. Current Opinion in Neurobiology 21, 269–274.

Fischl, B., Rajendran, N., Busa, E., Augustinack, J., Hinds, O., Yeo, B. T. T., Mohlberg, H., Amunts, K., Zilles, K., 2008. Cortical folding patterns and predicting cytoarchitecture. Cerebral Cortex 18, 1973–1980.

Forsythe, I. D., Tsujimoto, T., Barnes-Davies, M., Cuttle, M. F., dT. Takahashi, 1998. Inactivation of presynaptic calcium current contributes to synaptic depression at a fast central synapse. Neuron 20, 797–807.

Freeman, W. J., Ahlfors, S. P., Menon, V., 2009. Combining fMRI with EEG and MEG in order to relate patterns of brain activity to cognition. International Journal of Psychophysiology 73, 43–52.

Friston, K., 2005. A theory of cortical responses. Philosophical Transactions of the Royal Society 360, 815–836.

Friston, K. J., Harrison, L., Penny, W., 2003. Dynamic causal modelling. NeuroImage 19, 1273–1302.

Garrido, M. I., Kilner, J. M., Kiebel, S. J., Friston, K. J., 2009. Dynamic causal modeling of the response to frequency deviants. Journal of Neurophysiology 101, 2620–2631.

Garrido, M. I., Kilner, J. M., Kiebel, S. J., Stephan, K. E., Friston, K. J., 2007. Dynamic causal modelling of evoked potentials: a reproducibility study. NeuroImage 36, 571–580.

Grothe, B., Pecka, M., McAlpine, D., 2010. Mechanisms of sound localization in mammals. Physiological Reviews 90, 983–1012.

Hackett, T. A., 2011. Information flow in the auditory cortical network. Hearing Research 271, 133–146.

Hackett, T. A., 2015. Anatomic organization of the auditory cortex. Handbook of Clinical Neurology 129 (Chapter 2).

Hajizadeh, A., Matysiak, A., Brechmann, A., König, R., May, P. J. C., 2021. Why do humans have unique auditory event-related fields? Evidence from computational modeling and MEG experiments. Psychophysiology 58, e13769.

Hajizadeh, A., Matysiak, A., May, P. J. C., König, R., 2019. Explaining event-related fields by a mechanistic model encapsulating the anatomical structure of auditory cortex. Biological Cybernetics 113, 321–345.

Hajizadeh, A., Matysiak, A., Wolfrum, M., May, P. J. C., König, R., 2022. Auditory cortex modelled as a dynamical network of oscillators: understanding event-related fields and their adaptation. Biological Cybernetics 116, 475–499.

Hämäläinen, M., Hari, R., Ilmoniemi, R. J., Knuutila, J., Lounasmaa, O. V., 1993. Magnetoencephalography—theory, instrumentation, and applications to non-invasive studies of the working human brain. Reviews of Modern Physics 65, 413–497.

Hari, R., Kaila, K., Katila, T., Tuomisto, T., Varpula, T., 1982. Interstimulus interval dependence of the auditory vertex response and its magnetic counterpart: implications for their neural generation. Electroencephalography and Clinical Neurophysiology 54, 561–569.

Heschl, R. L., 1878. Über die vordere quere Schläfenwindung des menschlichen Großhirns. Braumüller, Wien.

Hopfield, J., Tank, D., 1986. Computing with neural circuits: a model. Science 233, 625–633.

Huang, Y., Matysiak, A., Heil, P., König, R., Brosch, M., 2016. Persistent neural activity in auditory cortex is related to auditory working memory in humans and nonhuman primates. eLife 5, e15441.

Ilmoniemi, R. J., Sarvas, J., 2019. Brain signal: Physics and mathematics of MEG and EEG. The MIT press, Cambridge, Massachusetts, London, England.

Inui, K., Okamoto, H., Miki, K., Gunji, A., Kakigi, R., 2006. Serial and parallel processing in the human auditory cortex: a magnetoencephalographic study. Cerebral Cortex 16, 18–30.

Kaas, J. H., Hackett, T. A., 2000. Subdivisions of auditory cortex and processing streams in primates. Proceedings of the National Academy of Sciences of the United States of America 97, 11793–11799.

Kandel, E. R., Schwartz, J. H., Jessell, T. M., Siegelbaum, S. A., Hudspeth, A. J., 2013. Principles of neural sciences, fifth edition. McGraw-Hill, New York.

Katznelson, R. D., 1981. Normal modes of the brain: neuroanatomical basis and a physiological theoretical model. In: Nunez, P. L. (Ed.), Electric fields of the brain: The neurophysics of EEG. Oxford University Press, pp. 401–442.

Kiebel, S. J., Garrido, M. I., Friston, K. J., 2007. Dynamic causal modelling of evoked responses: the role of intrinsic connections. NeuroImage 36, 332–345.

Kileny, P. R., Kripal, J. P., 1987. Test-retest variability of auditory event-related potentials. Ear and Hearing 8, 110–114.

Kudela, P., Boatman-Reich, D., Beeman, D., Anderson, W. S., 2018. Modeling neural adaptation in auditory cortex. Frontiers in Neural Circuits 12 (72).

Kuehn, C., 2015. Multiple time scale dynamics. Springer International Publishing, Cham, Switzerland.

Latimer, K. W., Barbera, D., Sokoletsky, M., Awwad, B., Katz, Y., Nelken, I., Lampl, I., Fairhall, A. L., Priebe, N. J., 2019. Multiple timescales account for adaptive responses across sensory cortices. Journal of Neuroscience 39, 10019–10033.

Loebel, A., Nelken, I., Tsodyks, M., 2007. Processing of sound by population spikes in a model of primary auditory cortex. Frontiers in Neuroscience 1, 197–209.

Lü, Z.-L., Williamson, J., Kaufman, L., 1992. Human auditory primary and association cortex have differing lifetimes for activation traces. Brain Research 572, 236–241.

Lu, Z.-L., Williamson, S. J., Kaufman, L., 1992. Behavioral lifetime of human auditory sensory memory predicted by physiological measures. Science 258, 1668–1670.

Lütkenhöner, B., Steinsträter, O., 1998. High-precision neuromagnetic study of the functional organization of the human auditory cortex. Audiology and Neuro-Otology 3, 191–213.

Ma, J., 2022. Layer-specific intracortical amplification shortens the lifetime of thalamocortical repetition suppression in primary auditory cortex. Doctoral dissertation, Otto von Guericke University, Magdeburg, Germany.

Mäkinen, V., Tiitinen, H., May, P., 2005. Auditory event-related responses are generated independently of ongoing brain activity. NeuroImage 24, 961–968.

May, P., Tiitinen, H., 2001. Human cortical processing of auditory events over time. Neuroreport 12, 573–577.

May, P., Tiitinen, H., Ilmoniemi, R. J., Nyman, G., Taylor, J. G., Näätänen, R., 1999. Frequency change detection in human auditory cortex. Journal of Computational Neuroscience 6, 99–120.

May, P., Tiitinen, H., Westö, J., 2015. Computational modelling suggests that temporal integration results from synaptic adaptation in auditory cortex. European Journal of Neuroscience 41, 615–630.

May, P. J. C., 2002. Do EEG and MEG measure dynamically different properties of neural activity? In: Nowak, H., Haueisen, J., Giesler, F., Huonker, R. (Eds.), Proceedings of the 13th International Conference on Biomagnetism. International Congress Series. Berlin: VDE Verlag GmbH, pp. 709–711.

May, P. J. C., 2021. The adaptation model offers a challenge for the predictive coding account of mismatch negativity. Frontiers in Human Neuroscience 15, 721574.

May, P. J. C., Tiitinen, H., 2010. Mismatch negativity (MMN), the deviance-elicited auditory deflection, explained. Psychophysiology 47, 66–122.

May, P. J. C., Tiitinen, H., 2013. Temporal binding of sound emerges out of anatomical structure and synaptic dynamics of auditory cortex. Frontiers in Computational Neuroscience 7 (152).

Mazaheri, A., Jensen, O., 2010. Rhythmic pulsing: linking ongoing brain activity with evoked responses. Frontiers in Human Neuroscience 4 (177).

Megela, A. L., Teyler, T. J., 1979. Habituation and the human evoked potential. Journal of Comparative and Physiological Psychology 93 (6), 1154–1170.

Michalewicz, Z., 1996. Genetic algorithm + data structure = evolution programs. Springer Berlin, Heidelberg.

Mill, R., Coath, M., Wennekers, T., Denham, S. L., 2011. A neurocomputational model of stimulus-specific adaptation to oddball and markov sequences. PLoS Computational Biology 7, e1002117.

Mitzdorf, U., 1994. Properties of cortical generators of event-related potentials. Pharmacopsychiatry 27, 49–51.

Morosan, P., Rademacher, J., Schleicher, A., Amunts, K., Schormann, T., Zilles, K., 2001. Human Primary Auditory Cortex: Cytoarchitectonic Subdivisions and Mapping into a Spatial Reference System. NeuroImage 13, 684–701.

Mosher, J. C., Lewis, P. S., Leahy, R. M., 1992. Multiple dipole modeling and localization from spatio-temporal MEG data. IEEE Transactions on Biomedical Engineering 39, 541–557.

Näätänen, R., Escera, C., 2000. Mismatch negativity: Clinical and other applications. Audiology and Neurotology 5, 105–110.

Näätänen, R., Gaillard, A. W., Mäntysalo, S., 1978. Early selective-attention effect on evoked potential reinterpreted. Acta Psychologica 42, 313–329.

Näätänen, R., Picton, T., 1987. The N1 wave of the human electric and magnetic response to sound: a review and an analysis of component structure. Psychophysiology 24, 375–425.

Nachstedt, T., Tetzlaff, C., 2017. Working memory requires a combination of transient and attractor-dominated dynamics to process unreliable timed inputs. Scientific Reports 7 (2473).

Nelken, I., 2004. Processing of complex stimuli and natural scenes in the auditory cortex. Current Opinion in Neurobiology 14, 474–480.

Nikulin, V. V., Linkenkaer-Hansen, K., Nolte, G., Lemm, S., Müller, K. R., Ilmoniemi, R. J., Curio, G., 2007. A novel mechanism for evoked responses in the human brain. European Journal of Neuroscience 25, 3146–3154.

Nourski, K. V., Steinschneider, M., McMurray, B., Kovach, C. K., Oya, H., Kawasaki, H., Howard III, M. A., 2014. Functional organization of human auditory cortex: Investigation of response latencies through direct recordings. NeuroImage 101, 598–609.

Nunez, P. L., 1981. Electric fields of the brain: the neurophysics of EEG. Oxford University Press, New York.

Pérez-González, D., Malmierca, M. S., 2014. Adaptation in the auditory system: an overview. Frontiers in Integrative Neuroscience 8, 1–10.

Rademacher, J., Morosan, P., Schleicher, A., Freund, H.-J., Zilles, K., 2001. Human primary auditory cortex in women and men. NeuroReport 12, 1561–1565.

Rayleigh, L., 1945. Theory of sounds (Volume 1). Dover publication, Inc., New York, N. Y.

Regehr, W. G., 2012. Short-term presynaptic plasticity. Cold Spring Harbor Perspectives in Biology 4, a005702.

Richards, C. D., 1973. On the mechanism of halothane anaesthesia. Journal of Physiology 233, 439–456.

Ritter, P., Schirner, M., Mclntosh, A. R., Jirsa, V. K., 2013. The virtual brain integrates computational modeling and multimodal neuroimaging. Brain Connectivity 3 (2), 121–145.

Roberts, T. P., Ferrari, P., Poeppel, D., 1998. Latency of evoked neuromagnetic M100 reflects perceptual and acoustic stimulus attributes. Neuroreport 9, 3265–3269.

Rozmarynowski, A., 2021. Computational modelling of signal processing in human auditory cortex: Fitting the model to experimental MEG data. Master's thesis, Wrocław University of Science and Technology, Wrocław, Poland.

Saenz, M., Langers, D. R. M., 2013. Tonotopic mapping of human auditory cortex. Hearing Research 307, 42–52.

Sams, M., Hari, R., Rif, J., Knuutila, J., 1993. The human auditory sensory memory trace persists about 10 sec: neuromagnetic evidence. Journal of Cognitive Neurosicence 5, 363–370.

Sauseng, P., Klimesch, W., Gruber, W. R., Hanslmayer, S., Freunberger, R., Doppelmayr, M., 2007. Are event-related potential components generated by phase resetting of brain oscillations? A critical discussion. Neuroscience 146, 1435–1444.

Sayers, B., Beagley, H. A., Menshall, W. R., 1974. The mechanism of auditory evoked EEG responses. Nature 247, 481–483.

Scherg, M., 1990. Fundamentals of dipole source potential analysis. In: Grandori, F., Hoke, M., Romani, G. L. (Eds.), Evoked Magnetic Fields and Electric Potentials. Vol. 6 of Advances in Audiology. Karger, Basel, pp. 40–69.

Schnupp, J., Nelken, I., King, A. J., 2011. Auditory neuroscience: Making sense of sound. MIT Press, Cambridge, Massachusetts.

Segalowitz, S. J., Barnes, K. L., 1993. The reliability of ERP components in the auditory oddball paradigm. Psychophysiology 30, 451–459.

Shah, A. S., Bressler, S. L., Knuth, K. H., Ding, M., Mehta, A. D., Ulbert, I., Schroeder, C. E., 2004. Neural dynamics and the fundamental mechanisms of event-related brain potentials. Cerebral Cortex 14, 476–483.

Squires, N. K., Squires, K. C., Hillyard, S. A., 1975. Two varieties of long-latency positive waves evoked by unpredictable auditory stimuli in man. Electroencephalography and Clinical Neurophysiology 38, 387–401.

Südhof, T. C., 2013. Neurotransmitter release: the last millisecond in the life of a synaptic vesicle. Neuron 80, 675–690.

Tasseh, N., Yaron, A., Nelken, I., 2011. Stimulus-specific adaptation and deviance detection in the rat auditory cortex. PLoS One 6, e23369.

Taub, A. H., Katz, Y., Lampl, I., 2013. Cortical balance of excitation and inhibition is regulated by the rate of synaptic activity. The Journal of Neuroscience 33, 14359–14368.

Telenczuk, B., Nikulin, V. V., Curio, G., 2010. Role of neuronal synchrony in the generation of evoked EEG/MEG responses. Journal of Neurophysiology 104, 3557–3567.

Tsodyks, M., Markram, H., 1997. The neural code between neocortical pyramidal neurons depends on neurotransmitter release probability. Proceedings of the National Academy of Sciences of the United States of America 94, 719–723.

Turczak, E., 2022. Investigating signal processing in the human auditory cortex. Master's thesis, Wrocław University of Science and Technology, Wrocław, Poland.

Ulanovsky, N., Las, L., Farkas, D., Nelken, I., 2004. Multiple time scales of adaptation in auditory cortex neurons. The Journal of Neuroscience 24, 10440–10453.

Ulanovsky, N., Las, L., Nelken, I., 2003. Processing of low-probability sounds by cortical neurons. Nature Neuroscience 6, 391–398.

von Békésy, G., Wever, E. G., 1960. Experiments in hearing. McGraw-Hill, New York.

Wang, P., Knösche, T. R., 2013. A realistic neural mass model of the cortex with laminar-specific connections and synaptic plasticity-evaluation with auditory habituation. PLoS One 8, e77876.

Williamson, S. J., Kaufman, L., 1981. Biomagnetism. Journal of Magnetism and Magnetic Materials 22, 129–201.

Wilson, H., Cowan, J., 1972. Excitatory and inhibitory interactions in localized populations of model neurons. Journal of Biophysics 12, 1–24.

Yarden, T. S., Nelken, I., 2017. Stimulus-specific adaptation in a recurrent network model of primary auditory cortex. PLoS Computational Biology 13, e1005437.

Yeung, N., Bogacz, R., Holroyd, C. B., Cohen, J. D., 2004. Detection of synchronized oscillations in the electroencephalogram: An evaluation of methods. Psychophysiology 41, 822–832.

Yvert, B., Fischer, C., Bertrand, O., Pernier, J., 2005. Localization of human supratemporal auditory areas from intracerebral auditory evoked potentials using distributed source models. NeuroImage 28, 140–153.

Zacharias, N., König, R., Heil, P., 2012. Stimulation-history effects on the M100 revealed by its differential dependence on the stimulus onset interval. Psychophysiology 49, 909–919.

Zawadka, P., 2022. Optimization of the parameters of a human auditory cortex model. Engineer's thesis, Wrocław University of Science and Technology, Wrocław, Poland.

Zucker, R. S., Regehr, W. G., 2002. Short-term synaptic plasticity. Annual Review of Physiology 64, 355–405.

Chapter 5

Explaining event-related fields by a mechanistic model encapsulating the anatomical structure of auditory cortex

Biological Cybernetics (2019) 113:321–345
https://doi.org/10.1007/s00422-019-00795-9

Biological
Cybernetics

ORIGINAL ARTICLE

Explaining event-related fields by a mechanistic model encapsulating the anatomical structure of auditory cortex

Aida Hajizadeh[2] · **Artur Matysiak**[2] · **Patrick J. C. May**[1,2] · **Reinhard König**[2]

Received: 20 September 2018 / Accepted: 8 February 2019 / Published online: 28 February 2019
© The Author(s) 2019

Abstract

Event-related fields of the magnetoencephalogram are triggered by sensory stimuli and appear as a series of waves extending hundreds of milliseconds after stimulus onset. They reflect the processing of the stimulus in cortex and have a highly subject-specific morphology. However, we still have an incomplete picture of how event-related fields are generated, what the various waves signify, and why they are so subject-specific. Here, we focus on this problem through the lens of a computational model which describes auditory cortex in terms of interconnected cortical columns as part of hierarchically placed fields of the core, belt, and parabelt areas. We develop an analytical approach arriving at solutions to the system dynamics in terms of normal modes: damped harmonic oscillators emerging out of the coupled excitation and inhibition in the system. Each normal mode is a global feature which depends on the anatomical structure of the entire auditory cortex. Further, normal modes are fundamental dynamical building blocks, in that the activity of each cortical column represents a combination of all normal modes. This approach allows us to replicate a typical auditory event-related response as a weighted sum of the single-column activities. Our work offers an alternative to the view that the event-related field arises out of spatially discrete, local generators. Rather, there is only a single generator process distributed over the entire network of the auditory cortex. We present predictions for testing to what degree subject-specificity is due to cross-subject variations in dynamical parameters rather than in the cortical surface morphology.

Keywords Analytical solutions · Auditory cortex · Computational modeling · Event-related field · Event-related response · Magnetoencephalography · Normal modes

1 Introduction

The event-related potential (ERP) and field (ERF) measured with electroencephalography (EEG) and magnetoencephalography (MEG), respectively, appear as a series of waves triggered by a stimulus event. First described by Davis (1939), these waves are thought to represent stimulus-related activations which are stationary, time-locked to stimulus presentation, and buried in ongoing oscillations and other activity unrelated to stimulus processing. Thus, to cancel out the signal not associated with the stimulus, ERPs and ERFs are obtained through stimulus repetition and averaging of the single-trial EEG/MEG signals with respect to stimulus onset. The peaks and troughs of event-related responses function as landmarks as they can be identified in most subjects. Even so, the morphology of these responses varies greatly from subject to subject (see, for example, Atcherson et al. 2006; Dalebout and Robey 1997; Zacharias et al. 2011; Matysiak et al. 2013; König et al. 2015). Importantly, despite the straightforwardness of the method to extract ERPs and ERFs and decades of its use, and regardless of improvements in localization methods, we still have a poor understanding

Communicated by Benjamin Lindner.

Patrick J. C. May
p.may1@lancaster.ac.uk

Aida Hajizadeh
aida.hajizadeh@lin-magdeburg.de

Artur Matysiak
artur.matysiak@lin-magdeburg.de

Reinhard König
reinhard.koenig@lin-magdeburg.de

[1] Department of Psychology, Lancaster University, Lancaster LA1 4YF, UK

[2] Special Lab Non-invasive Brain Imaging, Leibniz Institute for Neurobiology, Brenneckestraße 6, 39118 Magdeburg, Germany

of how event-related responses are generated and what they signify.

In contrast, the general biophysics of EEG and MEG generation and the neural processes giving rise to currents in the brain contributing to these signals are well known (Sarvas 1987; Williamson and Kaufman 1981). EEG (Buzsáki et al. 2012; Einevoll et al. 2013; Mitzdorf 1985, 1994) and MEG signals (Hämäläinen et al. 1993; Okada et al. 1997) represent primarily a weighted sum of synchronized synaptic activities of pyramidal neural populations, whereas inhibitory neurons, with shorter dendrites and a symmetric dendritic structure, contribute to a closed field which does not show up in EEG and MEG. With pyramidal neurons being the predominant cell type in cortex, cortical columns are characterized by the apical dendrites of these cells running in parallel to each other and orthogonally to the cortical surface. The activity of *excitatory* synapses on these dendrites translates into electric current (cations Ca^{2+} and Na^{+}) flowing into the apical dendrites, then along the dendrites as the primary/lead current, and out through the passive leak channels into the extracellular space, where the resulting volume current completes the circuit. The primary current along many synchronously activated pyramidal cells gives rise to a magnetic field which is visible in MEG and whose strength depends on the orientation and distance of the primary current in relation to the sensor. Similarly, the extracellular sinks and sources separated along the axis of the dendrites contribute to an open electric field which can be picked up in EEG and local field potential (LFP) measurements. Traditionally, *inhibitory* synapses onto pyramidal cells were thought to contribute only minimally to EEG/MEG, with the reversal potentials of these synapses being close to the resting membrane potential (Bartos et al. 2007; Mitzdorf 1985). Accordingly, an activated inhibitory synapse leads to minimal cross-membrane currents and hence a minimal contribution to EEG and MEG. However, when pyramidal neurons are spiking, for example, when spontaneous activity occurs, the membrane potential is elevated and so inhibitory synapses can significantly contribute to EEG and MEG generation (Trevelyan 2009; Glickfield et al. 2009; Bazelot et al. 2010).

The leap from biophysics to an understanding of the experimentally measured ERP and ERF waveforms is more difficult. A sensory stimulus (the event) sets off a series of neural activations propagating from the sensory organ to cortex. Cortical activations can be observed locally, in intracortical measurements, as increased spiking when, for example, the weak thalamocortical signal activates the local feedback circuits in cortical columns of the primary areas (Douglas et al. 1995), and this stimulus-evoked activation corresponds with the surface-recorded ERP (Shah et al. 2004). The auditory event-related response starts with small-amplitude, early-latency waves in the first 8 ms from stimulus onset; these are followed by mid-latency waves in the 8–40 ms range and, then, by large-amplitude, long-latency waves (e.g., Picton and Stuss 1980). In the passive recording condition, when the subject is not engaged in a task involving the stimuli, the most prominent waves of the auditory ERP are the long-latency P1, N1, and P2 responses, peaking at approximately 50, 100, and 200 ms, respectively. Their ERF counterparts are termed the P1m, N1m, and P2m.

Computational modeling can account for long-latency auditory ERPs purely in terms of interactions across cortical layers in primary auditory cortex (Wang and Knösche 2013). However, it seems unlikely that events in primary fields could represent the full intracortical counterpart of ERPs, which emerge as a superposition of activity across larger swathes of cortex. For example, in the case of auditory cortex (AC), anatomical studies in monkey show a hierarchical organization, with primary, core fields connecting to each other and to surrounding secondary, belt fields which, in turn, are connected with parabelt fields (Kaas and Hackett 2000; Hackett et al. 2014). There is physiological evidence to suggest that this hierarchical structure is reflected in feedforward activations progressing along the core–belt axis (Rauschecker 1997) and, hence, that cortical activations generating event-related responses should have temporal as well as spatial dynamics. This is supported by localization studies. Lütkenhöner and Steinsträter (1998) modeling the long-latency auditory ERF of a human subject with a single equivalent current dipole (ECD) found that the ECD location was non-stationary across the entire time course of the ERF: during the P1m, it lies on Heschls gyrus (HG) from where it slides to the planum temporale (PT) during the N1m and shifts back to HG during the P2m. Inui et al. (2006) performed multi-dipole analysis of auditory ERFs in a 120-ms post-stimulus time window using six ECDs located in the AC, and found that activity propagates along a roughly medial-lateral axis from HG to the superior temporal gyrus (STG). This was interpreted in terms of core–belt–parabelt activation. Similar results were reported by Yvert et al. (2005) who used minimum current estimates of recordings from intracerebral electrodes in human AC. Activity started in HG and Heschls sulcus (HS) at around 20 ms. The P1 time range (30–50 ms) was characterized by multiple areas becoming activated along medio-lateral and postero-anterior axes of propagation, successively involving HG and HS, PT, and STG. Subsequently, activity cycled back so that the rising slope of the N1 coincided with a similar series of activations as during the P1.

The above results point to event-related responses having both a temporal as well as a spatial dynamics whereby foci of activity in cortex shift over time. This addition of a spatial dimension to event-related responses adds to the descriptive palette but as such gives no deeper insight into what is going on, although there have been a number of approaches for gaining such insight. Research in the 1970s and 1980s posited that the event-related response is the linear sum of separable components, each generated by a spatially defined generator which also has a well-defined information processing function, such as stimulus onset detection or change detection (for reviews, see Näätänen and Picton 1987; Näätänen 1992). However, it has proven difficult to perform component separation in a reliable way (Lütkenhöner 1998) and to map components to anatomical structure (May and Tiitinen 2010). This emphasis on localization of activity was later complemented by considerations on the connections between cortical areas. In the framework of dynamical causal modeling (DCM), the event-related response is considered to arise out of a network of a small number of nodes arranged in a hierarchical structure and each representing an extended cortical area such as the primary or secondary AC (Friston et al. 2003; David et al. 2006). Stimulation-specific modulations in the response then arise out of changes in the strengths of connections, classified as bottom-up, lateral, or top-down. Such changes have been interpreted in the framework of predictive coding, whereby cortex attempts to predict incoming stimuli and in so doing generates prediction signals via top-down inhibitory connections. When there is a mismatch between stimulus and prediction, excitatory bottom-up connections relay a prediction error signal. In this view, the N1(m) signifies excitatory activity carrying the prediction error from AC toward frontal areas. In contrast, the P2(m) is due to inhibitory, feedback activity carrying the top-down prediction information (Garrido et al. 2007, 2009).

It appears then that we have a range of mutually exclusive explanations for event-related responses. First, these can be understood as arising purely locally, as the result of intra-laminar dynamics within primary areas (Wang and Knösche 2013). Second, they can be modeled as being generated by a single source with a continually shifting location (Lütkenhöner and Steinsträter 1998). Third, they can be seen to represent the linear sum of activity of a limited number of component generators, each performing an independent information processing task (Näätänen and Picton 1987). Fourth, they might arise out of a limited number of cortical areas interacting with each other in the performance of predictive coding (Friston et al. 2003). The spatial resolutions of these explanations seem to lie at the extremes, ranging from the single column to treating entire areas as single nodes (see also Ritter et al. 2013). None of these explanations are designed to represent transformations occurring within AC, because the internal dynamics of AC as a distributed system are not included. For this purpose, a more mechanistic view on how AC processes and represents sound is needed. Such a view could be based on the structure of the AC in order to account for the spatial dynamics occurring within the temporal lobe, as described above.

Thus, the purpose of the current study is to plug the resolution gap by bringing the anatomical structure of the AC into the explanation of the auditory event-related response. As a starting point we use a previously developed model of AC (May and Tiitinen 2010, 2013; May et al. 2015), and we restrict ourselves to examining ERF generation. The original model is highly nonlinear, and we simplify it in order to make an analytical approach possible. We derive analytical solutions to the model so as to characterize the dynamics of AC signal processing in terms of basic elements, so-called normal modes. This allows us then to address the following questions: How do ERFs originate from these dynamical elements? How do these elements depend on the anatomical core–belt–parabelt structure of the AC? And how is the ERF signal modulated by the topography of the primary currents, that is, by their orientation and distance from the MEG sensor? This analysis, then, lets us explore the origin of the subject-specificity of event-related responses: Why do subjects have unique ERF morphology? Can this be fully accounted for in terms of individual curvature of AC and its modulating effect on the MEG? Or do subjects also have unique dynamics of the auditory cortex?

2 Model of auditory cortex

May and colleagues (May and Tiitinen 2010, 2013; May et al. 2015; Westö et al. 2016) developed a computational model of AC with anatomical structure and short-term plasticity of the synapses as central features, and with the aim of linking non-invasive results with in-vivo single- and multi-unit observations. The intuition behind this previous modeling work has been that auditory phenomena emerge from large-scale interactions in the auditory cortex. With a detailed map of the human AC still missing, the model borrows the core–belt–parabelt organization of the primate AC (Baumann et al. 2013; Hackett et al. 2014), as shown in Fig. 1a, with multiple streams of feedforward and feedback activation indicated by the arrows. The model replicates a wide range of temporal binding (across-time) phenomena observed in invasive experiments. These include forward masking (Brosch and Schreiner 1997; Brosch and Scheich 2008), stimulus-specific adaptation (Ulanovsky et al. 2003, 2004), two-tone facilitation (Brosch et al. 1999), and selective responses to complex sounds such as speech and monkey calls (Rauschecker 1997). Non-invasively observed phenomena explained by the model include the adaptation of the N1(m), and the emergence of the mismatch response as a dependence of the N1(m) on stimulus statistics (May and Tiitinen 2010; May et al. 2015). We note that by including the hierarchical structure of the whole AC at the cost of keeping the local dynamics relatively simple, this approach diverges from modeling efforts which describe primary AC only and concentrate on certain aspects of auditory processing, such as frequency tuning and forward masking (Loebel et al. 2007), stimulus-specific adaptation

(Yarden and Nelken 2017), auditory induction (Noto et al. 2016), bird song discrimination (Larson et al. 2009), the N1/N1m response (Wang and Knösche 2013), or the mismatch response (May et al. 1999). Further, this approach is superficially similar to DCM in that both describe neural activations in terms of nodes in a hierarchically organized network. However, the DCM network is on a larger scale, extending across cortical lobes, and entire areas are compressed into single nodes. In contrast, the model of May and colleagues covers AC only, and it does so at a finer resolution, describing the organization of cortical columns in the various fields of the core, belt, and parabelt areas.

The dynamical unit of the model is a simplified description of the cortical column and it comprises two state variables u and v representing the population of excitatory (pyramidal) neurons and inhibitory interneurons, respectively. The dynamics are determined by the following two sets of coupled nonlinear differential equations (May and Tiitinen 2013; May et al. 2015):

$$\begin{aligned}\tau_{\mathrm{m}}\dot{\mathbf{u}}(t) = &-\mathbf{u}(t) + A(t) \circ W_{\mathrm{ee}} \cdot g[\mathbf{u}(t)] \\ &- W_{\mathrm{ei}} \cdot g[\mathbf{v}(t)] + \mathbf{I}_{\mathrm{aff,e}}(t)\end{aligned} \tag{1}$$

$$\begin{aligned}\tau_{\mathrm{m}}\dot{\mathbf{v}}(t) = &-\mathbf{v}(t) + W_{\mathrm{ie}} \cdot g[\mathbf{u}(t)] \\ &- W_{\mathrm{ii}} \cdot g[\mathbf{v}(t)] + \mathbf{I}_{\mathrm{aff,i}}(t).\end{aligned} \tag{2}$$

Here, τ_{m} is the membrane time constant, $\mathbf{u}(t) = [u_1(t), \ldots, u_N(t)]$ and $\mathbf{v}(t) = [v_1(t), \ldots, v_N(t)]$ are the time-dependent vectors of the state variables, with $N = 240$, and $\circ$ denotes entrywise multiplication (Hadamard product). The subcortical afferent input vectors $\mathbf{I}_{\mathrm{aff,e}}(t)$ and $\mathbf{I}_{\mathrm{aff,i}}(t)$ target the excitatory (index 'e') and inhibitory (index 'i') cell populations of the three core fields, respectively, through 16 tonotopically organized frequency channels per field. The synaptic weights between populations are defined by the four connection matrices W_{ee}, W_{ei}, W_{ie}, and W_{ii}. We assume that all between-column connections are excitatory and encapsulated in the matrices W_{ie} and W_{ee}; the latter also includes the long-range connections between fields. Further, we assume that W_{ie} has within-field elements only, and thus functional inhibition is of the lateral type. The matrices W_{ei} and W_{ii} have diagonal elements only and describe local, within-column inhibitory-to-excitatory and inhibitory-to-inhibitory connections. The output of each population is its mean spiking rate, which depends on the corresponding state variable through a continuous, nonlinear function g. Thus, the spiking rates $g[\mathbf{u}(t)]$ and $g[\mathbf{v}(t)]$ are zero for values of $\mathbf{u}(t)$ and $\mathbf{v}(t)$ smaller than a constant threshold θ, and for values above this threshold they are monotonically increasing functions of the corresponding state variables, converging toward a saturation value of unity. The function $A(t)$ is a time-varying matrix describing synaptic plasticity depending on pre-synaptic activity and governed by a differential equation of its own.

Equations (1) and (2) represent the mean-field leaky integrator neuron (LIN) model of classical neurodynamics as formulated by Hopfield (1984) and Hopfield and Tank (1986). The LIN model is related to the Wilson and Cowan (1972) model, which employs similar first-order differential equations to describe the interaction between neural populations, and where the state variables represent the proportion of neurons firing. The Hopfield-and-Tank formulation is slightly closer to the biologically realistic compartmental model, as the state variable can be seen as an approximation of the membrane potential whose time derivative depends on the cross-membrane currents. While originally intended as a single-unit description, the LIN model can be used as a population description by assuming that the units in the population are identically and symmetrically connected with each other, and that they all receive the same external input. In this case the population units behave identically with each other, and the population can be described by the unit equation. Because the equations refer to cross-membrane currents (i.e., synaptic and leak currents), it becomes easier to motivate the calculation of the MEG signal, as is discussed below. The LIN formulation also has the advantage that it opens up an analytical approach to the system dynamics.

Central to the model is the anatomical structure of AC (Fig. 1a). The AC organization is similar across mammals in the sense that a hierarchical core–belt–parabelt structure can be identified, although the number of fields and their connectivity with each other is species-specific (Budinger et al. 2000; Budinger and Heil 2005; Baumann et al. 2013; Hackett et al. 2014). In general, core fields are characterized by on-responses to pure tones and their preferential connections with the tonotopically organized division of the auditory thalamus. They have extensive local connections with each other and with the surrounding belt fields. Belt fields are also tonotopically organized, albeit with a lesser spatial frequency resolution. There are strong local connections of belt fields with core fields and neighboring parabelt fields as well as connections with other cortical areas. In addition to dense connections with the ventral division of the medial geniculate body, belt fields also have pronounced connections with non-tonotopic parts of the auditory thalamus. Parabelt fields are non-tonotopic and isocortical, with lower cell density than the belt fields and have connections mainly with non-tonotopic auditory and non-auditory thalamic nuclei and remote cortical areas.

The model mimics this structure with its 240 columns (32 subcortical, 208 cortical) being distributed into one field representing the inferior colliculus (IC), one thalamic field, three core fields, eight belt fields, and two parabelt fields, with each field comprising 16 columns. We note that the IC and thalamus were not part of the original model (May and Tiitinen 2013; May et al. 2015). As shown in Fig. 1a, the fields of the model are connected according to the scheme found

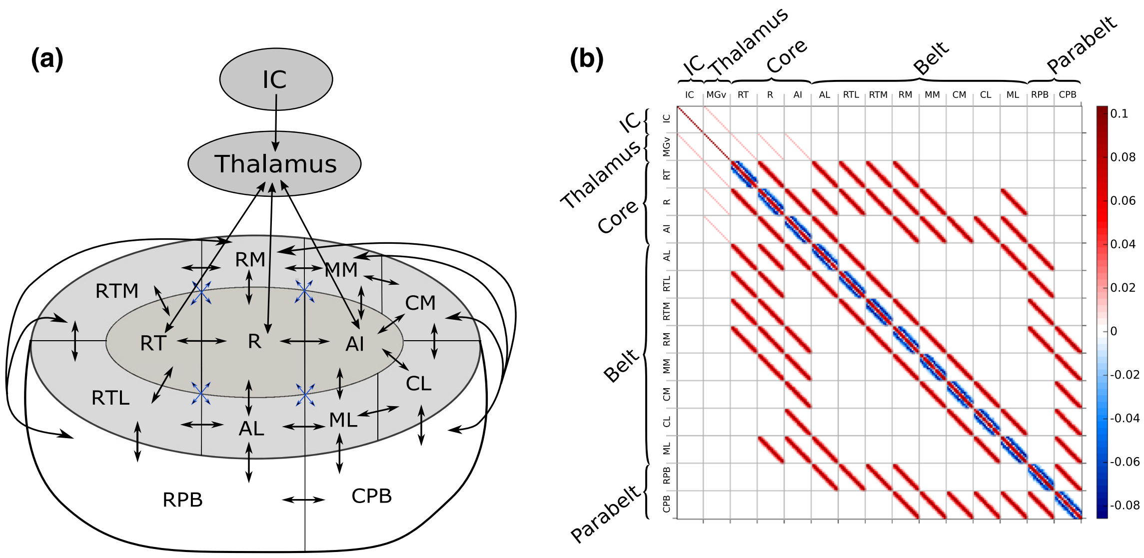

Fig. 1 The anatomical structure of the model. **a** The organization of the model mimics that of the primate AC, being subdivided into 13 fields—three core, eight belt, and two parabelt fields (Baumann et al. 2013; Kaas and Hackett 2000; Hackett et al. 2014). The model also includes two subcortical fields representing inferior colliculus (IC) and thalamus. Each field contains 16 columns comprising interacting excitatory and inhibitory mean-field populations. Connections between fields are indicated by black and blue arrows which signify high and low density of connections, respectively. The cortical connections are bi-directional and result in multiple streams of feedforward and feedback activation. The input to AC is guided along direct connections from thalamus to the three core fields. **b** The connections between the fields are given expression in connection matrices where each element denotes the strength of the connection between two columns; here, the matrix W_{AC} is shown as an example. The values of the matrix elements indicated by the color bar to the right represent the strength of the connections between any two columns: positive values stand for excitatory, negative values for inhibitory connections

in the macaque (Kaas and Hackett 2000). The connections between IC and thalamus as well as between thalamus and the three core fields are purely one-to-one tonotopic. The connections between cortical fields are likewise tonotopic, with each column projecting to its tonotopic counterpart in the recipient field. In addition, the projecting column also connects with columns neighboring the tonotopic counterpart. This spread of connections, which is symmetric and partly stochastic, is described by a Gaussian distribution and explained in more detail in Appendix A1. Hence, all the connections in the model are tonotopically organized, including those in the parabelt, and this simplification is unlikely to reflect the actual anatomical organization of AC. However, we note that the stochasticity in the connection matrix allows for the columns to exhibit multi-peaked and/or broad tuning curves.

3 Modeling auditory cortex dynamics with normal modes

The previous modeling work in May et al. (2015) used numerical simulations of the nonlinear state equations, and accounted for the generation of the N1m and the mismatch response of the ERF. However, this approach gives only a snapshot of the system dynamics at the particular parameter settings chosen for the simulation. This way there is limited access to the relationship between the ERF on the one hand and the system parameters such as the synaptic weights and the anatomical organization on the other. Further, numerical simulations alone will not reveal why and when the peaks and troughs of the ERF occur. Here, we attempt to gain deeper insight into the dynamics of AC by taking the analytical approach to find solutions to the AC system dynamics by simplifying the description even further. In particular, we ignore synaptic plasticity, and we assume that the state variables inhabit the linear portion of the spiking-rate nonlinearity. We use this linearization of the spiking rate together with assumptions of symmetry of the weight matrices to decouple the two sets of state equations based on the standard approach of eigenvalue decomposition. The decoupled equations are then analytically solvable, and their solutions are referred to as normal modes of the system. We end up with a complete description of the system dynamics and the generated ERF in terms of the parameters of the AC. We note that synaptic plasticity will be addressed in future work and that its omission does not affect the validity of the current results.

The idea of cell populations operating in the quasi-linear range of the spiking-rate function was already used by Katznelson (1981) in his approach of decomposing cortical activity into spherical harmonics. Also, May and Tiitinen (2001) found that, with the assumption of a linear spiking rate, a pair of excitatory and inhibitory LINs can be described as a driven harmonic oscillator with damping. We therefore expect that linearization of the current AC model will likewise lead to oscillatory solutions, which can be considered to be the fundamental elements of cortical dynamics (Nunez 1995; Buzsáki and Draguhn 2004; Buzsáki 2006). These approximations gain some validity from the experimental observations of Allen et al. (1975) who found that neuronal responses behave linearly for a broad span of membrane potentials.

Our analytical approach is based on the original state equations for $\mathbf{u}(t)$ and $\mathbf{v}(t)$ outlined in Eqs. (1) and (2), where we have defined the linear spiking-rate functions $g(x) = \alpha x$ and we set $\alpha = 1$. In this formulation, negative spiking rates are possible, and they should be interpreted as values relative to a resting state of continuous, spontaneous firing. A standard approach to obtain analytical solutions of Eqs. (1) and (2) is to diagonalize this system of first-order constant-coefficient differential equations via eigenvalue decomposition. Given the oscillating nature of brain activity (e.g., Nunez 1995; Buzsáki and Draguhn 2004; Buzsáki 2006), we attempted to obtain a more intuitive understanding of ERFs in terms of damped harmonic oscillators. Thus, we realized the eigenvalue decomposition by first transforming Eqs. (1) and (2) into second-order differential equations (see Appendix A2):

$$\ddot{\mathbf{u}}(t) + 2\Gamma_u \dot{\mathbf{u}}(t) + \Omega_{0,u}^2 \mathbf{u}(t) = \mathbf{q}(t) \tag{3}$$

$$\ddot{\mathbf{v}}(t) + 2\Gamma_v \dot{\mathbf{v}}(t) + \Omega_{0,v}^2 \mathbf{v}(t) = \mathbf{j}(t) \tag{4}$$

Eqs. (3) and (4) describe the well-known physical problem of a system of $2 \times N$ driven damped coupled harmonic oscillators, each characterized by N degrees of freedom, and with the definitions

$$\Gamma_u = \frac{\widetilde{W}_{\mathrm{ei}} \widetilde{W}_{\mathrm{ii}} \widetilde{W}_{\mathrm{ei}}^{-1} - \widetilde{W}_{\mathrm{ee}}}{2} \tag{5}$$

$$\Gamma_v = \frac{\widetilde{W}_{\mathrm{ii}} - \widetilde{W}_{\mathrm{ie}} \widetilde{W}_{\mathrm{ee}} \widetilde{W}_{\mathrm{ie}}^{-1}}{2} \tag{6}$$

$$\Omega_{0,u}^2 = \widetilde{W}_{\mathrm{ei}} \widetilde{W}_{\mathrm{ie}} - \widetilde{W}_{\mathrm{ei}} \widetilde{W}_{\mathrm{ii}} \widetilde{W}_{\mathrm{ei}}^{-1} \widetilde{W}_{\mathrm{ee}} \tag{7}$$

$$\Omega_{0,v}^2 = \widetilde{W}_{\mathrm{ie}} \widetilde{W}_{\mathrm{ei}} - \widetilde{W}_{\mathrm{ie}} \widetilde{W}_{\mathrm{ee}} \widetilde{W}_{\mathrm{ie}}^{-1} \widetilde{W}_{\mathrm{ii}} \tag{8}$$

$$\mathbf{q}(t) = \widetilde{W}_{\mathrm{ei}} \widetilde{W}_{\mathrm{ii}} \widetilde{W}_{\mathrm{ei}}^{-1} \mathbf{I}_{\mathrm{e}}(t) - \widetilde{W}_{\mathrm{ei}} \mathbf{I}_{\mathrm{i}}(t) + \dot{\mathbf{I}}_{\mathrm{e}}(t) \tag{9}$$

$$\mathbf{j}(t) = \widetilde{W}_{\mathrm{ie}} \mathbf{I}_{\mathrm{e}}(t) - \widetilde{W}_{\mathrm{ie}} \widetilde{W}_{\mathrm{ee}} \widetilde{W}_{\mathrm{ie}}^{-1} \mathbf{I}_{\mathrm{i}}(t) + \dot{\mathbf{I}}_{\mathrm{i}}(t). \tag{10}$$

The matrix terms with the capping tilde represent the connection matrices of the linearized canonical form [see Eq. (26) in Appendix A2]. The matrices $\widetilde{W}_{\mathrm{ei}}$ and $\widetilde{W}_{\mathrm{ie}}$ are invertible because they are diagonal matrices.

Analytical solutions for $\mathbf{u}(t)$ and $\mathbf{v}(t)$ of Eqs. (3) and (4) can be found in the current eigenvalue approach if the coefficients Γ_u and $\Omega_{0,u}^2$ as well as Γ_v and $\Omega_{0,v}^2$ fulfill certain requirements (see Appendix A2). In this case, the complex system of N degrees of freedom is transformed into a representation where there are N decoupled oscillators, each with a single degree of freedom, and where the coefficients are diagonalized as indicated by the subscript 'd' [see Eqs. (47) and (48) in Appendix A2]:

$$\ddot{\mathbf{u}}_{\mathrm{d}}(t) + 2\Gamma_{\mathrm{d}} \dot{\mathbf{u}}_{\mathrm{d}}(t) + \Omega_{0_{\mathrm{d}}}^2 \mathbf{u}_{\mathrm{d}}(t) = \mathbf{q}_{\mathrm{d}}(t) \tag{11}$$

$$\ddot{\mathbf{v}}_{\mathrm{d}}(t) + 2\Gamma_{\mathrm{d}} \dot{\mathbf{v}}_{\mathrm{d}}(t) + \Omega_{0_{\mathrm{d}}}^2 \mathbf{v}_{\mathrm{d}}(t) = \mathbf{j}_{\mathrm{d}}(t). \tag{12}$$

Each of the decoupled oscillators represents one normal mode with individual frequency and amplitude (Rayleigh 1945; Caughey 1960; Caughey and O'Kelly 1965). Normal modes are the basic elements of the decoupled system but they do not represent the dynamics of individual columns. Meaningful information on single-column dynamics as part of a network of columns can only be obtained after an inverse transformation whereby the normal modes are, in effect, coupled together.

The solutions for the decoupled equations for all 2×240 normal modes of the two state variables in their vector representation are then:

$$u_{\mathrm{d}}(t) = \exp(-\gamma_{\mathrm{d}} t)[a_{u_{\mathrm{d}}} \sin(\delta_{\mathrm{d}} t) + b_{u_{\mathrm{d}}} \cos(\delta_{\mathrm{d}} t)] + c_{u_{\mathrm{d}}} \tag{13}$$

$$v_{\mathrm{d}}(t) = \exp(-\gamma_{\mathrm{d}} t)[a_{v_{\mathrm{d}}} \sin(\delta_{\mathrm{d}} t) + b_{v_{\mathrm{d}}} \cos(\delta_{\mathrm{d}} t)] + c_{v_{\mathrm{d}}}, \tag{14}$$

with the coefficients of $u_{\mathrm{d}}(t)$ given by

$$\begin{aligned} a_{u_{\mathrm{d}}} &= \frac{w_{\mathrm{ei}} \gamma_{\mathrm{d}}}{\omega_{0_{\mathrm{d}}}^2 \delta_{\mathrm{d}}} I_{\mathrm{i}}(t) + \frac{\omega_{0_{\mathrm{d}}}^2 + w_{\mathrm{ei}} w_{\mathrm{ie,d}} - w_{\mathrm{ii}}^2}{2\omega_{0_{\mathrm{d}}}^2 \delta_{\mathrm{d}}} I_{\mathrm{e}}(t) \\ &\quad + \frac{w_{\mathrm{ii}} + w_{\mathrm{AC,d}}}{2\delta_{\mathrm{d}}} u_0 - \frac{w_{\mathrm{ie,d}}}{\delta_{\mathrm{d}}} v_0 \\ b_{u_{\mathrm{d}}} &= \frac{w_{\mathrm{ei}}}{\omega_{0_{\mathrm{d}}}^2} I_{\mathrm{i}}(t) - \frac{w_{\mathrm{ii}}}{\omega_{0_{\mathrm{d}}}^2} I_{\mathrm{e}}(t) + u_0 \\ c_{u_{\mathrm{d}}} &= -\frac{w_{\mathrm{ei}}}{\omega_{0_{\mathrm{d}}}^2} I_{\mathrm{i}}(t) + \frac{w_{\mathrm{ii}}}{\omega_{0_{\mathrm{d}}}^2} I_{\mathrm{e}}(t), \end{aligned} \tag{15}$$

and of $v_{\mathrm{d}}(t)$ given by

$$\begin{aligned} a_{v_{\mathrm{d}}} &= -\frac{w_{\mathrm{ie,d}} \gamma_{\mathrm{d}}}{\omega_{0_{\mathrm{d}}}^2 \delta_{\mathrm{d}}} I_{\mathrm{e}}(t) \\ &\quad + \frac{\omega_{0_{\mathrm{d}}}^2 + w_{\mathrm{ei}} w_{\mathrm{ie,d}} - w_{\mathrm{AC,d}}^2}{2\omega_{0_{\mathrm{d}}}^2 \delta_{\mathrm{d}}} I_{\mathrm{i}}(t) \\ &\quad - \frac{w_{\mathrm{ii}} + w_{\mathrm{AC,d}}}{2\delta_{\mathrm{d}}} v_0 + \frac{w_{\mathrm{ie,d}}}{\delta_{\mathrm{d}}} u_0 \\ b_{v_{\mathrm{d}}} &= \frac{w_{\mathrm{AC,d}}}{\omega_{0_{\mathrm{d}}}^2} I_{\mathrm{i}}(t) - \frac{w_{\mathrm{ie,d}}}{\omega_{0_{\mathrm{d}}}^2} I_{\mathrm{e}}(t) + v_0 \\ c_{v_{\mathrm{d}}} &= -\frac{w_{\mathrm{AC,d}}}{\omega_{0_{\mathrm{d}}}^2} I_{\mathrm{i}}(t) + \frac{w_{\mathrm{ie,d}}}{\omega_{0_{\mathrm{d}}}^2} I_{\mathrm{e}}(t). \end{aligned} \tag{16}$$

The decay constant γ_{d}, the angular frequency $\omega_{0_{\mathrm{d}}}^2$, and the damping frequency δ_{d} for both $u_{\mathrm{d}}(t)$ and $v_{\mathrm{d}}(t)$ depend on the connection matrices as follows:

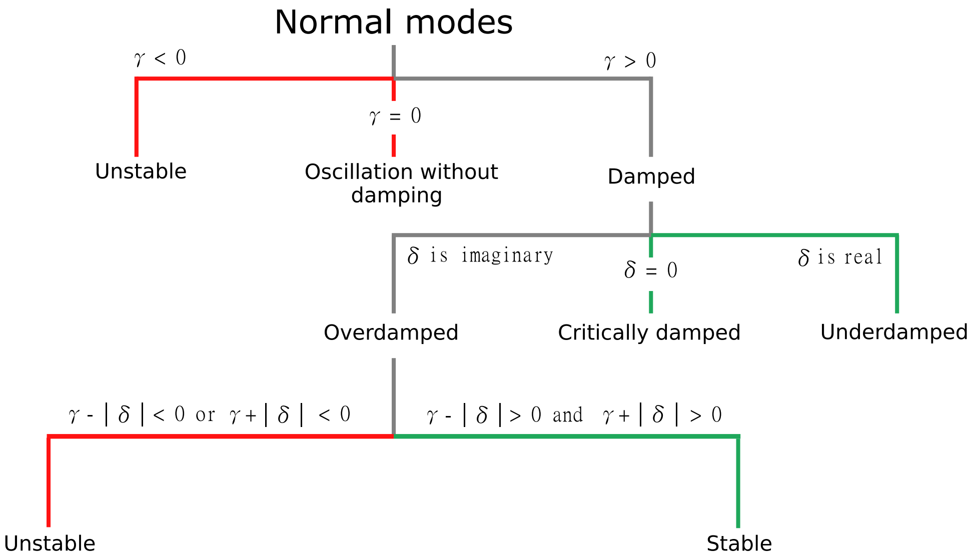

Fig. 2 Flowchart illustrating how the stability of normal modes depends on the decay constant γ and the damping frequency δ. In general, stable states can only be reached for $\gamma > 0$, i.e., in damped systems. If in a given damped system the damping frequency is real-valued, the system is in a stable underdamped state; if δ equals to zero, the system is critically damped. For imaginary damping frequencies, the system is overdamped, in which case its stability depends on the sign of both the difference and sum of γ and δ

$$\begin{aligned}\gamma_{\mathrm{d}} &= \frac{w_{\mathrm{ii}} - w_{\mathrm{AC,d}}}{2}\\ \omega_{0_{\mathrm{d}}}^2 &= w_{\mathrm{ei}} w_{\mathrm{ie,d}} - w_{\mathrm{ii}} w_{\mathrm{AC,d}}\\ \delta_{\mathrm{d}} &= \sqrt{\omega_{0_{\mathrm{d}}}^2 - \gamma_{\mathrm{d}}^2}.\end{aligned} \tag{17}$$

The flowchart in Fig. 2 shows the general dependence of the normal modes on the values of γ_{d}, $\omega_{0_{\mathrm{d}}}^2$, and δ_{d}, and, thus, on the connection matrices. The sign of the decay constant γ_{d} determines whether the solutions of Eqs. (13) and (14) are unstable (for $\gamma_{\mathrm{d}} \leq 0$) or whether they can be described in terms of a damped oscillator ($\gamma_{\mathrm{d}} > 0$). The value of the damping frequency δ_{d} further classifies the damped normal modes into overdamped (imaginary-valued δ_{d}), critically damped ($\delta_{\mathrm{d}} = 0$) and underdamped (real-valued δ_{d}) solutions. The corresponding equations for these solutions are summarized in Appendix A2.

We now have simple mathematical expressions for describing the fundamental dynamics of the excitatory and inhibitory cell populations. Equations (13) and (14) represent the normal modes, the individual building blocks of the dynamics of the auditory cortex which depend on anatomical structure. Figure 3 shows an example of decoupled and coupled state variables when the model is presented with a 50-ms stimulus targeting the excitatory population of column 8 of the IC (amplitude = 0.01 for corresponding elements of $\mathbf{I}_{\mathrm{aff,e}}$). In Fig. 3a, c, the 2×240 normal modes $u_{\mathrm{d}}(t)$ and $v_{\mathrm{d}}(t)$ are shown.

To gain access to the behavior of individual cortical columns, we have to couple the normal modes. This is achieved by multiplying the normal modes $\mathbf{u}_{\mathrm{d}}(t)$ with a mixing matrix $\varUpsilon$ according to

$$\mathbf{u}(t) = \varUpsilon \mathbf{u}_{\mathrm{d}}(t), \tag{18}$$

and likewise for $\mathbf{v}(t)$. The columns of the matrix $\varUpsilon$ are the eigenvectors of W_{AC} (see explanations of Eqs. (41) and (42) in Appendix A2). As a consequence, the structure of the AC as a whole determines the coupled response of each column. Specifically, the mixing matrix $\varUpsilon$ determines how the normal modes are combined—uniquely for each column—to produce the coupled response. The results are the solutions for the state variables $\mathbf{u}(t)$ and $\mathbf{v}(t)$, and the corresponding waveforms are shown in Fig. 3b and 3d, respectively. For both the excitatory and inhibitory state variables, the waveforms of the core fields (blue curves) have the largest amplitude and smallest peak latency. The belt (red curves) and parabelt (green curves) waveforms are successively shifted to larger peak latencies, and their peak magnitudes are clearly smaller than those in the core.

Note that the assignment of any normal mode to a particular location in the AC is not possible. Instead, one can consider how each normal mode contributes to the activity of each column and field. Figure 4 shows two examples of normal modes, the first with a high damping frequency δ_{d} (Fig. 4a) and the second with a low δ_{d} and a polarity opposite to that of the first (Fig. 4b). Figure 4c, d shows how these normal modes are mapped onto the structure of the AC (see Fig. 1) in terms of their contributions averaged over each cortical field. Note that the maps represent the mean contribution of each normal mode to the activities of the individual fields. Specifically, this occurs through the multiplication of the mixing matrix with the normal mode [see Eq. (18)]. Figure 4 represents the general observation that the AC mappings

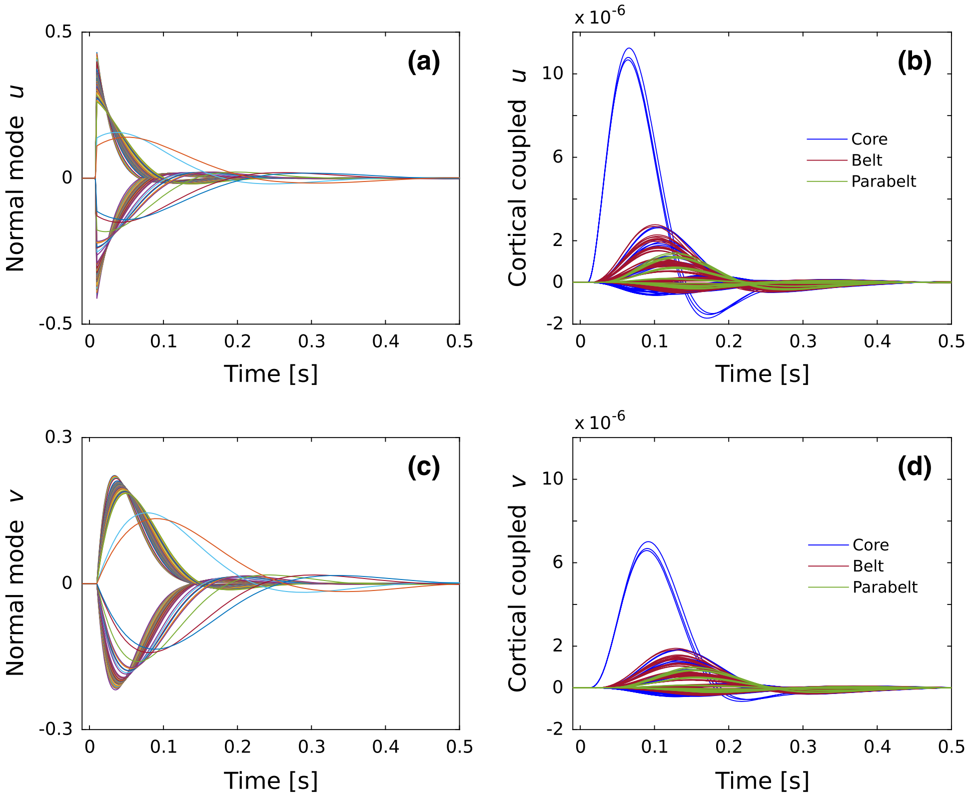

Fig. 3 An example of the normalized normal modes and state variables for the excitatory (**a, b**) and inhibitory (**c, d**) cell populations. In this example, the normal modes are rapidly decaying underdamped oscillations. Only about one-third of the normal modes have a peak magnitude significantly different from zero; the majority of the modes decay from a tiny magnitude toward zero. Note that the normal modes shown in **a** and **c** cannot be attributed to individual cortical columns and instead represent system-wide elements of the dynamics of AC. The coupling of the normal modes according to Eq. (18) results in the waveforms of the state variables of the individual cortical columns. These waveforms, color-coded according to cortical area, are shown in **b** and **d**. The three dominant waveforms in blue represent the responses of the columns receiving the thalamic input in the three core fields. In comparison, the waveforms for the other core columns (blue), for the belt (red), and for the parabelt (green) have smaller peak magnitudes and larger peak latencies. The normal modes have been normalized such that the area covered by each waveform equals unity

of high-frequency normal modes tend to have more structure than those of low-frequency normal modes.

4 A new framework for understanding ERF generation

The MEG signal arises out of the primary currents of synchronously active populations of pyramidal cells in cortex, and it is modified by topographical factors such as the current orientation and the distance to the MEG sensor. In this section, we describe how we approximate the primary currents, given that our model treats the neural populations as dimensionless dynamical units without an explicit term for dendritic current. We delineate how topographical factors can be included into the description, and how this produces two separate sets of parameters: one pertaining to the model dynamics and the other to topographical factors. We then demonstrate how the model replicates the ERF and what this reveals about ERF generation. Finally, we consider the cross-subject variability of the ERF with an eye to determining experimentally whether subject-specific responses are due to topographical factors only, or whether subject-specific cortical dynamics is also at play.

The MEG signal is proportional to the weighted sum of the primary currents, in the main those running in the apical dendrites of pyramidal neurons. While our description lacks a term for dendritic current, it does have terms equivalent to the synaptic input from each incoming connection. These are the spiking rates of the pre-synaptic populations multiplied by the connection strength. We approximated the primary current of each column to be directly proportional to the synaptic inputs to the excitatory populations. This approximation is justified by theoretical considerations and simulation results (May 2002) using realistic neuron models in the NEURON simulation environment (Hines and Carnevale 2001). These

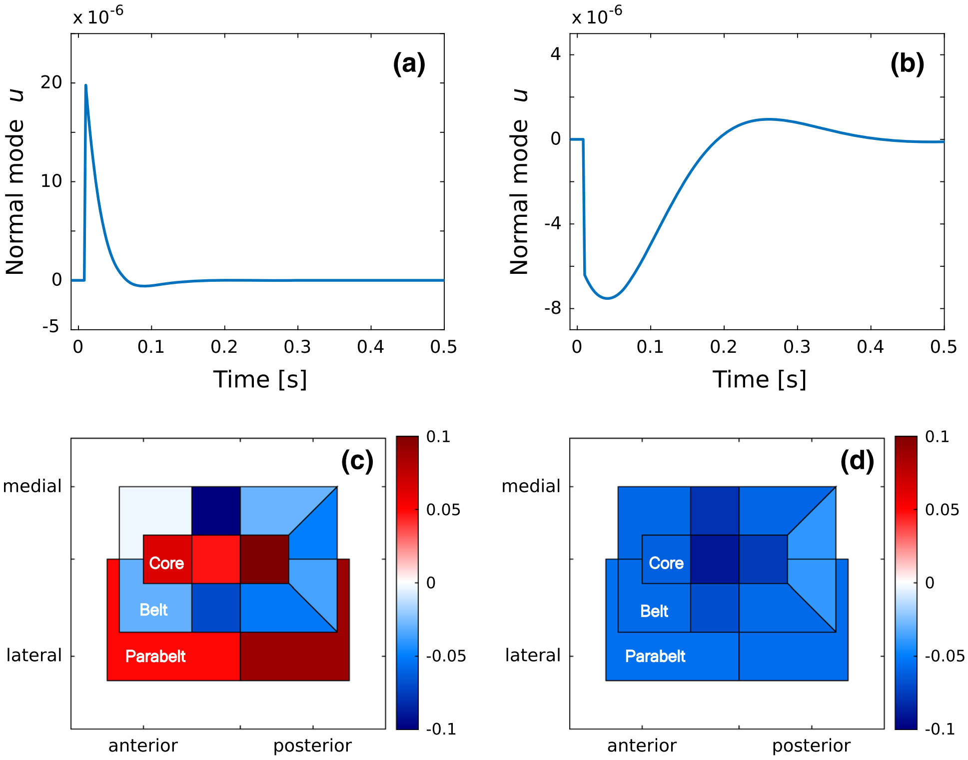

Fig. 4 Mapping normal modes to anatomical structure. **a, b** An example of a normal mode with high damping frequency δ_d and a normal mode with a low δ_d. The amplitude of the high-frequency normal mode dies away soon after 100 ms, whereas the low-frequency normal mode extends over 400 ms. **c, d** The normal modes shown in **a**, **b** are mapped onto anatomical structure (see Fig. 1a). For each normal mode, this mapping is achieved by identifying the elements in the mixing matrix Υ corresponding to a particular cortical field and then averaging these elements. The high-frequency normal modes tend to result in high-structure mappings. In this example, the contributions of the normal mode to the three core fields and two parabelt fields are of opposite polarity to the contributions to the eight belt fields surrounding the core. The mapping of the low-frequency normal mode has less structure, with the polarity being the same across all fields

previous results show that the synaptic input current has a near-linear relationship with the axial current in the dendrite and therefore with the contribution to the MEG signal produced by the neuron. In our model, the synaptic input term depends directly on the pre-connection state variable and, thus, the dynamical element of the MEG signal is found in the solutions to the state variables, see Eqs. (13)–(17). The dynamical element of the MEG is therefore governed by the set of system parameters P for the dynamical equations, with P comprising the elements of the various connection matrices, the time constant τ_m, and the input–output function $g(\cdot)$.

The MEG is not just a linear aggregate of the magnitude of the primary currents. Rather, in the aggregation, the contribution from each primary current is modulated by non-dynamical, topographical factors: the distance of the current to the MEG sensor, the geometry of the volume conductor, and the orientation of the current (Hämäläinen et al. 1993). The latter depends on multiple aspects: whether the synapse driving the current is excitatory or inhibitory, the location of the synapse on the apical dendrite, and the orientation of the pyramidal cell containing the current—which, in turn, depends on the subject-specific topography of the cortical surface. Thus, the contribution to the primary current of each synapse has a unique topographical multiplier. Translating this into the context of our model, the topographical modulation of the MEG signal can be represented by a set of matrices K_i, one for each connection matrix. Thus, the expression for the MEG signal is a sum over the synaptic inputs to the excitatory populations, weighted by the K_i matrices:

$$\begin{aligned} R(t) = \sum_{ij} [& K_1[i,j] \circ W^{+}_{\mathrm{AC}}[i,j] u_j(t) \\ & + K_2[i,j] \circ W_{\mathrm{ei}}[i,j] v_j(t) \\ & + K_3[i,j] \circ W^{-}_{\mathrm{AC}}[i,j] u_j(t)]. \end{aligned} \tag{19}$$

Here, the symbol $\circ$ represents the entrywise matrix multiplication, and the indices i and j refer to post- and pre-synaptic populations, respectively. The matrices W^{+}_{AC} and W^{-}_{AC} represent the excitatory connections and lateral inhibition of W_{AC}, respectively.

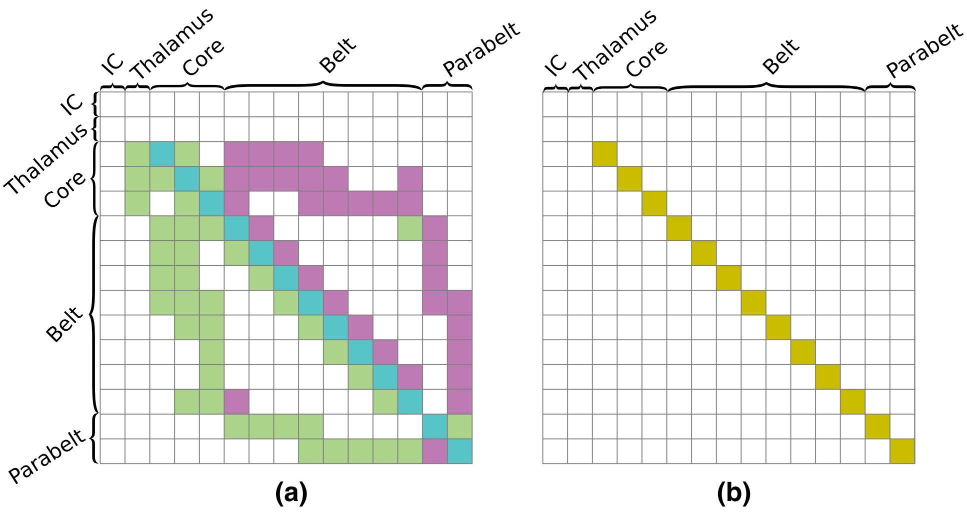

Fig. 5 The structure of the K_i matrices. The topographical modulations of the MEG signal are displayed as 15×15 field matrices, where each element represents 16×16 connections. The MEG signal is determined by the primary currents of the excitatory (pyramidal) cell populations and is thus driven by the excitatory and inhibitory inputs to these populations. **a** The matrix K_1 modulates the contribution to the MEG made via the excitatory connections. The 88 nonzero entries of this field matrix comprise positive and negative elements representing feedback (purple) and feedforward (light green) connections. The elements on the main diagonal represent within-field connections (cyan). **b** K_2 and K_3 modulate the contribution to the MEG signal made by the intra-column and lateral inhibitory connections, respectively. Only 13 within-field elements have nonzero elements because we are assuming that all inhibition is local, originating within the same field

Table 1 Default dynamical and topographical parameter values used in the simulations

Dynamical parameter set P	Value	Topographical parameter set K_i	Value
IC recurrent connections	0.09	K_1 (feedforward)	− 4
IC to Thalamus connections	0.015	K_1 (feedback)	20
Thalamus recurrent connections	0.09	K_1 (within field)	− 5
Thalamus to core connections	0.015	K_2 (within field)	2
W_{AC}	See Table 2	K_3 (within field)	2
$W_{ie,d}$	1		
W_{ei}	1		
W_{ii}	0.2		
τ_m	40 ms		

4.1 Calculating the MEG signal

In the sum of Eq. (19), the first term describes the contribution of the excitatory connections. The topographical information is embedded in the matrix K_1 as shown in Fig. 5a. The elements of K_1 represent three types of connection: feedforward, feedback, and within field (Table 1). Feedforward connections (light green in Fig. 5a) convey signals along the core–belt–parabelt direction. They contribute to the MEG with a polarity opposite to that of feedback connections (purple in Fig. 5a), which carry signals from the parabelt toward the core. This polarity reversal models the findings that feedforward signals tend to arrive in the middle layers, predominantly in layer IV, target proximal locations of the pyramidal dendrites, and thus result in a current flow which points upward, toward the cortical surface. In contrast, feedback signals result in a current flow downward because they arrive in upper layers I and II, and therefore target distal locations on the apical dendrite (Ahlfors et al. 2015). The feedforward–feedback organization of K_1 is in part supported by the results of Hackett et al. (2014) who mapped the layer-specific feedforward and feedback projections in belt and parabelt of the monkey. The polarity of the within-field connections (cyan elements in Fig. 5a) was taken to be the same as for the feedforward connections.

The second term of Eq. (19) is the contribution to the MEG of the inhibitory projections originating from within the column. The synaptic input is modulated by the matrix K_2, as represented in Fig. 5b. The third term of Eq. (19) accounts for the MEG contribution of lateral inhibition whereby W_{AC}^{-} is modulated by the matrix K_3. K_2 and K_3 have the same structure and values (Table 1). Further, the polarity of the

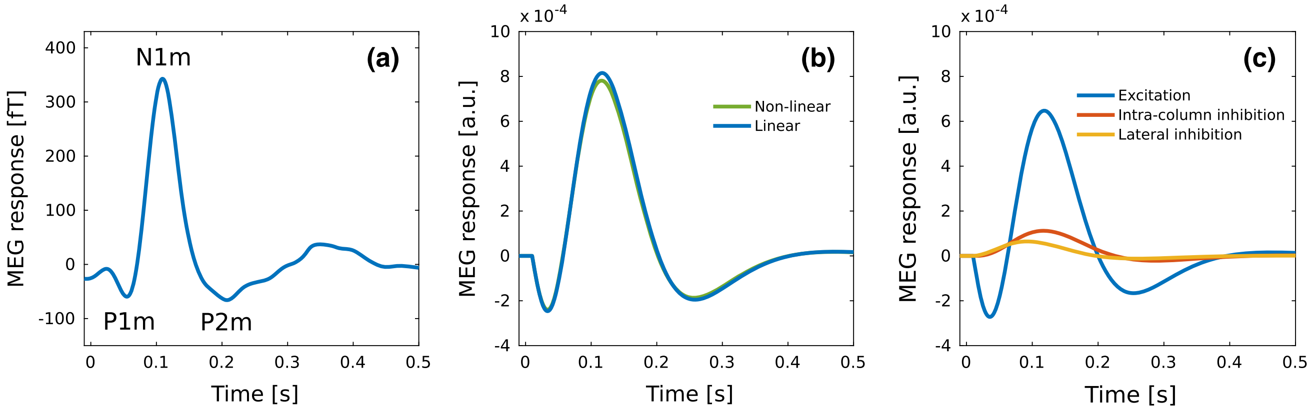

Fig. 6 Comparison of experimental and simulated ERFs. **a** The figure shows the grand mean of trial-averaged ERFs recorded from 15 subjects in response to 1.5-kHz tones of 100-ms duration and 80-dB sensation level presented with a stimulus-onset interval of 3 s (data from Matysiak et al. 2013). **b** The blue curve represents the ERF computed according to Eq. (19) as the sum of the primary currents modulated by the three K-matrices. The simulation replicates a typical ERF waveform with P1m, N1m, and P2m responses. The green curve shows the simulated ERF generated by the nonlinear model with sigmoid spiking-rate function, synaptic plasticity, but otherwise model parameters identical to those used in the analytical approach. For more information on synaptic plasticity, see May et al. (2015). In **c**, the MEG signal resulting from the analytical solutions shown in **b** is broken down into the contributions made by the excitatory connections (blue), the intra-column inhibitory connections (red), and the connections for lateral inhibition (orange). Only the contribution from the excitatory connections shows distinct P1m, N1m, and P2m deflections, which have peak latencies and amplitudes similar to those of the overall ERF shown in **b**. In comparison, the contributions from the inhibitory connections are unimodal, with earlier peak latencies and much smaller peak amplitudes. Thus, the P1m and the P2m deflections are driven by excitatory connections. The origin of the abscissa ($t = 0$) indicates stimulus onset

elements of K_2 and K_3 is the same as that of the elements of K_1 representing feedback connections. This polarity conveys the finding that inhibitory synapses tend to be located near the soma (Douglas et al. 2004, see, however, Kubota et al. 2016), and therefore their activation contributes to a current pointing downward in the apical dendrites of pyramidal neurons (Ahlfors and Wreh 2015). In general, inhibitory synapses contribute to the primary current if the pyramidal cell has an elevated membrane potential and is spiking (Trevelyan 2009; Glickfield et al. 2009; Bazelot et al. 2010). In our case, we are assuming that the resting state represents sustained, spontaneous activity, which corresponds to an elevated membrane potential.

4.2 Simulations of ERFs

In each simulation, the AC model started in the resting state and was presented with a 50-ms stimulus, with the afferent input $\mathbf{I}_{\mathrm{aff,e}}$ targeting the central column of the IC field (column 8) with amplitude = 0.01. We used a low amplitude to ensure a good correspondence between the ERFs produced by the linear and nonlinear versions of the model. A 10-ms delay—roughly the duration of auditory brain stem responses—was assumed to occur between stimulus onset and the signal reaching IC. The default values of the dynamical parameters P and topographical parameters K_i are listed in Table 1. The parameter values reflect the finding that recurrent connections in cortex are an order of magnitude stronger than afferent and between-field connections (Douglas and Martin 2007; Douglas et al. 1995). However, the exact values, while representing a balance between excitation and inhibition, are arbitrary and were chosen on the basis of reproducing realistic looking ERFs. The ERF was calculated using Eq. (19).

Figure 6a shows an example of an ERF from an MEG experiment using pure-tone stimulation (Matysiak et al. 2013). The waveform has a typical morphology and it shows the grand mean computed from the ERFs of several subjects. The blue curve in Fig. 6b represents the ERF waveform generated by the current linear model whose normal modes and coupled state variables are presented in Fig. 3. This simulation replicates the morphology shown for the experimental ERF in Fig. 6a: There is an initial P1m-like response peaking at 35 ms. The ERF then crosses polarity and builds up into a large-amplitude N1m-like response peaking at 115 ms. This then is followed by a shallow P2m response peaking at 260 ms. The green curve was generated in a simulation with the nonlinear version of the model. The linear and nonlinear models produce ERFs with very similar morphologies. The minute differences in the peak amplitudes are caused by the synaptic plasticity term of the nonlinear model.

Figure 6c shows the contributions to the ERF coming from excitation, intra-column inhibition, and lateral inhibition, as defined in Eq. (19). The contribution from excitation is characterized by deflections similar to the P1m, N1m, and P2m responses (Fig. 6b). In contrast, the contributions made via

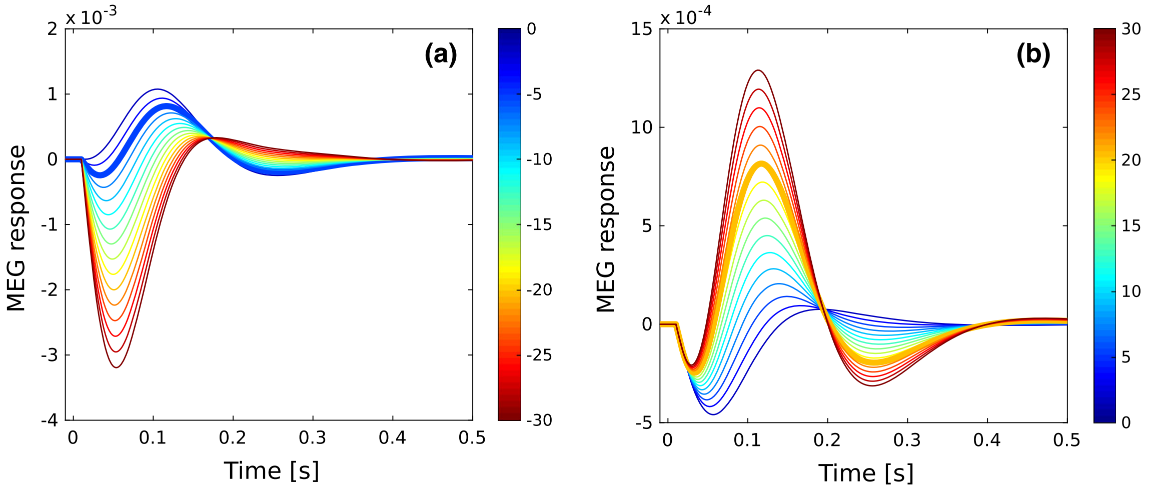

Fig. 7 The role of feedforward and feedback connections in shaping the ERF. **a** The contribution of the feedforward connections as specified in K_1 was varied from 0 (blue) to -30 (red) in steps of 2. All other parameters were fixed at their default values. With no feedforward contribution, the ERF comprises an N1m and P2m. As the feedforward term is increased, the P1m increases in prominence until it becomes the sole feature. **b** The contribution of the feedback connections was increased from zero (blue) to 30 (red) while the other parameters were kept at their default values. With no feedback contribution, the ERF contains a P1m response only. As the feedback contribution grows, the most noticeable change in the ERF is the emergence and increase of the N1m and P2m deflections. The thick blue curve in **a** and the thick yellow curve in **b** correspond to the simulated waveform shown in Fig. 6b

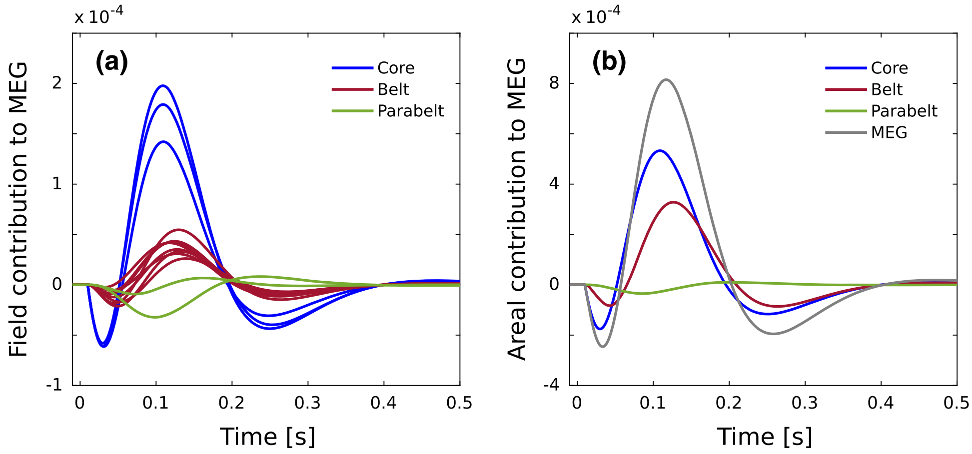

Fig. 8 Contributions from AC fields and areas to the ERF. **a** The contributions of the individual AC fields decrease sharply as one moves from core to belt to parabelt. **b** The larger number of belt fields (eight) compared to those of the core (three) compensates for this disparity such that the total contribution of the belt to the overall ERF is of the same order of magnitude as that of the core. The magnitude of the parabelt response is much weaker. For comparison, the overall ERF waveform (see Fig. 6b) is also displayed (gray line)

the inhibitory connections each comprise only a single N1m-like deflection of a small amplitude. Thus, the P1m and P2m responses are driven by excitation of the pyramidal cells.

To further examine the dependence of the ERF on the topography of the connections, we varied the K_1 weights of the contributions of the feedforward and feedback connections to the MEG signal. The results are shown in Fig. 7, where the thick blue line in (a) and the thick yellow line in (b) depict the waveform in Fig. 6b generated with the default parameter values (Table 1). In Fig. 7a, the contribution of the feedforward connections (light green elements in Fig. 5a; default value -4) was altered from 0 (top blue line) to -30 (bottom red line) in steps of 2 while keeping the other parameters constant. The largest effect is the emergence of the P1m and a marked monotonic increase in its peak amplitude as the feedforward contribution is increased. This is accompanied by an increase of the P1m peak latency from 26 to 54 ms. As the P1m becomes more and more substantial, it increasingly dwarfs the N1m, which is abolished at the largest contributions of the feedforward connections. A very

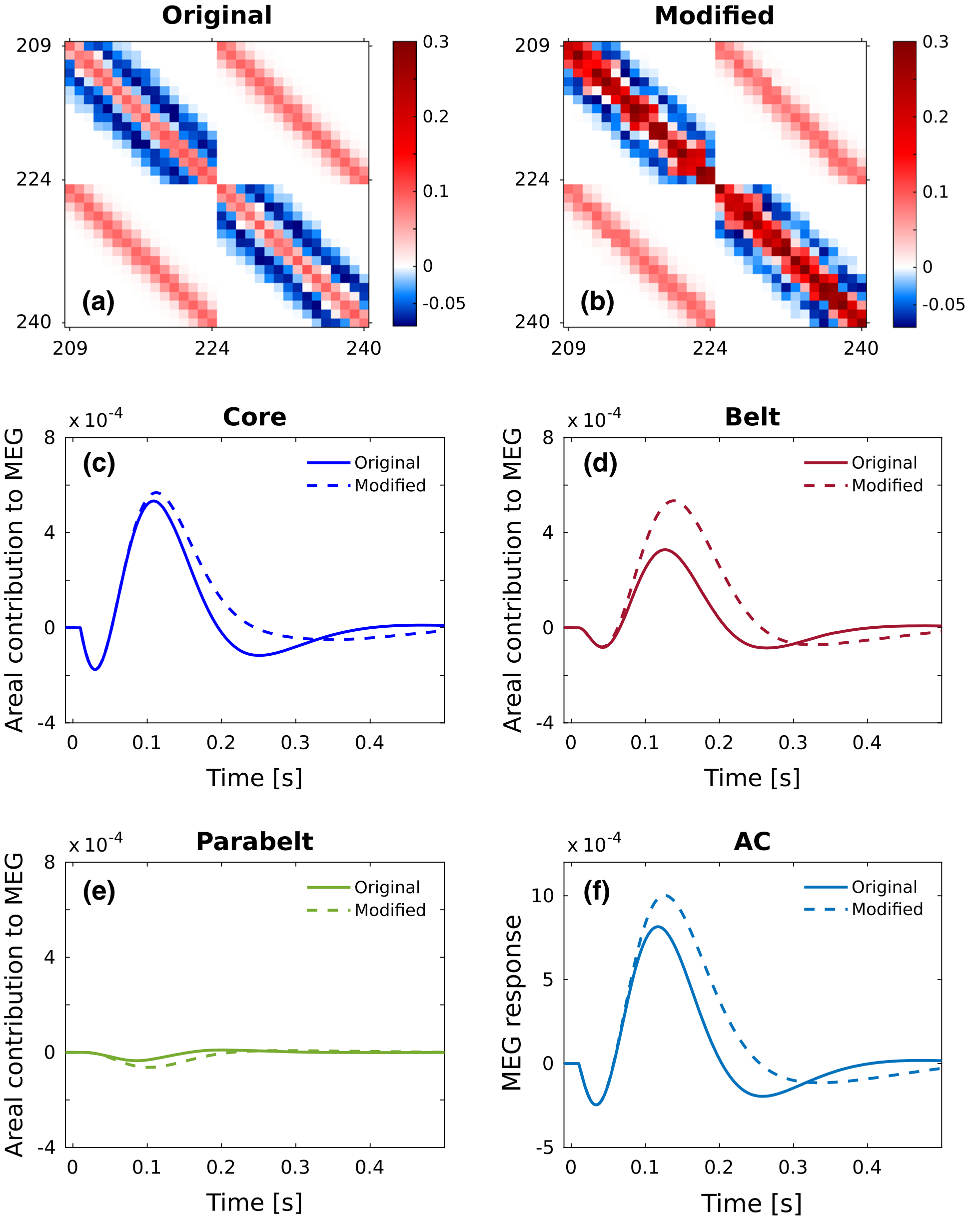

Fig. 9 Evoked responses are network properties as demonstrated by modulating the connections within the parabelt. **a** The original connections within and between the two parabelt fields are shown as a magnification of W_{AC} of Fig. 1b. **b** The weights of the within-field connections in parabelt were modified such that the default value of the amplitude r of the Gaussian distribution was multiplied by 3. Further, the default values of the stochasticity parameter s for both the within- and between-field connections in parabelt were multiplied by 2 (see Table 1 and Appendix A1). The color bars indicate the connection strength and polarity. **c–e** The contributions to the ERF are shown separately for the core, belt and parabelt. The solid curves represent simulations using the original parabelt connections, and they are identical to those shown in Fig. 8b. The dashed curves are from simulations using the parabelt-modified W_{AC} shown in **b**. The modification of the parabelt connections affects the ERF contributions from all areas, including the core. **f** This results in marked changes in the morphology of the ERF, including shifts in the peak latency and amplitude of the N1m and the abolition of the P2m

different pattern emerged when the feedback contribution to the MEG signal (purple elements in Fig. 5a; default value 20) was increased from 0 (bottom blue line) to 30 (top red line) in steps of 2 (Fig. 7b). With zero feedback contribution, the N1m and the P2m were missing, and the ERF comprised a P1m response only. The N1m and P2m emerged only with the presence of feedback contribution. As this contribution was increased, the largest growth in amplitude was for the N1m. These results suggest that the P1m mainly reflects feedforward activation, whereas the N1m and P2m reflect feedback activation.

In Fig. 8a, the source structure of the ERF shown in Fig. 6b is revealed in terms of the individual contributions from the 13 cortical fields. The total contributions from the core, belt and parabelt are shown in Fig. 8b, along with the overall MEG response. In general, as one moves along the core–belt–parabelt axis, the responses decrease in magnitude and increase in latency. The P1m has its main source in the core, with the belt also contributing. Similarly, the N1m is largely generated in the core, but the belt contribution is now much larger. The core and belt have similar contributions to the P2m. Because of their delay, the parabelt responses contribute to the ERFs with deflections of the opposite polarity of those produced by the core and belt. However, these contributions are very shallow and broad. We note that none of the peaks and troughs of the ERF (e.g., the P1m, N1m, P2m) has a dedicated response generator in the sense that activity in any particular region of the model would account for the deflection. Rather, activity is occurring in all parts of the AC throughout the ERF, with the exception of the parabelt being in its resting state during the P1m. What is changing between the ERF deflections is the relative contribution of each area to the signal.

Each field and area might play a more fundamental role in ERF generation than that of providing a source for each deflection. Namely, our analytical results in Eqs. (13)–(17) show that the anatomical structure of the entire AC, encapsulated in W_{AC}, is part of the solution to the dynamical equations. Thus, for each field, the way it is connected to other fields, and even the local structure within the field should impact on the entire ERF. This should be the case even at the fringe of the model, in the parabelt, which otherwise provides only a weak direct source to the ERF. Figure 9 shows the results of the simulations testing this idea. Here, while keeping all other parameters constant, we introduced variations to the weight values of W_{AC} representing the internal connections within and between the two parabelt fields (for details, see Appendix A1). These variations (Fig. 9a, b) had a minimal effect on the response produced by the parabelt (Fig. 9e) while, paradoxically, significantly altering the overall ERF (Fig. 9f). Figure 9c, d shows that the parabelt modification resulted in prominent changes in the core and belt contributions to the N1m. The end result in the ERF is a much broader N1m waveform, with a larger peak amplitude and latency, and an elimination of the P2m.

4.3 Separating dynamics from topography in ERF generation

Across-subject variability of the event-related response is likely to reflect diversity in the topography of the cortical surface. However, it is possible that variations in the dynamics of the auditory cortex also contribute. The current AC model suggests ways to tease apart these contributing factors. Given that in P and K_i we have separate parameter sets for the dynamical and topographical contributions to the MEG signal, the question becomes whether there are aspects of the ERF which change when P is modulated but not when K is modulated, and vice versa. To this end, we examined the ERF under two conditions. In the first condition, the dynamical parameters P were kept constant and the topographical parameters embedded in the three K-matrices were varied. For this, the elements of the K_1 matrix were grouped into a 15×15 field matrix as depicted in Fig. 5a, and then each of the 88 nonzero elements of this field matrix were randomized separately by multiplying the default value (Table 1) with a random number from a distribution in the $[0.5, 2]$ range. Similarly, the 13 nonzero elements of K_2 and K_3 were randomized separately using a random number from the same distribution. Figure 10a shows waveforms for 1000 such randomizations. In the second condition, the elements of the connection matrices found in P were randomized while the other parameters were left unchanged. For each simulation, each element of the diagonal matrices $W_{\mathrm{ie,d}}$, W_{ei}, and W_{ii} was generated separately by multiplying the default value with a random number in the $[0.5, 2]$ range. Also, for each simulation, we generated a new stochastic version of W_{AC} (see Appendix A1). Unstable solutions (see flowchart in Fig. 2) were excluded from further analysis. Figure 10f depicts 1000 waveforms produced this way, each one representing a stable solution.

The randomization of the topographical parameters K_i lead to a scaling of the ERF, while its overall morphology was maintained (Fig. 10a). Similar scaling effects are visible in Fig. 7 where the contribution of the K_1 feedforward and feedback connections to the ERF are studied independently in a systematic way. In contrast, randomizing the dynamical parameters P resulted in a much larger diversity of the ERF waveform (Fig. 10f). To quantify these effects, we plotted the N1m-peak amplitude of the simulated waveforms against the corresponding peak latency in Fig. 10b, g. Except for the waveforms with the smallest peak amplitudes $< 0.5 \times 10^{-3}$, the N1m-peak latencies of the waveforms obtained from the randomization of the topographical parameters are nearly independent of the peak amplitude and cover a narrow range between about 110 ms and 130 ms (Fig. 10b). In contrast, when the dynamical parameters are randomized, the N1m-peak latencies span a much wider range from approximately 70 ms to 160 ms (Fig. 10g). Further, we observe a strong correlation between peak amplitude and peak latency.

The diversity between the waveform morphology can further be expressed in terms of Fourier frequency f_{ERF} and decay time τ_{ERF} of the waveforms. The Fourier frequencies f_{ERF} shown in Fig. 10c, h were obtained through a standard fast Fourier transform (FFT) and represent the dominant frequency of the FFT analysis. As expected from Fig. 10a, variations in the topographical parameters resulted in a narrow distribution of f_{ERF} around 3 Hz. By comparison, when the dynamical parameters were varied, the distribution was much broader and peaked at 4 Hz. Note that the increase in the distribution at lower values of f_{ERF} is due to those broad MEG waveforms in Fig. 10f that do not reach baseline level even by $t = 500$ ms. The time constant τ_{ERF} describes the temporal decay of each waveform, and it was determined by first calculating the envelope of the ERF through the application of the Hilbert transform to the data. In a second step, an exponential decay function was fitted to the transformed data in a time interval ranging from the peak value of the envelope, at around 100 ms, to 600 ms where the MEG signal had sunk back to its baseline level. For both topographical and dynamical variations, the distribution of τ_{ERF} was centered in the 60–70 ms range. However, the distribution of τ_{ERF} was much broader for the dynamical variations than the topographical ones, as shown in Fig. 10d, i.

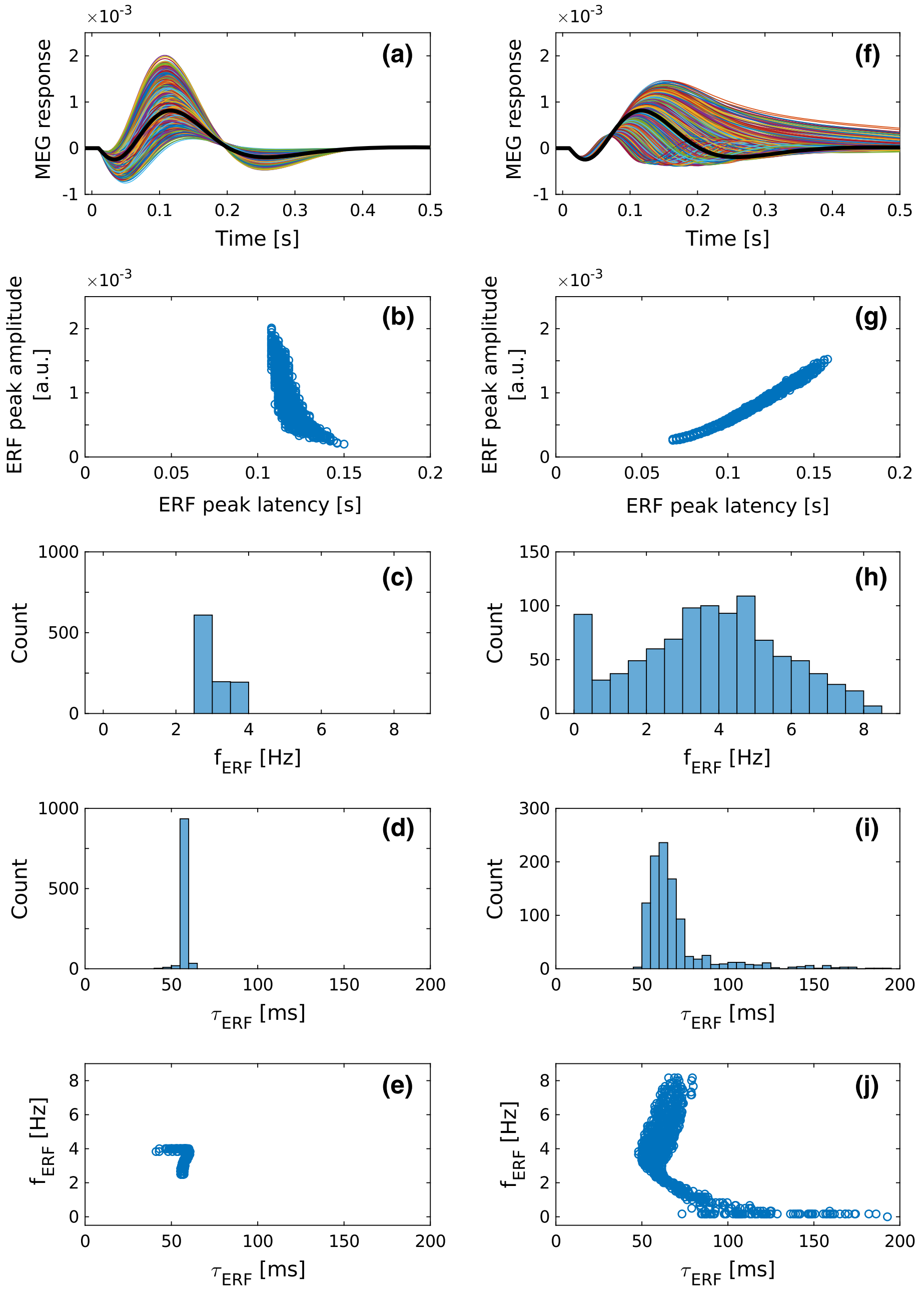

Fig. 10 The impact of variations of the topographical parameters (left column) and dynamical parameters (right column) on the ERF. **a** The effect of topographical factors was examined by randomizing the K_i-matrices while keeping the parameters P fixed. A total of 1000 ERF waveforms were generated such that for each simulation the default value of each element of the K_i-matrices was multiplied by a random number from a distribution in the [0.5, 2] range. The resulting waveforms are similar in shape. **b** While the N1m-peak amplitudes of these waveforms have a wide distribution, the corresponding peak latencies inhabit a narrow range, and there is only a weak dependency between the two. **c** The spectral analysis by means of FFT reveals a narrow distribution around a frequency f_{ERF} of about 3 Hz. **d** The time constants τ_{ERF} which describe the attenuation of the waveforms shown in **a** are narrowly distributed around 60 ms. **e** The tight distributions of f_{ERF} and τ_{ERF} result in a rather focal distribution in the f_{ERF}–τ_{ERF} plane. **f** In studying the effects of the dynamical parameters, P was randomized while the K_i-parameters were kept constant. For each simulation, each default-valued element of the scalar matrices $\widetilde{W}_{\mathrm{ie,d}}$, $\widetilde{W}_{\mathrm{ei}}$, and $\widetilde{W}_{\mathrm{ii}}$ was multiplied by a random number from a distribution in the [0.5, 2] range. Further, for each simulation, we generated a new stochastic version of W_{AC}. The resulting waveforms vary greatly in their morphology. **g** There is a strong correlation between the N1m-peak amplitude and peak latency, and both measures vary over a wide range. **h** The FFT analysis reveals a broad distribution of f_{ERF} around 4 Hz. **i** Also, τ_{ERF} is broadly distributed around 60 Hz. **j** The broad distributions translate into an L-shaped dependency between f_{ERF} and τ_{ERF}. Note that for the randomizations of the K_i-matrices as well as of the P-parameters, two subsets of random numbers with equiprobable distributions in the [0.5, 1]-range and in the [1, 2]-range were used. Whereas the K-modulation yielded solely stable solutions, 19% of the solutions of the P-modulation were unstable; these were excluded from further analysis. The thick black lines in **a** and **f** represent the default simulated waveform shown in Figs. 6b and 8b

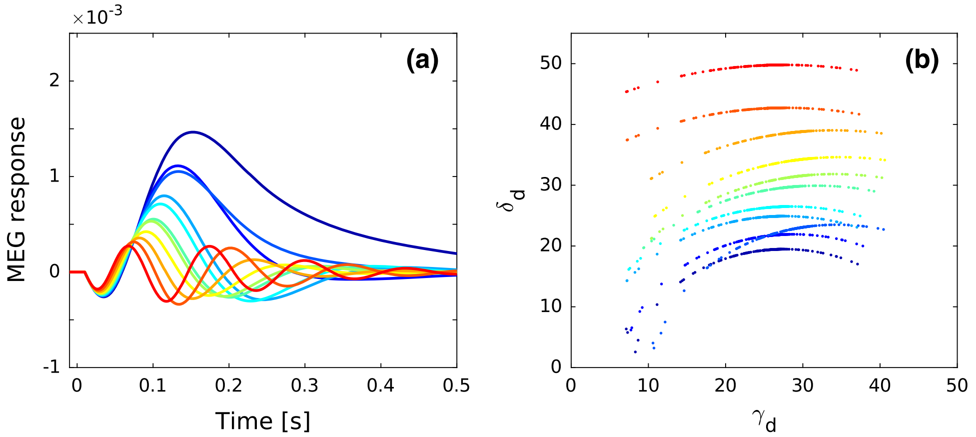

Fig. 11 Linking ERF waveforms to normal mode parameters. **a** A subset of 11 ERF waveforms from Fig. 10f are shown. These cover the full range of f_{ERF} shown in Fig. 10h. **b** The decay constants of the underlying normal modes are plotted against the corresponding damping frequencies. Waveforms with low f_{ERF} (blue) have small δ_{d} values and those with high f_{ERF} (red) have large δ_{d}. As f_{ERF} decreases, the dependence of δ_{d} on γ_{d} increases

Further differences between the effects of topographical and dynamical variations become evident when f_{ERF} is plotted against τ_{ERF}. In the case of topographical variations, the tight distributions of these morphological descriptors depicted in Fig. 10c, d translate into a rather focal distribution in the f_{ERF}–τ_{ERF} plane, as shown in Fig. 10e. Interestingly, the broader distributions of f_{ERF} and τ_{ERF} associated with dynamical variations did not translate into an even or random distribution in the f_{ERF}–τ_{ERF} plane. Instead, Fourier frequency and temporal decay showed a dependency on each other, with the distribution forming a distinct L shape, as is evident in Fig. 10j. Thus, there were two regions in the distribution: in the narrow range of $\tau_{\mathrm{ERF}} = (60 \pm 10)$ ms, the corresponding f_{ERF} had a wide distribution extending from 2 to 8 Hz. Conversely, when f_{ERF} was below 1 Hz, τ_{ERF} was distributed over a 70–200 ms range. Thus, there were no instances of fast temporal decay of the ERF waveform coupled with a high Fourier frequency.

Finally, we linked the variations in the ERF waveforms back to the parameters which characterize the normal modes. Figure 11a shows a subset of the ERFs shown in Fig. 10f covering a broad range of f_{ERF}. For each ERF, we plotted the damping frequency δ_{d} against the decay constant γ_{d} of the 240 underlying normal modes in Fig. 11b. While there was little variation of γ_{d} across the different ERFs, δ_{d} varied over a wide range not only in its absolute values but also in the dependence on γ_{d}. For ERFs with low f_{ERF} (blue curves in Fig. 11a), δ_{d} has small values and shows a strong dependence on γ_{d}. As f_{ERF} increases, so does δ_{d}, and the dependence of δ_{d} on γ_{d} becomes weaker.

In summary, these results predict that variations in the ERF waveform are specific to the type of parameter that is being varied. Thus, variations in dynamical parameters lead to a much broader selection of waveforms than do changes in topographic parameters. These results, depicted in Fig. 10, serve as predictions for testing in ERF measurements. We have confirmed these findings using multiple default models with realistic-looking N1m–P2m responses.

5 Discussion

Here, we presented a mechanistic explanation of long-latency auditory ERFs by developing analytical solutions for an already existing nonlinear model of AC signal processing. The model is based on the idiosyncratic architecture of AC in which information flows in a distinctly serial manner along multiple parallel streams within a core–belt–parabelt structure. We derived analytical solutions of the coupled differential equations for the state variables of the excitatory and inhibitory cell populations by assuming that the response to the synaptic input is linear in a wide range of spiking rates, and by using symmetric connections between the cell populations. The result is a description of the system dynamics in terms of normal modes, that is, decoupled damped harmonic oscillators. The ERF response reflects these dynamics but it is modulated by a set of non-dynamical factors comprising the topography of the primary currents and the effects of the type of connection contributing to the primary current. We showed that the ERF response originates from a mixture of normal modes, and that these directly depend on the anatomical structure as expressed in the connection matrices. In our account, each peak and trough of the ERF is not due to dedicated response generators but, rather, arises out of the network properties of the entire AC. The model generates predictions for testing whether the large inter-subject variability of ERFs is due merely to subject-specific cortical topographies or whether it also reflects subject-specific cortical dynamics.

5.1 The link between anatomy, dynamics, and ERFs

The current work accounts for auditory ERFs by decomposing them into a set of normal modes. Each normal mode is a solution to the equations for a driven damped harmonic oscillator [Eqs. (13) and (14)], and falls into one of three types: overdamped, critically damped, or underdamped. Further, a normal mode is defined by its amplitude [Eq. (15) or (16)] as well as by two physical terms, the decay constant γ_{d} and the damping frequency δ_{d} [Eq. (17)]. These parameters are, in turn, functions of the set of dynamical parameters we denote by P, which includes all the connection matrices. With each normal mode depending directly on the entire set of connection patterns and connection strengths of the system, the decomposition of the ERF into normal modes anchors the ERF waveform directly to the anatomical structure of AC. Thus, modifying the anatomical structure can change subtle aspects of the ERF, such as the amplitudes and latencies of individual peaks and troughs. However, anatomical structure also determines what the mixture of the normal modes are in terms of their type, and it is therefore reflected in the gross aspects of the ERF, that is, whether certain peaks and troughs appear at all.

We also see how the activity of each individual column depends not just on the synaptic input to the column but, rather, it directly reflects the entire anatomical structure of the AC. The connection matrix W_{AC} (Fig. 1b) plays a special role in the model. It consists of all the short- and long-range connections, including those which relay lateral inhibition, and thus encapsulates the anatomical structure of AC. Thus, for any specific pattern of connections and set of connection strenghts, $\widetilde{W}_{\mathrm{AC}}$ will have a specific set of eigenvalues and eigenvectors. For a given set of W_{ei}, W_{ii} and $W_{\mathrm{ie,d}}$ matrices, the eigenvalues of $\widetilde{W}_{\mathrm{AC}}$ define the distribution of frequencies δ_{d} of the normal modes [Eq. (17)]. Further, the eigenvectors regulate how the input is distributed among the normal modes [see Eqs. (45) and (46) in Appendix A2]. Using the eigenvectors gathered in the matrix Υ to couple the normal modes [Eq. (18)] gives expression to the state variables $\mathbf{u}(t)$ and $\mathbf{v}(t)$. Consequently, the state variable of any single column is a representation of all the normal modes, which themselves are functions of the structure of the AC network. Introducing variations in $\widetilde{W}_{\mathrm{AC}}$ leads to changes in its eigenvalues and eigenvectors and, thus, in the dynamics of the system both on the single-column level and in terms of the ERF. We generated multiple $\widetilde{W}_{\mathrm{AC}}$ matrices, and observed that δ_{d} depended strongly on the connection strengths while the distribution of γ_{d} was little affected (Fig. 11). ERFs with a single peak were produced by systems with a relatively wide distribution of low-valued δ_{d} which showed a strong dependence on γ_{d}. Multi-peaked ERFs were generated by systems with high-valued δ_{d} packed into a narrow range, with little dependence on γ_{d}.

The normal modes are dynamic units which cannot be localized to any particular single location in AC. Each one can be thought of as being spread over the whole AC in a unique fashion, contributing to the activity of the cortical columns with varying strengths and polarities. This spread is accessible in the analytical approach, allowing one to map the mean contribution that each normal mode makes to each cortical field (Fig. 4). The resulting anatomical maps of the normal modes tended to show that high damping frequencies were associated with increased spatial structure. Though not shown explicitly here, one upshot of this is that the early part of the ERF is generated by normal modes with large variations across cortical fields, resulting in lower field-to-field correlations in their activity. In contrast, the late part of the ERF is dominated by normal modes with a uniform effect over the fields, resulting in higher inter-field correlations. This view opens up the possibility to consider how the activity of different fields and columns are coupled to each other via the normal modes in dynamic connectivity maps. The full implications of these observations and resulting predictions will be returned to elsewhere.

The MEG signal arises out of the cortical primary currents, which are driven by the system dynamics, and this signal is modulated by topographical factors influencing the orientation of the current. One of these factors is whether the connection driving the primary current represents feedforward or feedback input to the cortical column (Ahlfors et al. 2015). As part of the dynamical parameters P, our model included both feedforward and feedback AC connections in the connection matrix W_{AC} (and the corresponding $\widetilde{W}_{\mathrm{AC}}$). The differential contributions of these two kinds of connections to the MEG signal was approximated through the use of the topographical K_1 matrix. By systematically varying the size of these contributions (while keeping the dynamics fixed), we found that the P1m reflects primarily feedforward activation and that feedback activations drive the N1m and P2m (Fig. 7). Due to the fixed dynamics, this investigation did not address how the feedback connections contribute to the dynamics of AC. A natural way to address this question would be to modify the actual feedback connections in W_{AC} (and in $\widetilde{W}_{\mathrm{AC}}$ respectively). However, our analytical approach does not allow this because of the requirement of symmetric connection matrices, and therefore numerical simulations would be required. We note that the role of feedback connections in neural processing is, in general, an open question, with earlier accounts labeling them weak and modulatory (Crick and Koch 1998; Sherman and Guillery 2011) and the predictive-coding framework requiring them generally to be functionally inhibitory (Bastos et al. 2012). In our model, feedback connections were symmetric with feedforward connections (Felleman and Essen 1991), as well as excitatory and of the driving kind (Covic and Sherman 2011). Leaving this to be addressed elsewhere, we suspect that feedback connections contribute to a larger τ_{ERF} and/or a lower f_{ERF}. That is, they might act as a memory mechanism by keeping the signal circulating in the AC for longer. This, in turn, might be beneficial for enhancing the signal-to-noise ratio in auditory processing, or for allowing the build-up of synaptic depression, which might be instrumental for representing the temporal structure of sound (May and Tiitinen 2013; May et al. 2015; Westö et al. 2016).

5.2 A novel approach for ERF generation

5.2.1 State of the art: ECD source localization and its variations

In MEG research, the ERF waveform is usually treated as a linear combination of the activity of spatially distributed sources in the brain, and the task becomes one of localizing and modeling the activity of each source. Accurate localization of MEG sources, however, suffers from the ill-posed inverse problem. As solutions to this problem, numerous approaches have been developed, including discrete and distributed source models (Mosher et al. 1992; Scherg 1990; Scherg and Berg 1996), along with several variants of beamformers, a spatial filtering technique often applied in the analysis of brain oscillations (see, for example, Darvas et al. 2004; Hillebrand and Barnes 2005; Wendel et al. 2009).

Discrete and distributed source models use time-varying ECDs as the simplest physiologically meaningful source model. The mathematical concept of the ECD is a point-like source, and it is an abstraction which is justified in those cases where the spatial extension of the activated brain region is small compared to its distance to the MEG sensors. For example, it is common practice in experiments with simple auditory stimuli to use a single ECD per hemisphere to explain the measured magnetic field distribution describing the N1m waveform as the result of a best match between forward and inverse solution. The multi-dipole model is often used when the brain activation can be described by a small number of stationary focal sources, which is commonly the case in simple sensory experiments. To determine an adequate number of sources, a conservative and rather subjective approach is to gradually increase the number of sources on condition that for each source a distinct contribution to the measured magnetic field pattern is verifiable, i.e. that the sources do not model noise. More exacting approaches use advanced classification algorithms, such as the "recursively applied and projected multiple signal classification" method (RAP-MUSIC; Mosher and Leahy 1999). In case of spatially extended brain activation, the concept of discrete sources is often replaced by distributed source models estimating simultaneously strengths and directions of dipoles located on a grid of hundreds or even thousands of brain locations (see, for example, Dale and Sereno 1993; Hämäläinen and Ilmoniemi 1994; Dale et al. 2000; Pascual-Marqui 2002).

Taken together, the ECD as source model is a simplification which makes the source localization problem mathematically tractable. However, there are numerous arbitrary choices that the researcher has to make. Notably, these include an a priori assumption on the number of sources in discrete source analysis, and constraints such as regularization parameters in distributed source models. Therefore, source localization carries with it unavoidable ambiguities: Has the correct number of underlying neural sources been assumed? Have these been reliably and correctly separated from each other, in particular when two or more sources are close to each other in space and in time (Lütkenhöner and Steinsträter 1998)? Thus, precise source localization based on trial-averaged ERFs is non-trivial not only due to the inverse problem per se, but also due to the unknown number of sources and their separability.

5.2.2 An alternative view on ERF generators

With conventional source modeling, the temptation is to understand an ERF generator in terms of a spatially and temporally constrained local process giving rise to a "component" of the ERF (Näätänen and Picton 1987; Näätänen 1992)—in effect equating sources (i.e., the primary currents) with generators (i.e., the neural tissue with the processes generating the primary currents). Thus, for example, the P1m generators are those cortical areas which are active during the peak of the P1m, and the objective of source modeling is to localize these generators. Conversely, each cortical area might be considered a generator of a component, and the challenge for source localization is to separate these generators out from each other so that the component structure of the event-related response can be identified. It follows that if the sources identified for the P1m are found to be different than those active during the N1m peak, the conclusion can be drawn that the P1m and the N1m have at least partially different (though possibly overlapping) generators. In this vein, cortical activation can be seen as signal propagation as successive generators become active, as is evident in source modeling assuming a single ECD (Lütkenhöner and Steinsträter 1998), multiple dipoles (Inui et al. 2006) and distributed sources (Yvert et al. 2005).

Our model opens up an alternative view on ERF generation. Rather than considering the ERF to be the linear sum of multiple spatially discrete sources, it becomes a combination of multiple normal modes. Here, the normal modes themselves and the way they are coupled are determined by the anatomical structure of AC and by other, dynamical parameters. This approach still approximates the ERF-generating system as a set of discrete sources—cortical columns—but it lays emphasis on the way these are connected to each other and to the dynamics of this connected system. In this way, the system can be described on three distinct levels: that of physiological and anatomical quantities, that of the normal modes, and that of the primary currents which are determined by the normal modes.

What, then, is an ERF generator in this normal mode view? In our simulations, the AC has well-defined sources of activity—those columns activated by the stimulus—and each field and area has a well-defined contribution to the ERF. Also, there is a serial progression of activation along the core–belt–parabelt axis (Figs. 3, 8), which fits in with experimental observations (Inui et al. 2006; Yvert et al. 2005; Guéguin et al. 2007). As such, these results add nothing to the conventional view of ERF generation: in our simulations, the main generators of the N1m response are clearly the core and belt areas; with the parabelt contributing very little, it seems clear that it cannot be counted as an N1m generator. However, this view is countered by the consideration that both single-column activity and the ERF represent the combination of multiple normal modes and that each normal mode is a function of the connection patterns and strengths of the entire AC system. Thus, the local connections in the parabelt, and so the parabelt fields themselves, are an intimate part of activity generation in the core and belt. This, in turn, means that one cannot consider individual columns, fields, or areas as separable ERF generators. The parabelt is just as much an N1m generator as the core and, similarly, the core is just as much a P2m generator as the parabelt.

The above principle of ERF generation is demonstrated in Fig. 9 which shows the effects of modifying the local connections within the parabelt fields. These modifications lead to modest changes in the parabelt response itself. Importantly, they entail significant changes in the activity of the core and belt. This finding is all the more intriguing since the contributions of the two parabelt fields to the overall ERF are significantly smaller than those of the core and belt (see Fig. 8b). Thus, while the parabelt does not function as a source of the N1m, it is clearly an important part of the N1m generator.

On a more fundamental level, there is an ongoing debate about the generation of event-related responses (de Munck and Bijma 2010; Sauseng et al. 2007; Telenczuk et al. 2010; Turi et al. 2012; Yeung et al. 2004). In the classical signal-plus-noise (SPN) model, the trial-averaged MEG response is treated as the superposition of a stationary stimulus-evoked signal and zero-mean Gaussian noise. In this view, an ERF is a time-locked phasic burst which is uncorrelated with the ongoing rhythmic activity (Arieli et al. 1996; Dawson 1954; Mäkinen et al. 2005; Mazaheri and Jensen 2006; Shah et al. 2004). The phase-reset model proposed by Sayers et al. (1974) (see also Makeig et al. 2002; Hanslmayr et al. 2007) provides an opposing view according to which stimulus-evoked responses are generated by partial stimulus-induced phase synchronization of the rhythmic background activity. The most recent model for ERF generation is the baseline-shift model introduced by Nikulin et al. (2007, 2010). This model is based on the asymmetric modulation of the amplitude of spontaneous alpha-band oscillations, although de Munck and Bijma (2010) argue that it could be viewed as a special case of the SPN model. The current results of our work do not as such contribute to this debate because we did not include oscillatory background activity in the simulations. However, while beyond the scope of the current study, such oscillatory activity would be easy enough to include in the model. The oscillator nature of the model implies that feeding the model with noise should already be sufficient to generate ongoing oscillations. Alternatively, the analytical solutions themselves show that the resting state of the model would be a limit cycle if the decay constant γ_d for one or more normal modes in Eqs. (13) and (14) is zero. A stimulus acting as an outside push to the individual harmonic oscillators represented by the normal modes could have a multitude of effects, depending on the amplitude of the ongoing oscillations, and this could be approached analytically by considering the unit impulse response of our model. Further, as our model operates on multiple spatial resolutions, from the single-column to the aggregated MEG signal, it might be useful for approaching the question of whether phasic responses and ongoing oscillations are generated by the same or different neural populations (Sauseng et al. 2007).

5.3 Subject-specificity of the event-related waveforms

Event-related responses are characterized by large between-subject variability. Although rarely an object of study, this variability is evident to any researcher using ERPs and ERFs (Luck 2014). It is also given expression in, for example, the large standard deviations of peak amplitudes and latencies in test–retest studies in which the reliability and reproducibility of event-related responses have been investigated in various subject populations (e.g., Michalewski et al. 1986; Kileny and Kripal 1987; Segalowitz and Barnes 1993; Dalebout and Robey 1997; Atcherson et al. 2006). These studies tend to show that between-subject variability is contrasted by the responses staying stable for a given subject across different measurement sessions and over long periods.

There are potentially two sources of the variability of event-related responses across subjects: the anatomical topography of the cortical surface and the dynamics of AC. Subject-specific topography is well-documented, with human subjects having large differences in the pattern and number of convolutions on the supratemporal plane (Yvert et al. 2005; Moerel et al. 2014). However, the question of subject-specific dynamics of AC has, to our knowledge, not been approached before. The current AC model allowed us to address this issue in simulations via separable sets of parameters: the P-parameters governing the system dynamics, and the K_i-matrices capturing the topographical properties influencing the MEG signal. We introduced random variations to these parameter sets and found that variations of the dynamical parameters have a much stronger effect on the waveform than variations of the topographical parameters. Specifically, K-randomizations mainly affect the N1m-peak amplitude while keeping intact the morphology of the waveform of the entire ERF (Fig. 10a). In contrast, P-randomizations result in a much larger variety of waveform morphologies (Fig. 10f), with N1m-peak amplitudes and latencies varying in a considerably larger range (Fig. 10g). Consequently, changes of dynamics parameters entail a much broader FFT frequency spectrum, and, likewise, a broader distribution of the time constant τ_{ERF} (Fig. 10h, i).

These results provide predictions for straightforward testing in populations of subjects: Characterizing single-subject ERFs in terms of frequency spectrum and τ_{ERF}, how are these estimates distributed over the population? If the distribution is narrowly focused, this would indicate that subjects have similar AC dynamics and that the subject-specificity of the ERF is due to topographical variations only. In contrast, subject-specific dynamics would be indicated by a wider distribution of frequency spectrum and τ_{ERF}, especially if this distribution is structured as in Fig. 10e. Previous research has pointed to a large variation in the N1/N1m peak latency (e.g., Michalewski et al. 1986; Kileny and Kripal 1987; Segalowitz and Barnes 1993; Dalebout and Robey 1997; Atcherson et al. 2006), and this would fit with the results of the current simulations utilizing dynamical parameter randomizations (Fig. 10g). Thus, we would expect to see evidence supporting the presence of subject-specific AC dynamics.

While our results suggest that the separation of dynamical and topographical effects might be possible on the population level, is there hope for such a separation when looking at single-subject data? This is a challenge since (random) combinations of P- and K-parameters lead to a wealth of waveforms. One way forward might be through systematic investigations of how waveform properties depend on parameters. This might enable us to identify major causal relationships between dynamical and topographical parameters on the one hand and the resulting waveforms on the other. One compelling example is our finding that the feedforward projections of the K_1-matrix are crucial for the generation of the P1m response.

The current model is based on the architecture of the monkey AC (Kaas and Hackett 2000; Hackett et al. 2014), as a comparable map of the organization of human AC is still missing (Nourski et al. 2014; Leaver and Rauschecker 2016). Might our approach offer a method for fitting anatomical organization of the AC to the ERF in humans? This would present an inverse problem quite different from the source localization one. Instead of using ECDs, the solution would be expressed in terms of normal modes and the underlying architecture coupled with the subject-specific cortical surface. Even in the presence of subject-specific ERF waveforms, this approach might become possible with the constraint that the coarse architecture in terms of cortical fields and their interconnections is a shared feature across human subjects. The first steps in this investigation will require computational studies on the effect of architecture on the ERF waveforms. Specifically, can species-specific event-related responses be explained by a species-specific constellation of fields in auditory cortex? Further, might the distributions of ERF descriptors such as those presented in Fig. 10 be used to decode anatomical structure on the population level?

Acknowledgements We are grateful for the support of André Brechmann, Michael Brosch, Peter Heil, Torsten Stöter, and Matthias Wolfrum. This research was supported by the Deutsche Forschungsgemeinschaft (He 1721/10-1, He 1721/10-2, and SFB TR31, A4) and by the European Union's Horizon 2020 research and innovation programme (Grant Agreement 763959). Further, we also acknowledge the support by an Alexander von Humboldt Polish Honorary Research Scholarship by the Foundation for Polish Science.

Open Access This article is distributed under the terms of the Creative Commons Attribution 4.0 International License (http://creativecommons.org/licenses/by/4.0/), which permits unrestricted use, distribution, and reproduction in any medium, provided you give appropriate credit to the original author(s) and the source, provide a link to the Creative Commons license, and indicate if changes were made.

Appendix

A1: Connection spread in W_{AC} described by means of Gaussian distributions

All inter-column connections are contained in W_{AC} as displayed in Fig. 1b. Here, W_{AC} refers to the connection matrix that contains all lateral and long-range connections (see Appendix A2). A cortical column at position i in the field is connected to itself and to neighboring columns j. Similarly, when making connections to another field, the column targets its tonotopic counterpart i as well as columns j in the neighborhood of this counterpart. In both cases, the spread of connections is described by a Gaussian distribution $Q(x) = r \exp[-(x + \mu + s\,\mathcal{N}(0,1))^2/2\sigma^2]$ where x is the tonotopic distance $|i - j|$, r is a scaling parameter, the variance σ^2 determines the width of the spread, μ is an offset parameter, s determines the level of stochasticity of the connections, and $\mathcal{N}(0,1)$ is the standard normal distribution. The default parameter values used for $Q(x)$ are listed in Table 2. As an example, Fig. 12a, b demonstrates the spread in the connections between and within the two core fields RT and R both in the deterministic ($s = 0$) and stochastic ($s > 0$) case, respectively.

Table 2 Default parameter values of the amplitude r, constant μ, variance σ^2, and stochasticity s of the Gaussian distributions $Q(x)$ for computing the between-field and within-field weights of W_{AC}

	r	μ	σ^2	s
Between-field excitatory	0.09	0	1.5	0.2
Within-field excitatory	0.105	0	2.0	0.4
Within-field inhibitory	0.09	3.0, − 3.0	1.5	0.4

Between-field connections These are all excitatory and described by a single Gaussian with $r = 0.09$, $\mu = 0$, $\sigma^2 = 1.5$. They are shown in the lower-left and upper-right quadrants of Figs. 12a ($s = 0$) and 12b ($s = 0.2$).

Within-field connections These are described by a sum of Gaussians so that excitatory connections for nearest neighbors give way to lateral inhibitory connections at larger distances. Excitatory weights are computed using $Q_{\mathrm{exc}}(x)$ with $r = 0.105$, $\mu = 0$, $\sigma^2 = 2.0$. For lateral inhibition, we have two Gaussians $Q_{\mathrm{inh},1}(x)$ and $Q_{\mathrm{inh},2}(x)$, both with $r = 0.09$, $\sigma^2 = 1.5$, but with $\mu = -3.0$ and $\mu = 3.0$, respectively. The total weights are $Q_{\mathrm{intra}}(x) = Q_{\mathrm{exc}}(x) - [Q_{\mathrm{inh},1}(x) + Q_{\mathrm{inh},2}(x)]$. These are shown in the upper-left and lower-right quadrants in the matrices in Figs. 12a ($s = 0$) and 12b ($s = 0.4$).

A2: Derivation of analytical solutions

As introduced in Sect. 2, the dynamics of the system are determined by $2 \times N$ coupled nonlinear differential equations [see Eqs. (1) and (2)]:

$$\tau_{\mathrm{m}}\dot{\mathbf{u}}(t) + \mathbf{u}(t) - A(t) \circ W_{\mathrm{ee}} \cdot g[\mathbf{u}(t)] \\ + W_{\mathrm{ei}} \cdot g[\mathbf{v}(t)] = \mathbf{I}_{\mathrm{aff,e}}(t) \tag{20}$$

$$\tau_{\mathrm{m}}\dot{\mathbf{v}}(t) + \mathbf{v}(t) - W_{\mathrm{ie}} \cdot g[\mathbf{u}(t)] \\ + W_{\mathrm{ii}} \cdot g[\mathbf{v}(t)] = \mathbf{I}_{\mathrm{aff,i}}(t). \tag{21}$$

Ignoring the synaptic plasticity term $A(t)$ and inserting the linear spiking-rate function $g(x) = \alpha x$ into Eqs. (20) and (21) results in the linearized state equations

$$\tau_{\mathrm{m}}\dot{\mathbf{u}}(t) + \mathbf{u}(t) - W_{\mathrm{ee}} \cdot [\alpha\mathbf{u}(t)] \\ + W_{\mathrm{ei}} \cdot [\alpha\mathbf{v}(t)] = \mathbf{I}_{\mathrm{aff,e}}(t) \tag{22}$$

$$\tau_{\mathrm{m}}\dot{\mathbf{v}}(t) + \mathbf{v}(t) - W_{\mathrm{ie}} \cdot [\alpha\mathbf{u}(t)] \\ + W_{\mathrm{ii}} \cdot [\alpha\mathbf{v}(t)] = \mathbf{I}_{\mathrm{aff,i}}(t). \tag{23}$$

Dividing Eqs. (22) and (23) by τ_{m} leads to

$$\dot{\mathbf{u}}(t) - \widetilde{W}_{\mathrm{ee}}\mathbf{u}(t) + \widetilde{W}_{\mathrm{ei}}\mathbf{v}(t) = \mathbf{I}_{\mathrm{e}}(t) \tag{24}$$

$$\dot{\mathbf{v}}(t) - \widetilde{W}_{\mathrm{ie}}\mathbf{u}(t) + \widetilde{W}_{\mathrm{ii}}\mathbf{v}(t) = \mathbf{I}_{\mathrm{i}}(t), \tag{25}$$

with

$$\begin{cases} \frac{\alpha W_{\mathrm{ee}} - I}{\tau_{\mathrm{m}}} \longrightarrow \widetilde{W}_{\mathrm{ee}} \\ \frac{\alpha W_{\mathrm{ei}}}{\tau_{\mathrm{m}}} \longrightarrow \widetilde{W}_{\mathrm{ei}} \\ \frac{\alpha W_{\mathrm{ie}}}{\tau_{\mathrm{m}}} \longrightarrow \widetilde{W}_{\mathrm{ie}} \\ \frac{\alpha W_{\mathrm{ii}} + I}{\tau_{\mathrm{m}}} \longrightarrow \widetilde{W}_{\mathrm{ii}} \\ \frac{\mathbf{I}_{\mathrm{aff,e}}(t)}{\tau_{\mathrm{m}}} \longrightarrow \mathbf{I}_{\mathrm{e}}(t) \\ \frac{\mathbf{I}_{\mathrm{aff,i}}(t)}{\tau_{\mathrm{m}}} \longrightarrow \mathbf{I}_{\mathrm{i}}(t). \end{cases} \tag{26}$$

The matrix terms with the capping tilde represent the connection matrices of the linearized canonical form. To obtain

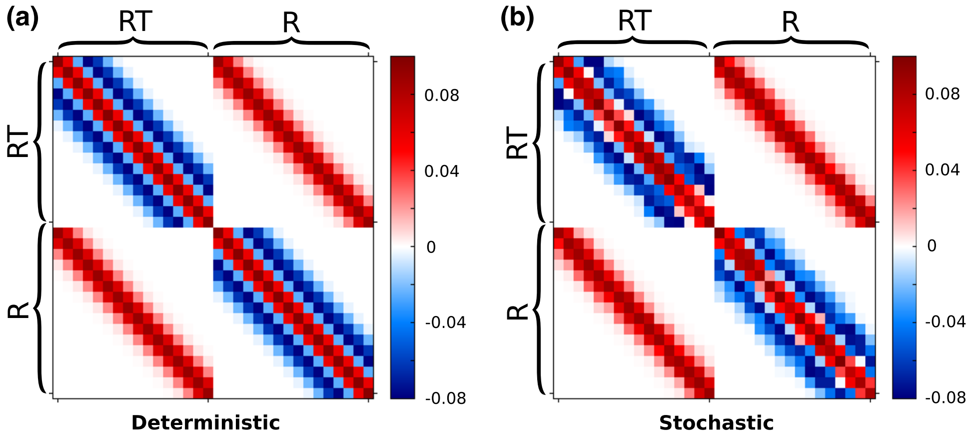

Fig. 12 The spread of between-field and within-field connections of W_{AC} described by a Gaussian distribution $Q(x)$. The core fields **RT** and **R** are used for illustration. **a** In the deterministic case, the parameter s which describes the level of stochasticity, was set to zero. The resulting connection pattern between column i and j depends solely on the distance between $|i - j|$. **b** In this example for a stochastic case, the parameter s was set to 0.2 and 0.4 for between- and within-field connections, respectively (see Table 2). Hence, the weight value assigned to the connection between column i and j is modified by a random value. Note that the scales to the right of both matrices indicate the sign (polarity) of the weights which is positive for excitatory (red) or negative for inhibitory (blue) connections

analytical solutions of this system of first-order differential equations, we transform it into a system of second-order differential equations:

$$\ddot{\mathbf{u}}(t) + 2\Gamma_u\dot{\mathbf{u}}(t) + \Omega^2_{0,u}\mathbf{u}(t) = \mathbf{q}(t) \tag{27}$$

$$\ddot{\mathbf{v}}(t) + 2\Gamma_v\dot{\mathbf{v}}(t) + \Omega^2_{0,v}\mathbf{v}(t) = \mathbf{j}(t), \tag{28}$$

with the definition of the coefficients given in Eqs. (5)–(10). Analytical solutions for $\mathbf{u}(t)$ and $\mathbf{v}(t)$ of Eqs. (27) and (28) can be found if Γ_u and $\Omega^2_{0,u}$ as well as Γ_v and $\Omega^2_{0,v}$ are simultaneously diagonalizable.

The matrices Γ_u and $\Omega^2_{0,u}$ as well as Γ_v and $\Omega^2_{0,v}$, are simultaneously diagonalizable if there exist single invertible matrices Υ_u and Υ_v such that

$$\Gamma_{u_\mathrm{d}} = \Upsilon_u^{-1}\Gamma_u\Upsilon_u \iff \Upsilon_u\Gamma_{u_\mathrm{d}}\Upsilon_u^{-1} = \Gamma_u \tag{29}$$

$$\Omega^2_{0,u_\mathrm{d}} = \Upsilon_u^{-1}\Omega^2_{0,u}\Upsilon_u \iff \Upsilon_u\Omega^2_{0,u_\mathrm{d}}\Upsilon_u^{-1} = \Omega^2_{0,u} \tag{30}$$

$$\Gamma_{v_\mathrm{d}} = \Upsilon_v^{-1}\Gamma_v\Upsilon_v \iff \Upsilon_v\Gamma_{v_\mathrm{d}}\Upsilon_v^{-1} = \Gamma_v \tag{31}$$

$$\Omega^2_{0,v_\mathrm{d}} = \Upsilon_v^{-1}\Omega^2_{0,v}\Upsilon_v \iff \Upsilon_v\Omega^2_{0,v_\mathrm{d}}\Upsilon_v^{-1} = \Omega^2_{0,v}, \tag{32}$$

where the subscript ‘d’ indicates a diagonal matrix. Note that Γ_u, $\Omega^2_{0,u}$, Γ_v, and $\Omega^2_{0,v}$ are governed by the connection matrices [see Eqs. (5)–(8)]. Inserting Eqs. (5) and (7) into Eqs. (29) and (30), and Eqs. (6) and (8) into Eqs. (31) and (32), yields

$$\Gamma_{u_\mathrm{d}} = \Upsilon_u^{-1}\left(\frac{\widetilde{W}_\mathrm{ei}\widetilde{W}_\mathrm{ii}\widetilde{W}_\mathrm{ei}^{-1} - \widetilde{W}_\mathrm{ee}}{2}\right)\Upsilon_u \tag{33}$$

$$\Omega^2_{0,u_\mathrm{d}} = \Upsilon_u^{-1}(\widetilde{W}_\mathrm{ei}\widetilde{W}_\mathrm{ie} - \widetilde{W}_\mathrm{ei}\widetilde{W}_\mathrm{ii}\widetilde{W}_\mathrm{ei}^{-1}\widetilde{W}_\mathrm{ee})\Upsilon_u \tag{34}$$

$$\Gamma_{v_\mathrm{d}} = \Upsilon_v^{-1}\left(\frac{\widetilde{W}_\mathrm{ii} - \widetilde{W}_\mathrm{ie}\widetilde{W}_\mathrm{ee}\widetilde{W}_\mathrm{ie}^{-1}}{2}\right)\Upsilon_v \tag{35}$$

$$\Omega^2_{0,v_\mathrm{d}} = \Upsilon_v^{-1}\left(\widetilde{W}_\mathrm{ie}\widetilde{W}_\mathrm{ei} - \widetilde{W}_\mathrm{ie}\widetilde{W}_\mathrm{ee}\widetilde{W}_\mathrm{ie}^{-1}\widetilde{W}_\mathrm{ii}\right)\Upsilon_v. \tag{36}$$

To make the diagonalization feasible, we simplify the terms in the brackets on the right hand sides of Eqs. (33)–(36). Note that $\widetilde{W}_\mathrm{ei}$ and $\widetilde{W}_\mathrm{ii}$ are scalar matrices and, thus, commute with any other matrix. The matrix $\widetilde{W}_\mathrm{ie}$ is non-diagonal. We approximate it by a scalar matrix $\widetilde{W}_\mathrm{ie,d}$ by discarding all its off-diagonal elements, i.e. by effectively removing lateral inhibition from $\widetilde{W}_\mathrm{ie}$. We return lateral inhibition to the dynamics by replacing $\widetilde{W}_\mathrm{ee}$ by $\widetilde{W}_\mathrm{AC}$ where elements of $\widetilde{W}_\mathrm{ee}$ representing excitatory connections are combined with elements of $\widetilde{W}_\mathrm{ie}$ describing lateral inhibition. With $\widetilde{W}_\mathrm{ei}$, $\widetilde{W}_\mathrm{ii}$, and $\widetilde{W}_\mathrm{ie,d}$ now being scalar matrices, Eqs. (33)–(36) can be further simplified to

$$\Gamma_{u_\mathrm{d}} = \frac{\widetilde{W}_\mathrm{ii} - \Upsilon_u^{-1}\widetilde{W}_\mathrm{AC}\Upsilon_u}{2} \tag{37}$$

$$\Omega^2_{0,u_\mathrm{d}} = \widetilde{W}_\mathrm{ei}\widetilde{W}_\mathrm{ie,d} - \widetilde{W}_\mathrm{ii}\Upsilon_u^{-1}\widetilde{W}_\mathrm{AC}\Upsilon_u \tag{38}$$

$$\Gamma_{v_\mathrm{d}} = \frac{\widetilde{W}_\mathrm{ii} - \Upsilon_v^{-1}\widetilde{W}_\mathrm{AC}\Upsilon_v}{2} \tag{39}$$

$$\Omega^2_{0,v_\mathrm{d}} = \widetilde{W}_\mathrm{ei}\widetilde{W}_\mathrm{ie,d} - \widetilde{W}_\mathrm{ii}\Upsilon_v^{-1}\widetilde{W}_\mathrm{AC}\Upsilon_v. \tag{40}$$

Due to the equality of Eq. (37) with Eq. (39), and of Eq. (38) with Eq. (40), the diagonalization problem can be reduced to the simultaneous diagonalization of two matrices Γ and Ω^2_0

$$\Gamma_\mathrm{d} = \frac{\widetilde{W}_\mathrm{ii} - \Upsilon^{-1}\widetilde{W}_\mathrm{AC}\Upsilon}{2} \tag{41}$$

$$\Omega^2_{0_\mathrm{d}} = \widetilde{W}_\mathrm{ei}\widetilde{W}_\mathrm{ie,d} - \widetilde{W}_\mathrm{ii}\Upsilon^{-1}\widetilde{W}_\mathrm{AC}\Upsilon, \tag{42}$$

which, in turn, requires the diagonalization of $\widetilde{W}_\mathrm{AC}$ only. Owing to its symmetry, the matrix $\widetilde{W}_\mathrm{AC}$ can be diagonalized since, in general, for any given real symmetric matrix X it holds that $\Upsilon^{-1}X\Upsilon = X_\mathrm{d}$, where X_d is a real diagonal matrix. The columns of the matrix Υ we are searching for to diagonalize $\widetilde{W}_\mathrm{AC}$ are the eigenvectors of $\widetilde{W}_\mathrm{AC}$, and the corresponding eigenvalues are the diagonal values of $\widetilde{W}_\mathrm{AC,d}$.

Hence, Eqs. (27) and (28) can be simplified to

$$\ddot{\mathbf{u}}(t) + 2\Gamma\dot{\mathbf{u}}(t) + \Omega^2_0\mathbf{u}(t) = \mathbf{q}(t) \tag{43}$$

$$\ddot{\mathbf{v}}(t) + 2\Gamma\dot{\mathbf{v}}(t) + \Omega^2_0\mathbf{v}(t) = \mathbf{j}(t). \tag{44}$$

By inserting $\Gamma = \Upsilon\Gamma_\mathrm{d}\Upsilon^{-1}$ and $\Omega^2_0 = \Upsilon\Omega^2_{0_\mathrm{d}}\Upsilon^{-1}$ into Eqs. (43) and (44) and multiplying the resulting equations with Υ^{-1} from the left side, we obtain

$$\Upsilon^{-1}\ddot{\mathbf{u}}(t) + 2\Gamma_\mathrm{d}\Upsilon^{-1}\dot{\mathbf{u}}(t) + \Omega^2_{0_\mathrm{d}}\Upsilon^{-1}\mathbf{u}(t) = \Upsilon^{-1}\mathbf{q}(t) \tag{45}$$

$$\Upsilon^{-1}\ddot{\mathbf{v}}(t) + 2\Gamma_\mathrm{d}\Upsilon^{-1}\dot{\mathbf{v}}(t) + \Omega^2_{0_\mathrm{d}}\Upsilon^{-1}\mathbf{v}(t) = \Upsilon^{-1}\mathbf{j}(t), \tag{46}$$

where the variables in bold are $N \times 1$ vectors, Υ^{-1} is a square matrix of order N, and Γ_d and $\Omega^2_{0_\mathrm{d}}$ are diagonal matrices of order N. By substituting $\ddot{\mathbf{u}}_\mathrm{d}(t) = \Upsilon^{-1}\ddot{\mathbf{u}}(t)$, $\dot{\mathbf{u}}_\mathrm{d}(t) = \Upsilon^{-1}\dot{\mathbf{u}}(t)$, $\mathbf{u}_\mathrm{d}(t) = \Upsilon^{-1}\mathbf{u}(t)$ and $\mathbf{q}_\mathrm{d}(t) = \Upsilon^{-1}\mathbf{q}(t)$ in Eq. (45), and doing similar substitutions in Eq. (46), we obtain the decoupled state equations:

$$\ddot{\mathbf{u}}_\mathrm{d}(t) + 2\Gamma_\mathrm{d}\dot{\mathbf{u}}_\mathrm{d}(t) + \Omega^2_{0_\mathrm{d}}\mathbf{u}_\mathrm{d}(t) = \mathbf{q}_\mathrm{d}(t) \tag{47}$$

$$\ddot{\mathbf{v}}_\mathrm{d}(t) + 2\Gamma_\mathrm{d}\dot{\mathbf{v}}_\mathrm{d}(t) + \Omega^2_{0_\mathrm{d}}\mathbf{v}_\mathrm{d}(t) = \mathbf{j}_\mathrm{d}(t). \tag{48}$$

Since Γ_d and $\Omega^2_{0_\mathrm{d}}$ in Eqs. (47) and (48) are diagonal matrices, we can replace them with their vector representations. The decoupled equations for each normal mode of the two state variables are then

$$\ddot{u}_\mathrm{d}(t) + 2\gamma_\mathrm{d}\dot{u}_\mathrm{d}(t) + \omega^2_{0_\mathrm{d}}u_\mathrm{d}(t) = q_\mathrm{d}(t) \tag{49}$$

$$\ddot{v}_\mathrm{d}(t) + 2\gamma_\mathrm{d}\dot{v}_\mathrm{d}(t) + \omega^2_{0_\mathrm{d}}v_\mathrm{d}(t) = j_\mathrm{d}(t), \tag{50}$$

with the solutions

$$u_{\mathrm{d}}(t)=\exp(-\gamma_{\mathrm{d}}t)[a_{u_{\mathrm{d}}}\sin(\delta_{\mathrm{d}}t)+b_{u_{\mathrm{d}}}\cos(\delta_{\mathrm{d}}t)]+c_{u_{\mathrm{d}}} \tag{51}$$

$$v_{\mathrm{d}}(t)=\exp(-\gamma_{\mathrm{d}}t)[a_{v_{\mathrm{d}}}\sin(\delta_{\mathrm{d}}t)+b_{v_{\mathrm{d}}}\cos(\delta_{\mathrm{d}}t)]+c_{v_{\mathrm{d}}}. \tag{52}$$

The coefficients $a_{u_{\mathrm{d}}}$, $b_{u_{\mathrm{d}}}$ and $c_{u_{\mathrm{d}}}$ as well as $a_{v_{\mathrm{d}}}$, $b_{v_{\mathrm{d}}}$, and $c_{v_{\mathrm{d}}}$ are given in Eqs. (15) and (16). The decay constant γ_{d} and the damping frequency δ_{d} for both $u_{\mathrm{d}}(t)$ and $v_{\mathrm{d}}(t)$ are defined in Eq. (17).

With the damping frequency δ_{d} being either real positive or imaginary positive as outlined in Fig. 2, the underdamped, critically damped, and overdamped oscillations have the following analytical solutions (Fowles and Cassiday 2005).

Underdamped oscillation: For $\delta_{\mathrm{d}} \in \mathbb{R}^+$, the expressions for $u_{\mathrm{d}}(t)$ and $v_{\mathrm{d}}(t)$ in the respective Eqs. (13) and (14) each become a product of a decaying exponential term describing the damping (since $\gamma_{\mathrm{d}} > 0$) and a sinusoidal term describing the oscillation:

$$u_{\mathrm{d}}(t) = \exp(-\gamma_{\mathrm{d}}t)C_{u_{\mathrm{d}}}\sin(\delta_{\mathrm{d}}t+\phi_{u_{\mathrm{d}}})+c_{u_{\mathrm{d}}}, \tag{53}$$

with $C_{u_{\mathrm{d}}} = \sqrt{a_{u_{\mathrm{d}}}^2 + b_{u_{\mathrm{d}}}^2}$ and $\phi_{u_{\mathrm{d}}} = \operatorname{atan2}(b_{u_{\mathrm{d}}}, a_{u_{\mathrm{d}}})$. The same formulation applies also to $v_{\mathrm{d}}(t)$ with $C_{v_{\mathrm{d}}}$ and $\phi_{v_{\mathrm{d}}}$. The system oscillates with a decaying magnitude that approaches zero.

Critically damped oscillation: The general solution for critical damping, i.e., for the case $\delta_{\mathrm{d}} = 0$, is given by

$$u_{\mathrm{d}}(t) = \exp(-\gamma_{\mathrm{d}}t)(a'_{u_{\mathrm{d}}}t + b_{u_{\mathrm{d}}}) + c_{u_{\mathrm{d}}} \tag{54}$$

with

$$\begin{aligned} a'_{u_{\mathrm{d}}} = {} & \frac{w_{\mathrm{ei}}\gamma_{\mathrm{d}}}{\omega_{0_{\mathrm{d}}}^2}I_{\mathrm{i}}(t) + \frac{\omega_{0_{\mathrm{d}}}^2 + w_{\mathrm{ei}}w_{\mathrm{ie,d}} - w_{\mathrm{ii}}^2}{2\omega_{0_{\mathrm{d}}}^2}I_{\mathrm{e}}(t) \\ & + \frac{w_{\mathrm{ii}} + w_{\mathrm{AC,d}}}{2}u_0 - w_{\mathrm{ie,d}}v_0. \end{aligned} \tag{55}$$

In the critically damped case, the system approaches zero without oscillations in the fastest possible way.

Overdamped oscillation: For $\delta_{\mathrm{d}} \in \mathbb{I}^+$, Eq. (51) turns into

$$\begin{aligned} u_{\mathrm{d}}(t) = {} & \exp(-(\gamma_{\mathrm{d}} - |\delta_{\mathrm{d}}|)t)\left(\frac{b_{u_{\mathrm{d}}} + |a_{u_{\mathrm{d}}}|}{2}\right) \\ & + \exp(-(\gamma_{\mathrm{d}} + |\delta_{\mathrm{d}}|)t)\left(\frac{b_{u_{\mathrm{d}}} - |a_{u_{\mathrm{d}}}|}{2}\right) + c_{u_{\mathrm{d}}}. \end{aligned} \tag{56}$$

The overdamped case consists of two exponential terms with two different decay constants, viz $(\gamma_{\mathrm{d}} - |\delta_{\mathrm{d}}|)$ and $(\gamma_{\mathrm{d}} + |\delta_{\mathrm{d}}|)$. The oscillator returns to the equilibrium state without oscillating. Depending on the values of γ_{d} and δ_{d}, the normal mode can be either overdamped unstable or overdamped stable (see Fig. 2).

References

Ahlfors SP, Wreh C (2015) Modelling the effect of dendritic input location on MEG and EEG source dipoles. Med Biol Eng Comput 53(9):879–887

Ahlfors SP, Jones SR, Ahveninen J, Hämäläinen MS, Belliveau JW, Bar M (2015) Direction of magnetoencephalography sources associated with feedback and feedforward contributions in a visual object recognition task. Neurosci Lett 585:149–154

Allen GI, Korn H, Oshima T (1975) The mode of synaptic linkage in the cerebro-ponto-cerebellar pathway of the cat. I. Responses in the branchium pontis. Exp Brain Res 24:1–14

Arieli A, Sterkin A, Grinvald A, Aertsen A (1996) Dynamics of ongoing activity: explanation of the large variability in evoked cortical responses. Science 273:1868–1871

Atcherson SR, Gould HJ, Pousson MA, Prout TM (2006) Long-term stability of N1 sources using low-resolution electromagnetic tomography. Brain Topogr 19(1/2):11–20

Bartos M, Vida I, Jonas P (2007) Synaptic mechanisms of synchronized gamma oscillations in inhibitory interneuron networks. Nat Rev 8:45–56

Bastos AM, Usrey WM, Adams RA, Mangun GR, Fries P, Friston KJ (2012) Canonical microcircuits for predictive coding. Neuron 76:695–711

Baumann S, Petkov CI, Griffiths TD (2013) A unified framework for the organization of the primate auditory cortex. Front Syst Neurosci 7:11

Bazelot M, Dinocourt C, Cohen I, Miles R (2010) Unitary inhibitory field potentials in the CA3 region of rat hippocampus. J Physiol 588:2077–2090

Brosch M, Schreiner CE (1997) Time course of forward masking tuning curves in cat primary auditory cortex. J Neurophysiol 77(2):923–943

Brosch M, Scheich H (2008) Tone-sequence analysis in the auditory cortex of awake macaque monkeys. Exp Brain Res 184:349–361

Brosch M, Schulz A, Scheich H (1999) Processing of sound sequences in macaque auditory cortex: response enhancement. J Neurophysiol 82(3):1542–1559

Budinger E, Heil P (2005) Anatomy of the auditory cortex. In: Greenberg S, Ainsworth WA (eds) Listening to speech. Lawrence Erlbaum Associates, Mahwah, pp 91–113

Budinger E, Heil P, Scheich H (2000) Functional organization of auditory cortex in the mongolian gerbil (*Meriones unguiculatus*). III. Anatomical subdivisions and corticocortical connections. Eur J Neurosci 12:2425–2451

Buzsáki G (2006) Rhythms of the brain. Oxford University Press, Oxford

Buzsáki G, Anastassiou CA, Koch C (2012) The origin of extracellular fields and currents: EEG, ECoG, LFP and spikes. Nat Rev 13:407–420

Buzsáki G, Draguhn A (2004) Neural oscillations in cortical networks. Science 304:1926–1929

Caughey TK (1960) Classical normal modes in damped linear dynamic systems. J Appl Mech 27:269–271

Caughey TK, O'Kelly MEJ (1965) Classical normal modes in damped linear dynamic systems. J Appl Mech 32:583–588

Covic EN, Sherman SM (2011) Synaptic properties of connections between the primary and secondary auditory cortices in mice. Cereb Cortex 21:2425–2441

Crick F, Koch C (1998) Constraints on cortical and thalamic projections: the no-strong-loops hypothesis. Nature 391:245–250

Dale A, Sereno M (1993) Improved localization of cortical activity by combining EEG and MEG with MRI cortical surface reconstruction: a linear approach. J Cogn Neurosci 5:162–176

Dale A, Liu A, Fischl B, Buckner R (2000) Dynamic statistical parametric neurotechnique mapping: combining fMRI and MEG for high-resolution imaging of cortical activity. Neuron 26:55–67

Dalebout SD, Robey RR (1997) Comparison of the intersubject and intrasubject variability of exogenous and endogenous auditory evoked potentials. J Am Acad Audiol 8(2):342–354

Darvas F, Pantazis D, Kucukaltun-Yildirim E, Leahy RM (2004) Mapping human brain function with MEG and EEG: methods and validation. NeuroImage 23:S289–S299

David O, Kiebel SJ, Harrison LM, Mattout J, Kilner JM, Friston KJ (2006) Dynamic causal modeling of evoked responses in EEG and MEG. NeuroImage 30:1255–1272

Davis PA (1939) Effects of acoustic stimuli on the waking human brain. J Neurophysiol 2(6):494–499

Dawson GD (1954) A summation technique for the detection of small evoked potentials. Electroencephalogr Clin Neurophysiol 6:65–84

de Munck JC, Bijma F (2010) How are evoked responses generated? The need for a unified mathematical framework. Clin Neurophysiol 121:127–129

Douglas RJ, Koch C, Mahowald M, Martin KAC, Suarez HH (1995) Recurrent excitation in neocortical circuits. Science 269:981–985

Douglas R, Markram H, Martin K (2004) Neocortex. In: Shepherd GM (ed) The synaptic organization of the brain. Oxford University Press, New York, pp 499–558

Douglas RJ, Martin KAC (2007) Mapping the matrix: the ways of neocortex. Neuron 56:226–238

Einevoll GT, Kayser C, Logothetis NK, Panzeri S (2013) Modelling and analysis of local field potentials for studying the function of cortical circuits. Nat Rev 14:770–785

Felleman DJ, Essen DCV (1991) Distributed hierarchical processing in the primate cerebral cortex. Cereb Cortex 1:1–47

Fowles GR, Cassiday GL (2005) Analytical mechanics, 7th edn. Thomson Brooks/Cole, Belmont

Friston KJ, Harrison L, Penny W (2003) Dynamic causal modelling. NeuroImage 19:1273–1302

Garrido MI, Kilner JM, Kiebel SJ, Stephan KE, Friston KJ (2007) Dynamic causal modelling of evoked potentials: a reproducibility study. NeuroImage 36:571–580

Garrido MI, Kilner JM, Kiebel SJ, Friston KJ (2009) Dynamic causal modeling of the response to frequency deviants. J Neurophysiol 101:2620–2631

Glickfield LL, Roberts JD, Somogyi P, Scanziani M (2009) Interneurons hyperpolarize pyramidal cells along their entire somatodendritic axis. Nat Neurosci 12(1):21–23

Guéguin M, Bouquin Jeannès RL, Faucon G, Chauvel P, Liégeois-Chauvel C (2007) Evidence of functional connectivity between auditory cortical areas revealed by amplitude modulation sound processing. Cereb Cortex 17:304–313

Hackett TA, de la Mothe LA, Camalier CR, Falchier A, Lakatos P, Kajikawa Y, Schroeder CE (2014) Feedforward and feedback projections of caudal belt and parabelt areas of auditory cortex: refining the hierarchical model. Front Neurosci 8:72

Hämäläinen M, Ilmoniemi R (1994) Interpreting magnetic fields of the brain: minimum norm estimates. Med Biol Eng Comput 32:35–42

Hämäläinen M, Hari R, Ilmoniemi RJ, Knuutila J, Lounasmaa OV (1993) Magnetoencephalography—theory, instrumentation, and applications to non-invasive studies of the working human brain. Rev Mod Phys 65:413–497

Hanslmayr S, Klimesch W, Sauseng P, Gruber W, Doppelmayr M, Freunberger R, Pechersdorfer T, Birbaumer N (2007) Alpha phase reset contributes to the generation of ERPs. NeuroImage 17:1–8

Hillebrand A, Barnes GR (2005) Beamformer analysis of MEG data. Int Rev Neurobiol 68:149–171

Hines M, Carnevale NT (2001) NEURON: a tool for neuroscientists. The Neuroscientist 7(2):123–135

Hopfield JJ (1984) Neurons with graded response have collective computational properties like those of two-state neurons. Proc Natl Acad Sci USA 81:3088–3092

Hopfield JJ, Tank DW (1986) Computing with neural circuits: a model. Science 233:625–633

Inui K, Okamoto H, Miki K, Gunji A, Kakigi R (2006) Serial and parallel processing in the human auditory cortex: a magnetoencephalographic study. Cereb Cortex 16:18–30

Kaas JH, Hackett TA (2000) Subdivisions of auditory cortex and processing streams in primates. Proc Natl Acad Sci USA 97:11793–11799

Katznelson RD (1981) Normal modes of the brain: neuroanatomical basis and a physiological theoretical model. In: Nunez PL (ed) Electric fields of the brain: the neurophysics of EEG. Oxford University Press, Oxford, pp 401–442

Kileny PR, Kripal JP (1987) Test-retest variability of auditory event-related potentials. Ear Hear 8:110–114

König R, Matysiak A, Kordecki W, Sielużycki C, Zacharias N, Heil P (2015) Averaging auditory evoked magnetoencephalographic and electroencephalographic responses: a critical discussion. Eur J Neurosci 41:631–640

Kubota Y, Karube F, Nomura M, Kawaguchi Y (2016) The density of cortical inhibitory synapses. Front Neural Circuits 10:27

Larson E, Billimoria CP, Sen K (2009) A biologically plausible computational model for auditory object recognition. J Neurophysiol 101(1):323–331

Leaver AM, Rauschecker JP (2016) Functional topography of human auditory cortex. J Neurosci 36:1416–1428

Loebel A, Nelken I, Tsodyks M (2007) Processing of sound by population spikes in a model of primary auditory cortex. Front Neurosci 1:197–209

Luck SJ (2014) An introduction to the event-related potential technique, 2nd edn. The MIT Press, Cambridge

Lütkenhöner B (1998) Dipole separability in a neuromagnetic source analysis. IEEE Trans Biomed Eng 45(5):572–581

Lütkenhöner B, Steinsträter O (1998) High-precision neuromagnetic study of the functional organization of the human auditory cortex. Audiol Neuro-Otol 3:191–213

Makeig S, Westerfield M, Jung TP, Enghoff S, Townsend J, Courchesne E, Sejnowski TJ (2002) Dynamic brain sources of visual evoked responses. Science 295:690–694

Mäkinen V, Tiitinen H, May P (2005) Auditory event-related responses are generated independently of ongoing brain activity. NeuroImage 24:961–968

Matysiak A, Kordecki W, Sielużycki C, Zacharias N, Heil P, König R (2013) Variance stabilization for computing and comparing grand mean waveforms in MEG and EEG. Psychophysiology 50:627–639

May PJC (2002) Do EEG and MEG measure dynamically different properties of neural activity? In: Nowak H, Haueisen J, Giesler F, Huonker R (eds) Proceedings of the 13th international conference on biomagnetism. International Congress Series. VDE Verlag GmbH, Berlin, pp 709–711

May P, Tiitinen H (2001) Human cortical processing of auditory events over time. NeuroReport 12(3):573–577

May P, Tiitinen H, Ilmoniemi RJ, Nyman G, Taylor JG, Näätänen R (1999) Frequency change detection in human auditory cortex. J Comput Neurosci 6:99–120

May PJC, Tiitinen H (2010) Mismatch negativity MMN, the deviance-elicited auditory deflection, explained. Psychophysiology 47:66–122

May PJC, Tiitinen H (2013) Temporal binding of sound emerges out of anatomical structure and synaptic dynamics of auditory cortex. Front Comput Neurosci 7:152

May PJC, Tiitinen H, Westö J (2015) Computational modelling suggests that temporal integration results from synaptic adaptation in auditory cortex. Eur J Neurosci 41:615–630

Mazaheri A, Jensen O (2006) Posterior alpha activity is not phase-reset by visual stimuli. Proc Natl Acad Sci USA 103:2948–2952

Michalewski HJ, Prasher DK, Starr A (1986) Latency variability and temporal interrelationships of the auditory event-related potentials (N1, P2, N2, and P3) in normal subjects. Electroencephalogr Clin Neurobiol 65:59–71

Mitzdorf U (1985) Current source-density method and application in cat cerebral cortex: investigation of evoked potentials and EEG phenomena. Physiol Rev 65(1):37–100

Mitzdorf U (1994) Properties of cortical generators of event-related potentials. Pharmacopsychiatry 27:49–51

Moerel M, Martino FD, Formisano E (2014) An anatomical and functional topography of human auditory cortical areas. Front Neurosci 8:225

Mosher JC, Leahy RM (1999) Source localization using recursively applied and projected (RAP) MUSIC. IEEE Trans Signal Process 47:332–340

Mosher JC, Lewis PS, Leahy RM (1992) Multiple dipole modeling and localization from spatio-temporal MEG data. IEEE Trans Biomed Eng 39:541–557

Näätänen R (1992) Attention and brain function. Lawrence Erlbaum Associates, Hillsdale

Näätänen R, Picton T (1987) The N1 wave of the human electric and magnetic response to sound: a review and an analysis of component structure. Psychophysiology 24:375–425

Nikulin VV, Linkenkaer-Hansen K, Nolte G, Lemm S, Müller KR, Ilmoniemi RJ, Curio G (2007) A novel mechanism for evoked responses in the human brain. Eur J Neurosci 25:3146–3154

Nikulin VV, Linkenkaer-Hansen K, Nolte G, Curio G (2010) Non-zero mean and asymmetry of neuronal oscillations have different implications for evoked responses. Clin Neurophysiol 121:186–193

Noto M, Nishikawa J, Tateno T (2016) An analysis of nonlinear dynamics underlying neural activity related to auditory induction in the rat auditory cortex. Neuroscience 318:58–83

Nourski KV, Steinschneider M, McMurray B, Kovach CK, Oya H, Kawasaki H, Howard MA III (2014) Functional organization of human auditory cortex: investigation of response latencies through direct recordings. NeuroImage 101:598–609

Nunez PL (1995) Neocortical dynamics and human EEG rhythms. Oxford University Press, New York

Okada YC, Wu J, Kyohou S (1997) Genesis of MEG signals in a mammalian CNS structure. Electroencephalogr Clin Neurophysiol 103:474–485

Pascual-Marqui R (2002) Standardized low resolution brain electromagnetic tomography (sLORETA): technical details. Methods Find Exp Clin Pharmacol 24(Suppl D):5–12

Picton T, Stuss DT (1980) The component structure of the human event-related potentials. Progr Brain Res 54:17–49

Rauschecker JP (1997) Processing of complex sounds in the auditory cortex of cat, monkey and man. Acta Oto Laryngol 117:34–38

Rayleigh L (1945) Theory of sounds, vol 1. Dover publication Inc., New York

Ritter P, Schirner M, Mclntosh AR, Jirsa VK (2013) The virtual brain integrates computational modeling and multimodal neuroimaging. Brain Connect 3(2):121–145

Sarvas J (1987) Basic mathematical and electromagnetic properties of the biomagnetic inverse problem. Phys Med Biol 32:11–22

Sauseng P, Klimesch W, Gruber WR, Hanslmayer S, Freunberger R, Doppelmayr M (2007) Are event-related potential components generated by phase resetting of brain oscillations? A critical discussion. Neuroscience 146:1435–1444

Sayers B, Beagley HA, Menshall WR (1974) The mechanism of auditory evoked EEG responses. Nature 247:481–483

Scherg M (1990) Fundamentals of dipole source potential analysis. In: Grandori F, Hoke M, Romani GL (eds) Evoked magnetic fields and electric potentials. Vol. 6 of Advances in Audiology. Karger, Basel, pp 40–69

Scherg M, Berg P (1996) New concepts of brain source imaging and localization. Electroencephalogr Clin Neurophysiol 46:127–137

Segalowitz SJ, Barnes KL (1993) The relaibility of ERP components in the auditory oddball paradigm. Psychophysiology 30:451–459

Shah AS, Bressler SL, Knuth KH, Ding M, Mehta AD, Ulbert I, Schroeder CE (2004) Neural dynamics and the fundamental mechanisms of event-related brain potentials. Cereb Cortex 14:476–483

Sherman SM, Guillery RW (2011) Distinct functions for direct and transthalamic corticocortical connections. J Neurophysiol 106:1068–1077

Telenczuk B, Nikulin VV, Curio G (2010) Role of neuronal synchrony in the generation of evoked EEG/MEG responses. J Neurophysiol 104:3557–3567

Trevelyan AJ (2009) The direct relationship between inhibitory currents and local field potentials. J Neurosci 29(48):15299–15307

Turi G, Gotthardt S, Singer W, Vuong TA, Munk M, Wibral M (2012) Quantifying additive evoked contributions to the event-related potential. NeuroImage 59:2607–2624

Ulanovsky N, Las L, Nelken I (2003) Processing of low-probability sounds by cortical neurons. Nat Neurosci 6(4):391–398

Ulanovsky N, Las L, Farkas D, Nelken I (2004) Multiple time scales of adaptation in auditory cortex neurons. J Neurosci 24:10440–10453

Wang P, Knösche TR (2013) A realistic neural mass model of the cortex with laminar-specific connections and synaptic plasticity—evaluation with auditory habituation. PLoS ONE 8:1–17

Wendel K, Väisänen O, Malmivuo J, Gencer NG, Vanrumste B, Durka P, Magjarević R, Supek S, Pascu ML, Fontenelle H, Grave de Peralta Menendez R (2009) EEG/MEG source imaging: methods, challenges, and open issues. Comput Intell Neurosci 2009, Article ID 656092, 12 pages

Westö J, May PJC, Tiitinen H (2016) Memory stacking in hierarchical networks. Neural Comput 28:327–353

Williamson SJ, Kaufman L (1981) Biomagnetism. J Magn Magn Mater 22:129–201

Wilson H, Cowan J (1972) Excitatory and inhibitory interactions in localized populations of model neurons. J Biophys 12:1–24

Yarden TS, Nelken I (2017) Stimulus-specific adaptation in a recurrent network model of primary auditory cortex. PLoS Comput Biol 13:e1005437

Yeung N, Bogacz R, Holroyd CB, Cohen JD (2004) Detection of synchronized oscillations in the electroencephalogram: an evaluation of methods. Psychophysiology 41:822–832

Yvert B, Fischer C, Bertrand O, Pernier J (2005) Localization of human supratemporal auditory areas from intracerebral auditory evoked potentials using distributed source models. NeuroImage 28:140–153

Zacharias N, Sielużycki C, König R, Kordecki W, Heil P (2011) The M100 component of evoked magnetic fields differs by scaling factors: Implications for signal averaging. Psychophysiology 48(8):1069–1082

Publisher's Note Springer Nature remains neutral with regard to jurisdictional claims in published maps and institutional affiliations.

Chapter 6

Why do humans have unique auditory event-related fields? Evidence from computational modeling and MEG experiments

Received: 20 August 2020 | Revised: 4 December 2020 | Accepted: 20 December 2020

DOI: 10.1111/psyp.13769

ORIGINAL ARTICLE

PSYCHOPHYSIOLOGY SPR WILEY

Why do humans have unique auditory event-related fields? Evidence from computational modeling and MEG experiments

Aida Hajizadeh[1] | **Artur Matysiak**[1] | **André Brechmann**[2] | **Reinhard König**[1] | **Patrick J. C. May**[1,3]

[1]Leibniz Institute for Neurobiology, Research Group Comparative Neuroscience, Magdeburg, Germany

[2]Leibniz Institute for Neurobiology, Combinatorial NeuroImaging Core Facility, Magdeburg, Germany

[3]Department of Psychology, Lancaster University, Lancaster, UK

Correspondence
Artur Matysiak, Leibniz Institute for Neurobiology, Research Group Comparative Neuroscience, Brenneckestraße 6, 39118 Magdeburg, Germany.
Email: Artur.Matysiak@lin-magdeburg.de

Funding information
This work has received funding from the European Union's Horizon 2020 research and innovation programme under grant agreement No. 763959

Abstract

Auditory event-related fields (ERFs) measured with magnetoencephalography (MEG) are useful for studying the neuronal underpinnings of auditory cognition in human cortex. They have a highly subject-specific morphology, albeit certain characteristic deflections (e.g., P1m, N1m, and P2m) can be identified in most subjects. Here, we explore the reason for this subject-specificity through a combination of MEG measurements and computational modeling of auditory cortex. We test whether ERF subject-specificity can predominantly be explained in terms of each subject having an individual cortical gross anatomy, which modulates the MEG signal, or whether individual cortical dynamics is also at play. To our knowledge, this is the first time that tools to address this question are being presented. The effects of anatomical and dynamical variation on the MEG signal is simulated in a model describing the core-belt-parabelt structure of the auditory cortex, and with the dynamics based on the leaky-integrator neuron model. The experimental and simulated ERFs are characterized in terms of the N1m amplitude, latency, and width. Also, we examine the waveform grand-averaged across subjects, and the standard deviation of this grand average. The results show that the intersubject variability of the ERF arises out of both the anatomy and the dynamics of auditory cortex being specific to each subject. Moreover, our results suggest that the latency variation of the N1m is largely related to subject-specific dynamics. The findings are discussed in terms of how learning, plasticity, and sound detection are reflected in the auditory ERFs. The notion of the grand-averaged ERF is critically evaluated.

KEYWORDS

anatomy, auditory cortex, computational modeling, dynamics, event-related field, ERF, latency, magnetoencephalography, MEG, N1m

1 | INTRODUCTION

The auditory event-related response is revealed by presenting a stimulus multiple times, and then, averaging the evoked magnetoencephalography (MEG) or electroencephalography (EEG) signal across the stimulus presentations. The resulting typical trial-averaged response is characterized by a sequence of peaks and troughs. The initial cortically generated ones,

This is an open access article under the terms of the Creative Commons Attribution License, which permits use, distribution and reproduction in any medium, provided the original work is properly cited.

© 2021 The Authors. *Psychophysiology* published by Wiley Periodicals LLC on behalf of Society for Psychophysiological Research

called long-latency responses, reach extrema at approximately 50, 100, and 200 ms after stimulus onset. The respective labels for these responses are P1, N1, and P2 when these are observed in EEG as the part of the event-related potential (ERP). The corresponding labels are P1m, N1m, and P2m when measurements are done in MEG to reveal the event-related field (ERF). Of these, the N1/N1m tends to be the most prominent response. However, there is a large between-subject variability of auditory event-related responses. The peak amplitude of the N1m ranges from several tens of fT to almost 1 pT, a similar order-of-magnitude variation can be seen with the N1, and the peak latency of the N1/N1m is observed in the 70–130 ms range. Thus, averaging the peak amplitude and the peak latency across subjects results in sizeable standard deviations. Also, the grand-averaged response tends to be broader than any of the individual responses because of the variations in peak latencies. Further, the waveform of the event-related response comes in many morphological varieties. The N1/N1m can have a double-peak structure, or its rising or falling slope can have a pronounced shoulder, and many subjects exhibit no clear P2/P2m response at all.

Importantly, the intersubject variability of the event-related response is not merely due to noise in the measurement. Rather, ERFs and ERPs are intrinsically subject-specific, remaining stable from measurement session to session, when these are separated by days, weeks, or even years (see, e.g., Ahonen et al., 2016; Atcherson et al., 2006; Dalebout & Robey, 1997; Michalewski et al., 1986; Sandman & Patterson, 2000; Segalowitz & Barnes, 1993). Figure 1 demonstrates the intrasubject stability (reproducibility) and the intersubject variability of auditory ERFs recorded from two subjects in our laboratory. The test–retest measurements were performed with the identical experimental paradigm and auditory stimuli (simple tone repetition), and the interval between the two MEG recordings was a year for one subject and 3 years for the other. For each subject, the two recordings are from the same MEG channel above the temporal lobe that shows the largest N1m response. There are two observations to be made. First, the two subjects produce substantially different waveforms, with subject-specific peak amplitudes and latencies. Second, the waveforms are reproducible across the long time intervals.

One interpretation of the between-subject differences in auditory ERFs relates to anatomical variations of the auditory cortex (AC) between individual subjects and, within a subject, between the two hemispheres. This is because the magnetic field generated by source activity in cortex depends on the source's orientation and on its distance to the measuring sensor, and these in turn are determined by the topography of the cortex, that is, the ridges and folds of the cortical surface (Hämäläinen et al., 1993). For example, Shaw et al. (2013) concluded that the rightward bias of the N1m amplitude, a phenomenon frequently observed in MEG measurements, is based on a larger degree of cortical folding in the left compared to the right hemisphere. Anatomical work has demonstrated that the morphology of Heschl's gyrus (HG), which harbors the primary auditory cortex, exhibits large cross-subject variability. Different morphotypes manifest themselves in different numbers of gyri, ranging from a single HG to a common stem and a complete posterior duplication to multiple duplications, which also vary between the two hemispheres (Heschl, 1878; Morosan et al., 2001; Rademacher et al., 2001; von Economo & Horn, 1930). Moreover, larger morphological differences can be observed in higher cortical areas as compared to primary areas (Fischl et al., 2008).

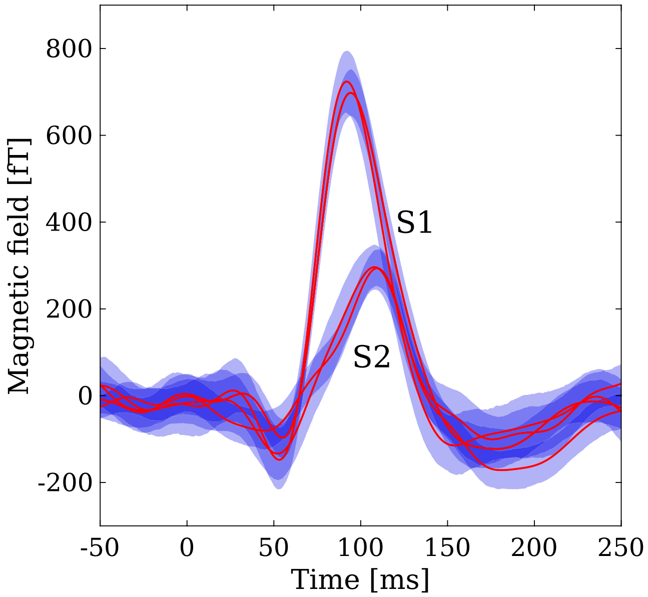

FIGURE 1 Examples of intrasubject reproducibility and subject-specificity of ERFs. The figure shows trial-averaged ERFs evoked in two subjects, S1 and S2, by a sequence of identical stimuli (1.5-kHz tone, sound-pressure level: 80 dB, stimulus onset interval: 7 s, approximately 100 stimulus repetitions). The interval between the two measurements was 3 years for S1 and 1 year for S2. Data show recordings from the MEG channels (magnetometers of the two MEG systems) with the maximum absolute N1m-peak amplitude above the posterior part of the right (S1) and left (S2) hemisphere. For each subject, we found a compelling agreement between the first and second measurements. The variability of the ERFs among subjects is clearly reflected in the large differences in the N1m-peak amplitudes and peak latencies. The waveforms of the second measurement were scaled by a factor of about 1.5 to achieve good agreement between the earlier and later record. This is because we show magnetic field responses from the sensors with the largest N1m amplitude. A slight difference in the positioning of the subject's head between the measurements will scale the response. The shaded region around each of the trial-averaged waveforms represent the 95% confidence interval (CI) of the estimated mean, which was achieved by applying 1,000 bootstrap repetitions (with replacement) to the single trials underlying the means. In each subject, there is a strong overlap of the 95% CI for the test and retest waveforms

Theoretically, the origin of cross-subject variability of ERFs is suggested by Maxwell's equations, which, in combination with the continuity equation, forms the mathematical basis for the computation of the MEG signal. Assuming that the brain is a conducting volume H with constant conductivity σ, the quasistatic approximation of Maxwell's equations, where all time-derivative terms can be ignored as source terms, provides simple solutions to this so-called forward problem. Specifically, the magnetic field $\mathbf{B}(\mathbf{r})$ at a location $\mathbf{r}$ outside the brain generated by electric currents at a location $\mathbf{r}'$ inside the brain follows the Ampère–Laplace law (Hämäläinen et al., 1993; Mosher et al., 1999; Sarvas, 1987; Williamson & Kaufman, 1981):

$$\mathbf{B}(\mathbf{r}) = \frac{\mu_0}{4\pi} \cdot \int_H \mathbf{J}\left(\mathbf{r}'\right) \times \frac{\mathbf{r} - \mathbf{r}'}{|\mathbf{r} - \mathbf{r}'|^3} d\mathbf{r}'. \tag{1}$$

The neural activity is described by the total current density $\mathbf{J}(\mathbf{r}') = \mathbf{J}^{\mathrm{P}}(\mathbf{r}') + \mathbf{J}^{\mathrm{V}}(\mathbf{r}')$. Its first component is the primary current density $\mathbf{J}^{\mathrm{P}}(\mathbf{r}')$ which describes the movement of electrical charge inside the dendritic tree. The second component is the volume current density $\mathbf{J}^{\mathrm{V}}(\mathbf{r}')$ which is proportional to $\mathbf{J}^{\mathrm{P}}(\mathbf{r}')$ and denotes the passive return current in extracellular space. Further, it is assumed that the magnetic permeability of tissue μ is equal to the permeability μ_0 of free space. The Ampère–Laplace law indicates that the generation of ERFs can be separated into two conceptually different components connected by their cross-product: (a) the total current density $\mathbf{J}(\mathbf{r}')$ is produced by neural activity and is thus determined by the brain as a dynamical system; (b) the term $\mathbf{r} - \mathbf{r}'$ denotes the position of the intracranial current source in relation to the extracranial position of the measurement sensor, and thus, reflects the anatomy of the brain, but not the brain dynamics. Notably, ERFs show distinct—and opposite—dependencies on these two components. $\mathbf{B}(\mathbf{r})$ increases linearly with increasing source strength and decreases nonlinearly with increasing distance from the source (Brody et al., 1973; Hämäläinen et al., 1993; Sarvas, 1987; Zhang, 1995). Thus, the ERF reflects neural dynamics via its linear relationship to source strengths, and it also reflects the gross anatomy of the brain, that is, the physical layout of the sources, via a nonlinear relationship to distance and orientation of the sources. Cross-subject variability of ERFs could, therefore, arise out of subject-specific dynamics, subject-specific anatomy, or a combination of both.

In our previous work, we addressed the impact of anatomical and dynamical contributions to the auditory ERF by using simulations of auditory cortex (Figure 10a,b in Hajizadeh et al., 2019). We found that when the modulating effect of the anatomy was varied while keeping the dynamics of the model fixed, the peak amplitude of the N1m became distributed across a wide range, whereas the peak latency of the N1m was little affected. A very different picture emerged when the simulated anatomy remained fixed but the dynamical parameters of the model were varied. In this case, both the peak amplitude and the peak latency of the N1m had a wide distribution, and these two measures were strongly correlated.

The aim of this work is to investigate why ERFs vary from subject to subject by testing the predictions of our computational model (Hajizadeh et al., 2019) in MEG measurements in human subjects. The current, largely unwritten understanding attributes the subject-specificity of ERFs mainly to well-established cross-subject differences in the gross anatomy of cortex. It remains an open question to which degree subject-specific ERFs also reflect the presence of brain dynamics that is specific to the subject. Here, we address this question by linking experimental observations from previous studies (König et al., 2015; Matysiak et al., 2013) and previously unpublished data to simulations from our computational model of auditory cortex.

2 | METHOD

2.1 | Computational model

Simulations were performed on a model of auditory cortex which was originally developed to examine the consequences of short-term synaptic plasticity on auditory processing (May et al., 2015; May & Tiitinen, 2010, 2013; Westö et al., 2016). Its basic dynamical unit is the cortical column, which is described as a pool of excitatory (pyramidal) neurons interacting with a pool of inhibitory interneurons, much as in Wilson and Cowan (1972). The dynamic equations for this interaction are those of the leaky-integrator neuron (LIN; e.g., Hopfield & Tank, 1986), whereby the time derivative of the state variable, which is equivalent to the membrane potential, is proportional to the sum of a leak term and the synaptic input currents. Each current depends linearly on the presynaptic spiking rate and the synaptic strength. Furthermore, the excitatory connections between the pyramidal neurons are modulated by a term describing short-term synaptic plasticity as in Loebel et al. (2007). The output of the LIN is the instantaneous spiking rate derived by passing the state variable through a nonlinear function. In the model, each pool of neurons is described by a single state variable and a single spiking rate representing the mean activity of the pool. Thus, each cortical column is described by a pair of ordinary differential equations, one for the pool of excitatory neurons, the other for the interneurons. In the current simulations, we also included two areas of subcortical processing: the inferior colliculus (IC) and the thalamus. As with cortical columns, we assumed that their dynamical units were interacting pools of inhibitory and excitatory neurons.

Structurally, the model mimics the AC of the macaque monkey with 13 cortical fields (Hackett et al., 2014; Kaas & Hackett, 2000). The input stage of the model represents tonotopically organized IC which feeds into a tonotopically organized thalamus. The thalamocortical input stream represents the lemniscal pathway and targets three tonotopically organized, interconnected fields of the core area, also known as the primary auditory cortex. From there, activity spreads along multiple, topographically organized feedforward pathways to eight surrounding belt fields, which form part of the secondary auditory cortex. Each belt field, in turn, is interconnected predominantly with its nearest neighboring belt fields. Activation from the belt fields is also fed forward to two parabelt fields, also part of the secondary auditory cortex. The feedforward pathways are complemented by reciprocal, feedback pathways. Though being a vastly simplified description of the AC, the model (May et al., 2015; May & Tiitinen, 2010, 2013) is able to reproduce a variety of intra- and extracortically measured effects showing that cortical activation depends both on the incoming stimulus and the historical context of that stimulation (e.g., Brosch & Schreiner, 1997, 2000; Näätänen, 1992).

The dynamical equations of the model comprising N cortical columns (May et al., 2015; May & Tiitinen, 2010, 2013) are given by:

$$\tau_{\mathrm{m}}\dot{\mathbf{u}}(t) = -\mathbf{u}(t) + S(t) \circ W_{\mathrm{ee}} \cdot g[\mathbf{u}(t)] - W_{\mathrm{ei}} \cdot g[\mathbf{v}(t)] + I_{\mathrm{aff,e}}(t), \tag{2}$$

$$\tau_{\mathrm{m}}\dot{\mathbf{v}}(t) = -\mathbf{v}(t) + W_{\mathrm{ie}} \cdot g[\mathbf{u}(t)] - W_{\mathrm{ii}} \cdot g[\mathbf{v}(t)] + I_{\mathrm{aff,i}}(t). \tag{3}$$

Here, τ_{m} is the membrane time constant, and $\mathbf{u}(t) = [u_1(t), \ldots, u_N(t)]$ and $\mathbf{v}(t) = [v_1(t), \ldots, v_N(t)]$ are time-dependent vectors of the state variables of excitatory (index "e") and inhibitory (index "i") cell populations, respectively. In the current simulations, there were 208 cortical columns in total distributed over 13 cortical fields, with 16 columns per field. The IC and thalamus, each comprising 16 column-like units, were also described by the above equations. Thus, there were a total of 240 dynamical units in the model. The connections between the cell populations are mathematically expressed by the four weight matrices W_{ee}, W_{ei}, W_{ie}, and W_{ii}. The elements of W_{ee} represent excitatory-to-excitatory connections, and the elements of W_{ie} describe lateral inhibition. The matrices W_{ei} and W_{ii} have diagonal elements only and describe local, within-column connections of the inhibitory-to-excitatory and inhibitory-to-inhibitory type, respectively. Note that a connection weight describes the intensity with which two populations can interact, and it encapsulates both the average synaptic strengths as well as the density of the connections. The nonlinear function $S(t)$ represents the short-term synaptic plasticity and modifies the weights between the excitatory cell populations in the weight matrix W_{ee} at each time point with an entry-wise multiplication (expressed by the symbol "$\circ$" for the Hadamard product). The spiking rate functions $g[\mathbf{u}(t)]$ and $g[\mathbf{v}(t)]$ are sigmoid functions of the state variables, and the vectors $\mathbf{I}_{\mathrm{aff,e}}(t)$ and $\mathbf{I}_{\mathrm{aff,i}}(t)$ represent the afferent input to the excitatory and inhibitory cell populations.

Due to the nonlinearities of the functions $S(t)$, $g[\mathbf{u}(t)]$, and $g[\mathbf{v}(t)]$, Equations (2) and (3) need to be solved numerically. Thus, simulations are required to investigate how the anatomical connectivity pattern and other model parameters shape the ERF. To gain deeper insight into the confluence of stimulation, system parameters, and cortical dynamics generating the event-related response, we recently developed a linear approximation of the model (for a full treatment, see Hajizadeh et al., 2019). This approach provides explicit solutions to the system dynamics and enables the characterization of AC activity in terms of normal modes. These are damped harmonic oscillators emerging out of the excitatory and inhibitory coupling of the cortical columns; they are described by:

$$u_{\mathrm{d}}(t) = \exp\left(-\gamma_{\mathrm{d}}t\right)\left[a_{\mathrm{ud}}\sin\left(\delta_{\mathrm{d}}t\right) + b_{\mathrm{ud}}\cos\left(\delta_{\mathrm{d}}t\right)\right] + c_{\mathrm{ud}}, \tag{4}$$

$$v_{\mathrm{d}}(t) = \exp\left(-\gamma_{\mathrm{d}}t\right)\left[a_{\mathrm{vd}}\sin\left(\delta_{\mathrm{d}}t\right) + b_{\mathrm{vd}}\cos\left(\delta_{\mathrm{d}}t\right)\right] + c_{\mathrm{vd}}. \tag{5}$$

Here, the decay constant γ_{d} and the damping frequency δ_{d} depend solely on the connection matrices, and the coefficients a_{ud}, a_{vd}, b_{ud}, b_{vd}, c_{ud}, and c_{vd} are functions of the connection matrices and the afferent inputs. Each normal mode depends explicitly on all parameters of the system, including the pattern of the connections between all columns. Therefore, a normal mode on its own does not represent the activity of any individual column. Instead, it should be thought of as a dynamic building block that is spread across the whole system, contributing to the activity of each column with a specific weight. Conversely, the activity of any one column represents the weighted sum of all the normal modes of the system, and, thus, is directly dependent on the anatomical structure of the AC.

In the original model (May et al., 2015; May & Tiitinen, 2013), lateral inhibition was realized by the excitatory populations making lateral connections to the inhibitory populations of neighboring columns so that W_{ie} had off-diagonal elements. In order to generate the analytical solutions, it was necessary to remove these off-diagonal elements. Lateral inhibition was included in the analytical model by introducing negative connections into W_{ee}, effectively combining the original matrices W_{ee} and W_{ie} into a matrix W_{AC}. This contained all lateral and long-range (i.e., nondiagonal) connections, both excitatory and inhibitory. In practice, W_{AC} was constructed by using Gaussians with stochastic terms to determine the connection strength as a function of the distance between the connecting columns on the tonotopic map (for details, see Hajizadeh et al., 2019).

2.2 | MEG simulation

The MEG signal was calculated by approximating the primary current in each column as being a linear function of the synaptic inputs targeting the excitatory cell population of the column. The contribution of each input was multiplied by a connection-specific anatomical factor. These factors account for the magnetic field depending not just on the strength of the primary current, but also on the distance of the current to the MEG sensor, and on the orientation of the current (Hämäläinen et al., 1993), as seen in Equation 1. The orientation of the current not only depends on the subject-specific folding of the cortical surface, which embeds the current, but it also depends on the apical-dendrite location of the synapse driving the current and on whether the synapse is excitatory or inhibitory. Thus, the MEG signal produced by the model is the product of two mutually independent factors: (a) the dynamics of the auditory cortex, as reflected in the synaptic inputs that the cortical columns receive, and (b) the subject-specific anatomical parameters.

The anatomical parameters, as described above, are denoted by A, which is a collection of multipliers, one per connection made onto the excitatory populations. As in Hajizadeh et al. (2019), we construct these multipliers by first defining three matrices K_1, K_2, and K_3 comprising multipliers according to connection type. K_1 modulates the contribution made by the excitatory connections in W_{AC}, and therefore, has the same structure as W_{ee}, which encapsulates how the 13 cortical fields are connected with each other (Figure 2a). The elements of K_1 are further divided into feedforward, feedback, and within-field (diagonal) types. The matrices K_2 and K_3 have an identical structure and modulate the contribution made by the

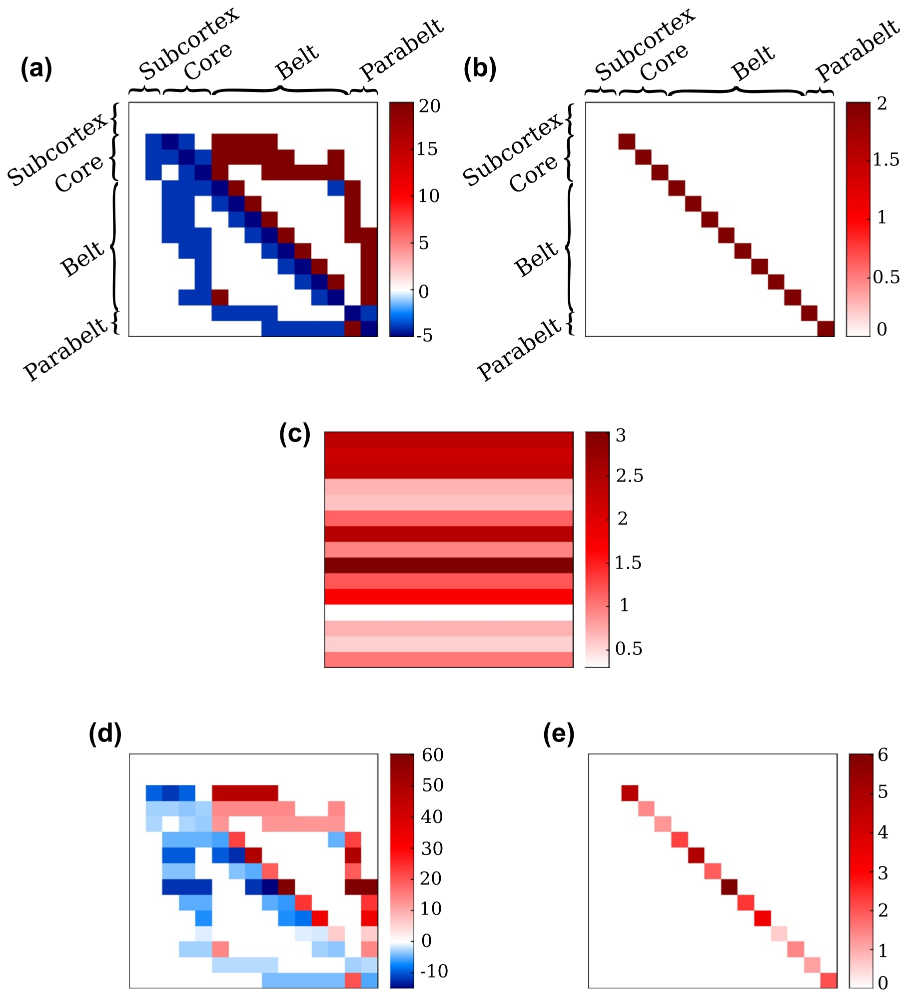

FIGURE 2 The matrices for computing the MEG signal. (a) The matrix K_1 contains the multipliers for the contribution of the MEG signal coming from the excitatory connections of type feedforward (blue), feedback (dark red), and intra-field (dark blue). (b) The matrices K_2 and K_3 are identical to each other, and they provide multipliers for the intra-column inhibitory connections and the lateral inhibitory connections, respectively. (c) The topography matrix T represents the gross anatomy of auditory cortex and it modulates the MEG in a field-specific way. Each row represents the field-specific effect that the field has on the MEG signal via orientation and distance to the sensor. (d, e) Element-wise multiplication of K_i and the T results in the final multipliers which modulate the contribution to the MEG from each connection. Note that this figure displays 15 × 15 matrices where the indexing runs over the 2 subcortical and 13 cortical fields. Each element represents 16 × 16 connections made by the 16 subcortical neuronal units or cortical columns per field

intra-column inhibitory connections in W_{ei} and lateral inhibition connections in W_{AC}, respectively (Figure 2b). These three K_{i}-matrices have default values that reflect the orientation of the current produced by the various types of connections (for details, see Section 4.1 of Hajizadeh et al., 2019). Extending from the approach in our previous study (Hajizadeh et al., 2019), the effect of subject-specific gross anatomy was taken into account in the generation of the MEG signal. To model the effect of the column orientation and distance to the MEG sensor—that is, of the gross anatomy of the cortical folding—the elements of K_i were multiplied by a random number that was specific to each of the 13 cortical fields. This is a simplification, which assumes that the columns in a field have approximately the same orientation and the same distance to the sensor. For notational convenience, these 13 random numbers are represented by a topography matrix T where each row has identical elements and each column is the vector of the 13 field-specific multipliers (see Figure 2c). Further, to model the effect of cross-subject variation of the topography of the cortical surface, multiple T-matrices were generated, so that each T-matrix represented a single subject. Note that in this approach, we are not concerned with describing or reconstructing the effect of the actual cortical gross anatomy of any particular subject but, rather, we are interested in the effect of cross-subject anatomical variation on the ERF response. Thus, each connection has an anatomical multiplier as part of the parameter set A, and this is the product of the elements in T and K_i corresponding to that connection.

The MEG response $R(t)$ of the model is computed as the sum over the synaptic inputs to the excitatory populations, weighted by the Hadamard product of the topography matrix T with the K_i-matrices:

$$\begin{aligned} R(t) = \sum_{j=1}^{N} \big[& T \circ K_1 \circ W_{\mathrm{AC}}^{+} u(t) \\ & + T \circ K_2 \circ W_{\mathrm{ei}} v(t) \\ & + T \circ K_3 \circ W_{\mathrm{AC}}^{-} u(t) \big]_j . \end{aligned} \tag{6}$$

where j runs over the number of cortical columns in the model. The matrices W_{AC}^{+} *and* W_{AC}^{-} represent the excitatory connections and lateral inhibition of W_{AC}, respectively. The default values for the dynamical and anatomical parameters used in the simulations are listed in Table 1. They were chosen such that the model replicated a typical ERF, with P1m, N1m, and P2m responses. We note that according to our normal-mode characterization (Hajizadeh et al., 2019), each of these responses is fundamentally a property of the whole system and does not have an anatomically localizable generator process. For example, in the model, subtle changes to the internal connections of the parabelt result in significant changes in the activation of the core and belt as they produce the N1m. Thus, the parabelt should be considered to be an integral part of the N1m generator process, even though its direct contribution to this response is small.

2.3 | Simulation experiments

We carried out simulations to test how cross-subject differences in dynamics and/or anatomy of the auditory cortex impacts on the auditory ERF. For this, we randomly varied the parameters of the dynamical equations of the model, denoted by D, as well as the anatomical parameter set A defined in Section 2.2. Further, each set of parameters produced in the randomizations represented an individual subject. The set of dynamical parameters D comprised the weight matrices W_{AC}, W_{ei}, W_{ie}, and W_{ii}. The membrane time constant τ_{m} is also a dynamical parameter, although it was not varied in the current simulations. For randomizing the D-parameters, the same method was used as in Hajizadeh et al. (2019). That is, for each of the diagonal matrices W_{ei}, W_{ie}, and W_{ii}, a random number was generated from a flat distribution over a predefined range. The elements of the matrix were then multiplied by that number. The matrix W_{AC}, describing the long-range excitatory and lateral inhibitory connections, was generated as a sum of Gaussians with stochastic terms (see Appendix A1 of Hajizadeh et al., 2019). Cross-subject random variation in these column-to-column connection strengths was achieved by regenerating W_{AC} while keeping the Gaussian parameters fixed. Because of the stochastic terms, the overall connectivity pattern remained the same, but weight values varied slightly from subject to subject. To summarize the effect of the randomizations, these essentially altered the balance between excitation and inhibition and they also modified the connectivity patterns at a fine resolution.

The A- and D-parameters were each randomized with five different ranges of the random multiplier. The distribution of random multipliers from each range was evenly distributed around unity, which generated the default value of the modulated parameter (see Table 1). This was achieved by dividing each range into two subsets of random numbers, those larger than unity and those smaller, and then, picking an equal number of multipliers from each subset. For randomizing the D-parameters, the lower bounds of these ranges were chosen as (1–1/2), (1–1/4), (1–1/8), (1–1/16), and unity (1–0). The upper bound was the inverse of the lower bound, and this resulted in the ranges [0.50, 2.00], [0.75, 1.33], [0.88, 1.14], [0.94, 1.07], and [1.00, 1.00] (i.e., no variation). Similarly, for randomizing the A-parameters, we used five different ranges from which the random multipliers were picked to populate the T-matrix (see Section 2.2). These ranges had lower bounds of (1/8), (1/4), (1/2), (3/4), and (1). Again, the upper bound was the inverse of the lower bound, producing the ranges [0.12, 8.00], [0.25, 4.00], [0.50, 2.00], [0.75, 1.33], and [1.00, 1.00]. With five ranges each for the D and A multipliers, there were a total of $5 \times 5 = 25$ combinations of parameter variations. For each combination of A- and D-parameters, 1,000 simulations representing 1,000 subjects were run with parameter values generated randomly with multipliers from the respective ranges of that combination. The resulting ERFs were

TABLE 1 Default dynamical and anatomical parameter values used in the simulations. The matrix W_{AC} includes lateral inhibition (within-field inhibitory) connections and column-to-column excitatory connections. It also contains pre-cortical connections from inferior colliculus (IC) to thalamus, from thalamus to the core areas as well as recurrent connections in IC and thalamus. The cortical intra- and inter-field connections in W_{AC} are defined by Gaussian distributions of the form $Q(x) = r\exp[-(x + \mu + s\,N(0,1))^2/2\sigma^2]$, with the distance x between column i and j, amplitude r, constant μ, variance σ^2, stochasticity s of the Gaussian distribution $Q(x)$, and the standard normal distribution $N(0,1)$ (for further details, see Hajizadeh et al., 2019)

Dynamical parameter set *D*			**Value**			
τ_m			25 ms			
W_{ei}			1.15			
W_{ie}			1.00			
W_{ii}			0.20			
W_{AC}	(subcortical)	IC recurrent	0.09			
		IC to Thalamus connections	0.015			
		Thalamus recurrent connections	0.09			
		Thalamus to core connections	0.015			
			r	μ	σ^2	s
W_{AC}	(cortical)	Between-field excitatory	0.09	0	1.5	0.2
		Within-field excitatory	0.105	0	2.0	0.4
		Within-field inhibitory	0.09	3.0, −3.0	1.5	0.4
Anatomical parameter set *A*			**Value**			
K_1 feedforward elements			−4			
K_1 feedback elements			20			
K_1 within-field elements			−5			
K_2			2			
K_3			2			

then analyzed in terms of the peak amplitude, peak latency, and 3-dB width of the N1m response. We focused on the N1m, because it is usually the most prominent ERF response generated by the auditory cortex. To account for the time delay due to subcortical processing, we added a 35-ms shift to the waveforms. This resulted in the N1m peaking at 100 ms with the default parameter values. Further, going beyond the analysis methods of Hajizadeh et al. (2019), we arithmetically grand-averaged the ERF waveforms across the subjects and inspected the mean waveform as well as its standard deviation.

2.4 | MEG experiments with human subjects

We present MEG data from two separate studies, which were conducted with two different subject populations, with the total number of subjects being 25. Here, we show the analyses of the ERFs from the right hemisphere, and we note that the left-hemispheric ERFs yield the same results with respect to the origin of subject-specificity. Further details on the first study (Experiment A) can be found in Zacharias et al. (2012). Data of the second study (Experiment B) have not been published before, and information on acquisition and pre-analysis is briefly summarized here. For both studies, subjects were recruited from the academic environment at the Leibniz Institute for Neurobiology and the Otto von Guericke University in Magdeburg. All subjects gave written informed consent to participate in the measurements, and both studies received independent approval by the Ethics Committee of Otto von Guericke University.

Both studies used the same experimental paradigm. Sequences of 1.5-kHz tones with 100-ms duration were presented at a sensation level of 80 dB in separate blocks where each block was characterized by a constant stimulus onset interval (SOI). Two consecutive blocks were separated by a pause of about 30 s, and the order in which the blocks were presented was randomized across subjects. In Experiment A, tones were delivered monaurally to the subjects' left ear, and the SOIs ranged from 0.5 to 10 s in five steps. The recording device was the Magnes 3600 WH system (4-D Neuroimaging) with 248 magnetometers. In Experiment B, tones were delivered binaurally, and 10 different SOIs were used in the 0.25-s to 7-s range. Magnetic fields were measured with the Elekta Neuromag TRIUX system which consists of 102 magnetometers and 204 planar gradiometers (102 measurement locations in total). For the current study, we focused on the measurements performed with the magnetometers of the two systems. The same standard preprocessing procedure (including artifact rejection, heartbeat correction, filtering and averaging across trials) was applied to the raw data of both experiments (Zacharias et al., 2012). The trial-averaged MEG responses were baseline-corrected (200 ms) and filtered with a band pass of 1–30 Hz (Butterworth, zero phase shift).

As with the simulated responses, the ERFs were analyzed in terms of the peak amplitude, peak latency, and 3-dB width of the N1m response, and also in terms of the grand-averaged ERF and its standard deviation. The measurements relating to the N1m were expressed in terms of histograms, for which we computed 95% confidence intervals for the individual bins. This was achieved via the bootstrap method, that is, random sampling with replacement (Efron, 1979). For this, we constructed 1,000 resamples of the data of the 25 subjects, and then, rejected the 2.5% smallest and the 2.5% largest values in each histogram bin. The remaining values fall in the range depicted in the error bars in the figures.

In Hajizadeh et al. (2019) and in the current study, we ignore the effect of synaptic plasticity, which has a lifetime of several seconds. Hence, for the experimental data, we selected the ERFs from the blocks with the longest SOIs, that is, SOI = 10 s in Experiment A and SOI = 7 s in Experiment B. The interval between individual stimuli in these blocks was long enough for full recovery from adaptation to occur (see, e.g., Lü et al., 1992; McEvoy et al., 1997; Zacharias et al., 2012). Further, the model offers only an approximation of AC dynamics in terms of damped harmonic oscillators. There are therefore ERF waveforms that it cannot produce but which can nonetheless be observed in a small number of subjects. These are double-peak structures of the N1m waveform and the emergence of a sustained field following the N1m. We excluded such cases from the experimental data to ensure comparability between the simulated waveforms and the experimental data. This led to a rejection of 2/15 subjects in Experiment A and 3/15 subjects in Experiment B.

3 | RESULTS

The current study uses simulations of auditory cortex and experimental data to address how the ERF is shaped by the anatomy of the auditory cortex, on the one hand, and by the system dynamics of the auditory cortex, on the other hand. In simulations, the ERFs of populations of subjects are generated with the assumption that, in each population, the anatomical parameters *A* and the dynamical parameters *D* vary across the population in a specified way. We compare simulated ERFs with ERFs from two different MEG experiments (Experiment A and Experiment B; recordings are from magnetometers above the right posterior temporal lobe where the largest ERF response was measured), focusing on the N1m response, the most prominent ERF wave generated in the auditory cortex. We characterize the N1m for each subject separately in terms of the peak amplitude, the peak latency, and the width of the N1m. Further, we consider the arithmetic mean and arithmetic standard deviation of the waveforms of populations of subjects.

3.1 | Experimental and simulated ERFs

Figure 3a shows trial-averaged MEG responses from individual subjects (thin gray curves) collected in Experiment A and B. Also shown is the corresponding arithmetic mean (grand mean, thick black curve) and arithmetic standard deviation (thick red curve). The subject-specificity of the waveform is apparent in the different peak amplitudes, peak latencies, and waveform widths of the N1m. We note that the peak latency of the N1m in the grand mean occurs at ~105 ms, and that the peaks of the individual waveforms are scattered around that value by ±20 ms, as indicated in the inset of Figure 3a. The standard deviation is time-dependent and shows a pronounced maximum ~15 ms before the peak of the N1m of the grand mean. This heteroscedasticity is due the fact that the individual waveforms, and their N1m peaks in particular, predominantly differ by a multiplicative factor, rather than by an additive amount (König et al., 2015; Matysiak et al., 2013).

We simulated cross-subject variability of the ERF by varying the anatomical *A*-parameters and the dynamical *D*-parameters of the model (see Table 1). Changing only the anatomical factors while keeping the dynamical parameters constant leads to a large distribution of the peak amplitudes of the P1m, N1m, and P2m responses (Figure 3b). However, the inset shows that there is only a small effect on the peak latencies, which cluster around the respective peak latency in the grand mean waveform. Therefore, the grand mean and the corresponding standard deviation exhibit maxima for the P1m, N1m, and P2m deflections roughly at the same latencies, respectively.

In contrast, a very different pattern is revealed in simulations where the anatomical parameters are fixed but the dynamical parameters are randomized (Figure 3c). In this scenario, the waveforms show very similar P1m deflections. These then evolve into N1m deflections through near-identical positive slopes which fan out into a wide distribution of N1m-peak amplitudes and latencies. There is a strong positive correlation between the peak amplitude and latency of the N1m, as shown in the inset, and the width of the N1m deflection becomes larger with increasing peak amplitude (as in the simulations of Hajizadeh et al., 2019). The spread of the waveforms continues beyond the N1m, and entails a large variety of P2m deflections—contrary to the situation where only anatomical variations are introduced (Figure 3b). The standard deviation shows a pronounced peak at around 130 ms, that is, *after* the N1m peak of the grand mean. Note that the simulated data in each panel was normalized such that the N1m-peak amplitude of the grand mean of the simulations was equal to the N1m-peak amplitude of the grand mean of the experimental data (350 fT).

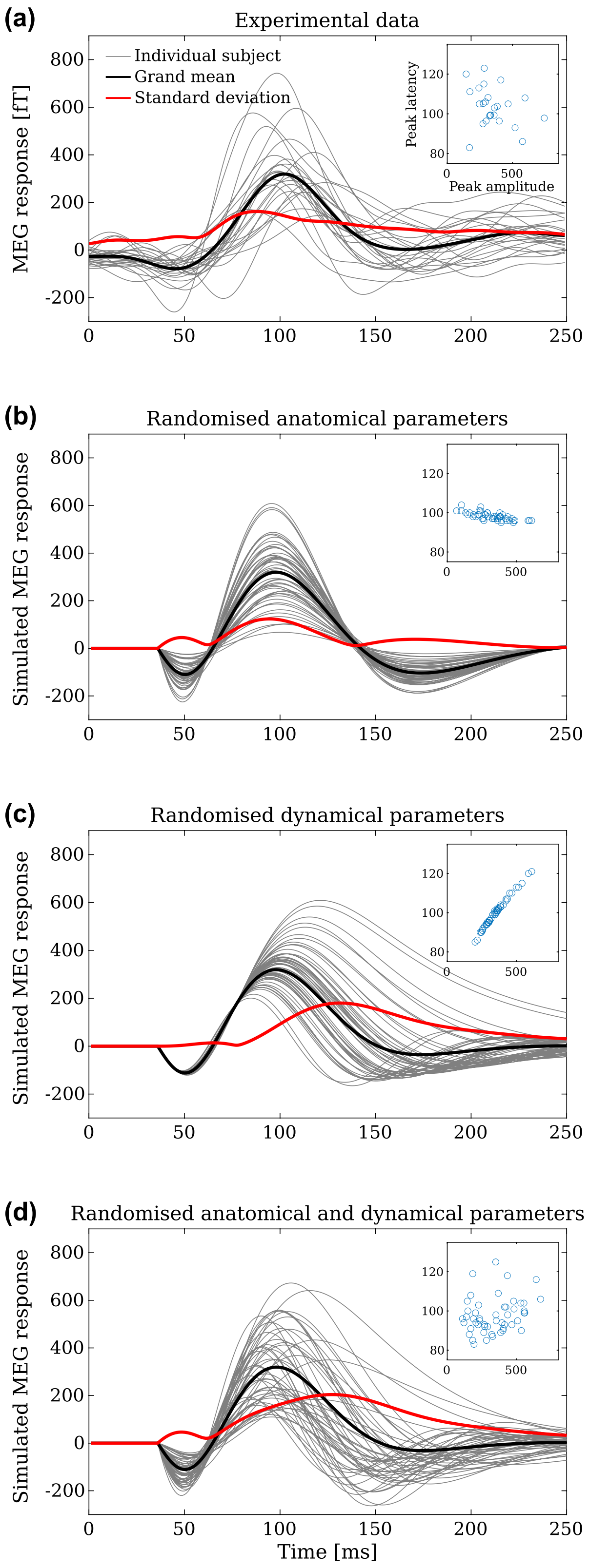

FIGURE 3 Comparison of experimental and simulated waveforms for two illustrative parameter ranges, with the N1m-peak latency plotted against the N1m-peak amplitude in the inset of each panel. (a) Waveforms of individual subjects (thin gray curves; $N = 25$) and their corresponding mean (black curve) and standard deviation (red curve) are shown for the two MEG experiments. The peak amplitude of the N1m varies in a range from about 200 to 800 fT [mean ± *SD*: (352 ± 140) fT]. The peak latency ranges from around 80 to 130 ms [(104 ± 10) ms]. (b) Simulated waveforms and the corresponding grand-averaged waveform and standard deviation were generated by randomizing the anatomical parameters A while keeping the dynamical parameters D fixed. A total of 50 waveforms were generated such that the elements of the topography matrix T were randomly picked from the [0.12, 8.00] range. The resulting waveforms are similar in shape. There is large variation in the peak amplitude of the N1m [(327 ± 126) fT] and a narrow variation of the peak latency [(98 ± 2) ms]. (c) The panel shows how varying the dynamical parameters (range of random multiplier [0.75, 1.33]) affects the waveform while the anatomical parameters were fixed. There is a strong positive correlation between the amplitude [(352 ± 90) fT] and latency [(100 ± 8) ms] of the N1m peak, as well as between peak amplitude and width of the N1m. (d) The simultaneous randomization of both D- and A-parameters leads to a set of ERF waveforms that resembles that obtained in the experiments and shown in (a). There is a large variation in the N1m-peak amplitude [338 ± 150] fT as well as in the N1m-peak latency [(98 ± 9) ms]. Note that the simulation results here show a random subset of 50 single-subject responses taken from the 1,000 single-subject simulations, which are the basis of the results shown in the subsequent figures

However, neither of the waveform dispersions in Figure 3b,c bears a close resemblance with that observed in the MEG experiments (Figure 3a). The dispersion due to anatomical variations (Figure 3b) resembles the experimental results in that the standard deviation peaks before the N1m of the grand mean. Nevertheless, the peak latencies of the simulated N1m and P2m are too concentrated. A better correspondence with experimental results is achieved in Figure 3d, which shows simulations where both the anatomical and the dynamical parameters were randomized simultaneously using the respective parameter ranges of the simulations shown in Figure 3b,c. This leads to a wider dispersion of the individual peak latencies of the N1m and P2m, as also demonstrated in the inset, and to a more realistic spread in the N1m widths. These observations suggest that both anatomy *and* dynamics might be the cause of the subject-specificity of ERFs.

3.2 | The N1m response

The dependence of the N1m response on anatomy and dynamics was investigated systematically by using five different ranges of variation for the A-parameters and another five for the D-parameters. Thus, parameter variations were generated in a total of $5 \times 5 = 25$ combinations of parameter ranges. For each range combination, 1,000 simulated single subjects were generated. The ERF of each subject was characterized in terms of the peak amplitude, the peak latency, and the 3-dB width of the N1m. The normalized distribution of each of these measures was then compared to the normalized distribution of the corresponding measure from the experimental data shown in Figure 3a. The results are shown in Figure 4, where the rows represent the results for the peak amplitude (top), peak latency (middle), and waveform width (bottom) of the N1m, and where the five columns represent the five variation ranges of the *D*-parameters in ascending order from left to right. Within each panel, the five colored curves represent the distributions of the N1m measure, each one gained for a specific range of *A*-parameters.

The gray histograms in the top row of Figure 4 show the distribution of the peak amplitude of the experimentally measured N1m (bin width 100 fT). The distribution is skewed and it has a maximum at the [200–300] fT bin. The corresponding distributions for the simulated ERFs exhibit no *A*-dependence for the largest *D*-range (Figure 4e), as is evident in the colored distribution curves resembling each other. As the *D*-range is decreased (moving from right to left), the amplitude distributions for the different *A*-ranges become increasingly diverse for each *D*-range. The best match between simulations and experiments is achieved with the *A*-ranges with the randomization factor [0.25, 4.00] (purple curves) and [0.12, 8.00] (orange curves). These produce N1m-amplitude distributions which are similar across all the *D*-ranges. On the basis of these results, the subjects have individual cortical anatomies, but no conclusion can be drawn on the presence of dynamical variations across subjects.

The distributions of the peak latency and width of experimentally measured N1m are shown in Figure 4 in the histograms of the middle and bottom row, respectively. The latency distribution is skewed, whereas the width distribution is symmetrical. In both cases, the distributions for the different *A*-ranges closely resemble each other for any given *D*-range, with the one exception of the leftmost panel of the latency row (Figure 4f), where the *D*-range is [1.00, 1.00], that is, when there is no randomization of the dynamical parameters. The best match between experiment and simulation occurs with the *D*-range [0.75, 1.33] both in the case of peak latency (Figure 4i) and in the case of waveform width (Figure 4n). From these findings, we conclude that the subject-specific peak latency and width of the N1m response is explained by cross-subject variations in dynamical parameters, rather than by variations in anatomical factors. This corroborates our observations in Figure 3 that dynamical variations are needed to produce N1m latency variations across subjects.

Figure 5 summarizes the similarity between experimental and simulated data shown in Figure 4. This similarity was quantified separately for each *D*-range and *A*-range combination through the histogram intersection algorithm (Swain & Ballard, 1991). The similarity results for the peak amplitude, peak latency, and width of the N1m response are shown as similarity maps in Figure 5a-c, respectively. The *x* and *y* axis represent the *D*-ranges and *A*-ranges, respectively, and the color codes the similarity measure, with red elements referring to high and blue elements to low similarity. For the peak amplitude of the N1m (Figure 5a), we note a high similarity across many *D*- and *A*-ranges, with the exception of the narrowest ones (blue panels in the bottom left corner). For the peak latency (Figure 5b), there is a narrow, vertical band of high similarity stretching across all *A*-ranges at the *D*-range of [0.75, 1.33]. Likewise, for the N1m width (Figure 5c), there is a similar vertical band at the *D*-range of [0.75, 1.33]. To identify an overall similarity pattern, the three similarity maps have been averaged in Figure 5d. The dark orange element of this mean map shows which *D*- and *A*-range combination yields the overall best match between experimental and simulated data. This indicates that the subject-specificity of the ERFs is not only based on anatomical variations across subjects, but it also reflects subject-specific dynamics of the auditory cortex.

3.3 | The grand-averaged ERF versus the standard deviation

The correspondence between experimental and simulated data can be examined by looking at the entire ERF waveform rather than at singular time points or deflections such as the N1m response, as was done above. For this broader examination, we used two measures: the ERF waveform grand-averaged across subjects, and the corresponding standard deviation. The results are shown in Figure 6, where the standard deviation is plotted against the grand mean for each of the 25 *D*- and *A*-range combinations (red curves). The five columns represent the five *D*-ranges in increasing order from left (narrow range) to right (wide range), and the five rows represent the *A*-ranges in increasing order from bottom (narrow range) to top (wide range). Each panel also shows the same standard-deviation-versus-mean plot (black curves) for the experimental data extracted from the waveforms shown in Figure 3a. As noted above, the experimental data are heteroscedastic, and this is evident in the characteristic balloon shape of the standard-deviation-versus-mean plot.

In Figure 6, the plots for the simulated data come in a variety of patterns, many of them revealing heteroscedasticity, but only a few of them resemble the experimental data. The panels with the light gray background indicate the best matches in terms of the root mean square analysis between the simulated and the experimental data. They are found in the region with large variations of the *A*-parameters and intermediate variations of the *D*-parameters. These best cases largely overlap with the best matches seen in

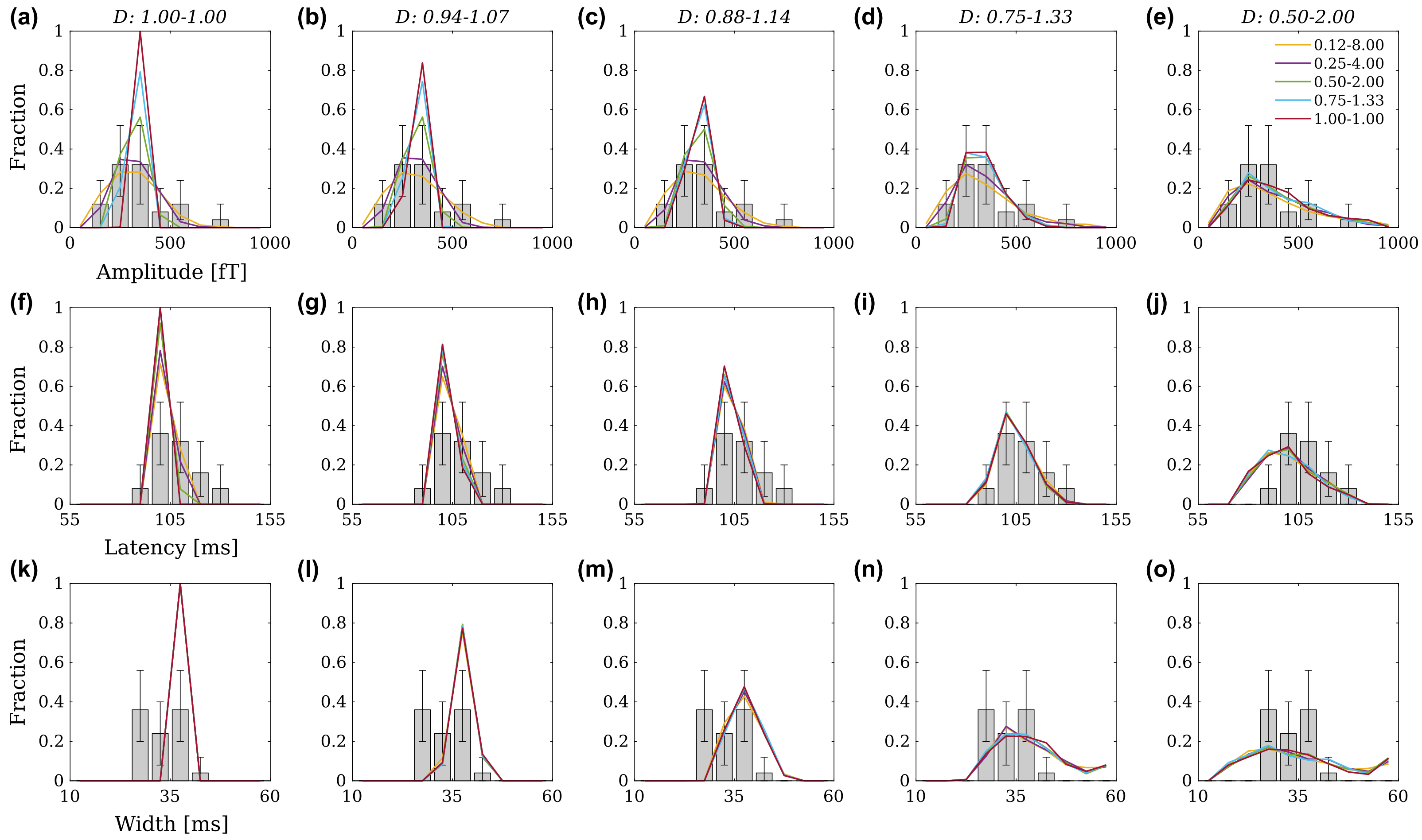

FIGURE 4 Distributions of the peak amplitude (top row), peak latency (middle row), and 3-dB width (bottom row) of the N1m obtained from the experimental data (histograms) and simulations (colored lines). Columns represent the five variation ranges of the dynamical parameters *D*, in increasing order from left to right. The set of five curves per panel represent five histograms, one for each variation range of the anatomical parameters *A* (see panel e for color coding of ranges). In each row, the histogram for the experimental results (see Figure 3a) is duplicated across the panels. (a–e) The top row shows the data for the peak amplitude of the N1m. In the simulations, the distribution of the peak amplitude is little affected by varying the *A*-parameters when the variation of *D* is large (right-most panels). Conversely, with small *D*-variations (left-most panels), the distribution has a strong dependence on how *A* is varied. The best match between simulation and experiment is achieved with the specific *A*-range of [0.25, 4.00] (purple curves), irrespective of how *D* is varied. (f–j) The middle row presents the data for the peak latency of the N1m. In simulations, the distributions depend almost exclusively on the variation of the *D*-parameters, the exception being the case where the *D*-parameters are kept unchanged (panel f). The best match between the simulation and experimental results are seen when the randomization range for *D* is [0.75, 1.33] (panel i). (k–o) The bottom row displays the distributions of the N1m widths. As with the peak latency, the widths of the simulated N1m responses depend only on the *D*-parameters, and the best match with experimental results is obtained with the randomization range [0.75, 1.33] (panel n)

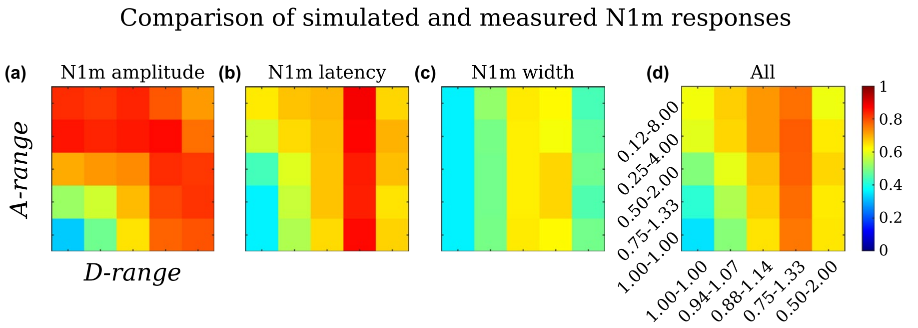

FIGURE 5 Comparison of simulated and measured N1m responses. (a) The distribution of the simulated N1m-peak amplitude resembles the experimental results maximally when the *D*-parameter variation range is [0.75, 1.33] and the *A*-parameter range is [0.25, 4.00]. (b) For the peak latency of the N1m, the best correspondence between simulation and experiment is reached with the variation ranges [0.75, 1.33] and [0.12, 8.00] for the *D*- and *A*-parameters, respectively. (c) In the case of the N1m width, the best match is reached with the same range [0.75, 1.33] for the *D*- and *A*-parameters. (d) Averaging over the previous similarity measures reveals that, overall, the best match between simulation results and experimental data occurs when the variation range of the *D*-parameters is [0.75, 1.33] and that of the *A*-parameters is [0.25, 4.00]. Thus, these results are consistent in indicating that the distributions from experimental data are explained by both the cortical anatomy and the cortical dynamics varying from subject to subject. Each panel represents simulations carried out with the 25 combinations of variations of the dynamical parameters *D* and the anatomical parameters *A*. The ranges of the *D*- and *A*-variations are represented on the abscissa and ordinate, respectively, with the ranges increasing from left to right and from bottom to top. The similarity between distributions was measured with the histogram intersection algorithm (Swain & Ballard, 1991), with high similarity coded in red and low similarity in blue. The actual distributions are shown in Figure 4

Figure 5, where the correspondence between the experimental and simulated N1m response is displayed. All other panels show marked differences between simulations and experiments. For example, simulations displayed in the final column, with the largest *D*-range [0.50, 2.00], show a wide loop. In these cases, the dynamical parameters dominate the characteristics of the ERFs, leading to a wide distribution of the peak latencies of the N1m, and, consequently, to a shift of the maximum of the standard deviation to a value larger than the maximum of the grand mean (see, e.g., Figure 3d). Similar loops, though less pronounced, and therefore, matching the experimental data, can be seen in the fourth column with a *D*-range [0.75, 1.33]. When there is no *A*-variation ([1.00, 1.00], bottom row) and as the range of the *D*-variation is decreased (from right to left), the relationship between the standard deviation and grand mean approaches homoscedastic behavior, which is finally reached in the case where neither *D*- nor *A*-parameters are varied. As the range of the *A*-variation is increased, homoscedasticity gradually turns into heteroscedasticity, and the relationship between standard deviation and grand mean gradually approaches the pattern identified in the experiments. This pattern indicates both in experiment and simulations, that the individual waveforms in the vicinity of the N1m peak predominantly differ by factors, not by amounts (see Matysiak et al., 2013). In sum, these results confirm the N1m analyses in Section 3.2 according to which the cross-subject variability of the ERF can best be explained by both the cortical anatomy and the dynamical parameters of auditory cortex varying across subjects.

4 | DISCUSSION

While the auditory ERF often comprises a series of landmark deflections identified as the P1m, N1m, and P2m, there is considerable variability across subjects in the peak amplitudes and latencies of these deflections and in the shape of the ERF in general. Indeed, the ERF is much like a fingerprint—in that it is both specific to the individual subject and reproducible across repeated measurements (see Figure 1). We pursued the question of whether this subject-specificity is due to different gross anatomies of the AC, or whether it also reflects subject-specific dynamics. We compared experimental MEG data with simulations of a computational model of the auditory cortex. Our results indicate that the subject-specificity of ERFs is due to a mixture of effects, with both the gross anatomy and dynamics varying across subjects.

4.1 | Main findings

Our model of auditory cortex is based on the anatomical organization of AC in terms of core, belt, and parabelt fields (Hajizadeh et al., 2019; May et al., 2015). There were two sets of parameters that we manipulated in simulations. First, the anatomical parameters represented the effect of the cortical gross anatomy on the generation of the ERF signal, without having an effect on the dynamics. Second, the dynamical parameters were the strengths of the connections between cortical columns. In our simulations, changing these led to a modulation of the balance between excitation and inhibition, and it also affected the patterns of long-range connectivity at

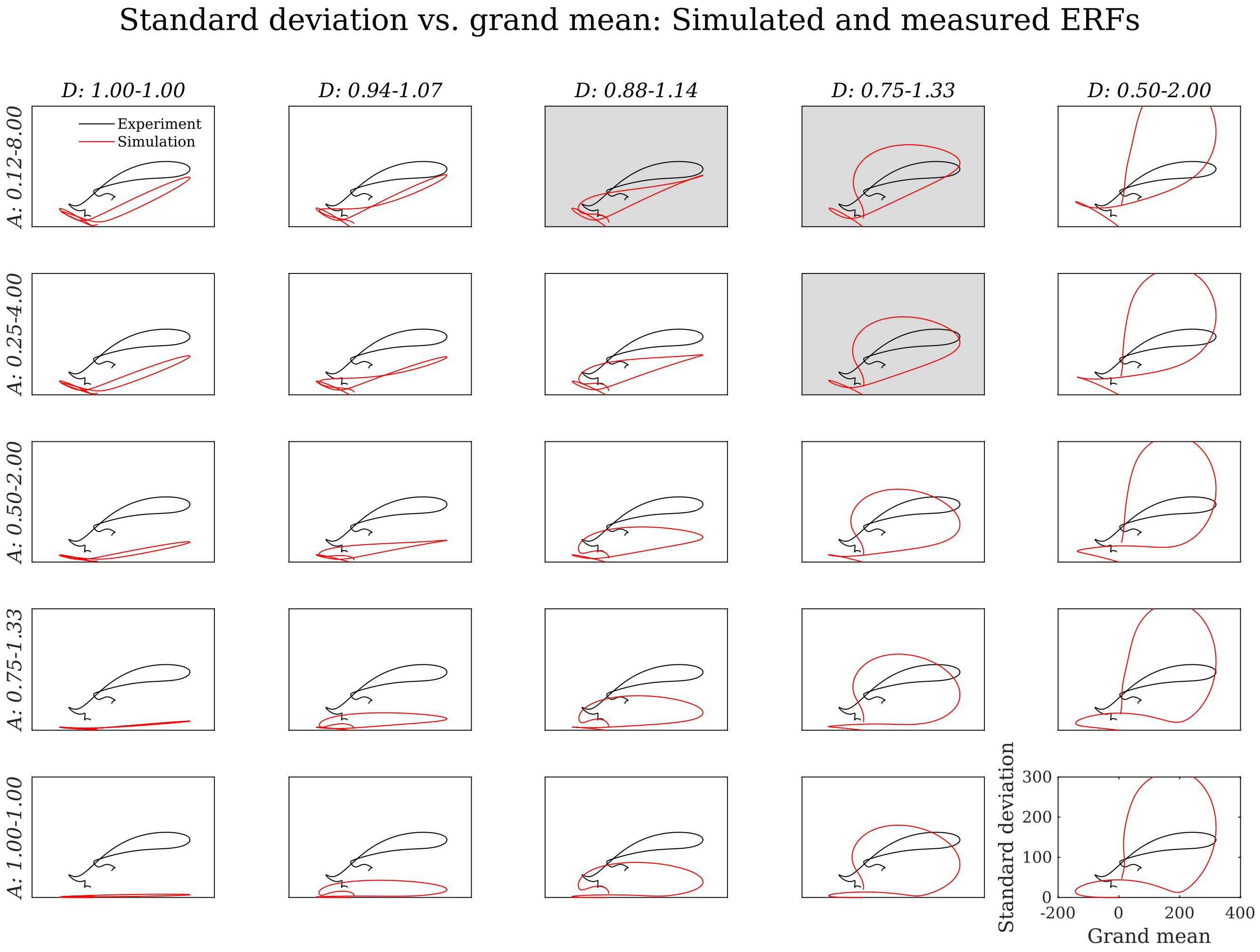

FIGURE 6 Standard deviation versus grand mean: Comparison of simulated and measured ERFs. The experimental data are represented by the black curve, which is replotted in each panel. The simulated data are in red and it represents the 25 combinations of the variation ranges of the dynamical parameters *D* (abscissa) and anatomical parameters *A* (ordinate). The width of the *D*-ranges increases from left to right, and the width of the *A*-ranges increases from bottom to top. The three best matches between simulations and experiment (based on the root-mean-square differences) are highlighted, and they all display heteroscedastic behavior. These best matches coincide with those shown in Figure 5, and they confirm that the cross-subject variation of the ERF is due to a combination of subject-specific cortical anatomy and subject-specific cortical dynamics. The single-subject ERFs measured in the MEG experiments are shown in Figure 3a. A subset of the waveforms corresponding to the top panel in the fourth column is shown in Figure 3d

a fine resolution. The default parameter values were chosen such that the model replicated a typical ERF. We then introduced variations to both sets of parameter values to generate subject specificity. The simulations thus included 25 sets of ERFs resulting from different combinations of anatomical and dynamical parameter variations. Each set represented the ERFs measured from a subject group, with each individual ERF representing the ERF of a single subject.

The data were analyzed in two ways. First, we considered characteristic quantities of the N1m response, namely its peak amplitude, peak latency, and waveform width. The N1m was chosen for this analysis because it tends to be a landmark response in most subjects, reaching higher peaks than the other ERF responses. On each of these measures, the experimental data reached a best match with the simulations in which both anatomical and dynamical parameters were varied. Second, we considered the arithmetic mean plotted against the corresponding standard deviation. In simulations, these plots took on a wide variety of shapes, ranging from wide circular orbits to linear-like behavior. Again, we found that the best match between simulations and experiment occurred for the simulations where both the anatomical and dynamical parameters are varied. Furthermore, the variation ranges for the best matches agreed well with each other across the different analyses (compare Figure 5d with Figure 6). In all our comparisons, the experimental results deviated considerably from the predictions at the extremes, whereby either anatomical factors or dynamical factors alone would explain the subject-specificity of the ERF. Overall, our results agree—unsurprisingly—with the well-established notion that individual subjects have individual cortical gross anatomies. Importantly, they indicate that subjects display cortical dynamics, which is specific to the subject.

We emphasize that our approach relies on analyzing population data and that we are drawing conclusions on subject-specificity on the basis of population data. While this allows us to conclude that both the gross anatomy and the cortical dynamics are subject-specific, it does not, however, permit us to say much about particular individual subjects. For example, our method cannot be used to pinpoint the origin of ERF differences between two subjects, because the number of data points would be too low.

4.2 | N1m-peak latency as an index of group differences in auditory function

On a general level, one might expect that dynamical variation of AC has perceptual consequences. For example, in our model, this variation was brought about by changing the connection strengths between the cortical columns. Connection strengths are fundamental to information processing in that they determine how a stimulus representation is mapped from one stage of processing to the next. Our results suggest that the peak latency of the N1m is a good indicator of cross-subject dynamical variations because it is weakly influenced by anatomy. In contrast, the N1m-peak amplitude is a less sensitive indicator because it is influenced both by dynamical and anatomical variation. Thus, on the group level, it is to be expected that latency should correlate better than amplitude with perception as measured in psychoacoustic experiments, and latency variance should correlate with variance of perception. Indirect evidence suggests that this is indeed the case.

First, the transient sound detection response reported by Mäkinen et al. (2004) and Tiitinen et al. (2005) is an ERF response elicited by long-duration sounds that slowly (over hundreds of milliseconds to seconds) increase in intensity from an imperceptible to a clearly perceptible level. During such looming sound stimulation there emerges a response that is like the N1m in terms of its morphology, polarity, width, and source location in the AC. Furthermore, the timing of the response militates against a fixed-amplitude threshold model, which is also the case with the N1m (Biermann & Heil, 2000). Importantly, the peak latency of this N1m-like response predicts extremely well the behavioral reaction time (RT) indicating sound detection. On the group level, subjects with a short RT display the sound detection response at an earlier latency than subjects with a long RT. Also, the variance in the peak latency of the response is correlated with the variance of the RT.

Second, subjects with musical training tend to produce ERFs that differ from those produced by nonmusicians. Amemiya et al. (2014) presented short melodies to subjects and measured the N1m response elicited by the final tone. They found that musicians have shorter right-hemispheric N1m latencies than nonmusicians. There was no difference in the N1m-peak amplitude between the groups, and the P2m was also unaffected by musical training. The behavioral task was to report on the sense of completeness of the melody. No differences were found between musicians and nonmusicians in this relatively nondemanding task. Similarly, Kuriki et al. (2006) reported that musical training resulted in shorter peak latencies of the N1m, but that the peak latencies of the P1m and P2m were unaffected. Further, Park et al. (2018) found that musicians, compared to nonmusicians, produced N1m responses of shorter peak latency but similar peak amplitude. Interestingly, multiplications of Heschl's gyrus are much more common in musicians (in 90% of the cases, Benner et al., 2017) than in the general population (Marie et al., 2015). Therefore, it seems that both the dynamics and gross anatomy of auditory cortex are changed by musical training.

Further evidence for event-related responses reflecting dynamical variations might be found by looking at the effect of perceptual learning. In this case, the gross anatomy remains unchanged, but cortex undergoes functional changes due to synaptic plasticity (for a review, see Weinberger, 2015). Based on the current results, perceptual learning should be reflected in the group mean of the latency, and/or in the variance of the latency. In line with this, Reincke et al. (2003) found that the N1 and P2 latency shifted earlier and the P2 amplitude became larger when subjects learned to discriminate vowels. This should be contrasted with the results of Tremblay et al. (2001) and Tremblay and Kraus (2002), who found learning to discriminate consonant-vowel syllables was reflected in N1 and P2 amplitudes rather than in their latency. However, the analyses of the above studies were carried out for group means only, and the latency variance was not addressed at the single-subject level.

In sum, previous studies indicate that the latency with which the auditory cortex reaches peak activity in an N1m-like response is a good predictor of sound detection. Further, musical training and perceptual learning affects the aspect of the ERF—the N1m latency—which we suggest is the sensitive indicator of dynamical variation in AC. Also, latency seems to be a consistent indicator of musical training, whereas the N1m amplitude is less so. Thus, the N1m latency appears to be functionally meaningful, reflecting perception and learning. Our results presented in Figures 3–5 explain why this should be the case: variations in cortical dynamics show up in the N1m latency, whereas the amplitude of N1m represents a mixture of dynamical and anatomical effects, which can cancel each other out.

4.3 | On the usefulness of the grand mean of ERF waveforms

The current findings give us pause to consider the usefulness of grand means in ERF research. Grand-averaging the ERF waveform is a continuation of averaging single trial responses. It is rooted in the idea of noise cancelation and in the notion that there is a true population response buried in the noise carried by each single-subject measurement. This practice can be criticized from several viewpoints. First, it almost always relies on arithmetic averaging, which is the convention in ERF research. Arithmetic averaging is based on the assumption of the so-called additive model whereby one response differs from another by a constant. Whereas this assumption is appropriate for single trials (König et al., 2015), the additive model does not apply when computing the grand mean across trial-averaged waveforms. This is because ERFs of individual subjects do not differ from each other by amounts but, rather, they differ predominantly by factors, and follow the so-called mixed model. Therefore, the use of arithmetic averaging is not recommended for comparing the grand mean of ERFs across stimuli or conditions; instead geometric grand-averaging—or, more precisely, arithmetic averaging of the asinh-transformed data—should be used (König et al., 2015; Matysiak et al., 2013). Further, the test–retest reliability of event-related responses of individual subjects is high, meaning that single-trial averaging is successful in removing noise and revealing a response that is stable. These results taken together with the findings of the current study imply that response stability emanates from an unchanging gross anatomy of each subject and from the cortical dynamics of each subject remaining stable. That is, each subject does not introduce noise that should be removed through further cross-subject averaging. If cross-subject variation of ERFs reflected individual gross anatomies only, then, geometric grand-averaging might arguably produce a waveform that represented the true dynamics of the brain, undistorted by measurement noise. However, as the ERF of each subject emerges from the subject-specificity of both gross anatomy and dynamics, it is unclear what the grand mean represents. It blurs the waveforms of individual subjects, and it is unlikely to represent a response produced by average dynamics in an average gross anatomy, even assuming that such notions are useful and can be defined. Therefore, when using grand-averaging, one must ensure that the end justifies the means. We used arithmetic averaging (see Figure 3) to investigate the origin of the subject-specificity of ERFs. If the focus is on differences between groups or experimental conditions, then, geometric averaging or the arithmetic averaging of asinh-transformed waveforms should be employed.

4.4 | Outlook

Our current modeling approach is, to our knowledge, unique for two reasons. First, we are including a description of the entire AC, as opposed to concentrating on a specific cortical field (e.g., A1). As described in our previous study (Hajizadeh et al., 2019), this allows us to characterize the ERF as a holistic waveform being generated by the entire system of the AC, rather than as a series of responses—P1m, N1m, and P2m—with dedicated, spatially constrained generator processes. Second, we are interested in describing subject-specific dynamics and subject-specific anatomical effects on the generation of the auditory ERF, and how these are reflected in group statistics and grand-averaged responses. These strengths should be juxtaposed with the simplifications of the model: For example, it is based on the anatomy of the macaque monkey AC and gross anatomy is modeled as a set of random variables. These simplifications might be seen as springboards for further development, given elasticity by the strengths of our approach. The anatomy of the human auditory cortex is at present unknown in the detail of the macaque monkey (Baumann et al., 2013; Besle et al., 2019; Norman-Haignere et al., 2019). We are not certain how many fields the human AC has and what the connection patterns between the fields are. In contrast, the gross anatomy of subjects is accessible through high-resolution MRI imaging (Moerel et al., 2014). It might be possible to adapt our approach to assist in the mapping of the cortical fields of human AC. This could involve constructing forward models, with multiple MEG sensor locations, on the basis of actual subject-specific cortical topographies. It should be possible to project various field constellations onto these topographies to model the ERF. This might allow one to find the best fits between simulation and experiment in terms of number of fields and general connection patterns between fields, with the constraint that these features are shared across subjects.

Although the current model includes multiple feedback pathways, it is dynamically driven by the afferent input. Looking beyond the auditory cortex, we suspect that the auditory cortex might function as a forum where oscillations driven by the bottom-up sensory input mix with oscillations driven by top-down internal models generated beyond the parabelt. This could be one of the ways that the cognitive auditory cortex (Scheich et al., 2007) manifests itself dynamically and where the top-down-driven oscillations function as filters for the oscillations driven by the afferent input (Morillon & Schroeder, 2015) or vice versa. Thus, the approach of the current study might be extended to examine the auditory ERF—and therefore, the functioning of auditory cortex—in terms of this mixing of these two kinds of oscillations.

ACKNOWLEDGMENT

Open Access funding enabled and organized by ProjektDEAL. WOA Institution: Leibniz-Institut fur Neurobiologie Blended DEAL : ProjektDEAL.

CONFLICT OF INTEREST

The authors have no conflict of interest to declare.

AUTHOR CONTRIBUTIONS

Aida Hajizadeh: Conceptualization; Data curation; Formal analysis; Investigation; Methodology; Software; Validation; Visualization; Writing-original draft; Writing-review & editing. **Artur Matysiak:** Conceptualization; Data curation; Formal analysis; Investigation; Methodology; Software; Validation; Visualization; Writing-review & editing. **André Brechmann:** Conceptualization; Investigation; Methodology; Resources; Writing-review & editing. **Reinhard König:** Conceptualization; Data curation; Funding acquisition; Investigation; Methodology; Project administration; Resources; Supervision; Writing-review & editing. **Patrick J. C. May:** Conceptualization; Funding acquisition; Investigation; Methodology; Project administration; Supervision; Writing-review & editing.

ORCID

Artur Matysiak https://orcid.org/0000-0002-1395-8520

REFERENCES

Ahonen, L., Huotilainen, M., & Brattico, E. (2016). Within- and between-session replicability of cognitive brain processes: An MEG study with an N-back task. *Physiology & Behavior*, *158*, 43–53. https://doi.org/10.1016/j.physbeh.2016.02.006

Amemiya, K., Karino, S., Ishizu, T., Yumoto, M., & Yamasoba, T. (2014). Distinct neural mechanisms of tonal processing between musicians and non-musicians. *Clinical Neurophysiology*, *125*, 738–747. https://doi.org/10.1016/j.clinph.2013.09.027

Atcherson, S. R., Gould, H. J., Pousson, M. A., & Prout, T. M. (2006). Long-term stability of N1 sources using low-resolution electromagnetic tomography. *Brain Topography*, *19*, 11–20. https://doi.org/10.1007/s10548-006-0008-8

Baumann, S., Petkov, C. I., & Griffiths, T. D. (2013). A unified framework for the organization of the primate auditory cortex. *Frontiers in Systems Neuroscience*, *7*, 11. https://doi.org/10.3389/fnsys.2013.00011

Benner, J., Wengenroth, M., Reinhardt, J., Stippich, C., Schneider, P., & Blatow, M. (2017). Prevalence and function of Heschl's gyrus morphotypes in musicians. *Brain Structure & Function*, *222*, 3587–3603. https://doi.org/10.1007/s00429-017-1419-x

Besle, J., Mougin, O., Sánchez-Panchuelo, R.-M., Lanting, C., Gowland, P., Bowtell, R., Francis, S., & Krumbholz, K. (2019). Is human auditory cortex organization compatible with the monkey model? Contrary evidence from ultra-high-field functional and structural MRI. *Cerebral Cortex*, *29*, 410–428. https://doi.org/10.1093/cercor/bhy267

Biermann, S., & Heil, P. (2000). Parallels between timing of onset responses of single neurons in cat and of evoked magnetic fields in human auditory cortex. *Journal of Neurophysiology*, *84*, 2426–2439. https://doi.org/10.1152/jn.2000.84.5.2426

Brody, D. A., Terry, F. H., & Ideker, R. E. (1973). Eccentric dipole in a spherical medium: Generalized expression for surface potentials. *IEEE Transactions on Biomedical Engineering*, *20*, 141–143. https://doi.org/10.1109/TBME.1973.324177

Brosch, M., & Schreiner, C. E. (1997). Time course of forward masking tuning curves in cat primary auditory cortex. *Journal of Neurophysiology*, *77*, 923–943. https://doi.org/10.1152/jn.1997.77.2.923

Brosch, M., & Schreiner, C. E. (2000). Sequence sensitivity of neurons in cat primary auditory cortex. *Cerebral Cortex*, *10*, 1155–1167. https://doi.org/10.1093/cercor/10.12.1155

Dalebout, S. D., & Robey, R. R. (1997). Comparison of the intersubject and intrasubject variability of exogenous and endogenous auditory evoked potentials. *Journal of the American Academy of Audiology*, *8*(5), 342–354.

Efron, B. (1979). Bootstrap methods: Another look at the jackknife. *The Annals of Statistics*, *7*, 1–26. https://doi.org/10.1214/aos/1176344552

Fischl, B., Rajendran, N., Busa, E., Augustinack, J., Hinds, O., Yeo, B. T. T., Mohlberg, H., Amunts, K., & Zilles, K. (2008). Cortical folding patterns and predicting cytoarchitecture. *Cerebral Cortex*, *18*, 1973–1980. https://doi.org/10.1093/cercor/bhm225

Hackett, T. A., de la Mothe, L. A., Camalier, C. R., Falchier, A., Lakatos, P., Kajikawa, Y., & Schroeder, C. E. (2014). Feedforward and feedback projections of caudal belt and parabelt areas of auditory cortex: Refining the hierarchical model. *Frontiers in Neuroscience*, *8*, 72. https://doi.org/10.3389/fnins.2014.00072

Hajizadeh, A., Matysiak, A., May, P., & König, R. (2019). Explaining event-related fields by a mechanistic model encapsulating the anatomical structure of auditory cortex. *Biological Cybernetics*, *113*, 321–345. https://doi.org/10.1007/s00422-019-00795-9

Hämäläinen, M., Hari, R., Ilmoniemi, R. J., Knuutila, J., & Lounasmaa, O. V. (1993). Magnetoence-phalography—Theory, instrumentation, and applications to non-invasive studies of the working human brain. *Reviews of Modern Physics*, *65*, 413–497. https://doi.org/10.1103/RevModPhys.65.413

Heschl, R. L. (1878). *Über die vordere quere Schläfenwindung des menschlichen Großhirns*, Braumüller.

Hopfield, J. J., & Tank, D. W. (1986). Computing with neural circuits: A model. *Science*, *233*, 625–633. https://doi.org/10.1126/science.3755256

Kaas, J. H., & Hackett, T. A. (2000). Subdivisions of auditory cortex and processing streams in primates. *Proceedings of the National Academy of Sciences of the United States of America*, *97*, 11793–11799. https://doi.org/10.1073/pnas.97.22.11793

König, R., Matysiak, A., Kordecki, W., Sielużycki, C., Zacharias, N., & Heil, P. (2015). Averaging auditory evoked magnetoencephalographic and electroencephalographic responses: A critical discussion. *The European Journal of Neuroscience*, *41*, 631–640. https://doi.org/10.1111/ejn.12833

Kuriki, S., Kanda, S., & Hirata, Y. (2006). Effects of musical experience on different components of MEG responses elicited by sequential piano-tones and chords. *The Journal of Neuroscience*, *26*, 4046–4053. https://doi.org/10.1523/JNEUROSCI.3907-05.2006

Loebel, A., Nelken, I., & Tsodyks, M. (2007). Processing of sounds by population spikes in a model of primary auditory cortex. *Frontiers in Neuroscience*, *1*, 197–209. https://doi.org/10.3389/neuro.01.1.1.015.2007

Lü, Z. L., Williamson, S. J., & Kaufman, L. (1992). Human auditory primary and association cortex have differing lifetimes for activation traces. *Brain Research*, *572*, 236–241. https://doi.org/10.1016/0006-8993(92)90475-o

Mäkinen, V., May, P., & Tiitinen, H. (2004). Transient brain responses predict the temporal dynamics of sound detection in humans. *NeuroImage*, *21*, 701–706. https://doi.org/10.1016/j.neuroimage.2003.10.009

Marie, D., Jobard, G., Crivello, F., Perchey, G., Petit, L., Mellet, E., Joliot, M., Zago, L., Mazoyer, B., & Tzourio-Mazoyer, N. (2015). Descriptive anatomy of Heschl's gyri in 430 healthy volunteers, including 198 left-handers. *Brain Structure & Function*, *220*, 729–743. https://doi.org/10.1007/s00429-013-0680-x

Matysiak, A., Kordecki, W., Sielużycki, C., Zacharias, N., Heil, P., & König, R. (2013). Variance stabilization for computing and comparing grand mean waveforms in MEG and EEG. *Psychophysiology*, *50*, 627–639. https://doi.org/10.1111/psyp.12047

May, P. J., & Tiitinen, H. (2010). Mismatch negativity (MMN), the deviance-elicited auditory deflection, explained. *Psychophysiology*, *47*, 66–122. https://doi.org/10.1111/j.1469-8986.2009.00856.x

May, P. J., & Tiitinen, H. (2013). Temporal binding of sound emerges out of anatomical structure and synaptic dynamics of auditory cortex. *Frontiers in Computational Neuroscience*, *7*, 152. https://doi.org/10.3389/fncom.2013.00152

May, P. J., Westö, J., & Tiitinen, H. (2015). Computational modelling suggests that temporal integration results from synaptic adaptation in auditory cortex. *The European Journal of Neuroscience*, *41*, 615–630. https://doi.org/10.1111/ejn.12820

McEvoy, L., Levänen, S., & Loveless, N. (1997). Temporal characteristics of auditory sensory memory: Neuromagnetic evidence. *Psychophysiology*, *34*, 308–316. https://doi.org/10.1111/j.1469-8986.1997.tb02401.x

Michalewski, H. J., Prasher, D. K., & Starr, A. (1986). Latency variability and temporal interrelationships of the auditory event-related potentials (N1, P2, N2, and P3) in normal subjects. *Electroencephalography and Clinical Neurophysiology*, *65*, 59–71. https://doi.org/10.1016/0168-5597(86)90037-7

Moerel, M., De Martino, F., & Formisano, E. (2014). An anatomical and functional topography of human auditory cortical areas. *Frontiers in Neuroscience*, *8*, 225. https://doi.org/10.3389/fnins.2014.00225

Morillon, B., & Schroeder, C. E. (2015). Neuronal oscillations as a mechanistic substrate of auditory temporal prediction. *Annals of the New York Academy of Sciences*, *1337*, 26–31. https://doi.org/10.1111/nyas.12629

Morosan, P., Rademacher, J., Schleicher, A., Amunts, K., Schormann, T., & Zilles, K. (2001). Human primary auditory cortex: Cytoarchitectonic subdivisions and mapping into a spatial reference system. *NeuroImage*, *13*, 684–701. https://doi.org/10.1006/nimg.2000.0715

Mosher, J. C., Leahy, R. M., & Lewis, P. S. (1999). EEG and MEG: Forward solutions for inverse methods. *IEEE Transactions on Bio-Medical Engineering*, *46*, 245–259. https://doi.org/10.1109/10.748978

Näätänen, R. (1992). *Attention and brain function*, : . Lawrence Erlbaum Associates.

Norman-Haignere, S. V., Kanwisher, N., McDermott, J. H., & Conway, B. R. (2019). Divergence in the functional organization of human and macaque auditory cortex revealed by fMRI responses to harmonic tones. *Nature Neuroscience*, *22*, 1057–1060. https://doi.org/10.1038/s41593-019-0410-7

Park, J. M., Chung, C. K., Kim, J. S., Lee, K. M., Seol, J., & Yi, S. W. (2018). Musical expectations enhance auditory cortical processing in musicians: A magnetoencephalography study. *Neuroscience*, *369*, 325–335. https://doi.org/10.1016/j.neuroscience.2017.11.036

Rademacher, J., Morosan, P., Schleicher, A., Freund, H. J., & Zilles, K. (2001). Human primary auditory cortex in women and men. *NeuroReport*, *12*, 1561–1565. https://doi.org/10.1097/00001756-200106130-00010

Reinke, K. S., He, Y., Wang, C., & Alain, C. (2003). Perceptual learning modulates sensory evoked response during vowel segregation. *Cognitive Brain Research*, *17*, 781–791. https://doi.org/10.1016/s0926-6410(03)00202-7

Sandman, C. A., & Patterson, J. V. (2000). The auditory event-related potential is a stable and reliable measure in elderly subjects over a 3-year period. *Clinical Neurophysiology*, *111*, 1427–1437. https://doi.org/10.1016/s1388-2457(00)00320-5

Sarvas, J. (1987). Basic mathematical and electromagnetic concepts of the biomagnetic inverse problem. *Physics in Medicine and Biology*, *32*, 11–22. https://doi.org/10.1088/0031-9155/32/1/004

Scheich, H., Brechmann, A., Brosch, M., Budinger, E., & Ohl, F. W. (2007). The cognitive auditory cortex: Task-specificity of stimulus representations. *Hearing Research*, *229*, 213–224. https://doi.org/10.1016/j.heares.2007.01.025

Segalowitz, S. J., & Barnes, K. L. (1993). The reliability of ERP components in the auditory oddball paradigm. *Psychophysiology*, *30*, 451–459. https://doi.org/10.1111/j.1469-8986.1993.tb02068.x

Shaw, M. E., Hämäläinen, M. S., & Gutschalk, A. (2013). How anatomical asymmetry of human auditory cortex can lead to a rightward bias in auditory evoked fields. *NeuroImage*, *74*, 22–29. https://doi.org/10.1016/j.neuroimage.2013.02.002

Swain, M. J., & Ballard, D. H. (1991). Color indexing. *International Journal of Computer Vision*, *7*, 11–32. https://doi.org/10.1007/BF00130487

Tiitinen, H., Mäkinen, V. T., Kicić, D., & May, P. J. (2005). Averaged and single-trial brain responses in the assessment of human sound detection. *NeuroReport*, *16*, 545–548. https://doi.org/10.1097/00001756-200504250-00005

Tremblay, K. L., & Kraus, N. (2002). Auditory training induces asymmetrical changes in cortical neural activity. *Journal of Speech, Language, and Hearing Research*, *45*, 564–572. https://doi.org/10.1044/1092-4388(2002/045)

Tremblay, K., Kraus, N., McGee, T., Ponton, C., & Otis, B. (2001). Central auditory plasticity: Changes in the N1–P2 complex after speech-sound training. *Ear and Hearing*, *22*, 79–90. https://doi.org/10.1097/00003446-200104000-00001

von Economo, C., & Horn, L. (1930). Über Windungsrelief, Maße und Rindenarchitektonik der Supratemporalfläche, ihre individuellen und ihre Seitenunterschiede. *Zeitschrift für die gesamte Neurologie und Psychiatrie*, *130*, 678–757. https://doi.org/10.1007/BF02865945

Weinberger, N. M. (2015). New perspectives on the auditory cortex: Learning and memory. *Handbook of Clinical Neurology*, *129*, 117–147. https://doi.org/10.1016/B978-0-444-62630-1.00007-X

Westö, J., May, P. J., & Tiitinen, H. (2016). Memory stacking in hierarchical networks. *Neural Computation*, *28*, 327–353. https://doi.org/10.1162/NECO_a_00803

Williamson, S. J., & Kaufman, L. (1981). Biomagnetism. *Journal of Magnetism and Magnetic Materials*, *22*, 129–201. https://doi.org/10.1016/0304-8853(81)90078-0

Wilson, H. R., & Cowan, J. D. (1972). Excitatory and inhibitory interactions in localized populations of model neurons. *Biophysical Journal*, *12*, 1–24. https://doi.org/10.1016/S0006-3495(72)86068-5

Zacharias, N., König, R., & Heil, P. (2012). Stimulation-history effects on the M100 revealed by its differential dependence on the stimulus onset interval. *Psychophysiology*, *49*, 909–919. https://doi.org/10.1111/j.1469-8986.2012.01370.x

Zhang, Z. (1995). A fast method to compute surface potentials generated by dipoles within multilayer anisotropic spheres. *Physics in Medicine and Biology*, *40*, 335–349. https://doi.org/10.1088/0031-9155/40/3/001

How to cite this article: Hajizadeh A, Matysiak A, Brechmann A, König R, May PJC. Why do humans have unique auditory event-related fields? Evidence from computational modeling and MEG experiments. *Psychophysiology*. 2021;58:e13769. https://doi.org/10.1111/psyp.13769

Chapter 7

Auditory cortex modelled as a dynamical network of oscillators: understanding event-related fields and their adaptation

Biological Cybernetics
https://doi.org/10.1007/s00422-022-00936-7

Biological Cybernetics

ORIGINAL ARTICLE

Auditory cortex modelled as a dynamical network of oscillators: understanding event-related fields and their adaptation

Aida Hajizadeh[1] · Artur Matysiak[1] · Matthias Wolfrum[2] · Patrick J. C. May[1,3] · Reinhard König[1]

Received: 1 July 2021 / Accepted: 7 May 2022
© The Author(s) 2022

Abstract

Adaptation, the reduction of neuronal responses by repetitive stimulation, is a ubiquitous feature of auditory cortex (AC). It is not clear what causes adaptation, but short-term synaptic depression (STSD) is a potential candidate for the underlying mechanism. In such a case, adaptation can be directly linked with the way AC produces context-sensitive responses such as mismatch negativity and stimulus-specific adaptation observed on the single-unit level. We examined this hypothesis via a computational model based on AC anatomy, which includes serially connected core, belt, and parabelt areas. The model replicates the event-related field (ERF) of the magnetoencephalogram as well as ERF adaptation. The model dynamics are described by excitatory and inhibitory state variables of cell populations, with the excitatory connections modulated by STSD. We analysed the system dynamics by linearising the firing rates and solving the STSD equation using time-scale separation. This allows for characterisation of AC dynamics as a superposition of damped harmonic oscillators, so-called normal modes. We show that repetition suppression of the N1m is due to a mixture of causes, with stimulus repetition modifying both the amplitudes and the frequencies of the normal modes. In this view, adaptation results from a complete reorganisation of AC dynamics rather than a reduction of activity in discrete sources. Further, both the network structure and the balance between excitation and inhibition contribute significantly to the rate with which AC recovers from adaptation. This lifetime of adaptation is longer in the belt and parabelt than in the core area, despite the time constants of STSD being spatially homogeneous. Finally, we critically evaluate the use of a single exponential function to describe recovery from adaptation.

Keywords Auditory cortex · Event-related field · Adaptation · Synaptic depression · Normal modes · Slow-fast dynamics

1 Introduction

Most sounds, speech sounds in particular, make sense only when perceived against the backdrop of what came immediately before, in a time window extending some seconds into the past—the so-called psychological present (Michon 1978). The task of the auditory system is to retain information and to integrate it with representations of incoming stimuli. This process of memory and integration is likely to occur in auditory cortex, whereas the subcortical auditory pathway carries out the analysis of spectral structure and sound source localisation (Nelken 2004). While our understanding of the functioning of auditory cortex is limited, especially in comparison to that of the visual cortex (King and Nelken 2009), a number of memory phenomena have been identified in auditory cortex that operate on the time scale of

---

Communicated by Jan Benda.

Patrick J. C. May and Reinhard König shared last authorship

Aida Hajizadeh
aida.hajizadeh@lin-magdeburg.de

Artur Matysiak
artur.matysiak@lin-magdeburg.de

Matthias Wolfrum
matthias.wolfrum@wias-berlin.de

Patrick J. C. May
p.may1@lancaster.ac.uk

Reinhard König
reinhard.koenig@lin-magdeburg.de

[1] Research Group Comparative Neuroscience, Leibniz Institute for Neurobiology, Brenneckestraße 6, 39118 Magdeburg, Germany

[2] Weierstrass Institute for Applied Analysis and Stochastics, Mohrenstraße 39, 10117 Berlin, Germany

[3] Department of Psychology, Lancaster University, Lancaster LA1 4YF, UK

Published online: 20 June 2022

hundreds of milliseconds to seconds. As reviewed below, these include context-sensitivity: the dependence of a neuronal response not just on the eliciting stimulus but also on preceding stimuli—the historical context. Further, the memory phenomena observed in the physiological responses of auditory cortex have been linked to behaviourally measured sensory memory (Tiitinen et al. 1994) and working memory (Brechmann et al. 2007; Huang et al. 2016).

The simplest form of context sensitivity can be observed by repeating the stimulus within a time window on the order of seconds. The repeated stimulus elicits an auditory response with a reduced amplitude, with the reduction tending to be inversely related to the stimulus onset interval (SOI). This phenomenon is called adaptation, and it is also known as repetition suppression or habituation (Megela and Teyler 1979; Pérez-González and Malmierca 2014). Adaptation is observed in both non-invasive and invasive measurements. When adaptation does not generalise to all stimuli, a neuron can produce a large-magnitude response to a stimulus that is different from the repeated one. This is known as stimulus-specific adaptation (SSA), a phenomenon seen in the primary auditory cortex of animal models (Ulanovsky et al. 2003, 2004). In magnetoencephalography (MEG) and electroencephalography (EEG) measurements in humans, adaptation manifests itself most clearly in variations of the most prominent auditory evoked response, the N1m or N1, respectively. Here, we use N1(m) to denote both the MEG and EEG variety of the response. Several studies have shown that the peak amplitude of the N1(m) attenuates with stimulus repetition and is inversely related to stimulation rate (see, for example, Davis et al. 1966; Hari et al. 1982; Imada et al. 1997; Ioannides et al. 2003; Loveless et al. 1996; Lü et al. 1992; Lu et al. 1992; McEvoy et al. 1997; Megela and Teyler 1979; Nelson et al. 1969; Sable et al. 2004; Wang et al. 2008; Zacharias et al. 2012). Further, this adaptation develops rapidly in that already the second stimulus elicits a diminished response (e.g., Budd et al. 1998; May and Tiitinen 2004; Rosburg et al. 2010). The monotonic increase of the N1(m) amplitude as a function of SOI which then plateaus out at large SOI ($>$5 s) can be approximated with an exponentially saturating function. The time constant of this function provides an estimate of the time span it takes for the auditory system to recover from adaptation (Lü et al. 1992; Lu et al. 1992). The picture becomes complicated when short SOIs of under 500 ms are used. In this case, the SOI dependence of the N1(m) amplitude can take on a non-monotonic v-shape (Budd and Michie 1994; Wang et al. 2008; Zacharias et al. 2012), and the rapid presentation of tones elicits a sustained response upon which the diminished N1(m) responses ride (May and Tiitinen 2004, 2010).

Adaptation due to stimulus repetition can be found in all parts of the auditory system. It tends to have a shorter recovery time subcortically than in cortex, especially in the lemniscal pathway (for a review, see, Pérez-González and Malmierca 2014). For example, the auditory nerve recovers within 25-35 ms (Yates et al. 1983). In the superior olivary complex, both the onset and the recovery from adaptation have respective time constants of 20 ms and 106 ms (Finlayson and Adam 1997). Studies using relatively high stimulus rates of above 3 Hz have reported adaptation in the inferior colliculus (IC) (Palombi and Caspary 1996; Nuding et al. 1999). For the majority of units in the IC, SSA requires SOIs shorter than 250 ms (Pérez-González et al. 2005; Malmierca et al. 2009). However, Zhao et al. (2011) observed SSA in the IC even with a SOI of 1 s, although these authors were not able to determine whether the units were in the lemniscal or non-lemniscal pathway. The lemniscal division of the auditory thalamus shows SSA only with SOIs shorter than 250 ms, although SSA could be observed in the non-lemniscal thalamus even with SOIs of up to 2 s (Antunes et al. 2010). Neurons in auditory cortex display SSA with SOIs up to several seconds (Tasseh et al. 2011).

The most plausible mechanism underlying cortical adaptation is short-term synaptic depression, STSD (Wehr and Zador 2003, 2005), a form of synaptic plasticity based on vesicle depletion as well as inactivation of release sites and calcium channels (Fioravante and Regehr 2011). This type of plasticity has decay times of hundreds of milliseconds to several seconds, and this coincides with the time course of cortical adaptation (Ulanovsky et al. 2004). STSD is also present in subcortical stations (for a review, see, Friauf et al. 2015). STSD can contribute to efficient information transfer between two neurons (Benda et al. 2005; Salmasi et al. 2019), to temporal filtering occurring at synapses (Fortune and Rose 2001; Rosenbaum et al. 2012), and to gain control (Abbott et al. 1997). Also, recovery from STSD during communication pauses has been linked to maximising the effect of post-pause communication signals (Kohashi et al. 2021). Computational models show that STSD accounts for different forms of context sensitivity in the AC (Loebel et al. 2007; May and Tiitinen 2010; Mill et al. 2011; Wang and Knösche 2013; May and Tiitinen 2013; Yarden and Nelken 2017; Kudela et al. 2018). Further, simulations show that STSD can function as a memory mechanism that allows for the representation of temporally extended, complex auditory information such as speech and species-specific communication sounds (David and Shamma 2013; May and Tiitinen 2013; Motanis et al. 2018). In sum, rather than signifying mere neuronal fatigue, adaptation might instead reflect the fundamental dynamics of synaptic depression which endows the auditory cortex with the ability to represent auditory information across different time scales (Benda 2021).

Adaptation of the N1(m) has been linked to information processing in auditory cortex. The recovery time from adaptation is a subject-specific parameter, and it correlates well with the time span of working memory in a forced-choice discrimination task (Lü et al. 1992; Lu et al. 1992). Adaptation is also the major determinant in the evoked responses elicited in the oddball paradigm. Here, standard stimuli presented with a high rate elicit a smaller event-related field (ERF) response than the infrequent deviant stimuli (Butler 1968), and the difference in response amplitude is termed the mismatch negativity (MMN) (Näätänen et al. 1978). The mismatch response is brimming with functional significance: it might serve the orienting reflex, it is linked to a large number of memory and learning phenomena, and it is altered in several clinical conditions (for reviews, see, Näätänen 1990, 1992; May and Tiitinen 2010). Adaptation is likely to be at the root of the mismatch response both directly and indirectly. First, the differential between the deviant and standard response reflects the high and low level of adaptation of the N1(m) response elicited by the standards and deviants, respectively, due to their different presentation rates (Butler 1968; May et al. 1999; May and Tiitinen 2010). Further, May et al. (2015) used simulations of auditory cortex to show that short-term synaptic depression has multiple consequences: not only does it cause the adaptation of the response elicited by the frequently presented standards, but it could be the mechanism which integrates auditory information across time more generally. This integration shows up as context-sensitive single- and multi-unit responses to tone pairs (Brosch et al. 1999; Brosch and Schreiner 2000), and as mismatch responses in the ERF to deviations in tone-sequence structure (Näätänen et al. 1993). In this view, STSD not only underlies repetition suppression and the mismatch response, but it also allows the auditory cortex to represent complex, temporally-evolving sounds. Note that the adaptation-related explanation of the mismatch response (May and Tiitinen 2010; May et al. 2015) is only one alternative. Näätänen (1990, 1992) proposed that MMN is unrelated to adaptation of the evoked response, instead reflecting a process separate from that generating the N1(m). Also, the currently dominant predictive coding explanation suggests that repetition suppression is due to a top-down, inhibitory prediction signal matching the bottom-up sensory signal, and that the MMN is an indication of prediction error when the two signals do not match (Friston 2005; Bastos et al. 2012) (however, see, Rescorla 2021; May 2021).

Observing adaptation in the human brain generally requires the use of non-invasive techniques. MEG and EEG are well suited to this because they have a high temporal resolution of milliseconds, the time scale of neuronal responses. However, these methods have the drawback that it is difficult to identify the sources of the activity and their distribution. The response to a stimulus represents the simultaneous activation of around a million synapses on pyramidal cells forming an intricate network across auditory cortex, but what we observe is a spatial average of this activity (Hämäläinen et al. 1993). Therefore, MEG and EEG measurements in themselves reveal very little of the underlying neuronal dynamics. One way to move forward beyond observation is to use computational modelling. The aim of such modelling needs not be a faithful reproduction of the brain. Instead, modelling attempts to explain experimental observations by capturing the key mechanisms of the system under investigation. While no model should be required to duplicate the modelled system, a useful model is a device which reveals something about the system which would otherwise remain hidden, buried in the experimental data.

In our previous work (Hajizadeh et al. 2019, 2021), we sought to understand the generation of the event-related field in terms of a dynamical system with the spatial organisation of the auditory cortex (Kaas and Hackett 2000; Hackett et al. 2014). Our starting point was the model introduced by May and Tiitinen (2013) and May et al. (2015). This describes auditory cortex as a system of hundreds of units representing cortical columns, distributed across multiple fields in the core, belt, and parabelt areas. Synaptic strengths are dynamically modulated by STSD so that the interactions between the units become dependent not only on the current stimulus but also on the stimulation history. As explained above, this model captures the phenomenology of context sensitivity of auditory responses. However, it is highly non-linear and analytically impenetrable, and can only be studied one simulated trajectory at a time. Therefore, in Hajizadeh et al. (2019), we made the original model tractable by assuming that the input-output relationship of the model unit is linear and by using fixed connection strengths thereby ignoring the effects of STSD. This allowed us to study the explicit solutions of the dynamical equations of the model and to characterise the system in terms of its oscillatory properties. In this view, while the cortical column is the system's structural unit, the dynamical building block is the normal mode: a damped harmonic oscillator emerging out of coupled excitation and inhibition.

The approach in Hajizadeh et al. (2019), which we also adopt here, is not just to replicate the ERF so as to explain it in terms of parameter dependencies. Rather, we are exploring and interpreting ERF generation in the context of a fundamentally new view on AC activity: First, auditory cortex behaves as a set of independent oscillators—normal modes—each characterised by a specific frequency, decay rate, and spatial profile. These oscillators do not reside in any one unit of auditory cortex but, rather, each oscillator is spread across the whole auditory cortex. Conversely, the activity of each unit is a weighted superposition of all the normal modes of the system. Second, the neural activity observed at the local level of individual columns as well as that observed on the global level as the ERF are both explicitly dependent on the anatomical structure of the entire AC. Third, the spatiotemporal pattern of the cortically generated ERF represents a superposition of all the oscillating normal modes. The

ERF in the normal-mode picture is therefore fundamentally a system property of the *whole AC*. In a sense, this interpretation is an alternative to the classical equivalent-current dipole (ECD) description of discrete (see, for example, Scherg 1990; Mosher et al. 1992; Scherg and Berg 1996) and distributed (see, for example, Dale and Sereno 1993; Hämäläinen and Ilmoniemi 1994; Mosher and Leahy 1999) source modelling approaches in which ERFs are considered to arise from a linear sum of *multiple spatially distributed point-like sources (ECDs)*. The magnetic fields generated by ECDs are determined by the physics of electromagnetic fields described by the quasi-static Maxwell's equations. Importantly, the ECD approach does not account for the dynamical interaction between the sources but instead limits the explanation to which location is active at any time point. The normal-mode approach, however, lays emphasis on the ERF as an emergent property of the systems dynamics of the entire auditory cortex. In this normal-mode view, adaptation is the result of a complete reorganisation of AC dynamics rather than of a reduction of activity in discrete sources. From this point of view, the spatially distributed normal mode is an even more fundamental building block of the ERF than the individual source.

The aim of the current study is to understand adaptation of the ERF. Building on our previous work presented in Hajizadeh et al. (2019), May and Tiitinen (2013), and May et al. (2015), we focus on this issue by extending normal mode analysis when the stimulus is repeated. To this end, we first provide general solutions to the state equations of the model, without the constraints that were necessary in our previous study (Hajizadeh et al. 2019). This allows us to reintroduce short-term synaptic depression into the model and to probe its adaptation behaviour when stimuli are presented at different repetition rates. Comparisons of model simulations with experimental MEG data are made. We go beyond describing adaptation of ERFs merely as an attenuation of the ERF response amplitude. Instead, we describe how the normal modes of the network dynamics, that is, the dynamics of the entire auditory cortex, changes as a result of stimulus repetition. Further, we investigate how adaptation lifetime depends on other factors than the dynamics of synaptic depression, namely gross anatomical structure and the balance between excitation and inhibition.

2 Unfurling the model of auditory cortex

2.1 Model description

We start with the model of AC, developed by May and colleagues (May and Tiitinen 2010, 2013; May et al. 2015; Westö et al. 2016). The model is based on the anatomical core-belt-parabelt organisation of AC. This coarse structure of auditory areas is similar across mammals, although species strongly differ in the number of auditory fields per area and the connectivity between fields (Kaas and Hackett 2000). The dynamics of the model were inspired by the work of Wilson and Cowan (1972) and Hopfield and Tank (1986). Its basic unit is a simplified description of the cortical column and comprises a mean-field excitatory and a mean-field inhibitory cell population that are characterised by the state variables $\boldsymbol{u}(t) = (u_1(t), \ldots, u_N(t))^\top$ and $\boldsymbol{v}(t) = (v_1(t), \ldots, v_N(t))^\top$, respectively, where N is the number of columns. Moreover, the dynamics of the excitatory state variables is also coupled with the synaptic efficacy $\boldsymbol{q}(t) = (q_1(t), \ldots, q_N(t))^\top$. The dynamics of the model are then governed by the following set of coupled first-order differential equations (May and Tiitinen 2013; May et al. 2015; Hajizadeh et al. 2019)

$$\tau_\mathrm{m}\dot{\boldsymbol{u}}(t) = -\boldsymbol{u}(t) + W_\mathrm{ee}Q(t)\cdot g[\boldsymbol{u}(t)] - W_\mathrm{ei}\cdot g[\boldsymbol{v}(t)] + \boldsymbol{i}_\mathrm{aff,e}(t), \tag{1}$$

$$\tau_\mathrm{m}\dot{\boldsymbol{v}}(t) = -\boldsymbol{v}(t) + W_\mathrm{ie}\cdot g[\boldsymbol{u}(t)] - W_\mathrm{ii}\cdot g[\boldsymbol{v}(t)] + \boldsymbol{i}_\mathrm{aff,i}(t), \tag{2}$$

$$\dot{\boldsymbol{q}}(t) = -\frac{\boldsymbol{q}(t)g[\boldsymbol{u}(t)]}{\tau_\mathrm{o}} + \frac{\boldsymbol{1}-\boldsymbol{q}(t)}{\tau_\mathrm{rec}}, \quad Q(t) = \mathrm{diag}(\boldsymbol{q}(t)). \tag{3}$$

Here, τ_m is the membrane time constant. The connections between excitatory (e) and inhibitory (i) cell populations are organised according to the anatomical structure of auditory cortex (Kaas and Hackett 2000) and are expressed by the four weight matrices W_ee, W_ei, W_ie, and W_ii. The elements of the matrices W_ee and W_ie describe excitatory-to-excitatory and excitatory-to-inhibitory connections, respectively, and encompass all the connections *between* the columns. Note that only W_ee includes long-range connections between areas, and W_ie describes lateral inhibition. W_ei and W_ii comprise local inhibitory-to-excitatory and inhibitory-to-inhibitory connections, which only occur *within* a column, and these matrices are, thus, diagonal. The firing rates $g[\boldsymbol{u}(t)]$ and $g[\boldsymbol{v}(t)]$ are component-wise sigmoid functions of the form $g[\boldsymbol{x}] = \tanh[\alpha\boldsymbol{x}]$ where $\boldsymbol{x}$ stands for $\boldsymbol{u}(t)$ or $\boldsymbol{v}(t)$. The parameter α is a scalar which determines the sensitivity of the firing rate to the value of the respective state variable. The variables $\boldsymbol{i}_\mathrm{aff,e}(t)$ and $\boldsymbol{i}_\mathrm{aff,i}(t)$ are time-dependent subcortical afferent inputs. Equation (1) indicates that the excitatory-to-excitatory connections are not static and are modulated by short-term synaptic depression, which is defined as $\boldsymbol{d}(t) = \boldsymbol{1} - \boldsymbol{q}(t)$. This is expressed by the matrix multiplication of the elements of W_ee with the synaptic efficacy $Q(t)$, which is a time-dependent diagonal matrix. Further, τ_o and τ_rec are the time constants of the release and the replenishment of neurotransmitters at each synapse; and $\boldsymbol{1}$ is the 1-vector of size N. Note that $\boldsymbol{q}(t)$ is also a vector and the multiplication between the vectors is a component-wise operation. Equation (3) implies that the synaptic strength between pre- and post-synaptic cell populations depends only on the activity of the state variable $\boldsymbol{u}(t)$ of the pre-synaptic excitatory cell population. Inclusion of synaptic plasticity as it is given in Eq. (3)

in the model was inspired by Tsodyks and Markram (1997) and Loebel et al. (2007). With known connectivity matrices W_{ee}, W_{ei}, W_{ie}, and W_{ii} as well as the input terms $\boldsymbol{i}_{\mathrm{aff,e}}(t)$ and $\boldsymbol{i}_{\mathrm{aff,i}}(t)$, the nonlinear system described by Eqs. (1)–(3) can be solved numerically to provide a picture of the spatiotemporal activity of AC.

There is a richness of dynamical behaviour that the model can display. This is because the diagonal entries of the connectivity matrices determine the oscillator properties of each column. For values used in our parametrisation (see Table 1), any single column without coupling and input behaves as a damped oscillator. For larger values on the diagonal elements of W_{ee} and W_{ei}, self-sustained oscillations can appear. For the case of damped oscillators, we may use linear firing rates $g[x] = \alpha x$ such that Eqs. (1) and (2) with fixed synaptic efficacy $\boldsymbol{q}(t) = \boldsymbol{q}$ behave essentially as a network of coupled linear filters. However, when synaptic efficacy is a dynamical variable due to STSD, the full model represented in Eqs. (1), (2), and (3) remains nonlinear through the $Q(t)\boldsymbol{u}(t)$ terms in Eqs. (1) and (3).

2.2 Solution by normal modes

Hajizadeh et al. (2019) demonstrated that, under certain assumptions, the solutions for Eqs. (1) and (2) can be written as a linear combination of normal modes. These assumptions are that the firing rate is linear ($g[x] = \alpha x$) (see also, Allen et al. 1975; Katznelson 1981; May and Tiitinen 2001), synaptic efficacy is constant, i.e., $Q(t) \equiv I$, and the connection matrices are symmetric. Hajizadeh et al. (2019), then, realized eigenvalue decomposition by first transforming Eqs. (1) and (2) into second-order differential equations which refer to the oscillating nature of brain activity.

In contrast to the approach of Hajizadeh et al. (2019), we strive here for general solutions of Eqs. (1) and (2) by including the dynamics of STSD and without a diversion via a system of second-order differential equations. To this end, the homogeneous part of Eqs. (1) and (2) is rewritten in the form of a standard linear system

$$\begin{pmatrix} \dot{\boldsymbol{u}}(t) \\ \dot{\boldsymbol{v}}(t) \end{pmatrix} = M \begin{pmatrix} \boldsymbol{u}(t) \\ \boldsymbol{v}(t) \end{pmatrix} \quad \text{with} \\ M = \frac{1}{\tau_{\mathrm{m}}} \begin{pmatrix} \alpha W_{\mathrm{ee}} Q - I & -\alpha W_{\mathrm{ei}} \\ \alpha W_{\mathrm{ie}} & -\alpha W_{\mathrm{ii}} - I \end{pmatrix}, \tag{4}$$

where I is the identity matrix. The general solution to Eq. (4) is then given by linear combinations

$$\begin{pmatrix} \boldsymbol{u}(t) \\ \boldsymbol{v}(t) \end{pmatrix} = \sum_{n=1}^{2N} c_n \exp(\lambda_n t) \begin{pmatrix} \boldsymbol{x}_n \\ \boldsymbol{y}_n \end{pmatrix}, \tag{5}$$

where $\lambda_n \in \mathbb{C}$, $n = 1, \ldots, 2N$ are the eigenvalues of the coefficient matrix M in Eq. (4). The eigenvectors $\left(\boldsymbol{x}_n, \boldsymbol{y}_n\right)^{\top}$ are the normal modes, where $\boldsymbol{x}_n$ and $\boldsymbol{y}_n$ represent the collection of the $\boldsymbol{u}$ and $\boldsymbol{v}$ components of the n-th eigenvector. For a specific initial condition $(\boldsymbol{u}(0), \boldsymbol{v}(0))^{\top} = (\boldsymbol{u}_0, \boldsymbol{v}_0)^{\top}$, the complex coefficients c_n are given as scalar products

$$c_n = \left\langle \begin{pmatrix} \boldsymbol{u}_0 \\ \boldsymbol{v}_0 \end{pmatrix}, \begin{pmatrix} \boldsymbol{\xi}_n \\ \boldsymbol{\eta}_n \end{pmatrix} \right\rangle, \tag{6}$$

with the corresponding left eigenvectors $\left(\boldsymbol{\xi}_n, \boldsymbol{\eta}_n\right)^{\top}$ of the coefficient matrix M. For all reasonable choices of the weight matrices in Eq. (4), the matrix M is stable, that is, all the eigenvalues $\lambda_n = \gamma_n + i\omega_n$ for a given angular frequency ω_n have a decay rate $\gamma_n < 0$. If $\omega_n \neq 0$, the normal mode dynamics are of the underdamped type and, thus, the eigenvalues and their corresponding eigenvectors appear in complex conjugate pairs. For real initial values $(\boldsymbol{u}(0), \boldsymbol{v}(0))^{\top}$, the corresponding pair of complex coefficients c_n has to be complex conjugate as well. The modulus of the complex coefficient c_n is the initial amplitude of the mode whilst its argument provides the initial phase. If $\omega_n = 0$, the normal modes are of the overdamped type, and the eigenvectors together with their coefficients are real.

2.3 Dynamics of STSD and the slow-fast approximation

Here, we study adaptation dynamics in AC using a paradigm where the AC is excited by a sequence of tones periodically delivered S times with an identical stimulus onset interval between two consecutive stimuli. With repetitive stimulation, the system responds most strongly to the first stimulus; we refer to this condition as the *initial state*. Within the next few stimuli, STSD increases and, therefore, the response magnitude rapidly decreases and finally approaches a constant value. We call this state of the system the *adapted state*, where further incoming stimuli induce only small changes in the response. The adapted state is described by a balance between fast depression and recovery from depression—governed by the time constants in Eq. (3)—and strongly depends on the temporal pattern of the stimulation. Without any further stimulation, the system recovers back to its initial state with the time constant τ_{rec}, which is much larger than τ_{o}.

Assuming that the stimulus duration is short compared to the time scales of the system, we can include the stimuli in our model as input functions of the form

$$\boldsymbol{i}_{\mathrm{aff,e}}(t) = \boldsymbol{a} \sum_{s=0}^{S} \delta(t - t_s), \tag{7}$$

where the s-th stimulus appears at $t_s = s \cdot \mathrm{SOI}$, and the vector $\boldsymbol{a}$ gives the input strengths at each column in the network. Here, only the first element of $\boldsymbol{a}$ is non-zero. That is, the afferent input occurs only and specifically in the excitatory cell population of IC, i.e., $\boldsymbol{i}_{\mathrm{aff,i}}(t) = 0$. From IC the signal propagates to the AC via thalamus. Note that, in principle, the model is able to deal with any type of input function. However, describing the stimuli as delta functions allows us to treat the impact of the stimuli as jumps of $\boldsymbol{u}(t)$ and $\boldsymbol{v}(t)$ at the stimulation times t_s, while in the time intervals between the stimuli, we can use the homogeneous Eq. (4). Together with further slight simplifications of the model, which we describe below, this will enable us to perform a stimulus-wise normal mode analysis of the system as it adapts to repetitive stimulation.

Since $\tau_{\mathrm{o}} \ll \tau_{\mathrm{rec}}$, the dynamics of $\boldsymbol{q}(t)$, given in Eq. (3), is characterised by two different time scales: First, there is a fast drop-off $(-1/\tau_{\mathrm{o}})(\boldsymbol{q}(t) g[\boldsymbol{u}(t)])$ occurring directly after a stimulus when the firing rate $g[\boldsymbol{u}(t)]$ is non-zero. Second, there is a slow recovery phase when the firing rates $g[\boldsymbol{u}(t)]$ have decayed and Eq. (3) is governed by the recovery term $(1/\tau_{\mathrm{rec}})(\mathbf{1} - \boldsymbol{q}(t))$. Following the general mathematical theory for slow-fast systems (see, for example, Kuehn 2015), we can use this time-scale separation to introduce a slow-fast approximation of the STSD process. We keep the synaptic efficacy at a constant value $Q(t) = Q_s$ in each time interval $t \in [t_s, t_{s+1}]$ between two consecutive stimuli and update it together with the stimulus-induced jumps of $\boldsymbol{u}(t)$ and $\boldsymbol{v}(t)$ at the stimulation times t_s.

For the updating $Q_s \mapsto Q_{s+1}$, we separate the processes of fast drop-off during the stimulus-induced activity from the slow recovery after the stimulus-induced activity. The fast drop-off $\mathcal{F}_s(\boldsymbol{q}_s)$ is obtained by integrating the first term in Eq. (3)

$$\mathcal{F}_s(\boldsymbol{q}_s) = \boldsymbol{q}_s \exp\left(-\frac{1}{\tau_{\mathrm{o}}} \int_{t_s}^{t_{s+1}} g[\boldsymbol{u}(t')]dt'\right), \tag{8}$$

whereby we treat neurotransmitter release as a process independent of vesicle replenishment. Inserting this as initial value into the slow recovery process, which can be explicitly integrated, we obtain the combined update as given by

$$\boldsymbol{q}_{s+1} = \mathbf{1} - \left(\mathbf{1} - \mathcal{F}_s(\boldsymbol{q}_s)\right) \exp\left(-\frac{t_{s+1} - t_s}{\tau_{\mathrm{rec}}}\right). \tag{9}$$

Inserting the general solution from Eq. (5) in Eq. (8), $\mathcal{F}_s(\boldsymbol{q}_s)$ can be rewritten as

$$\mathcal{F}_s(\boldsymbol{q}_s) = \boldsymbol{q}_s \prod_{n=1}^{2N} \exp\left(\frac{-c_{n,s}\left(\exp\left(\lambda_{n,s}\left(t_{s+1} - t_s\right)\right) - 1\right)}{\tau_{\mathrm{o}} \lambda_{n,s}} \boldsymbol{x}_{n,s}\right). \tag{10}$$

Note that for each time interval $[t_s, t_{s+1}]$, we have to use the step-wise adapting coefficient matrix $M_s = M(Q_s)$ to recalculate the normal modes $\left(\boldsymbol{x}_{n,s}, \boldsymbol{y}_{n,s}\right)^{\top}$, the eigenvalues $\lambda_{n,s}$, and the coefficients $c_{n,s}$ for which we also need the left eigenvectors $\left(\boldsymbol{\xi}_{n,s}, \boldsymbol{\eta}_{n,s}\right)^{\top}$. Further, we assume that between two consecutive stimuli the state variables $\boldsymbol{u}(t)$ and $\boldsymbol{v}(t)$ have decayed to zero so that the next stimulus induces an abrupt increase of $\boldsymbol{u}(t)$ and $\boldsymbol{v}(t)$. This means that at each time point t_s, based on the stimulus history, the dynamics of Eq. (4) are reparameterised by updating Q_s, and $\boldsymbol{u}(t)$ and $\boldsymbol{v}(t)$ are set to a new stimulus-induced starting value. In particular, although the input $\boldsymbol{a}\delta(t - t_s)$ is the same at the beginning of each interval, the effective input to the normal modes differs. It is determined by the adapting connectivity pattern of the network, which itself depends on the stimulus history by means of STSD. In this way, the slow-fast approximation allows for stimulus-wise normal mode analysis of Eq. (4) in each time interval $t \in [t_s, t_{s+1}]$ between two consecutive stimuli, where the synaptic efficacy variables $Q(t) = Q_s$ stay piecewise constant. We will use this later as a tool for analysing the STSD induced changes in the generation of the ERF signals.

2.4 An auditory cortex model with a simplified structure

For the simulations presented in this work, we used a model with a strongly simplified anatomical structure that encompassed two subcortical areas, viz. IC and thalamus, and three cortical areas representing the core, the belt, and the parabelt (see Fig. 1a). For reasons of simplicity, each of the five areas consisted of only one auditory field, which, in turn, comprised just one column with an excitatory and an inhibitory cell population. A central feature of this network is its serial connectivity, i.e., only neighbouring areas are directly connected with each other via feedforward and feedback connections, as illustrated for the connection matrix W_{ee} in Fig. 1b. The only type of connection *between* two columns are excitatory-to-excitatory connections. All other connections are assumed to be local and existing within a single area. Therefore, their corresponding connection matrices are diagonal and of the order five given by $W_{\mathrm{ie}} = w_{\mathrm{ie}}^{(\mathrm{d})} I$, $W_{\mathrm{ei}} = w_{\mathrm{ei}}^{(\mathrm{d})} I$, and $W_{\mathrm{ii}} = w_{\mathrm{ii}}^{(\mathrm{d})} I$.

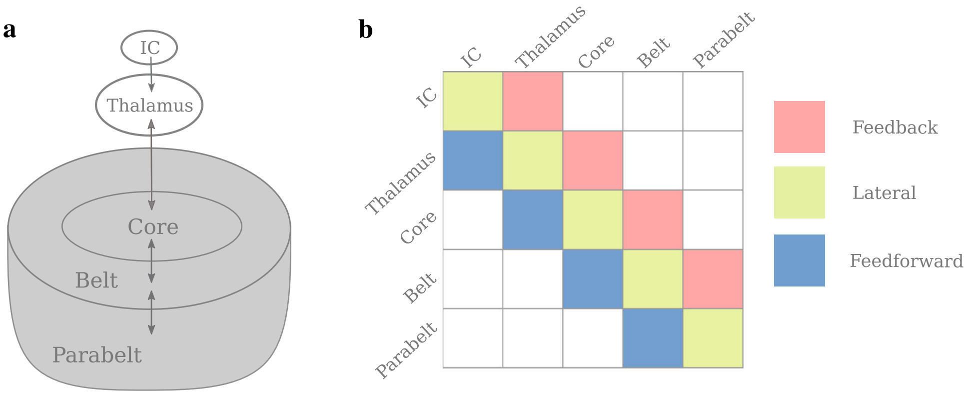

Fig. 1 Schematic representation of the anatomical structure of the model. **a** The structure is divided into subcortical and cortical regions. The subcortical areas IC and thalamus provide the afferent input to the AC. The AC consists of the serially organised core, belt, and parabelt areas. There are therefore a total of five areas, and each area is represented by a population of excitatory and a population of inhibitory neurons; each population is described by a single state variable. Additionally, the connections from each excitatory population are modulated by STSD. Thus, the model is a 15-dimensional system of coupled first-order differential equations. **b** The structure is represented in the connection matrix W_{ee} with non-zero matrix elements $w_{\mathrm{ee}}^{(\mathrm{ff})}$ (feedforward, blue), $w_{\mathrm{ee}}^{(\mathrm{fb})}$ (feedback, red), and $w_{\mathrm{ee}}^{(\mathrm{d})}$ (lateral, yellow). Note that the other three weight matrices, not shown here, are diagonal square matrices of order five

Figure 2a shows an example of the model output in terms of the state variable $\boldsymbol{u}(t)$ based on the slow-fast approximation for a repeated stimulation of the network with SOI = 0.5 s. The parameters used for the computation are summarised in Table 1. For each stimulus, the peak magnitudes of $\boldsymbol{u}(t)$ gradually decrease—and the corresponding peak latencies increase—as one moves up the hierarchy from the core to the parabelt. The excitatory-to-excitatory connections of W_{ee} weaken due to STSD (i.e., due to a lowering of synaptic efficacy Q in Eq. (4)). Consequently, in each area, the peak amplitude of $\boldsymbol{u}(t)$ decreases across stimulus presentation.

Figure 2b shows the state variable $\boldsymbol{u}(t)$ from the numerical simulations with nonlinear (blue) and linear (black) firing rates, and from the slow-fast approximation (red). All simulations were computed using the same set of model parameters displayed in Table 1 and the identical input function given in Eq. (7). There is a close correspondence between the simulations: the simplifications induced by linear firing rates and the slow-fast approximation have no relevant impact on the waveforms and their adaptation. The evolution of the corresponding STSD variables $\boldsymbol{d}(t) = \boldsymbol{1} - \boldsymbol{q}(t)$ is shown in Fig. 2c. Again, there are only minor discrepancies between the nonlinear (blue) and linear (black) solutions. For the slow-fast approximation, the STSD variables are updated only at the stimulation times t_s (red points). Figure 2d illustrates the operation of the slow-fast approximation where, in Eq. (4), the evolution of $\boldsymbol{u}(t)$ and $\boldsymbol{v}(t)$ is computed using the piecewise constant values (green) of the STSD process. Note that, as explained in the Sect. 2.3, the combination of the approximations for the fast drop (Eq. (8)) and the slow recovery (Eq. (9)) (red dashed) are only used to obtain the values of $\boldsymbol{q}_s$ which stay piecewise constant during the evolution of $\boldsymbol{u}(t)$ and $\boldsymbol{v}(t)$. Note also that the lemniscal subdivisions of IC and thalamus have much faster recovery time constants compared to the cortical regions (Asari and Zador 2009; Pérez-González and Malmierca 2014; Ulanovsky et al. 2004). Therefore, in our simulations, IC and thalamus do not adapt, i.e., the corresponding values of synaptic efficacy $Q(t)$ for the two subcortical areas are set to unity in all simulations. Figure 2 demonstrates that the slow-fast approximation, described in Sect. 2.3, provides good estimations of the numerical simulations of Eqs. (1), (2), and (3). Therefore, it can be used in lieu of numerical solutions to study the adaptation dynamics of AC.

2.5 Computing MEG signals

MEG signals are generated mainly by primary currents running in the apical dendrites of synchronously active pyramidal cells in the cortex (Hämäläinen et al. 1993). The apical dendrites are locally aligned with each other and point in a direction perpendicular to the cortical surface. When a portion of the cortex becomes active, its contribution to the MEG signal is proportional to the total current running in the apical dendrites. This is weighted by the distance to the MEG sensor and by the orientation of the current, which is determined by the local gyrification of the cortical surface. The primary current in each apical dendrite is driven by the synaptic inputs to the dendrite. This means that each synaptic input contributes to the MEG signal, and the magnitude and polarity of this contribution depends on the location of the synapse on the dendritic tree and on the type of the synapse (Ahlfors and Wreh 2015). An excitatory synapse near the cell body will cause a positive current to be pumped up the tree, towards

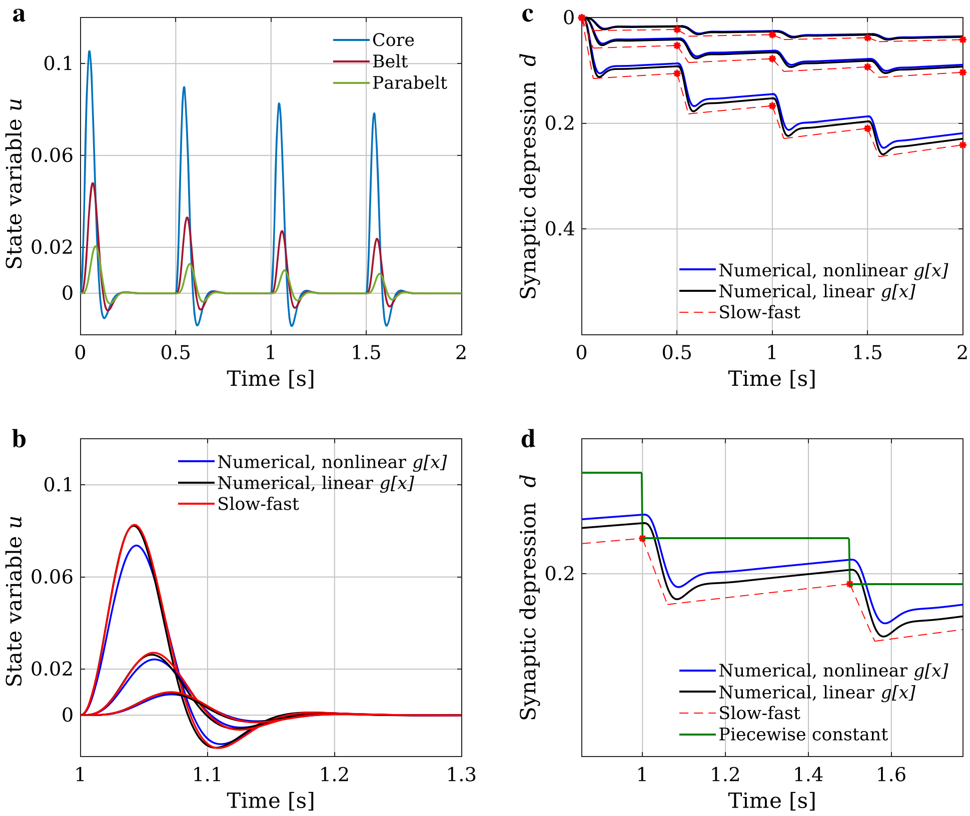

Fig. 2 State variable $u(t)$ and STSD $d(t)$ derived with the slow-fast approximation compared with the numerical simulations of the full model given in Eqs. (1)–(3). **a** The state variable $u(t)$ as a response to a sequence of identical stimuli with constant SOI of 0.5 s is shown for core (blue), belt (red), and parabelt (green) areas. For each area, the first stimulus generates the largest response. Although the state variables decay to zero during the interval between two consecutive stimuli, the excitatory-to-excitatory connections are weakened by STSD and this effect carries over the silent period of the SOI so that the peak amplitude of $u(t)$ decreases until it levels off after a few stimuli. **b** The state variable $u(t)$ as a response to one stimulus computed with the slow-fast approximation (red) is contrasted with that gained in numerical simulations using nonlinear firing rates $g[x] = \tanh(\alpha x)$ (blue) and linear firing rates $g[x] = \alpha x$ (black). The solutions based on the slow-fast approximation provide a good estimation of numerical solutions. The high-, intermediate-, and low-amplitude responses are from the core, belt, and parabelt, respectively. **c** The STSD time course estimated with the slow-fast approximation (red) agrees well with the numerical simulations with nonlinear (blue) and linear (black) firing rates. The red dashed lines represent solutions to Eq. (9), and the red dots indicate the onset of stimulus presentation, at which the fast drop-off according to Eq. (8) is computed. **d** This plot is an enlarged version of the STSD variable of the corresponding time interval shown in (**b**). In order to compute the state variables using the slow-fast approximation, we assumed that STSD is piecewise constant in the time interval between the onsets of two consecutive stimuli as indicated by the green horizontal line. The corresponding STSD value at each stimulus onset (red dots) was derived from the slow-fast approximation given in Eqs. (8) and (9)

the cortical surface. Conversely, an excitatory synapse near the distal end of the tree will cause the current to travel in the opposite direction, away from the cortical surface. Consequently, feedforward connections, which generally target the proximal dendrites in layer IV, result in a current pointing towards the cortical surface. In contrast, feedback input arriving in the upper layers produce a current pointing downward (Ahlfors et al. 2015).

We modelled MEG generation with the above considerations in mind. Given that the MEG signal of a pyramidal cell is quite well approximated by the synaptic input current of the neuron (May 2002), the MEG contribution from each area is assumed to be proportional to the input to the column representing the area. These inputs are defined by the second and third term on the right hand side of Eq. (1). Each input is weighted by a connection-specific multiplier which depends on the connection type (feedforward, feedback, excitatory, inhibitory) (for more information, see Hajizadeh et al. 2019, 2021). This topological information is expressed in the matrices K_1 and K_2, whose structures are shown in Fig. 3. They specify how each synaptic connection contributes to the MEG signal by an element-wise multiplication (Hadamard product $\circ$) with the matrices W_{ee} and W_{ei}. Thus, the total MEG signal is the product of K_1 and K_2 representing the topography, the synaptic strengths represented in W_{ee} and W_{ei}, and the firing rate of the pre-synaptic cell population. Therefore, the MEG signal $R(t)$ is computed as

Table 1 Default parameter values used for the simulations. These values were chosen to replicate realistic-looking ERFs

Dynamical parameters	Value	Topographical parameters	Value
$w_{\mathrm{ee}}^{(\mathrm{d})}$	2	$k_1^{(\mathrm{d})}$	-1
$w_{\mathrm{ee}}^{(\mathrm{ff})}$	0.5	$k_1^{(\mathrm{ff})}$	-1
$w_{\mathrm{ee}}^{(\mathrm{fb})}$	0.4	$k_1^{(\mathrm{fb})}$	15
$w_{\mathrm{ie}}^{(\mathrm{d})}$	3.5	$k_2^{(\mathrm{d})}$	2
$w_{\mathrm{ei}}^{(\mathrm{d})}$	2.2		
$w_{\mathrm{ii}}^{(\mathrm{d})}$	2.5		
τ_{m}	0.03 s		
τ_{o}	0.04 s		
τ_{rec}	5 s		
a	0.02		
α	1		

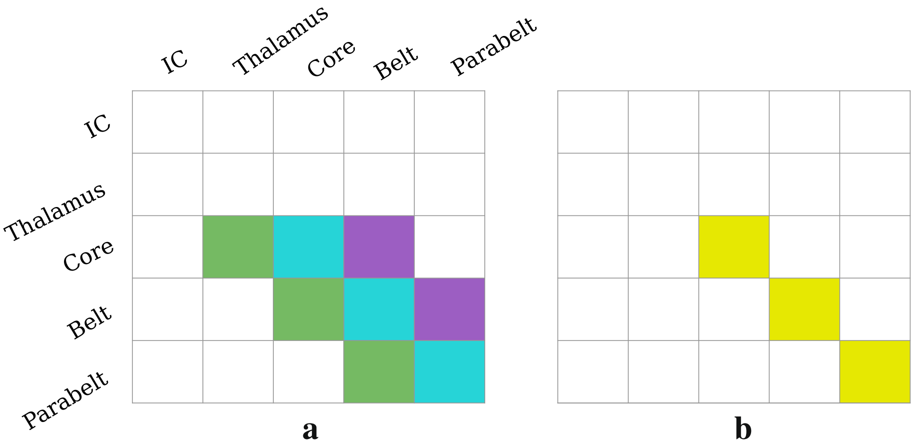

Fig. 3 The K_1 (**a**) and K_2 (**b**) matrices, which contain the information about the topology of the primary currents, provide connection-specific multipliers of W_{ee} and W_{ei} in the computation of the MEG signal, respectively. **a** The green ($k_1^{(\mathrm{ff})}$) and purple ($k_1^{(\mathrm{fb})}$) elements in K_1 represent feedforward and feedback connections, respectively. The cyan elements ($k_1^{(\mathrm{d})}$) on the diagonal represent the lateral connections. Contributions of IC and thalamus to the MEG are zero, but the excitatory connections from the thalamus to the core contribute to the MEG. **b** The yellow elements ($k_2^{(\mathrm{d})}$) in K_2 represent the weights of inhibitory connections

$$R(t) = \sum_{j=1}^{2N} \left[\begin{pmatrix} K_1 \circ W_{\mathrm{ee}} & O \\ O & K_2 \circ W_{\mathrm{ei}} \end{pmatrix} \begin{pmatrix} \boldsymbol{u}(t) \\ \boldsymbol{v}(t) \end{pmatrix} \right]_j , \qquad (11)$$

where j runs over the number of cortical columns in the model, and O is the zero matrix of order N.

In Fig. 4, we compare experimental MEG data with simulations based on the slow-fast approximation using Eq. (11). MEG signals were recorded from a single subject who passively listened to sequences of tones. These tones (audio frequency 1.5 kHz, duration 100 ms, sound-pressure level 80 dB) were presented in five different blocks (111 tone repetitions per block) with constant SOI between two consecutive tones. The SOIs of the blocks were 0.5 s, 1 s, 2.5 s, 5 s, and 10 s, corresponding to stimulation rates of 2 Hz, 1 Hz, 0.4 Hz, 0.2 Hz, and 0.1 Hz, respectively (Zacharias et al. 2012). Figure 4a shows the trial-averaged waveforms for the five SOIs. With increasing SOI, the N1m peak magnitude and the corresponding peak latency (except for the 0.5-s SOI) increases, thus presumably reflecting the different speed of recovery from STSD for short and long SOIs. Furthermore, the rising slope of the N1m is unaffected by the SOI, whereas the falling slope clearly differs between the five waveforms. Also, P2m seems to be more affected by the adaptation process than the P1m deflection.

Using the same stimulation paradigm as described for the experimental data, we performed simulations of ERFs based on the normal mode analysis (Eq. (11)) with the slow-fast approximation and using the parameters given in Table 1. As shown in Fig. 4b, the simulations replicate the main characteristics of the experimental data (Fig. 4a): (1) As SOI is increased, both the peak amplitude and the peak latency of the N1m become larger, (2) the rising slope of the N1m is

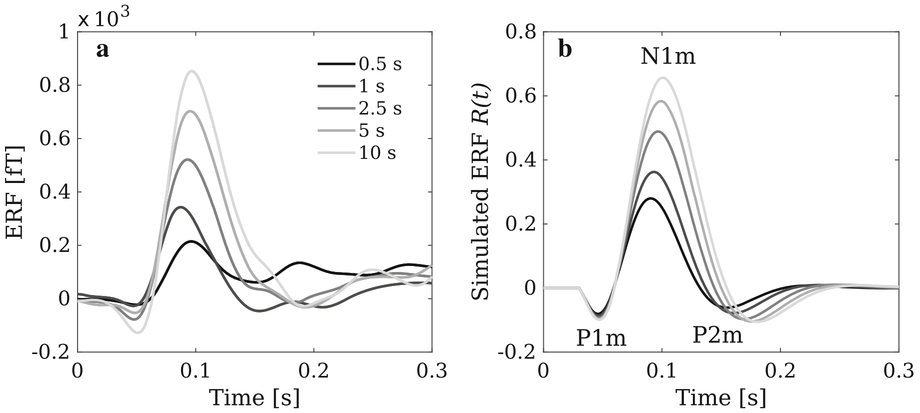

Fig. 4 Comparison of experimental and simulated ERFs showing the dependence of the ERF response on SOI. **a** Trial-averaged ERF responses from an MEG sensor in the vicinity of auditory cortex recorded from a single subject. The peak amplitude of the N1m shows a high sensitivity to changes in SOI (data from Zacharias et al. (2012)). **b** Simulated ERF responses calculated by use of the slow-fast approximation. These replicate all the major landmarks of the dependence of the experimental ERF on SOI: the P1m as well as the rising slope of the N1m are least affected by SOI. As SOI is increased, the peak latency of the N1m grows and the falling slope of the N1m becomes steeper. We have added a 30-ms shift to the simulated waveforms to account for the time delay due to sub-cortical processing

unaffected by SOI, (3) the falling slope of the N1m becomes systematically steeper as SOI grows, and (4) the width of the N1m waveform increases as a function SOI. With the use of the slow-fast approximation we have now a tool at hand that enables us to investigate how stimulus repetition modifies the dynamics of AC.

3 Modelling results: novel views on ERF adaptation

In this section, we first show how normal modes in time and space contribute to the formation of ERFs and to their adaptation with stimulus repetition. Second, we show how ERF adaptation can be viewed from the perspective of different physiological connections. Third, we demonstrate that the recovery from adaptation depends not only on the system parameters, such as time constants which directly regulate the STSD dynamics. Rather, adaptation reflects also the network structure and varies from area to area in terms of recovery time. Finally, we use our model to quantify the adaptation of the N1m for smaller and larger SOIs and in this way discuss the limitations of the widely-used single exponential function as a description of adaptation recovery.

3.1 Adaptation of ERFs as a result of adapting normal modes

According to Eq. (11), the MEG signal $R(t)$ is a function of the excitatory and inhibitory state variables $\boldsymbol{u}(t)$ and $\boldsymbol{v}(t)$. By a change of coordinate, $R(t)$ can be expressed in terms of normal modes so that the only time-varying term is the normal mode amplitude, whereas the oscillation frequency and damping rate remain constant. Substituting Eq. (5) in Eq. (11) results in

$$R(t) = \sum_{j=1}^{2N} \left[\begin{pmatrix} K_1 \circ W_{\mathrm{ee}} & O \\ O & K_2 \circ W_{\mathrm{ei}} \end{pmatrix} \sum_{n=1}^{2N} c_n \exp(\lambda_n t) \begin{pmatrix} \boldsymbol{x}_n \\ \boldsymbol{y}_n \end{pmatrix} \right]_j . \tag{12}$$

The left column of Fig. 5 shows the simulated ERF waveforms and the underlying normal modes of the adapted states for the five different SOIs presented in Fig. 4b. The ERFs are displayed as grey curves, with the same shades of grey used in Fig. 4b. The normal modes are depicted in different colours; they are identifiable by their characteristic frequencies $\nu = \omega/2\pi$ in the legend. The ERF decomposition results in normal modes whose polarities are preserved across SOI. For all SOIs, each normal mode peaks well before the N1m, during the first 50 ms. The two normal modes with the lowest ν (purple and green curves) show by far the largest amplitude. They have opposite phases and a peak latency at around 50 ms. In contrast, the two modes with the highest frequencies (blue and red) have much smaller magnitudes and decay faster. The mode with the intermediate frequency (yellow) has a prominent peak magnitude with a small latency. As a consequence of this diversity of normal modes, the P1m of the ERFs is composed from all the modes, whereas the N1m and P2m are predominantly formed by the two modes with the lowest frequencies.

The middle column of Fig. 5 shows the dispersion relation of the normal modes underlying the ERFs. At both initial and adapted states, the normal modes are of the underdamped type because their frequencies ν are non-zero and their corre-

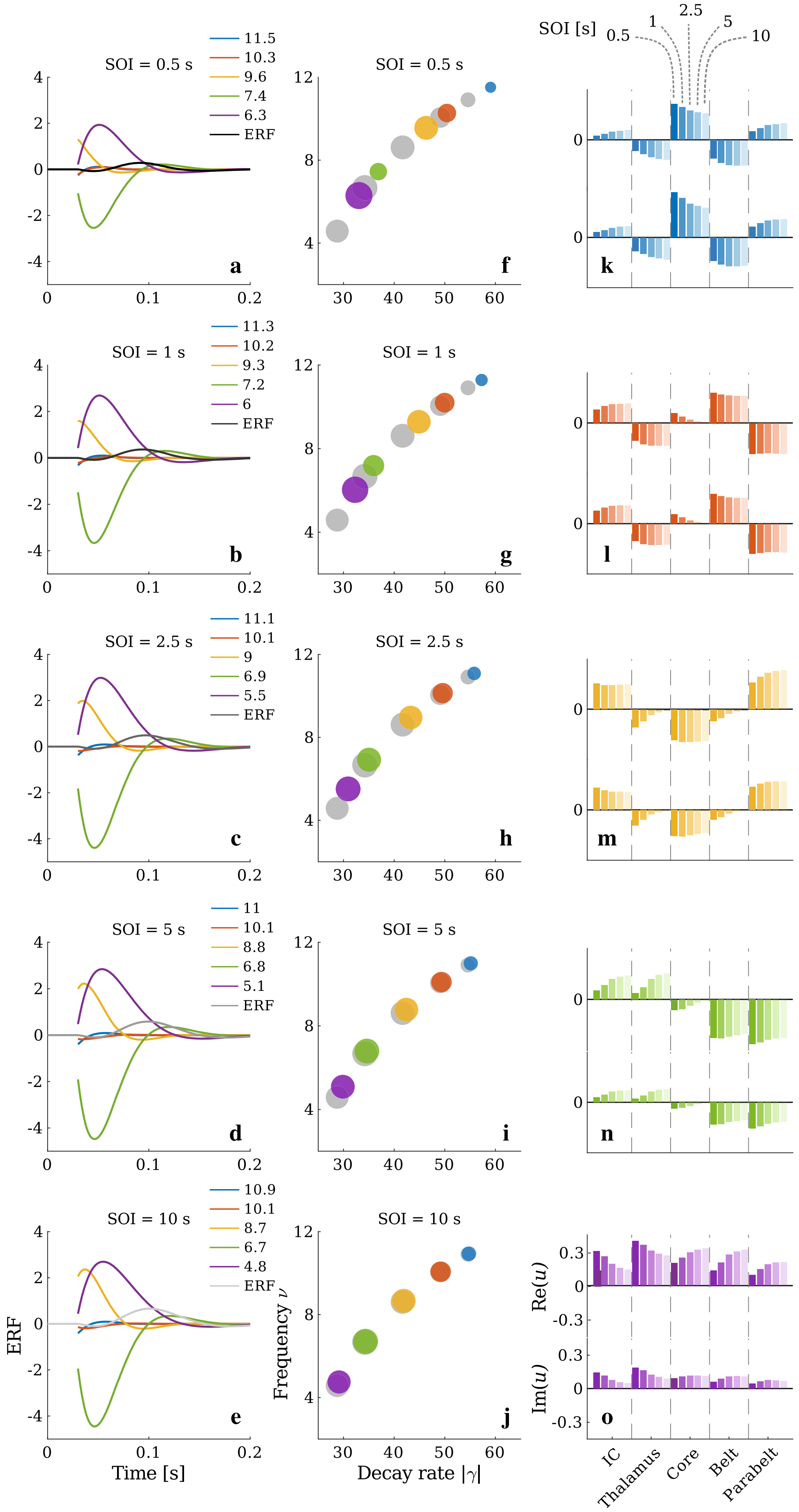

Fig. 5 Decomposition of the simulated ERFs into normal modes. **a–e** Each ERF (shaded grey) is displayed together with the underlying normal modes, represented by different colours which stay consistent in the left, middle, and right columns of this figure. The ERFs are the same as those presented in Fig. 4b. For each SOI, all normal modes peak earlier than the corresponding N1m, and the main contributor to the ERFs are the low-frequency normal modes (purple and green) appearing in opposite phase. The high-frequency normal modes (blue and red) decay fast and contribute only very weakly to the N1m and P2m responses. **f–j** Dispersion relation between frequency ($\mathrm{Im}(\lambda)/2\pi = \nu$) and the absolute value of the decay rate ($|\mathrm{Re}(\lambda)| = |\gamma|$). The spectral information shows that all normal modes are of the underdamped type. The grey discs represent the dispersion relation at the initial state, which is the same for all SOIs. The coloured discs correspond to the dispersion relation of the adapted state. In general, frequency and decay rate of the normal modes increase with decreasing SOI. The size of the discs are proportional to the initial amplitude $|c_n|$ of the normal modes. In both the initial state and the adapted state, the low-frequency normal modes have a larger amplitude than the high-frequency normal modes. **k–o** The spatial wave patterns for different modes in different SOIs are given in the eigenvectors $(\boldsymbol{x}_n, \boldsymbol{y}_n)^\top$. Here, the real and the imaginary parts of the excitatory state variables $\boldsymbol{u}(t)$ are shown, which, for each mode individually, follow the same pattern. As indicated in panel **k**, the different shades signify different SOIs. The high-frequency modes **k–l** occur with large spatial wave number, whereas the low-frequency modes **m–o** appear with low wave number in space. Moreover, the same spatial wave pattern is observed for all SOIs

sponding decay rates γ are negative. Moreover, for all SOIs there is a typical common dispersion relation between frequency and decay rate, implying that modes with higher frequency also decay faster. Additionally, for all SOIs, the frequencies and the decay rates of the modes in the adapted state shift to larger values compared to the initial state; this shift is larger the smaller the SOI is. For the largest SOI, there are only minute differences between the dispersion relation at the initial and the adapted state, because the 10-s interval between two successive stimuli provides sufficient time for the synaptic efficacy $q(t)$ to return to the initial state.

Stimulus history changes not only the frequency and the decay rate of the normal modes but also their initial amplitude $|c_n|$ after each stimulus (see Eq. (6)). These amplitudes are indicated by the size of each disc in Fig. 5f–j: the larger the size of a disc, the larger the initial amplitude of the respective normal mode. Further, Fig. 5 shows that, in the initial state (grey discs), there is a gradual decrease of the initial amplitude $|c_n|$ from low- to high-frequency modes, whereas in the adapted state there is no systematic pattern except that, for all stimulation rates, the normal mode with the highest frequency (blue discs) has the smallest initial amplitude.

Normal modes are not only oscillations in time but they manifest themselves as spatial wave patterns. This information is provided by the eigenvectors $\left(\boldsymbol{x}_n, \boldsymbol{y}_n\right)^\top$ of the coefficient matrix M. The real and the imaginary parts for the state variables $\boldsymbol{u}(t)$ for the five areas of the network are represented in the right column of Fig. 5, with the mode with the highest frequency ν on top and the one with the lowest frequency ν at the bottom of the column. As indicated in Fig. 5k, different shades of each colour stand for different SOIs. Note the strong similarity of the spatial wave patterns between the real and imaginary parts of $\boldsymbol{u}(t)$ for all modes. For all SOIs and for both the real and imaginary parts of $\boldsymbol{u}(t)$, the wave number in space decreases from the high-frequency mode (blue, Fig. 5k) to the low-frequency mode (purple, Fig. 5o). The same pattern is also observed for the state variable $\boldsymbol{v}(t)$, which is not shown here.

Input efficiency and MEG efficiency

Figure 5 indicates that the normal modes contributing to the generation of the ERFs are all different from one another. According to Eq. (12), these different contributions do not only originate from the differences in the initial amplitudes. Reformulating Eq. (12) as

$$R(t) = \sum_{n=1}^{2N} c_n \kappa_n \exp(\lambda_n t) \qquad \text{with}$$
$$\kappa_n = \sum_{j=1}^{2N} \left[\begin{pmatrix} K_1 \circ W_{\text{ee}} & O \\ O & K_2 \circ W_{\text{ei}} \end{pmatrix} \begin{pmatrix} \boldsymbol{x}_n \\ \boldsymbol{y}_n \end{pmatrix} \right]_j , \tag{13}$$

we see that the contribution of each normal mode to the MEG signal is proportional to two factors:

(1) the initial amplitude $|c_n|$ of the mode, interpreted as the *input efficiency* with respect to the stimulation pattern, and
(2) the *MEG efficiency* κ_n, describing to which extent the MEG device is able to detect the mode.

This information is illustrated in Fig. 6, where the input efficiency $|c_n|$ and MEG efficiency κ_n of each normal mode in the initial (grey) and adapted (coloured) states are characterised by a rectangle of width $|c_n|$ and height κ_n. The area of each rectangle is proportional to the absolute value of the total contribution of a given normal mode to the ERFs presented in Fig. 4b. This figure shows that the two low-frequency modes (purple and green) are the major contributors to the MEG signals. As SOI decreases, the MEG efficiency of the lowest frequency normal mode (purple) decreases, but its input efficiency increases. In contrast, the contribution of the second mode (green) increases in MEG efficiency and decreases in input efficiency. The input efficiency of the third mode (yellow) is relatively unaffected by SOI, whereas its MEG efficiency decreases considerably for smaller SOIs. The total contribution of the two high-frequency modes is negligibly small.

Initial phases and mode interference

In order to fully understand the composition of the MEG signal in terms of the normal modes, one has to appreciate that the result of a linear superposition of damped oscillations does not only depend on the amplitude of each contribution, but also on the corresponding phase. We can see from Eq. (12) that a single oscillating normal mode leads to a complex contribution of the form $r_n(t) = c_n \kappa_n \exp(\lambda_n t)$ to the ERF. For a complex conjugate pair λ_n and $\lambda_{n+1} = \overline{\lambda_n}$, we obtain the real contribution to the MEG of the form

$$\begin{aligned} r_n(t) + r_{n+1}(t) &= 2\text{Re}(r_n(t)) \\ &= 2|c_n|\kappa_n \exp(\gamma_n t) \cos\left(\omega_n t + \arg(c_n)\right). \end{aligned} \tag{14}$$

Summing up such oscillatory terms with different initial phases $\arg(c_n)$ and different angular frequencies ω_n leads to complicated interference patterns, where terms at different time points may add up or cancel each other. This is illustrated in Fig. 7, which shows the amplitude and the phase of each normal mode at three time points: at stimulus onset, at the peak latency of the P1m, and at the peak latency of the N1m. Each dot represents the contribution $r_n(t)$, while the corresponding complex conjugate $r_{n+1}(t) = \overline{r_n}(t)$ is omitted. At stimulus onset, the leading modes (purple and green) have almost opposite phases such that their real parts cancel

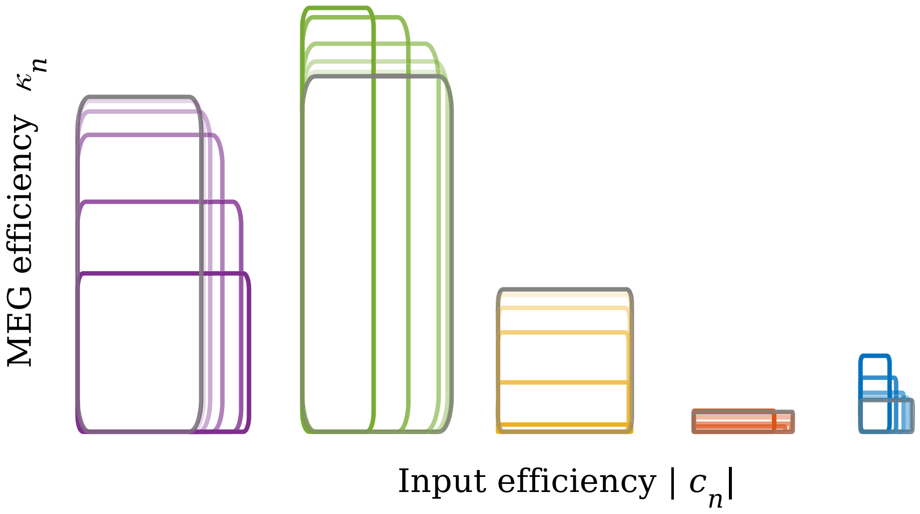

Fig. 6 Characterisation of normal modes in terms of MEG efficiency κ_n and input efficiency $|c_n|$. The normal modes are clustered according to the five frequency bands and they are colour-coded as in Fig. 5. Frequency increases from left to right. Within each band, each normal mode is represented by a rectangle, whose width (Δx) and height (Δy) is equivalent to $|c_n|$ and κ_n, respectively. SOI is represented by the colour shade, with dark shades indicating the smallest and light shades the largest SOI. The initial state is in grey. For all SOIs, the two low-frequency modes (purple and green) contribute most to the ERFs, whereas the contributions of the two high-frequency modes (red and blue) are negligible. Input efficiency shows less variability than MEG efficiency, with the exception of the normal mode with the second-lowest frequency (green)

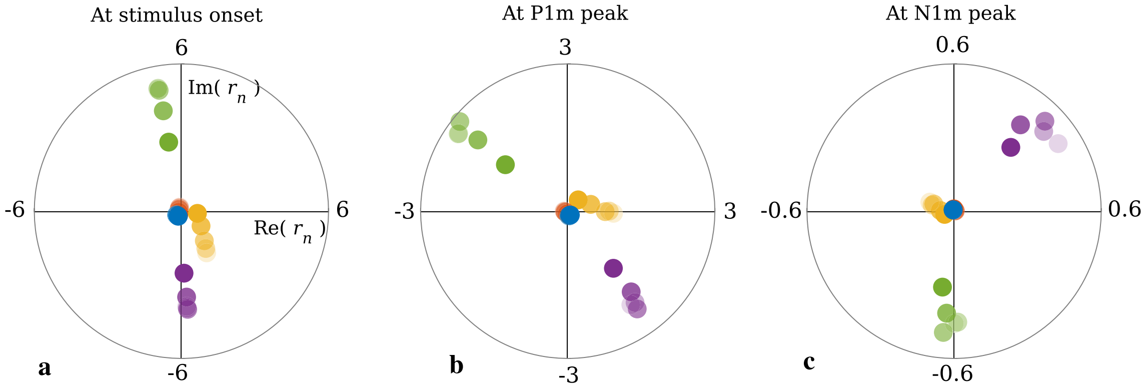

Fig. 7 Normal modes r_n underlying the ERF presented in the complex plain at three distinct time points. **a** At stimulus onset, the normal modes are at their largest complex amplitudes. However, due to their phases they form a destructive pattern such that the sum of their corresponding complex amplitudes is zero. **b** At the peak latency of the P1m, the largest contributions are from the two lowest-frequency modes (green and purple). These appear in nearly opposite phases, and the summed amplitude is low. **c** At the peak latency of the N1m, the normal modes with the second-lowest frequency (green) have a minute real part for all SOIs, meaning that they barely contribute to the N1m peak. Notably, the N1m peak is predominately formed by the mode with the lowest frequency (purple). The colour coding is the same as in Figs. 5 and 6, and the entire ERFs are shown in Fig. 4b

out each other (Fig. 7a). The contributions from the higher-frequency modes (blue, red) are negligible. The same holds for the P1m peak shown in Fig. 7b, where the two leading modes have very similar amplitudes but almost opposite phases. Therefore, their overall contributions are quite small, explaining why the P1m has a relatively low amplitude even though the underlying normal modes are near their extrema. After the P1m, a constructive superposition of the first and second mode starts to emerge. This superposition builds into a large-amplitude N1m (Fig. 7c). This shows that the main frequency component of an ERF can be explained as a beating frequency, that is, the frequency difference between the two leading modes. Moreover, the N1m emerges as late as it does because the leading modes are initially in opposite phase. This means that the N1m should not be interpreted as a delayed response produced by some dedicated N1 generator. This is underlined also by the fact that the activity in the core area peaks at a much earlier latency than the ERF response (see Fig. 2). The results shown in Fig. 7 highlight the fact that ERF generation is a result of a complex interplay between the spatial and temporal structure of the AC response given by the mode spectrum and the corresponding input efficiencies. Additionally, the spatial shapes of the normal modes determine their different MEG efficiencies.

3.2 Adaptation of ERFs in terms of different types of connections

We have shown above that ERF responses can be represented as a superposition of the contributions of different normal modes. Alternatively, we can decompose the ERF according to the physiological structure in our model illustrated in Fig. 1b. Recall that according to Eq. (11), MEG signals arise as a weighted sum of contributions from individual connections in W_{ee} and W_{ei}. These connections can be viewed in three ways: First, each area can be characterised in terms of the incoming connections received by that area (Fig. 8a). Second, we can describe each area according to its outgoing connections, those originating from the area (Fig. 8b). Third, connections can be categorised as feedforward (leading away from the midbrain), feedback (leading towards the midbrain), and of the lateral (intrafield) type (Fig. 8c). In terms of the connection matrices, the rows of W_{ee} and W_{ei} represent incoming connections per area and the columns represent outgoing connections per area. The diagonal elements of W_{ee} and W_{ei} are the lateral connections, and the elements below and above the diagonal of W_{ee} represent feedforward and feedback connections, respectively. Equation (11) enables us to break down the MEG signal into the contributions from these different types of connections.

Figure 8a1 to a5 show the decomposition of the simulated ERFs (grey) into the contributions of each area according to the incoming connections (Fig. 8a). This is equivalent to "source modelling", looking at the contribution that the activity in each area directly contributes to the ERF in virtue of it generating a magnetic field. Note that we are assuming that the ERF is blind to activity in IC and thalamus. For all SOIs, the core area (purple) is the sole generator of the P1m and it is also the largest contributor to the N1m. The core (purple) and the belt (red) together account for almost the entire ERF, including the P2m, whereas the contribution of the parabelt (green) is minute. Note that the ratio between the magnitude of the belt and the core contribution decreases with decreasing SOI. Further, the simulations reveal an increase in the latency of the contribution to the N1m as one moves from the core to the belt and then to the parabelt.

Figure 8b1 to b5 show how the outgoing connections (Fig. 8b) contribute to the ERF (grey). These results look at the indirect contribution that each area makes via its output to other areas and to itself. Connections originating in the thalamus (blue) drive activity in the core through feedforward connections and thereby contribute to the P1m response. For the short SOIs of 0.5 s and 1 s, the core (purple) makes the largest contribution to the N1m, whereas for the longer SOIs of 2.5 s, 5 s, and 10 s, the belt's contribution is the largest (red). The parabelt (green) with its long peak latency remains the weakest contributor to the N1m throughout all SOIs.

Figure 8c1 to c5 show how the input arriving via feedforward (purple), feedback (orange), and lateral (blue) connections contribute to the ERF. We assume that feedforward and lateral connections drive currents away from the cortical surface, whereas feedback connections drive currents towards the surface (Ahlfors and Wreh 2015; Ahlfors et al. 2015). Therefore, feedforward and lateral connections account for the P1m and P2m deflections, whereas the feedback and the inhibitory connections are responsible for the N1m. A clear pattern can be seen: the contributions driven by the feedforward and lateral connections grow only a little as SOI is increased from 0.5 s to 10 s. In contrast, the contribution from the feedback connections show strong adaptation, with a three-fold increase in magnitude over the SOI range. This differential in adaptation behaviour explains why the P1m has a weak SOI dependence and why the N1m shows the strongest adaptation.

3.3 The role of network structure in ERF adaptation

To inspect whether the anatomical structure of AC impacts on adaptation, we derived the lifetime of adaptation in three versions of the AC model. The default version (network DEF) was the one described above, implementing the serial anatomical structure of AC (Hackett 2015). In the second version (network CP), we modified W_{ee} by adding a direct excitatory-to-excitatory connection between core and parabelt. In the third version (network TB), we included a direct connection between the thalamus and the belt. CP and TB represent steps towards full connectivity and are no longer serial networks. The inclusion of extra excitatory-to-excitatory connections in these networks alters the excitation-inhibition balance compared to that of the DEF network. Therefore, we also constructed normalised versions of networks CP and TB, where W_{ee} is modified such that it has the same norm as W_{ee} in the DEF network. The norm is defined as the sum of all matrix elements. The normalised structures CPN and TBN retained the excitation-inhibition balance of the original default network.

Simulations employed the stimulus-repetition paradigm described in Sect. 2.5. We used the traditional method for calculating adaptation lifetime (Lü et al. 1992; Lu et al. 1992). This was to measure the peak amplitude of the N1m for each SOI and then to fit the following exponential function to the measurements

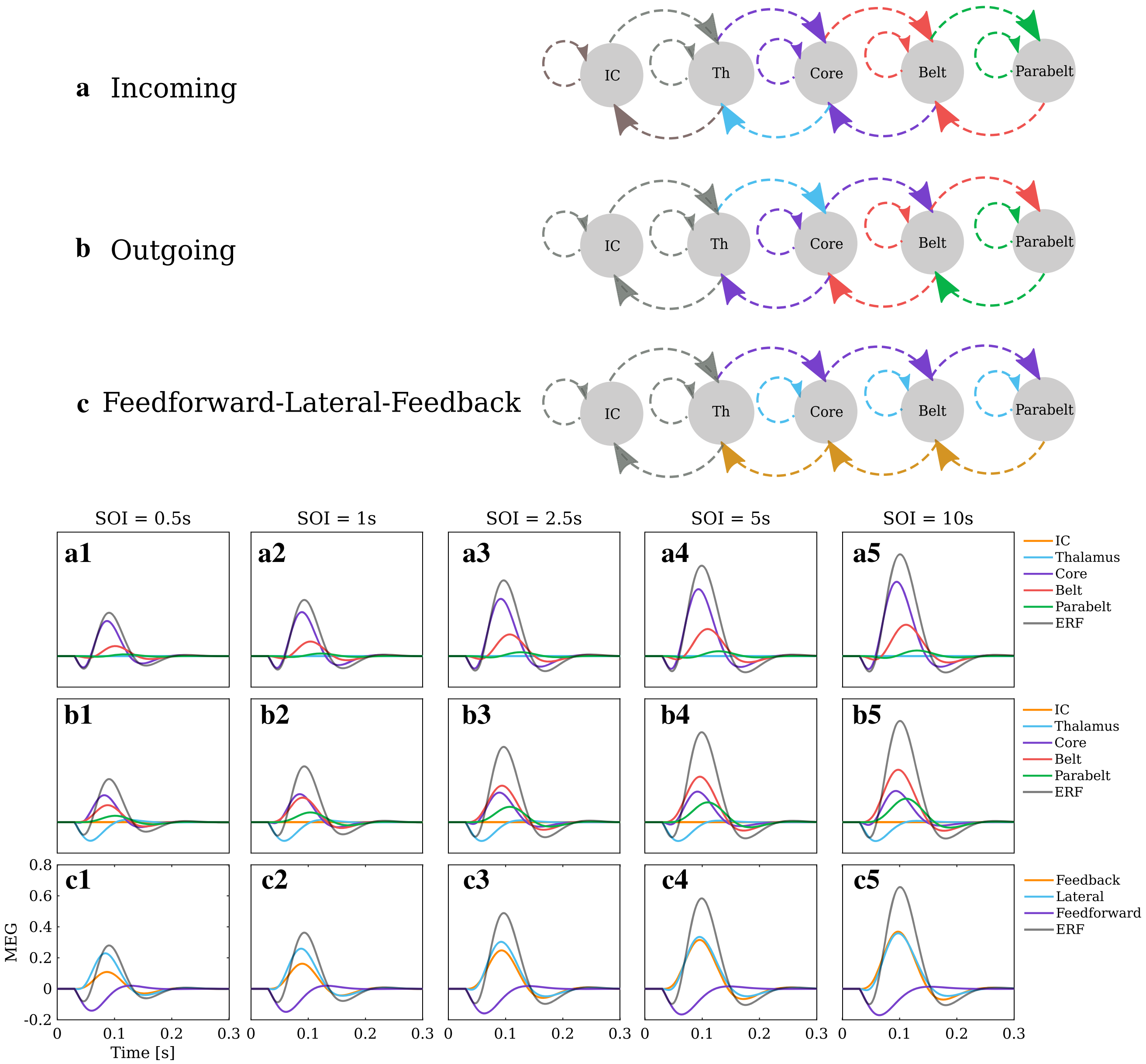

Fig. 8 ERF contributions by connection type and area. **a1–a5** When inspecting the contributions to the ERF according to incoming connections (equivalent to source modelling), the relative contributions from each area remained the same across SOI, and each contribution was scaled similarly by the adaptation process. The main contributors to the ERF are the core (purple) and the belt (red). **b1–b5** The contributions according to outgoing connections present a different picture. Here, the belt (red) and the parabelt (green) contributions show the strongest adaptation. They both increase steeply with increasing SOI, whereas the thalamus (blue) and core (purple) contributions remain relatively stable. **c1–c5** Feedback connections (orange) contribute to the ERF with a strongly adapting component which grows as a function of SOI. In contrast, the contributions from feedforward connections (purple), responsible for the P1m, show only weak adaptation. The contribution from lateral connections (blue) displays intermediate adaptation. Therefore, the adaptation of the N1m is largely due to the adaptation of the feedback connections

$$P_{\mathrm{fit}}(\mathrm{SOI}) = A\left(1 - \exp\left(-\frac{\mathrm{SOI} - t_0}{\tau_{\mathrm{soi}}}\right)\right). \tag{15}$$

Here, τ_{soi} is the time constant expressing the lifetime of adaptation; t_0 is the intercept with the abscissa, and A is the amplitude at which the exponential function saturates. All three parameters in Eq. (15) were fitting parameters. Note that in the model the saturation level A is equivalent to the peak amplitude of the response to the first stimulus, i.e., the initial state. For fitting we implemented an integral linear regression method to find suitable initial values (Jacquelin 2009) and, then, used a nonlinear regression function (nlin-

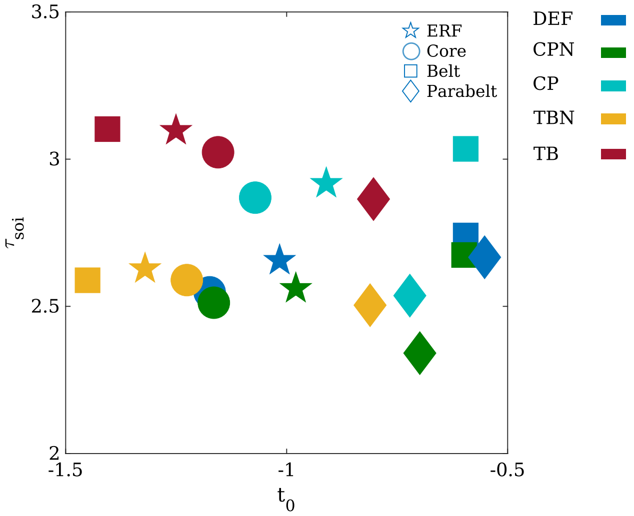

Fig. 9 The impact of network structure and excitation-inhibition balance on adaptation. The recovery time constant τ_{soi} and the intercept t_0 were obtained by fitting Eq. (15) to the peak amplitude of the simulated N1m (star), and of the state variables $u(t)$ of core (circle), belt (square), and parabelt (diamond). Blue symbols show τ_{soi} and t_0 for the default AC network (DEF, see Fig. 1). Adding a thalamocortical connection between thalamus and belt area (TB, red) has the strongest effect on τ_{soi} and t_0. The same network with normalised balanced excitation-inhibition (TBN, yellow) leads to smaller values of τ_{soi} and to little change of t_0. The addition of a corticocortical connection between core and parabelt (CP, cyan) leads to an increase of τ_{soi} everywhere except in parabelt. However, the same network with normalised excitation-inhibition balance (CPN, green) shows smaller values of τ_{soi}

fit) from MATLAB (The MathWorks, version R2018b) to estimate the fitting parameters. We performed the fitting procedure not only to the N1m peak amplitudes, but also to the peak amplitudes of the state variables $u(t)$ of the core, belt, and parabelt.

Figure 9 shows the fitting parameters τ_{soi} and t_0 characterising the SOI-dependence of the peak amplitude in the case of the ERF (star) and of the core (circle), belt (square), and parabelt (diamond) state variable $u(t)$. The results demonstrate that these parameters are sensitive to the network structure as well as to the excitation-inhibition balance. Two important observations can be made. First, the impact of the structural changes can be identified by comparisons between the default network (DEF, blue) and the normalised TBN (yellow) and CPN (green) network, which differ from DEF solely in terms of structure. Whereas τ_{soi} appears to be weakly affected, with values between 2.3 s and 2.7 s, the variation of t_0 is stronger, covering the range from − 1.5 s to − 0.5 s. Second, the effect of the excitation-inhibition balance on τ_{soi} and t_0 is revealed by comparisons between TBN (yellow) and TB (red) and between CPN (green) and CP (cyan). In each case, the normalised network versions TBN and CPN show less excitation than the non-normalised versions TB and CP. We see that the effect of adding excitation is to push τ_{soi} up by 500 ms. In contrast, t_0 of core and parabelt is only weakly affected by added excitation. Taken together, Fig. 9 shows that the modification of the excitation-inhibition balance has a larger effect on τ_{soi} and t_0 than a change of the network structure.

3.4 Is a single exponential function sufficient to explain recovery from adaptation?

Adaptation is traditionally quantified through fitting the single-exponential function of Eq. (15) to the peak amplitudes of the N1m. But does a single exponential actually describe the dependence of the ERF amplitude on SOI? Figure 10a indicates that this appears to be the case, at least when the number of data points is low. However, with our model we can easily generate ERF peak amplitudes for an arbitrary number of SOIs which would not be feasible experimentally. This is illustrated in Fig. 10b where 99 simulated ERF peak amplitudes (red points) are plotted as a function of SOI together with the corresponding fit (blue line). Figure 10b shows a systematic deviation of the fitting function (Eq. (15)) from these data. This deviation is highlighted in Fig. 10c where the data points in Fig. 10b are transformed by the $log(x)$ function. Figure 10c shows that at small SOIs ($\leq$1.5 s), the simulated data deviate much stronger from the fit than data at larger SOIs. This deviation might seem negligibly small. However, it indicates two major shortcomings of such exponential functions for explaining recovery from adaptation. First, the strong deviation at small SOIs, highlighted in the logarithmically scaled plot in Fig. 10c, puts a question mark on the general applicability of a single-exponential function for the description of the recovery process. Second, it questions the explanatory power of the fitting parameter t_0. This deviation between fit and data can be quantified more precisely by the local exponential saturation rate

$$f_j = \frac{F_j - F_{j+1}}{(F_j - F_{\text{inf}})(\text{SOI}_{j+1} - \text{SOI}_j)}, \tag{16}$$

where the Fs are simulated ERF peak amplitudes and j is the index of the data points (red points in Fig. 10b–d). F_{inf} is the amplitude at which the data points saturate. It is equivalent to the ERF peak amplitude at the initial state, this being the maximum possible value the simulated ERFs can have. The results of the computation of the local exponential saturation rate for the simulated data as well as the fit are shown in Fig. 10d, which for the fitting function given in Eq. (15) always provides the constant value $1/\tau_{soi}$. However, it also shows that simulated data points (red) deviate substantially from a constant value for SOIs smaller than 5 s.

In summary, the above results show that our description of the adaptation process as a collective reorganisation of the AC as a dynamical network also captures the behaviour of the N1m peak amplitude variation as a function of SOI.

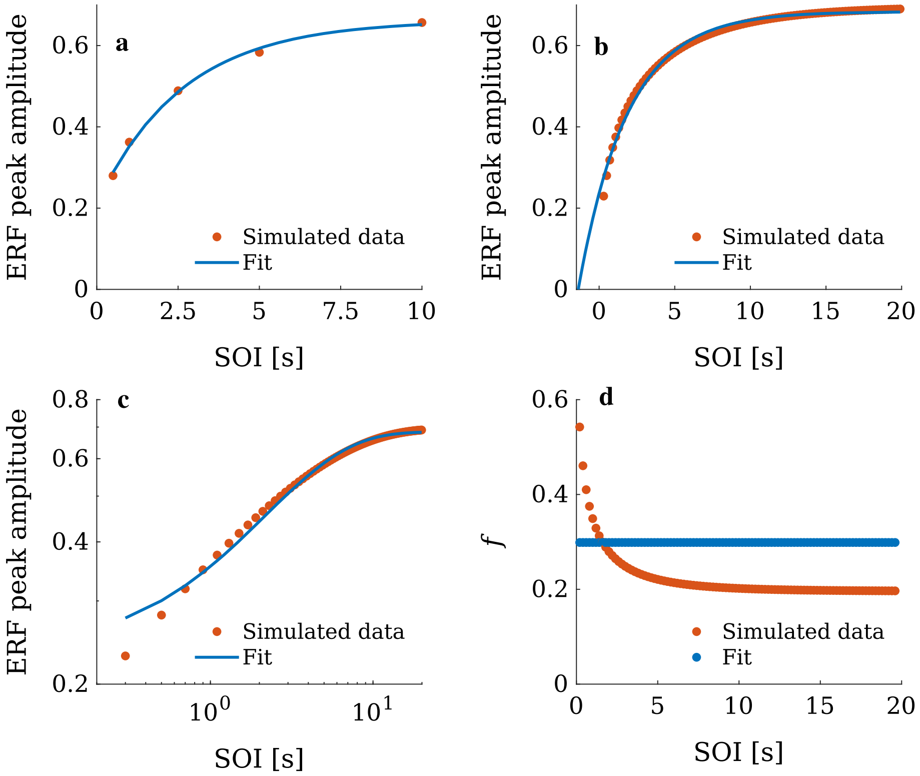

Fig. 10 A single exponential function does not capture the recovery from adaptation. **a** The fitting function of Eq. (15) appears to offer a reasonable approximation (blue line) of the SOI-dependence of the N1m peak amplitudes (red points) when there are only a few measurement points. **b** The situation, however, is different when a much larger number of SOIs can be used for revealing the true SOI-dependence of the N1m. There is a systematic deviation between the fitting function and the peak amplitudes. **c** The $log(x)$ transformation of the data points emphasises that there are clear differences between the data points and the fit for small and larger SOIs. **d** This deviation between the data points and the fit can be quantified by computing the local saturation rate f, given in Eq. (16), for any two consecutive data points. For the exponential fit, the local saturation rate f is constant, whereas for the simulated data points it monotonically decreases with increasing SOI and converges towards a constant value (≈ 0.2), different from the f obtained from the fit (≈ 0.3), only at large SOIs (≥ 10 s)

It turns out that for smaller SOIs this adaptation behaviour differs substantially from the widely-used single exponential function. As a consequence, if one estimates adaptation lifetimes through fitting such a function to amplitude data, the result might strongly depend on the choice of the sampling point.

4 Discussion

4.1 Main findings

We used mathematical modelling to investigate context sensitivity of auditory cortex specifically, how STSD modifies the systems dynamics of auditory cortex and how this modification becomes visible as the adaptation of the ERF associated with stimulus repetition. We took an approach similar to the one in our previous study (Hajizadeh et al. 2019) whereby the auditory cortex was characterised as a set of spatially distributed, mutually independent oscillators—normal modes—exposed through explicitly solving the state equations. Each normal mode is a global feature because it contributes to the activity of all cortical columns and depends on the anatomical structure of the entire auditory cortex. Compared to the traditional view that the ERF arises out of spatially discrete, local generators, our approach offers an alternative: the ERF is generated by a set of processes where each one is distributed over the whole network of the auditory cortex. That is, we go beyond describing activity of auditory cortex in terms of amplitude variations of the activity of spatially fixed cortical columns. In contrast, in our account, the activity of auditory cortex is described as oscillations of normal modes which are spread over the whole AC anatomy. In this view, the activity of an individual column emerges out of the interplay between the amplitudes, frequencies, and phases of all the normal modes of the system. An analogy for understanding stimulus-elicited brain activity in terms of normal modes is to think of a pebble thrown into a still pond. The ripples formed on the water's surface are functions of the size, shape, and the speed of the pebble (i.e., the stimulation), but also depend on the size, shape, and water quality of the pond (i.e., the system). If new pebbles are thrown before the previously formed ripples fade away, different locations on the pond surface oscillate based on the interference pattern of the old and the new ripples. The dynamics of AC as a spatially extended structure is no different than the pond. By stimulating AC, the activity propagates in time and space through the system. This propagation is then a function of the stimulus and of the anatomical structure of AC. The activity at each AC location oscillates as a result of the interference pattern of the normal modes which are spread over the whole AC (see Fig. 5k–o). That is, each location participates in multiple, overlapping oscillations that are occurring both in time and space. The MEG device then projects these oscillations onto single magnetic field values.

Expanding from Hajizadeh et al. (2019), the current study addressed adaptation due to stimulus repetition through the introduction of dynamical synapses to the model. This was achieved through two manoeuvres: First, we derived complete solutions to the system of Eqs. (1) and (2) even in cases where the connections are asymmetric, such as when STSD is in operation. Second, we used time-scale separation of the dynamics of STSD (Eq. (3)), exploiting the relative slowness of recovery from STSD in comparison to the fast evolution of the state variables (Eqs. (1) and (2)). As a result, we were able to describe the adapting auditory cortex as a set of normal modes modulated by the stimulation. In this approach, all possible system trajectories are solved in one go rather than simulated one at a time.

The current model replicates the experimentally observed adaptation of the ERF resulting from stimulus repetition. This can be observed as, for example, the peak amplitude of the N1m increasing monotonically as a function of SOI, roughly according to an exponentially saturating function. The N1m can be understood as an interference pattern of the superimposed normal modes, and in this view, its adaptation is explained as resulting from the modulations not only of the amplitudes but also of the angular frequencies ω_n of the normal modes. Indeed, adaptation should be seen as a complete reorganisation of the AC network where the reduction of the N1m amplitude is a by-product of the stimulation shifting the dispersion of the angular frequencies ω_n and decay rates γ_n of the normal modes.

While the adaptation of the N1m can be accounted for by changes in the underlying normal modes, the N1m is only a single landmark in the ERF. To gain a more complete view of how the dynamics of the system are modulated by previous stimulation, we inspected how the normal modes change as a function of SOI in the adapted state. The main characteristics of a normal mode are its frequency ν and decay rate γ, as displayed in Fig. 5f–j. Two observations could be made. First, there is a neat dispersion of the normal modes in the ν-γ plane where they land on a monotonically increasing curve, so that the higher the frequency, the faster the decay rate. Second, the effect of STSD is to push the normal modes upwards on this dispersion curve with respect to the initial state, this effect being larger the smaller the SOI is. We can thus view adaptation of the ERF in a novel way: each incoming stimulus leaves a memory trace behind as a change in the system dynamics so that all normal modes are shifted towards higher frequencies and faster decay rates. During the interval between successive stimuli, the memory trace decays so that the normal modes slide back towards their respective unadapted states. The degree to which a normal mode contributes to the MEG signal depends on two efficiency factors (see Eq. (13) and Fig. 6) and their product determines the actual contribution made by the normal mode to the MEG signal. Adaptation due to stimulus repetition shows up as a modulation of the efficiencies, which can either expand, shrink, or remain the same as SOI is modulated, depending on the normal mode.

Further, we found that adaptation is a network effect that depends not only on STSD. Namely, changing the anatomical structure of the network and/or the balance between excitation and inhibition led to marked changes in the lifetime of N1m adaptation, even though the parameters of STSD were kept constant. Also, inspecting the individual contributions to the ERF from the various areas, we found that the lifetime of adaptation varied across anatomical location.

4.2 Adaptation of the N1m: what are we measuring?

The current model of the AC replicates well the experimentally observed SOI-dependence of the ERF (see Fig. 4), and all main features of the waveforms can be traced back to the distinct contributions of the individual cortical areas, as laid out in Fig. 8. The identical rising slopes of the waveforms derive from the core, which provides the largest contribution to the MEG waveform at all SOIs and is also the main source of variation of the magnitude of the N1m peak. The belt also contributes to the overall amplitude, especially at longer SOIs. The magnitude of the parabelt contribution to the ERF is negligible at all SOIs. However, this disguises the influence of the parabelt on the overall dynamics of the system, as shown by our previous results (Hajizadeh et al. 2019): small changes in the connection values within the parabelt result in sizeable modulations of the N1m response, even though the parabelt's direct contribution to the N1m is minimal. Further, we found that the adaptation of the N1m is largely due the adaptation of the contribution generated by the feedback connections, while the feedforward and lateral (intrafield) components remained relatively stable across SOI (Fig. 8).

We emphasise that in the model, the ERF signal is the weighted superposition of multiple normal modes as distributed over the core, belt, and parabelt (Fig. 5). Therefore, the N1m peak represents an event in an interference pattern rather than anything real. That is, the peak of the N1m at about 100 ms is incidental in the sense that it does not represent the peak of any normal mode nor that of the activity of any individual area in the AC. In consequence, observing adaptation as SOI-related changes in the N1m on its own reveals very little of how the underlying dynamics are changing. To understand what is driving N1m adaptation, we investigated how the interference pattern of the normal modes changes as SOI is varied.

Figure 5 shows the ERF in terms of its normal mode components, which paint a consistent pattern across the five SOI conditions. These components come in a variety of peak amplitudes and latencies, and they can also have opposite phases, which contributes to mutual cancellations when the modes are summed up to the ERF signal (see also Fig. 7). Interestingly, each normal mode reaches its global absolute peak well before the N1m even starts to emerge. Yet, in the ERF, the N1m is the dominating wave. This is due to the low-frequency modes largely cancelling each other out during the first 70 ms, when the modes reach their global extrema. Because of this cancellation effect, the P1m response has a low amplitude, even though it occurs when the normal modes are at their most vigorous (see Fig. 7). Subsequently, when all the normal modes are well into their decay phase, the N1m emerges as an interference pattern of the two low-frequency normal modes with the highest amplitudes but opposite phases.

On the above basis, we can understand the adaptation of the N1m in terms of the behaviour of the two dominating normal modes of auditory cortex. That is, adaptation arises out of two factors which contribute unequally in different SOI ranges. As shown in the left column of Fig. 5, with the fast stimulation rates (SOIs of 0.5 s, and 1 s), the normal modes are clearly attenuated in amplitude compared to their counterparts in the 10-s SOI condition (representing the unadapted state). Furthermore, mirroring the adaptation of the N1m (Fig. 4), this attenuation is much larger when SOI is 0.5 s than when SOI is 1 s. In contrast, when the SOI is larger (2.5 s, 5 s, and 10 s), the amplitudes of the normal modes become insensitive to changes in SOI. Indeed, the normal mode with the lowest frequency (purple curve in Fig. 5) *decreases* slightly in amplitude as SOI is increased from 2.5 s to 10 s, while the N1m grows in amplitude. In this case, the attenuation of the N1m is explained by the changes in the frequencies rather than the amplitudes of the two dominating normal modes: the mode with the largest absolute magnitude (green curve in Fig. 5) remains relatively stable in terms of amplitude and frequency, while the mode with the second-largest magnitude but opposing phase (purple curve in Fig. 5) increases in frequency as SOI decreases. Because of this difference in their frequency behaviour and phase, the dominant normal modes sum up to an N1m response that decreases with decreasing SOI.

The adaptation of the N1m is usually described with the single exponentially saturating function of Eq. (15). This captures the behaviour of the peak amplitude of the N1m, namely, its initially rapid increase as a function of SOI followed by a levelling off at longer SOI. This description might be adequate when the number of data points is low (Fig. 10a). However, our model predicts that the true dependence of the N1m peak amplitude on SOI is insufficiently described by a single exponential function (Fig. 10b–d). This could be a consequence of the N1m peak amplitude being determined by two different normal-mode properties, viz. due to normal mode modulations at short SOIs and to frequency modulations at longer SOIs. Thus, adaptation lifetime as estimated with the single exponential might work better as a relative rather than an absolute measure. Even if it fails to describe amplitude behaviour at short SOIs, it still allows one to compare lifetimes across experimental conditions, brain regions, and subjects.

4.3 Linking ERF adaptation to the network structure of auditory cortex

Physiological studies usually consider the link between STSD and adaptation from the point of view of single-unit dynamics (Ulanovsky et al. 2004; Wehr and Zador 2003, 2005). When one observes a global, spatially-averaged measure of neuronal activity such as the ERF, our results indicate that STSD is not the only factor shaping adaptation. Instead, adaptation becomes a system property, modulated by anatomical structure. This is unsurprising given that all normal-mode properties (angular frequency ω, decay rate γ, phase, spatial structure) arise from the coefficient matrix in Eq. (4), which in turn depends on the anatomical structure of AC as expressed in the weight matrices. We varied the structure of the original AC model (Fig. 1) by adding shortcut connections from the thalamus to the belt, or from the core to the parabelt. We also varied the balance between excitation and inhibition. All other aspects of the model were kept untouched, including the time constants of the state equations and those of STSD. Nevertheless, the structural modulations in themselves caused sizeable variations in the way the N1m became adapted by repeated stimulation: the parameter t_0 varied between -1.4 and -0.9 s, and τ_{soi}, the adaptation lifetime, varied between 2.5 and 3.1 s. In general, changing the excitation-inhibition balance by adding excitatory connections increased the lifetime of adaptation.

We also derived the individual contributions from each cortical area (core, belt, parabelt) to the overall ERF in order to inspect whether adaptation has a spatial variation. This was done for all the structural modulations studied above. Experimentally, this would be equivalent to applying source modelling to the ERF signal to tease out the contributions from various areas of cortex. We found that, in general, the adaptation of the ERF did not coincide with that of any of the contributions of the individual areas in terms of t_0 and τ_{soi}. The lifetime of adaptation tended to be some 200 ms shorter in the core than in the belt. The parabelt had the shortest τ_{soi}, except in the default AC model, where the belt and the parabelt had similar lifetimes of adaptation. These results agree qualitatively with those of Lu et al. (1992), who found that the contribution of primary auditory cortex to the N1m has a shorter lifetime of adaptation (by seconds) than the contribution from association areas. A similar pattern was observed by Uusitalo et al. (2006) in visual cortex, where the adaptation lifetime increases (by seconds) as one moves further away from primary visual cortex. The spatial variation of adaptation lifetime produced by our model is much smaller than that found experimentally, and the factors determining the size of this effect will be addressed elsewhere.

Importantly, the above spatial variation of adaptation belies a much stronger effect of anatomy on adaptation. This is evident in Fig. 8b1–b5 which break down the ERF according to the connections originating from each area. For each area, this measure is proportional to the output emanating from that area, that is, to the firing rate multiplied by the connection strength. It can therefore be interpreted as the de facto impact that the area has on its neighbours and on itself. The impact of the core remains stable, increasing only around 10 % over the SOI range. In stark contrast, the impact of the belt and parabelt is highly sensitive to stimulation rate: it increases linearly by a factor of three as one increases SOI from 0.5 s to 10 s. That is, there is hardly any adaptation present in the impact that the core has, while the impact of the belt and the parabelt exhibits strong adaptation. Although we did not determine τ_{soi} for these impacts, it is evident that on this metric, adaptation lifetime is orders of magnitude larger in the belt and parabelt than in the core. We emphasise that these effects are not directly visible in the ERF, even if one measures τ_{soi} separately for each area (corresponding to source modelling). Further, the presence of a spatial gradient of adaptation lifetime would have interesting implications for understanding memory in auditory cortex. Namely, the anatomy of AC may serve as a temporal map, where secondary areas, in functional terms, hold information over several seconds and where the core integrates the current signal with the memory-laden feedback from the secondary areas. This style of temporal mapping might be crucial for the processing of auditory signals with a complex spectrotemporal structure and warrants further investigation.

4.4 Comparison to other models of auditory cortex and ERF generation

The role of STSD in AC dynamics has been investigated in a number of previous modelling studies. Loebel et al. (2007) developed a model of the primary AC where each iso-frequency column was described as a network with Wilson and Cowan (1972) dynamics and with STSD. The model can account for multiple experimental findings such as the frequency tuning curves of neurons and the dependence of forward masking in two-tone stimulation on the temporal separation between the tones. In a later work, Yarden and Nelken (2017) demonstrated that this model is able to replicate stimulus-specific adaptation. Goudar and Buonomano (2014) modelled primary auditory cortex with simulated spiking neurons and found that short-term synaptic plasticity accounted for context-dependent suppression and enhancement of the response to the second tone in a two-tone paradigm. Similar order-selectivity in responses to vocalisation stimuli was found by Lee and Buonomano (2012), who modelled a single cortical column with spiking neurons. Again, STSD accounted for the neurons responding differentially to vocalisations presented in the forward and reverse directions. Wang and Knösche (2013) replicated the adaptation of the N1m due to stimulus repetition in a model of a single cortical area, where each unit was an expanded version of the neural mass model of Jansen and Rit (1995), which describes interactions between neurons in the granular, supragranular, and infragranular layers. The model included STSD of excitatory synapses, and good agreement with experimental data was achieved by adjusting the inter- and intralaminar connections via Bayesian inference.

The above studies are thematically related to the current approach in that synaptic depression is shown to account for experimental data. However, they are limited to describing either primary auditory cortex or a single column with a relatively high resolution and, with the exception of Wang and Knösche (2013), replicate single-unit activity. In contrast, our approach for understanding ERF generation is to capture the dynamics of the whole of AC, rather than that of a single field. To this end, we implemented the serial core-belt-parabelt structure in a model that anchors ERF generation to spatially distributed normal modes. Therefore, our approach diverges from the above studies in terms of how AC is described and in the kind of explanation given for the data. We note that while we employed the extreme low resolution of describing each area as a single unit, our approach is not wedded to any particular spatial resolution. Our previous studies (Hajizadeh et al. 2019, 2021) used spectral methods similar to the ones employed here (though without STSD) for investigating the normal modes in a system of 240 units representing cortical columns distributed over subcortical areas and 13 tonotopically organised cortical fields. Importantly, the current results open up the possibility of applying spectral methods for studying STSD modulation of AC dynamics in an expanded model with a much higher spatial resolution than here. We note that boosting the number of units adds very little computational cost. Numerical simulations based on Eqs. (1), (2), and (3) are computationally expensive for large coupled networks and can be error-prone due to numerical errors and sensitivity to initial conditions. The spectral approach championed here, in comparison, is computationally fast and readily unveils the dependencies between the systems parameters and the solutions.

Probably the most influential style of neural mass modelling is Dynamic Causal Modelling (DCM) introduced by Friston et al. (2003). This estimates the coupling between different brain regions and how this is modulated by stimulation. Each region is described by a biophysical neural mass model, and Bayesian inference is then used for the parameter estimation to identify the best model to explain the experimental data. The DCM approach has been applied to ERPs and ERFs (see, for example, David et al. 2006; Garrido et al. 2007; Kiebel et al. 2006, 2009), the hemodynamic response of functional magnetic resonance imaging (fMRI) (for example Friston et al. 2019; Stephan et al. 2007) and the neurovascular coupling underlying combined fMRI and MEG/EEG data (for example, Friston et al. 2019; Jafarian et al. 2020). When applying the method to ERPs and ERFs, the biophysical model is based on the Jansen and Rit (1995) approach. Estimates are then derived for intrinsic connections within brain regions as well as for feedforward, feedback, and lateral connections between brain regions.

While our spectral approach and DCM both seek to explain evoked responses, the two diverge on a number of points. First, DCM aims to explain single-subject ERF data in terms of connection strengths between discrete sources. The method is essentially a refinement of source localisation, where source location is complemented by information about the coupling strength between the sources. In contrast, our approach regards individual sources and their connections as only part of the explanation. From the point of view of the system dynamics, the spatially distributed normal modes provide a more revealing account of the ERF. Of course, whether normal modes can be observed experimentally is an interesting question beyond the scope of the current study. Second, while the spatial resolution in the current model was at one unit per cortical area—the same as in Garrido et al. (2009)—spatial resolution is not a limiting issue in our approach, as discussed above. In comparison, DCM places bounds on the size of the network that can be used for modelling brain activity. Namely, increasing the number of units leads to an exponential increase in the number of connections, which are all free parameters to be estimated. As pointed out by Garrido et al. (2009), this results in inter-subject variability becoming larger, making it hard to establish patterns of coupling changes across subjects. Third, DCM is designed to be used with discrete source models of the ERP and ERF, with each area represented by a single unit of the biophysical model. In contrast, the number of units per area is not limited in our approach, and is determined by the phenomenon to be explained. For example, modelling frequency interactions (e.g., the frequency mismatch response) with one unit per area can be done with DCM (Garrido et al. 2007) but with our approach, an expansion of the model to include tonotopic maps in each area would be required. This essentially reflects the fundamentally mechanistic nature of our modelling style.

5 Outlook

There is scope for expanding the current model in several ways. First, as mentioned above, the modelling of cross-frequency effects would require the implementation of tonotopic maps, such as in the previous versions of the model (Hajizadeh et al. 2019, 2021; May and Tiitinen 2013; May et al. 2015). This would allow one to gain fresh insight into the generation of the MMN and SSA in terms of normal modes. Time constants for SSA have been reported to occur on multiple time scales (Ulanovsky et al. 2004), and there might be scope to study this with our modelling approach, in view of our finding that anatomical structure in itself introduces variations to adaptation lifetime, even when the time constants for STSD are spatially homogeneous.

Second, while the core-belt-parabelt structure of AC is a common feature among the auditory cortices of mammals (Hackett 2015), there is a wide variety in the size and organisation of AC areas across species, and the functional consequences of this variety are unknown. Hence, a logical next step would be to expand the model towards more realistic structures of auditory cortex of different species, and to investigate to what extent adaptation is a network effect whose cross-species variations can be explained in terms of differences in the anatomical structure of the AC. Further, one might be able to use the current methodology as a tool for exploring the currently unknown organisation of the human auditory cortex. One possibility might be to combine the current methods with DCM by using the current model as the biophysical DCM model. The free parameters would be the STSD time constants as well as the parcellation of the core, belt, and parabelt into individual fields, each one represented by a unit of the model. While the STSD would presumably be subject-specific, the parcellation would be fixed across subjects.

Lastly, while the brain is usually regarded as highly nonlinear, it might turn out to be a clandestine self-lineariser, using STSD as a mechanism which pushes the system dynamics into the linear range. This might allow the transition from chaotic regions into states where normal modes appear. As Kerschen et al. (2009) pointed out, normal modes of linear systems differ from those of non-linear systems in that they are decoupled from one another. This means that they have two special properties: (1) invariance, whereby several normal modes can coexist in the system at the same time without modulating each other; (2) modal superposition whereby the oscillations of a unit is a linear combination of individual normal modes. We suspect that these properties could have functional benefits: normal modes of linear systems, each with its own spatial profile, could function as stable and overlapping representational tokens supporting population coding, where each neuron can take part in representing more than one thing at the same time. This style of representation might aid processes such as sensory binding and attention control. Namely, the features of sensory stimuli are represented in a distributed fashion, in specialised regions across cortex, yet this information is melded together into unitary percepts. Sensory binding refers to this process of melding, and it seems to involve the long-distance synchronisation of the spatially disparate neuronal populations representing the individual features (Bertrand and Tallon-Baudry 2000; Ghiani et al. 2021). Selective attention is likewise associated with coherence: the cortical neurons representing the attended stimulus produce enhanced, synchronised gamma-band oscillations (Fries 2015). Normal modes could provide instantaneous coupling needed in binding and attention, allowing for individual cortical neurons separated by long distances to become synchronised even without direct connections between them. The dominant normal mode in cortex might then correspond to the attended, perceptually bound stimulus. A corollary of this is that functional cell assemblies generated in this fashion cannot be predicted just by observing the anatomical connections between the cells. This widens the view onto the generation of cell assemblies, which are usually understood in terms of communication between senders and receivers (Hahn et al. 2019) and strong interconnections arising out of Hebbian learning (Gerstein et al. 1989; Wennekers et al. 2003). With normal modes, the synchronisation between two cells depends more on the afferent stimulation and system dynamics than it does on the strength or quality of the interconnection. Moreover, normal modes might provide the mechanism whereby weakly connected populations can synchronise, before Hebbian learning has had time to take effect.

Funding Open Access funding enabled and organized by Projekt DEAL. This work has received funding from the European Union's Horizon 2020 research and innovation programme (Grant Agreement 763959). Further, this research was supported by the project "Erweiterung translationaler Forschung zu neuronalen Mechanismen des Lernens (M. mulatta)" from the European Regional Development Fund (ERDF; project identifier ZS/2018/11/96066). We also acknowledge the support by a Mathematical Modeling and Simulation (MMS) seed money grant provided by the Leibniz-MMS-Network of the Leibniz association.

Data availability The data analysed during the current study is available from the corresponding author on reasonable request.

Code availability The code used in the current study is available from the corresponding author on reasonable request.

Declarations

Conflicts of interest The authors declare no conflict of interest.

Ethical approval The MEG study was approved by the Ethics Committee of the Otto-von-Guericke University Magdeburg.

Consent to participate The subject gave written informed consent to participate in the MEG study.

Consent for publication All the authors of this study declare their consent for publishing this research.

Open Access This article is licensed under a Creative Commons Attribution 4.0 International License, which permits use, sharing, adaptation, distribution and reproduction in any medium or format, as long as you give appropriate credit to the original author(s) and the source, provide a link to the Creative Commons licence, and indicate if changes were made. The images or other third party material in this article are included in the article's Creative Commons licence, unless indicated otherwise in a credit line to the material. If material is not included in the article's Creative Commons licence and your intended use is not permitted by statutory regulation or exceeds the permitted use, you will need to obtain permission directly from the copyright holder. To view a copy of this licence, visit http://creativecommons.org/licenses/by/4.0/.

References

Abbott LF, Varela JA, Sen K, Nelson SB (1997) Synaptic depression and cortical gain control. Science 275:220–224

Ahlfors SP, Wreh C (2015) Modelling the effect of dendritic input location on MEG and EEG source dipoles. Med Biol Eng Comput 53:879–887

Ahlfors SP, Jones SR, Ahveninen J, Hämäläinen MS, Belliveau JW, Bar M (2015) Direction of magnetoencephalography sources associated with feedback and feedforward contributions in a visual object recognition task. Neurosci Lett 585:149–154

Allen GI, Korn H, Oshima T (1975) The mode of synaptic linkage in the cerebro-ponto-cerebellar pathway of the cat. I. Responses in the branchium pontis. Exp Brain Res 24:1–14

Antunes FM, Nelken I, Covey E, Malmierca MS (2010) Stimulus-specific adaptation in the auditory thalamus of the anesthetized rat. PLoS ONE 5:e14071

Asari H, Zador AM (2009) Long-lasting context dependence constraints neural coding models in rodent auditory cortex. J Neurophysiol 102:2638–2656

Bastos AM, Usrey WM, Adams RA, Mangun GR, Fries P, Friston KJ (2012) Canonical microcircuits for predictive coding. Neuron 76:695–711

Benda J (2021) Neural adaptation. Curr Biol 31:R110–R116

Benda J, Longtin A, Maler L (2005) Spike-frequency adaptation separates transient communication signals from background oscillations. J Neurosci 25:2312–2321

Bertrand O, Tallon-Baudry C (2000) Oscillatory gamma activity in humans: a possible role for object representation. Int J Psychophysiol 38:211-233

Brechmann A, Gaschler-Markefski B, Sohr M, Yoneda K, Kaulisch T, Scheich H (2007) Working memory-specific activity in auditory cortex: potential correlates of sequential processing and maintenance. Cereb Cortex 17:2544–2552

Brosch M, Schreiner CE (2000) Sequence sensitivity of neurons in cat primary auditory cortex. Cereb Cortex 10:1155–1167

Brosch M, Schulz A, Scheich H (1999) Processing of sound sequences in macaque auditory cortex: response enhancement. J Neurophysiol 82:1542–1559

Budd TW, Michie PT (1994) Facilitation of the N1 peak of the auditory ERP at short stimulus intervals. NeuroReport 5:2513–2516

Budd TW, Barry RJ, Gordon E, Rennie C, Michie PT (1998) Decrement of the N1 auditory event-related potential with stimulus repetition: habituation vs. refractoriness. Int J Psychophysiol 31:51–68

Butler RA (1968) Effect of changes in stimulus frequency and intensity on habituation of the human vertex potential. J Acoust Soc Am 44:945–950

Dale A, Sereno M (1993) Improved localization of cortical activity by combining EEG and MEG with MRI cortical surface reconstruction: a linear approach. J Cogn Neurosci 5:162–176

David SV, Shamma SA (2013) Integration over multiple timescales in primary auditory cortex. J Neurosci 33:19154–19166

David O, Kiebel SJ, Harrison LM, Mattout J, Kilner JM, Friston KJ (2006) Dynamic causal modeling of evoked responses in EEG and MEG. Neuroimage 30:1255–1272

Davis H, Mast T, Yoshie N, Zerlin N (1966) The slow response of the human cortex to auditory stimuli: recovery process. Electroencephalogr Clin Neurophysiol 21:105–113

Finlayson PG, Adam TJ (1997) Excitatory and inhibitory response adaptation in the superior olive complex affects binaural acoustic processing. Hear Res 103:1–18

Fioravante D, Regehr WG (2011) Short-term forms of presynaptic plasticity. Curr Opin Neurobiol 21:269–274

Fortune ES, Rose GJ (2001) Short-term synaptic plasticity as a temporal filter. Trends Neurosci 24:381–385

Friauf E, Fischer AU, Fuhr MF (2015) Synaptic plasticity in the auditory system: a review. Cell Tissue Res 361:177–213

Fries P (2015) Rhythms for cognition: communication through coherence. Neuron 7:220–235

Friston K (2005) A theory of cortical responses. Philos Trans R Soc 360:815–836

Friston KJ, Harrison L, Penny W (2003) Dynamic causal modelling. Neuroimage 19:1273–1302

Friston KJ, Preller KH, Mathys C, Cagnan H, Heinzle J, Razi A, Zeidman P (2019) Dynamic causal modelling revisited. Neuroimage 199:730–744

Garrido MI, Kilner JM, Kiebel SJ, Stephan KE, Friston KJ (2007) Dynamic causal modelling of evoked potentials: a reproducibility study. Neuroimage 36:571–580

Garrido MI, Kilner JM, Kiebel SJ, Stephan KE, Baldeweg T, Friston KJ (2009) Repetition suppression and plasticity in the human brain. Neuroimage 48:269–279

Gerstein GL, Bedenbaugh P, Aersten AMHJ (1989) Neural assemblies. IEEE Trans Biomed Eng 36:4–14

Ghiani A, Maniglia M, Battaglini L, Melcher D, Ronconi L (2021) Binding mechanisms in visual perception and their link with neural oscillations: a review of evidence from tACS. Front Psychol 12:643677

Goudar V, Buonomano DV (2014) Useful dynamic regimes emerge in recurrent networks. Nat Neurosci 17:487–489

Hackett TA (2015) Anatomic organization of the auditory cortex. Handbook of clinical neurology, vol 2, p 129

Hackett TA, de la Mothe LA, Camalier CR, Falchier A, Lakatos P, Kajikawa Y, Schroeder CE (2014) Feedforward and feedback projections of caudal belt and parabelt areas of auditory cortex: refining the hierarchical model. Front Neurosci 8:72

Hahn G, Ponce-Alvarez A, Deco G, Aersten A, Kumar A (2019) Portraits of communication in neural networks. Nat Rev Neurosci 20:117–127

Hajizadeh A, Matysiak A, May PJC, König R (2019) Explaining event-related fields by a mechanistic model encapsulating the anatomical structure of auditory cortex. Biol Cybern 113:321–345

Hajizadeh A, Matysiak A, Brechmann A, König R, May PJC (2021) Why do humans have unique auditory event-related fields? Evidence from computational modeling and MEG experiments. Psychophysiology 58:e13769

Hämäläinen M, Ilmoniemi R (1994) Interpreting magnetic fields of the brain: minimum norm estimates. Med Biol Eng Comput 32:35–42

Hämäläinen M, Hari R, Ilmoniemi RJ, Knuutila J, Lounasmaa OV (1993) Magnetoencephalography-theory, instrumentation, and applications to non-invasive studies of the working human brain. Rev Mod Phys 65:413–497

Hari R, Kaila K, Katila T, Tuomisto T, Varpula T (1982) Interstimulus interval dependence of the auditory vertex response and its magnetic counterpart: implications for their neural generation. Electroencephalogr Clin Neurophysiol 54:561–569

Hopfield J, Tank D (1986) Computing with neural circuits: a model. Science 233:625–633

Huang Y, Matysiak A, Heil P, König R, Brosch M (2016) Persistent neural activity in auditory cortex is related to auditory working memory in humans and nonhuman primates. eLife 5:e15441

Imada T, Watanabe M, Mashiko T, Kotani M (1997) The silent period between sounds has a stronger effect than the interstimulus interval on auditory evoked magnetic fields. Electroencephalogr Clin Neurophysiol 102:37–45

Ioannides AA, Popescu M, Otsuka A, Bezerianos A, Liu L (2003) Magnetoencephalographic evidence of the interhemispheric asymmetry in echoic memory lifetime and its dependence on handedness and gender. Neuroimage 19:1061–1075

Jacquelin J (2009) Régressions et équations intégrales. https://www.scribd.com/doc/14674814/Regressions-et-equations-integrales. Accessed 11 Sept 2020

Jafarian A, Litvak V, Cagnan H, Friston K, Zeidman P (2020) Comparing dynamic causal models of neurovascular coupling with fMRI and EEG/MEG. Neuroimage 216:116734

Jansen BH, Rit VG (1995) Electroencephalogram and visual evoked potential generation in a mathematical model of coupled cortical columns. Biol Cybern 73:357–366

Kaas JH, Hackett TA (2000) Subdivisions of auditory cortex and processing streams in primates. Proc Natl Acad Sci USA 97:11793–11799

Katznelson RD (1981) Normal modes of the brain: neuroanatomical basis and a physiological theoretical model. In: Nunez PL (ed) Electric fields of the brain: the neurophysics of EEG. Oxford University Press, pp 401–442

Kerschen G, Peeters M, Golinval JC, Vakakis AF (2009) Nonlinear normal modes, part I: a useful framework for the structural dynamicist. Mech Syst Signal Process 23:170–194

Kiebel SJ, David O, Friston KJ (2006) Dynamic causal modelling of evoked responses in EEG/MEG with lead field parameterization. Neuroimage 30:1273–1284

Kiebel SJ, Garrido MI, Moran R, Chen C-C, Friston KJ (2009) Dynamic causal modelling for EEG/MEG. Hum Brain Mapp 30:1866–1876

King AJ, Nelken I (2009) Unraveling the principles of auditory cortical processing: can we learn from the visual system? Nat Neurosci 12:698–701

Kohashi T, Lube AJ, Yang JH, Roberts-Gaddipati PS, Carlson BA (2021) Pauses during communication release behavioral habituation through recovery from synaptic depression. Curr Biol 13:3145–3152

Kudela P, Boatman-Reich D, Beeman D, Anderson WS (2018) Modeling neural adaptation in auditory cortex. Front Neural Circuits 12:72

Kuehn C (2015) Multiple time scale dynamics. Springer, Cham

Lee TP, Buonomano DV (2012) Unsupervised formation of vocalisation-sensitive neurons: a cortical model based on short-term and homeostatic plasticity. Neural Comput 24:2579–2603

Loebel A, Nelken I, Tsodyks M (2007) Processing of sound by population spikes in a model of primary auditory cortex. Front Neurosci 1:197–209

Loveless N, Levänen S, Jousmäki V, Sams M, Hari R (1996) Temporal integration in auditory sensory memory: neuromagnetic evidence. Electroencephalogr Clin Neurophysiol 100:220–228

Lü Z-L, Williamson J, Kaufman L (1992) Human auditory primary and association cortex have differing lifetimes for activation traces. Brain Res 572:236–241

Lu Z-L, Williamson SJ, Kaufman L (1992) Behavioral lifetime of human auditory sensory memory predicted by physiological measures. Science 258:1668–1670

Malmierca MS, Cristaudo S, Pérez-González D, Covey E (2009) Stimulus-specific adaptation in the inferior colliculus of the anesthetized rat. J Neurosci 29:5483–5493

May PJC (2002) Do EEG and MEG measure dynamically different properties of neural activity? In: Nowak H, Haueisen J, Giesler F, Huonker R (eds) Proceedings of the 13th international conference on biomagnetism. International congress series. VDE Verlag GmbH, Berlin, pp 709–711

May PJC, Tiitinen H (2004) Auditory scene analysis and sensory memory: the role of the auditory N100m. Neurol Clin Neurophysiol 19

May PJC (2021) The adaptation model offers a challenge for the predictive coding account of mismatch negativity. Front Hum Neurosci 15:721574

May P, Tiitinen H (2001) Human cortical processing of auditory events over time. NeuroReport 12:573–577

May PJC, Tiitinen H (2010) Mismatch negativity (MMN), the deviance-elicited auditory deflection, explained. Psychophysiology 47:66–122

May PJC, Tiitinen H (2013) Temporal binding of sound emerges out of anatomical structure and synaptic dynamics of auditory cortex. Front Comput Neurosci 7:152

May P, Tiitinen H, Ilmoniemi RJ, Nyman G, Taylor JG, Näätänen R (1999) Frequency change detection in human auditory cortex. J Comput Neurosci 6:99–120

May P, Tiitinen H, Westö J (2015) Computational modelling suggests that temporal integration results from synaptic adaptation in auditory cortex. Eur J Neurosci 41:615–630

McEvoy L, Levänen S, Loveless N (1997) Temporal characteristics of auditory sensory memory: neuromagnetic evidence. Psychophysiology 34:308–316

Megela AL, Teyler TJ (1979) Habituation and the human evoked potential. J Comp Physiol Psychol 93(6):1154–1170

Michon JA (1978) The making of the present: a tutorial review. In Requin J (ed) Attention and performance, vol VII, pp 89–109

Mill R, Coath M, Wennekers T, Denham SL (2011) A neurocomputational model of stimulus-specific adaptation to oddball and markov sequences. PLoS Comput Biol 7:e1002117

Mosher JC, Leahy RM (1999) Source localization using recursively applied and projected (RAP) MUSIC. IEEE Tans Signal Process 47:332–340

Mosher JC, Lewis PS, Leahy RM (1992) Multiple dipole modeling and localization from spatio-temporal MEG data. IEEE Trans Biomed Eng 39:541–557

Motanis H, Seay MJ, Buonomano DV (2018) Short-term synaptic plasticity as a mechanism for sensory timing. Trends Neurosci 41:701–711

Näätänen R (1990) The role of attention in auditory information processing as revealed by event-related potentials and other brain measures of cognitive function. Behav Brain Sci 13:201–288

Näätänen R (1992) Attention and brain function. Lawrence Erlbaum Associates, Hillsdale

Näätänen R, Gaillard AW, Mäntysalo S (1978) Early selective-attention effect on evoked potential reinterpreted. Acta Physiol (Oxf) 42:313–329

Näätänen R, Schröger E, Karakas S, Tervaniemi M, Paavilainen P (1993) Development of a memory trace for a complex sound in the human brain. NeuroReport 4:503–506

Nelken I (2004) Processing of complex stimuli and natural scenes in the auditory cortex. Curr Opin Neurobiol 14:474–480

Nelson A, Lassman FM, Hoel RL (1969) The effect of variable-interval and fixed-interval signal presentation schedules on the auditory evoked response. J Speech Hear Res 12:199–209

Nuding SC, Chen GD, Sinex DG (1999) Monaural response properties of single neurons in the chinchilla inferior colliculus. Hear Res 131:89–106

Palombi PS, Caspary DM (1996) Physiology of the aged fischer 344 rat inferior colliculus: responses to contralateral monaural stimuli. J Neurophysiol 76:3114–3125

Pérez-González D, Malmierca MS (2014) Adaptation in the auditory system: an overview. Front Integr Neurosci 8:1–10

Pérez-González D, Malmierca MS, Covey E (2005) Novelty detector neurons in the mammalian auditory midbrain. Eur J Neurosci 22:2879–2885

Rescorla M (2021) Bayesian modeling of the mind: from norms to neurons. Wiley Interdiscip Rev Cognit Sci 12:e1540

Rosburg T, Zimmerer K, Huonker R (2010) Short-term habituation of auditory evoked potential and neuromagentic field components in dependence of the interstimulus interval. Exp Brain Res 205:559–570

Rosenbaum R, Rubin J, Soiron B (2012) Short term synaptic depression imposes a frequency dependent filter on synaptic information transfer. PLoS ONE 8:e1002557

Sable JJ, Low KA, Maclin EL, Fabiani M, Gratton G (2004) Latent inhibition mediates N1 attenuation to repeating sounds. Psychophysiology 41:636–642

Salmasi M, Loebel A, Glasauer S, Stemmler M (2019) Short-term synaptic depression can increase the rate of information transfer at a release site. PLoS Comput Biol 15:1–21

Scherg M (1990) Fundamentals of dipole source potential analysis. In: Grandori F, Hoke M, Romani GL (eds) Evoked magnetic fields and electric potentials, vol 6. Advances in audiology. Karger, Basel, pp 40–69

Scherg M, Berg P (1996) New concepts of brain source imaging and localization. Electroencephalogr Clin Neurophysiol 46:127–137

Stephan KE, Weiskopf N, Drysdale PM, Robinson PA, Friston KJ (2007) Comparing hemodynamic models with DCM. Neuroimage 38:387–401

Tasseh N, Yaron A, Nelken I (2011) Stimulus-specific adaptation and deviance detection in the rat auditory cortex. PLoS ONE 6:e23369

Tiitinen H, May PJC, Reinikainen K, Näätänen R (1994) Attentive novelty detection in humans is governed by pre-attentive sensory memory. Nature 372:90–92

Tsodyks M, Markram H (1997) The neural code between neocortical pyramidal neurons depends on neurotransmitter release probability. Proc Natl Acad Sci USA 94:719–723

Ulanovsky N, Las L, Nelken I (2003) Processing of low-probability sounds by cortical neurons. Nat Neurosci 6:391–398

Ulanovsky N, Las L, Farkas D, Nelken I (2004) Multiple time scales of adaptation in auditory cortex neurons. J Neurosci 24:10440–10453

Uusitalo MA, Williamson SJ, Seppä MT (2006) Dynamical organisation of the human visual system revealed by lifetimes of activation traces. Neurosci Lett 213:149–152

Wang P, Knösche TR (2013) A realistic neural mass model of the cortex with laminar-specific connections and synaptic plasticity-evaluation with auditory habituation. PLoS ONE 8:e77876
Wang AL, Mouraux A, Liang M, Ianetti GD (2008) The enhancement of the N1 wave elicited by sensory stimuli presented at very short inter-stimulus intervals is a general feature across sensory systems. PLoS ONE 3:e3929
Wehr M, Zador AM (2003) Balanced inhibition underlies tuning and sharpens spike timing in auditory cortex. Nature 426:442–446
Wehr M, Zador AM (2005) Synaptic mechanisms of forward suppression in rat auditory cortex. Neuron 47:437–445
Wennekers T, Sommer F, Aersten A (2003) Cell assemblies. Theory Biosci 122:1–4
Westö J, May P, Tiitinen H (2016) Memory stacking in hierarchical networks. Neural Comput 28:327–353
Wilson H, Cowan J (1972) Excitatory and inhibitory interactions in localized populations of model neurons. J Biophys 12:1–24
Yarden TS, Nelken I (2017) Stimulus-specific adaptation in a recurrent network model of primary auditory cortex. PLoS Comput Biol 13:e1005437
Yates GK, Cody AR, Johnstone BM (1983) Recovery of eighth nerve action potential thresholds after exposure to short, intense pure tones: similarities with temporary threshold shift. Hear Res 12:305–322
Zacharias N, König R, Heil P (2012) Stimulation-history effects on the M100 revealed by its differential dependence on the stimulus onset interval. Psychophysiology 49:909–919
Zhao L, Liu Y, Shen L, Feng L, Hong B (2011) Stimulus-specific adaptation and its dynamics in the inferior colliculus of rat. Neuroscience 181:163–174

Publisher's Note Springer Nature remains neutral with regard to jurisdictional claims in published maps and institutional affiliations.

Declaration of honour

I hereby declare that I prepared this thesis without the impermissible help of third parties and that none other than the aids indicated have been used; all sources of information are clearly marked, including my own publications.
In particular, I have not consciously:

- fabricated data or rejected undesirable results,
- misused statistical methods with the aim of drawing other conclusions than those warranted by the available data,
- plagiarized external data or publications,
- presented the results of other researchers in a distorted way.

I am aware that violations of copyright may lead to injunction and damage claims by the author and also to prosecution by law enforcement authorities. I hereby agree that the thesis may be electronically reviewed with the aim of identifying plagiarism.
This work has not been submitted as a doctoral thesis in the same or a similar form in Germany, nor in any other country. It has not yet been published as a whole.

Magdeburg, June 21, 2022

Aida Hajizadeh